

Aerodynamics of a Dragonfly

by

Adrián Antón Álvarez

Submitted to the Department of Flow Physics and Technology
in partial fulfillment of the requirements for the degree of

Master of Science in Aerospace Engineering.

at the

TECHNISCHE UNIVERSITEIT DELFT

December 2024

© Technische Universiteit Delft 2024. All rights reserved.

Author
Adrián Antón Álvarez
Dec 4, 2024

Certified by
Stefan Hickel
Full Professor
Thesis Supervisor

Accepted by
Committee on Master Thesis

Aerodynamics of a Dragonfly

by

Adrián Antón Álvarez

Submitted to the Department of Flow Physics and Technology
on Dec 4, 2024, in partial fulfillment of the
requirements for the degree of
Master of Science in Aerospace Engineering.

Abstract

Nature has been optimizing for millions of years the aerodynamics of dragonflies. The main goal of the present thesis is to understand these mechanisms so that they can be further applied in future bio-inspired designs.

To start with, the experimental and numerical methodology is described (chapter 3). Next, a single flapping wing is studied under different conditions (chapter 4). Reynolds number, angle of attack, wing shape and corrugation effects are characterized. It is shown that dragonflies leading edge vortex is responsible for a great amount of lift production. Leading edge vortex circulation increases with Reynolds number, and so does lift. However, drag is also found to be a crucial contributor to the force balance that sustains dragonflies hovering. Additionally, corrugation effects improve aerodynamic efficiency in the studied flow regime.

Finally, wing-wing interaction effects are studied numerically in a whole dragonfly chapter 5. It is illustrated that phase changes between hindwings and forewings can maximize force production or be tuned to achieve a more stable and efficient hovering. However, not all phases are appropriate for maximum efficiency. Phase has to be tuned to maximize wake-capturing mechanisms and therefore flying efficiency. Finally, vorticity removal mechanisms are depicted to maintain a clean and uniform background flow that optimizes hovering efficiency.

Thesis Supervisor: Stefan Hickel

Title: Full Professor

Acknowledgments

I would like to thank Stefan Hickel and Ata Başkaya for their guidance and support. Dealing with numerical codes can be sometimes frustrating, but they were always willing to help and make things much easier.

Mention also the teachers, professors and people who have contributed to my education and have made it possible to reach this achievement. Special thanks to Inés for showing me another life perspective that is also necessary.

Finally, thanks to my family and friends, without you this would not be possible.

Contents

List of Figures	V
List of Tables	XIII
1 Introduction	1
2 Literature Review	9
2.1 Flying mechanisms and kinematics	9
2.1.1 Counter-stroking, hovering	11
2.1.2 Phased-stroking, forward flight	22
2.1.3 Synchronized and non-symmetric stroking, accelerated flight and turning ma- neuvers	26
2.1.4 Free flight, gliding	28
2.2 Aerodynamics and lift generation	31
2.2.1 Quasi-steady approximation and wake models	31
2.2.2 Unsteady methods	33
2.2.3 Leading edge vortex stability and 3D structure	37
2.2.4 Drag as a vertical force	44
2.2.5 Rotational force and wake capture	47
2.3 Wings interaction	51
2.4 Corrugation	57
2.4.1 Steady analysis	57
2.4.2 Unsteady analysis	58
2.5 Conclusions and summary of literature review	62
3 Methodology	65
3.1 Numerical formulation	65
3.1.1 Verification cases	66
3.2 Experiment design	74

3.2.1	Error analysis	75
3.2.2	Servo-motor	75
3.2.3	PIV	77
4	Experimental and numerical analysis of a single flapping wing	79
4.1	Comparison between experiments and numerical simulations	80
4.1.1	3D structure of the LEV	80
4.1.2	Analysis of the wake	85
4.2	Reynolds number effect	91
4.3	Angle of attack effect	97
4.4	Start up effect	103
4.5	Corrugation and actual dragonfly wing analysis	107
5	Numerical analysis of wing-wing interaction effects	115
5.1	Numerical set up	115
5.1.1	Hovering	115
5.1.2	Forward-flight	116
5.2	Comparison between different flapping strokes	117
5.3	Self-induced-dipole vorticity removal	128
6	Conclusions	131
A	Multibody solver	135
A.1	Theoretical formulation	136
A.1.1	Kinematic equations	136
A.1.2	Kinetic energy and generalized forces	140
A.1.3	Solid dynamic equations	142
A.1.4	Constraints	144
A.1.5	Constraints controller	148
A.1.6	Solver of the systems of equations	149
A.1.7	Time integration	150
A.1.8	Additional corrections	151
A.2	Verification cases	154
A.2.1	Simple Pendulum	154
A.2.2	Euler-Poinsot solid	162
A.2.3	Spherical Pendulum	166
A.2.4	Double Pendulum	172

B Dragonfly strokes visualization	179
B.1 Hovering, phased-stroking $\psi_0 = 0^\circ$	181
B.2 Hovering, leading-hindwing $\psi_0 = 90^\circ$	185
B.3 Hovering, leading-forewing $\psi_0 = -90^\circ$	189
B.4 Forward flight, counter-stroking $\psi_0 = 180^\circ$	193
C Dragonfly results for the 4 first strokes	197
Bibliography	207

List of Figures

1-1	Species evolution of <i>Odonata</i> into dragonflies and damselflies.	2
1-2	Flight performance of nine species of Odonata. PDF showing the frequency of each type of maneuver.	3
1-3	Analysis of hovering efficiencies of insects and actual propulsive systems.	4
1-4	Analysis of hovering efficiencies of insects and actual propulsive systems.	6
1-5	Reverse flow region in helicopter disk in forward flight.	7
2-1	Yaw, pitch and roll, 3-1-3 intrinsic rotation for body reference system \mathbf{X}_B	10
2-2	Chosen kinematic parameters of a generic dragonfly wing and body.	11
2-3	Horizontal stroke hovering.	12
2-4	Sketch of the "clap and fling" technique.	13
2-5	Inclined stroke hovering.	14
2-6	Kinematics of forewings and hindwings in dragonfly <i>Aeschna Juncea L.</i> during free flight and hovering. [74]	15
2-7	Detailed flapping kinematics of <i>Aeschna Juncea L.</i>	16
2-8	Summary of <i>Aeshna Cyanea</i> properties in pure hovering.	17
2-9	Power consumption at different flight speeds of dragonfly <i>Anax Parthenope</i>	18
2-10	Actual wing kinematics reported during dragonfly flight.	19
2-11	Dragonfly morphology of wing muscles and joints.	22
2-12	Wings kinematics in forward flight for <i>Libellula Pulchella</i>	23
2-13	Main kinematic parameters of dragonfly <i>Anax Parthenope Julius</i> . 4 experiments performed, 3 with specimen A, and 1 with specimen B.	24
2-14	Flapping angle ψ within the stroke plane. \circ , forewing; \diamond , hindwing. (A) Experiment 1 ($V = 0.7 \text{ ms}^{-1}$); (B) Experiment 2 ($V = 1.5 \text{ ms}^{-1}$); (C) Experiment 3 ($V = 2.3 \text{ ms}^{-1}$); (D) Experiment 4 ($V = 3.2 \text{ ms}^{-1}$).	25

2-15	Flapping angle ψ with respect to the stroke plane. Span position, \circ , $0.75R$; \diamond , $0.50R$; \triangle , $0.25R$. (A) Experiment 1 ($V = 0.7 \text{ ms}^{-1}$); (B) Experiment 2 ($V = 1.5 \text{ ms}^{-1}$); (C) Experiment 3 ($V = 2.3 \text{ ms}^{-1}$); (D) Experiment 4 ($V = 3.2 \text{ ms}^{-1}$). [9]	27
2-16	Wings kinematics of dragonfly <i>Libellula pulchella</i> in accelerated flight.	28
2-17	Kinematics of dragonfly <i>Polycanthagyna melanictera Selys</i> during a turning maneuver. 29	29
2-18	Experimentally measured polar of three specimens of dragonfly <i>S. sanguineum</i> forewing and hindwing.	29
2-19	Lift vs drag coefficient for different airfoils. $Re = 2 \times 10^4$	30
2-20	Above, ratio of quasi-steady circulation Γ_q to instantaneous circulation Γ , and quasi-steady lift and instantaneous lift. Below, ratio of quasi-steady lift and instantaneous lift. Flat plate suddenly set into transitional motion. λ is the number of chords covered by the flat plate.	32
2-21	Modelling wake vorticity.	33
2-22	Modelling wake vorticity.	34
2-23	Comparison of lift coefficients for pure-plunge and pitch-plunge.	35
2-24	Vorticity contours. Left, PIV measurements. Right, CFD simulation.	36
2-25	Reynolds number effect during pitch-plunge mode. Smoke visualization.	36
2-26	Dynamic stall. 3D numerical simulation. $Re = 10K$. High frequency, small amplitude during pure plunge.	37
2-27	Characteristic smoke patterns associated with the forewing downstroke in normal counterstroking flight. The video images show a tethered hawkler <i>Aeshna grandis</i> . Visualizations are shown for 5 spanwise stations along the wing (A–E), marked by colour-coded slices in the figure.	38
2-28	Different 3D LEV structures.	39
2-29	Creation of a secondary vortex structure that has opposite circulation: the lambda vortex (colored in red).	39
2-30	3D LEV structure.	40
2-31	Stabilizing the LEV. Spanwise blowing.	40
2-32	LEV dependence with Rossby and Reynolds numbers.	41
2-33	LEV vortex stability with higher aspect ratios AR.[68]	42
2-34	Stable LEV in a revolving wing.	44
2-35	Drag role during dragonflies hovering.	45
2-36	Experimental flapping of a flat plate.	46
2-37	Flapping of a flat plate. Experimental results.	48
2-38	Vertical forces in hovering depending on point of the stroke where rotation is started. 50	50
2-39	Wake capture and dependence of circulation with rotational axis.	50

2-40	Performance dependence with phase shift between forewing and hindwing.	52
2-41	Advection of vorticity in the wake is what really conditions the forces. This depends on phase and distance between ipsilateral hindwinds.	53
2-42	Velocity field in the wake of a flapping plate.	54
2-43	Vorticity contours of 2D numerical simulations. Blue indicates clock-wise vorticity and red counter-clock-wise vorticity. First column: single airfoil. Second column: in phase flapping, 0° . Third column: phased stroking, 90° . Fourth column: counter stroking, 180° . Each row contains the exact same point of the stroke of the hindwing. [20]	55
2-44	2D numerical simulation. LEV accumulation during hovering. [109]	56
2-45	Dipole self induction as a mechanism of vortex shedding. [129]	56
2-46	Flow visualization around corrugated wings.	57
2-47	Understanding the vortex dynamics within the corrugated valleys.	59
2-48	Numerical simulation of 3D corrugated wing.	60
2-49	Numerical simulation of a 2D flapping wing. Comparison between corrugated and flat plate.	61
3-1	Structured grid, with AMR ($n = 16$).	66
3-2	Snapshot of the instantaneous vorticity field in the 2D cylinder simulation. $Re = 100$. $n = 128$	67
3-3	$Re = 100$. $\Omega^* = 0.25$. Q criterion isocontours coloured by streamwise vorticity (ω_x). Yellow, downstream vorticity orientation; purple, upstream vorticity orientation. . .	69
3-4	Comparison of lift and drag coefficient for different non-dimensional rotation speeds Ω^* . $Re = 100$. References used: Giacobello [47], Kurose [60] and Niazmand [73] . . .	70
3-5	Comparison of streamlines contained on the $x - z$ plane (only considering u and v components), see axis system Figure 3-3. $Re = 100$. $\Omega^* = 0.25$	71
3-6	Present results in test case selected from. [71]	72
3-7	Convergence of pendulum trajectory with mesh refinement. Reference from [71]. . .	73
3-8	Experiment design. The laser sheet for PIV (blue) is active in both pictures.	74
3-9	Zoom into the experiment set up.	76
3-10	3D printed wings with different angles of attack. Blue bottom, 90° ; grey middle, 10° ; grey top, 25°	76
3-11	Photo of the planar PIV laser sheet with the flat plate at $\psi_0 = 0^\circ$. Note that the photo was not taken neither with the camera used for PIV, nor from the position of the PIV camera.	77
3-12	CAD of the 90° AoA flat plate at two different initial positions ψ_0 . For reference, $\psi_0 = 0^\circ$ is the position of the flat plate perpendicular to the depicted blue laser sheet.	77

3-13	Selection of image sampling rate for PIV and analysis of out of place displacement. [106]	78
4-1	$\psi_0 = 20^\circ$. Streamlines colored by velocity magnitude of the flow field at different span section. Flat plate flapping to the right. Shadow region colored in red. $Re = 392.7$. Instantaneously accelerated plate, constant ω . $\alpha = 70^\circ$	81
4-2	$\psi_0 = 40^\circ$. Streamlines colored by velocity magnitude of the flow field at different span section. Flat plate flapping to the right. $Re = 392.7$. Instantaneously accelerated plate, constant ω . $\alpha = 70^\circ$	82
4-3	$\psi = 40^\circ$. Q-criterion isorcontours colored by background vorticity. Slice colored by velocity magnitude. $Re = 392.7$. $\alpha = 70^\circ$	83
4-4	$\psi = 40^\circ$. Vorticity isocontour colored by wall distance. Velocity streamlines projected on the isocontour. $Re = 392.7$. $\alpha = 70^\circ$	84
4-5	$\psi_0 = 20^\circ$. Wake results for $Re = 392.7$. Instantaneously accelerated flat plate, $\alpha = 70^\circ$.	85
4-6	$\psi_0 = 20^\circ$. Wake results for $Re = 392.7$. Instantaneously accelerated flat plate, $\alpha = 70^\circ$.	86
4-7	$\psi_0 = 40^\circ$. Wake results for $Re = 392.7$. Instantaneously accelerated flat plate, $\alpha = 70^\circ$.	87
4-8	$\psi_0 = 60^\circ$. Wake results for $Re = 392.7$. Instantaneously accelerated flat plate, $\alpha = 70^\circ$.	87
4-9	PIV resolved spanwise velocity component. Wake results for $Re = 392.7$. Instantaneously accelerated flat plate, $\alpha = 70^\circ$. Approximated position of the LEV core indicated with a red line.	89
4-10	Fins placement in experiment published in [13].	90
4-11	$\psi_0 = 20^\circ$. Q-criterion isocontours colored by spanwise vorticity for different Reynolds numbers. Instantaneously accelerated flat plate, $\alpha = 70^\circ$	92
4-12	$\psi_0 = 40^\circ$. Q-criterion isocontours colored by spanwise vorticity for different Reynolds numbers. Instantaneously accelerated flat plate, $\alpha = 70^\circ$	93
4-13	$\psi_0 = 20^\circ$. $Re = 392.7$. Violet and red: slices at different spanwise distances, colored by spanwise vorticity. Yellow and blue: slices parallel to the flapping plane colored by vorticity normal to the flapping plane. Instantaneously accelerated flat plate, $\alpha = 70^\circ$.	94
4-14	$\psi_0 = 20^\circ$. Black and red: slices at different spanwise distances, colored by spanwise vorticity. White and purple: velocity slices parallel to the flapping plane colored by vertical velocity. Instantaneously accelerated flat plate, $\alpha = 70^\circ$	96
4-15	Comparison of lift and power coefficient dependence with Reynolds number. $AoA = 70^\circ$, instantaneously accelerated flat plate.	97
4-16	$\psi_0 = 20^\circ$. Q-criterion isocontours colored by spanwise vorticity for different AoA. Instantaneously accelerated flat plate, $Re = 392.7$	98
4-17	$\psi_0 = 40^\circ$. Q-criterion isocontours colored by spanwise vorticity for different AoA. Instantaneously accelerated flat plate, $Re = 392.7$	99

4-18	$Re = 392.7$. Flapping plate viewed from downstream. Slice colored by spanwise velocity component with projected streamlines. Blue (from root to tip) and red (from tip to root). Q-criterion that denotes the position of the LEV also colored with the same spanwise velocity color code.	100
4-19	$\psi_0 = 20^\circ$. $Re = 392.7$. Violet and red: slices at different spanwise distances, colored by spanwise vorticity. White and blue: slices parallel to the flapping plane colored by vertical velocity. Instantaneously accelerated flat plate, $\alpha = 70^\circ$	101
4-20	Assessment of flat plate at different angles of attack. Instantaneously accelerated flat plate, $Re = 392.7$	102
4-21	Evolution of the flapping angle and angular speed with time for the different start ups.	104
4-22	$\psi_0 = 20^\circ$. Streamlines colored by velocity magnitude projected onto the slice. $0.75b$. $\alpha = 70^\circ$	104
4-23	$\psi_0 = 40^\circ$. Wake results for $Re = 392.7$. $\alpha = 70^\circ$	105
4-24	$\psi_0 = 60^\circ$. Wake results for $Re = 392.7$. $\alpha = 70^\circ$	105
4-25	$\psi_0 = 20^\circ$. Q-criterion isocontours colored by spanwise vorticity for different AoA. Instantaneously accelerated flat plate, $Re = 392.7$	106
4-26	Comparison of the lift coefficient for the instantaneously accelerated flat plate $k = 0$ and the flat plate accelerating with a transient $k = 0.004$. $Re = 392.7$	106
4-27	Dragonfly species <i>Neurobasis Daviesi</i> hindwing.	108
4-28	$\psi_0 = 40^\circ$, $\alpha = 70^\circ$ and $Re = 91.7$. Green streamlines start upstream from the wing and are advected downstream. Black streamlines are generated along the the vortex core. Wing surface colored by pressure (suction red, pressure blue).	109
4-29	$\psi = 20^\circ$, $\alpha = 70^\circ$ and $Re = 91.7$. Corrugated wing.	109
4-30	$\psi_0 = 20^\circ$, $\alpha = 70^\circ$. Slices colored by spanwise vorticity for two different flapping angles. $Re = 91.7$. Wing surface colored by pressure (suction green, pressure blue).	110
4-31	$\alpha = 70^\circ$ and $Re = 91.7$. Q-criterion isocontours colored by spanwise vorticity. Streamlines projected onto the isocontour.	111
4-32	$\alpha = 70^\circ$ and $Re = 91.7$. Comparison of corrugated and smooth wing.	112
4-33	Shear stress magnitude (red high, blue low). $\alpha = 70^\circ$, $\psi = 40^\circ$ and $Re = 91.7$. Comparison of corrugated and smooth wing.	113
4-34	Pressure field contours (blue suction, red pressure). $\alpha = 70^\circ$, $\psi = 40^\circ$ and $Re = 91.7$. Comparison of corrugated and smooth wing. Slice at half span.	114
5-1	Q-criterion isocontours colored by z-vorticity component. Hovering $\psi_0 = 0^\circ$. End of fourth flapping cycle: $4.00 t/T$	117
5-2	Q-criterion, colored by z-vorticity component.	119
5-3	Norfolk-hawker dragonfly at rest [1].	120

5-4	Lift coefficients of all strokes. 4th flapping cycle.	123
5-5	Drag coefficients of all strokes. 4th flapping cycle.	123
5-6	Power coefficients of all strokes. 4th flapping cycle.	124
5-7	x-coordinate of the point of resultant force application, non-dimensionalized with the length of the dragonfly wing body. 4th flapping cycle.	124
5-8	2 forewings results. Hindwing effects on the forewings.	126
5-9	2 hindwings results. Forewings effects on the hindwings.	127
5-10	Self induction dipole mechanism in a dragonfly with $\psi_0 = 0^\circ$, phased-stroking. Slices with z-vorticity.	129
A-1	Sketch of the notation used in the different reference systems and position of each body.	136
A-2	(3-1-3) rotation sequence with Euler angles.	137
A-3	System of an airfoil and a flap. Modified configuration for landing.	148
A-4	Dependencies of constraints within the "tree system".	153
A-5	Variables that define the simple pendulum verification case.	155
A-6	Simple pendulum. Comparison of analytical (black line) and numerical solution (blue x). $N = 500$, $t = 0$ to $t = 50$. $\omega = 1$ and $\theta_0 = 0.001$ [rad].	156
A-7	Simple pendulum. Analysis of numerical error with time for $N = 500$ and $N = 1000$. $t = 0$ to 50 . $\omega = 1$ and $\theta_0 = 0.001$ [rad].	157
A-8	Simple pendulum. $N = 500000$, $t = 0$ to 5 . $\omega = 1$ and $\theta_0 = \frac{\pi}{2}$ [rad].	157
A-9	Simple pendulum. Convergence of numerical error with the number of time steps N . $t = 0$ to 5 . $\omega = 1$ and $\theta_0 = \frac{\pi}{2}$ [rad]. Newmark Trapezoidal time integration.	158
A-10	Simple pendulum. Energy preservation with the number of time steps N . $t = 0$ to 5 . $\omega = 1$ and $\theta_0 = \frac{\pi}{2}$ [rad]. Newmark Trapezoidal time integration.	159
A-11	Simple pendulum. Energy preservation with time. $N = 500000$ and $t = 0$ to 5 . $\omega = 1$ and $\theta_0 = \frac{\pi}{2}$ [rad]. Newmark Trapezoidal time integration.	160
A-12	Simple pendulum. Convergence of constraints error with time step N . $t = 0$ to 5 . $\omega = 1$ and $\theta_0 = \frac{\pi}{2}$ [rad]. Newmark Trapezoidal time integration.	161
A-13	Simple pendulum. Analysis of numerical error with time for $N = 500$ and $N = 1000$. $t = 0$ to 5 . $\omega = 1$ and $\theta_0 = \frac{\pi}{2}$ [rad]. Newmark Trapezoidal time integration.	162
A-14	Axial symmetric Poincot solid. Schematic of Euler angle velocities with 3-1-3 notation. \mathbf{H}_O is the angular momentum, and $\boldsymbol{\omega}$ the angular velocity. z_1 is the inertial axis, and z the one attached to the body reference frame. [69]	163
A-15	Poincot solid. Comparison of numerical and exact solution. $t = 0$ to 10 . $N = 50$. Newmark Trapezoidal time integration.	165
A-16	Poincot solid. Analysis of numerical error with time for $N = 50$ and $N = 100$. $t = 0$ to 10 . Newmark Trapezoidal time integration.	165

A-17 Poinso solid. Analysis of convergence of numerical error with time step size. $t = 0$ to 10. Newmark Trapezoidal time integration.	166
A-18 Spherical pendulum. Analysis of convergence of numerical error with time step size. $t = 0$ to 10. Newmark Trapezoidal time integration.	167
A-19 Spherical pendulum. Comparison of ψ and θ between numerical solution with $N = 50$ and exact values. $t = 0$ to 2. Newmark Trapezoidal time integration.	168
A-20 Spherical pendulum. Comparison of x and y between numerical solution with $N = 50$ and exact values. Newmark Trapezoidal time integration.	169
A-21 Spherical pendulum. Euler Angles error evolution with time. Compared cases: $N =$ 50 and $N = 100$. $t = 0$ to 2. Newmark Trapezoidal time integration.	170
A-22 Spherical pendulum. Analysis of convergence of numerical error in position with time step size. $t = 0$ to 2. Newmark Trapezoidal time integration.	170
A-23 Spherical pendulum. Convergence of energy preservation with time step size. $t = 0$ to 2. Newmark Trapezoidal time integration.	171
A-24 Spherical pendulum. Energy preservation evolution with time. $N = 5000$. $t = 0$ to 2. Newmark Trapezoidal time integration.	172
A-25 Double pendulum. Sketch of the double pendulum system with parameters that define the problem.	173
A-26 Double pendulum. Comparison of the <i>Reference</i> $x-y$ coordinates with the numerical data obtained with the Multibody solver for $N = 50$. $t = 0$ to 5. Pendulum 1 X_1 , and pendulum 2 X_2 . Newmark Trapezoidal time integration.	174
A-27 Double pendulum. Evolution of θ with time. Comparison of the <i>Reference</i> and numerical data obtained with the Multibody solver for $N = 50$. $t = 0$ to 5. Pendulum 1 X_1 , and pendulum 2 X_2 . Newmark Trapezoidal time integration.	174
A-28 Double pendulum. Analysis of Δz and Δy position error with respect to the <i>Reference</i> . $t = 0$ to 5. $N = 50$ and $N = 100$. Newmark Trapezoidal time integration.	175
A-29 Double pendulum. Analysis of convergence of numerical error with time step size. $t = 0$ to 5. Newmark Trapezoidal time integration.	176
A-30 Double pendulum. Energy preservation with smaller time steps. $t = 0$ to 5. Newmark Trapezoidal time integration.	177
A-31 Double pendulum. Energy conservation with time. $t = 0$ to 5. $N = 5000$ and $N = 10000$. Newmark Trapezoidal time integration.	177
B-1 Q-criterion, colored by z-vorticity component.	181
B-2 Vorticity z-component slices.	182
B-3 Vertical y-velocity component slices.	183
B-4 Q-criterion, colored by z-vorticity component.	185

B-5	Vorticity z-component slices.	186
B-6	Vertical y-velocity component slices.	187
B-7	Q-criterion, colored by z-vorticity component.	189
B-8	Vorticity z-component slices.	190
B-9	Vertical y-velocity component slices.	191
B-10	Q-criterion, colored by z-vorticity component.	193
B-11	Vorticity z-component slices.	194
B-12	Vertical y-velocity component slices.	195
C-1	Lift coefficients for different strokes. 4 first flapping cycles.	199
C-2	Drag coefficients for different strokes. 4 first flapping cycles.	201
C-3	Power coefficients for different strokes. 4 first flapping cycles.	203
C-4	Non-dimensional x-coordinate of point of force application. 4 first flapping cycles.	205

List of Tables

1.1	Propeller system characteristics for hovering. HE = Hovering Efficiency, D = Dimensional, C = Corrected.	5
2.1	Kinematics reported of living dragonflies in nature during hovering.	19
2.2	Kinematics implemented in computational and experimental studies of hovering dragonflies. Wing angles are described with respect to the inertial (horizontal) reference frame.	21
3.1	Grid convergence of the 2D cylinder simulation. $Re = 100$	67
3.2	Comparison of present results with the literature. $Re = 100$	68
5.1	Statistics of each dragonfly body component and stroke type in the 4th flapping cycle.	122
A.1	Family of Newmark integration schemes.	150

Chapter 1

Introduction

Dragonflies belong to the insect order *Odonata*. *Odonata* contains both dragonflies *Anisoptera* and damselflies *Zygoptera*. Dragonfly origins can be traced back to 250 million years ago, see Figure 1-1, when the *Odonata* subdivided into damselflies and dragonflies. Data has been found that proves that the first dragonflies were much bigger than the ones existing today, with wing spans of 70 *cm* [58]. However, they quickly reduced their size to adapt to the predominant smaller size of other insects. This makes sense, as dragonflies with a smaller size consume less energy, and therefore did not need to hunt so many small insects. Despite this, morphological features of dragonflies have remained almost unchanged for almost 200 million years. This tends to indicate that according to Darwin's evolutionary theory, their physiology was already well developed since long ago. Their hunting abilities were clearly superior to other insects, and they quickly expanded all across the globe. Nowadays, more than 3000 dragonfly species are known, and they can be found in the five continents [58].

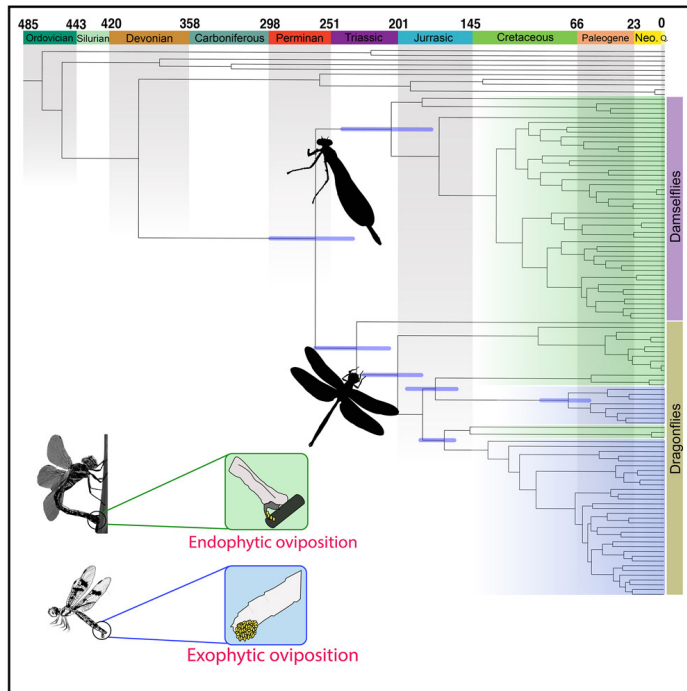


Figure 1-1: Species evolution of *Odonata* into dragonflies and damselflies.

[58]

Dragonflies are insects with notable flying capabilities. *Pantala Flavescens*, widely known as the *globe skimmers*, cross the Indian Ocean during their life span, a distance of more than 6000 km [16]. This is one of the largest known migrations of insects, and is a remarkable feat that shows the superior endurance and efficient flight of dragonflies. Moreover, apart from their stamina and long range capabilities, they are also incredibly agile flyers. This species is considered one of the "high-performance" flying insects [7]. Taylor [116] was able to measure speeds up to 5 ms^{-1} , 100 times per second their body length. To put this into perspective, the fighter jet *F-35 Lightning*, can only reach maximum speeds of 35 times per second their body length [50]. Moreover, dragonflies can achieve maximum accelerations of $6g$ and turn rates of more than 1000 degrees per second, almost three 360 degree turns in a second, see Figure 1-2.

Additionally, dragonflies have much more degrees of freedom during flight than a conventional aircraft or helicopter. They can fly backwards, forwards, upwards, downwards, hover, glide, accelerate and do quick turns, and even fly upside down [138]. All these flight modes are achieved thanks to the independent control of each of their four wings. Subtle changes of phase, amplitude or feathering angle of each wing are key to achieve such remarkable aerodynamic characteristics. They can even control their tail position to balance their centre of mass and achieve a great longitudinal stability [79].

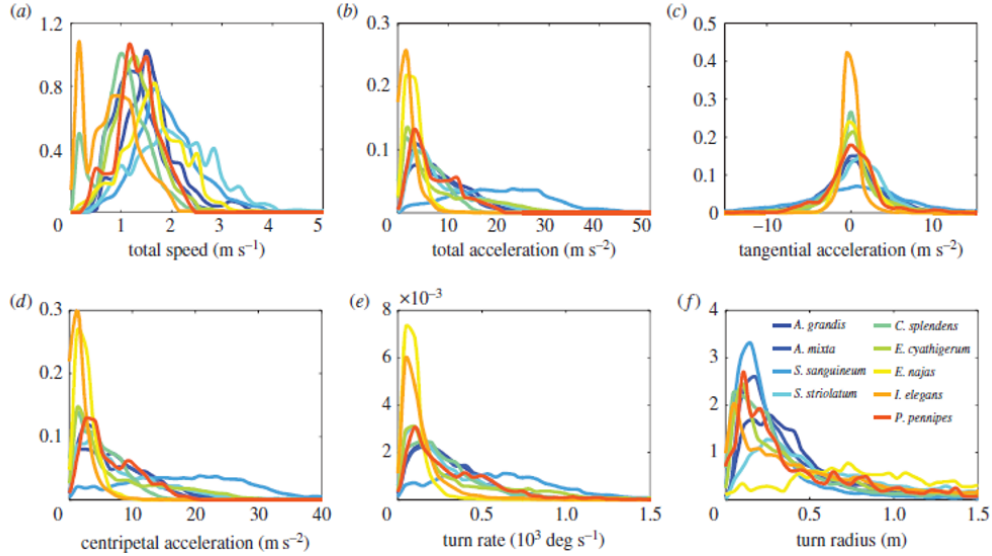


Figure 1-2: Flight performance of nine species of Odonata. PDF showing the frequency of each type of maneuver.

[16]

These accelerations and maneuverability are unattainable by most insects. Dragonflies in nature have capture success rates from 83 % to 97 % [82] [32]. This is a strikingly high success rate, and it is rare that other animal species can even come close to these numbers [82]. This puts into perspective the dominance and superiority of dragonflies agility, being almost unavoidable killers.

Several researchers have considered dragonflies as especially efficient flyers. For example, Wang [127] asserted that dragonflies "are some of the best hoverers" due to the incredibly high lift coefficients they can achieve: between 2 and 6. Note that maximum steady lift coefficients of dragonfly wings are around 1, which means that dragonflies are able to control super-lift via highly unsteady aerodynamics. The natural question that follows is if these insects are still superior when compared to modern flying systems created by humans. This is going to be studied for hovering, the flying mode that is going to occupy most of the present thesis. Helicopters are clearly the reference to take when considering dragonfly hovering. A first, comparison could be done looking at the Hovering Efficiency in its dimensional form:

$$HE, D = \frac{m}{P}, \quad (1.1)$$

where m is the mass that can be sustained in hovering provided a given power consumption P . Following this definition, HE, D as high as possible would be desirable. Liu [65] did a comparative analysis of insects typical $Specific\ Power = \frac{1}{HE, D}$ and human-made propulsive systems. It can be seen that the $Specific\ Power$ required to lift a mass is one order of magnitude smaller in insects

using flapping mechanisms, see Figure 1-3a. This seems to clearly indicate that insects flapping technique, and in particular dragonflies, have a superior efficiency. However, this is not so simple, as only systems with equivalent *Disk Loading* = $DL = \frac{m}{S}$ (S is the disk area for propellers or wing area for insects) should be compared. The reason for this can be explained following a simple disk actuator model [88]. In hovering, thrust T should be equal to weight $W = mg$ so:

$$W = mg = 2\rho S V_D^2 \rightarrow V_D = \sqrt{\frac{mg}{2\rho S}} \quad (1.2)$$

$$P = TV_D = mgV_D = \frac{(mg)^{3/2}}{\sqrt{2\rho S}} \rightarrow \frac{m}{P} = \sqrt{\frac{2\rho S}{m}} (g)^{-3/2} = (g)^{-3/2} \sqrt{2\rho} \frac{1}{\sqrt{DL}}, \quad (1.3)$$

where V_D is the induced velocity, and ρ the density, both at the actuator disk. It can be seen how indeed the dimensional hover efficiency depends on the disk loading DL . This scaling with $\frac{1}{\sqrt{DL}}$ was proved in detail with different modern propellers in Qin *et al.* study [88], see Figure 1-3b.

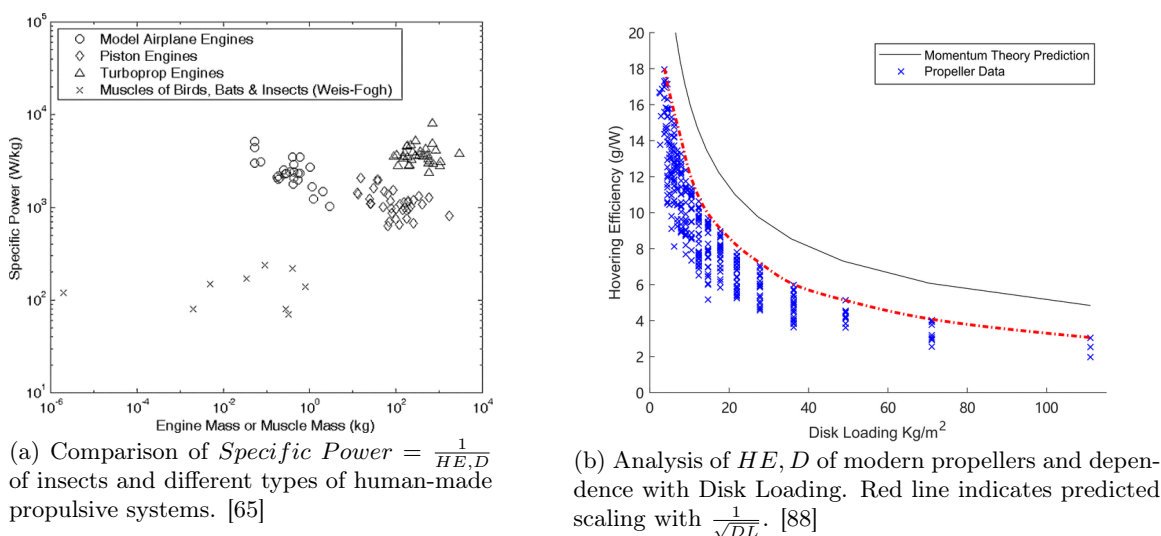


Figure 1-3: Analysis of hovering efficiencies of insects and actual propulsive systems.

Therefore, to take into account the *Disk Loading* dependence, a new parameter is going to be defined:

$$HE, C = \frac{m}{P} \sqrt{DL}. \quad (1.4)$$

Two helicopters are going to be compared with generic dragonfly species using this new Hovering Efficiency definition: AeroVelo Atlas and CH53 E Super Stallion. AeroVelo Atlas was designed as an extreme case with a minimum Disk Loading, so as to minimize the required power to lift

for a certain mass. See in Figure 1-4a how the disk area is exaggeratedly increased. Because of this, the non corrected Hovering Efficiency HE, D of the AeroVelo Atlas is the biggest one of the three vehicles as it can be seen in *Table 1.1*. However, when a fair comparison is done, that is the optimal lift generation strategy given a disk area and the mass of the object, then it is seen that the dragonfly (*S. sanguineum*) has a similar performance compared to the Super Stallion. Nevertheless, *S. sanguineum* HE, D was found using a quasi-steady approximation, and Sun *et al.* reported that it underestimates by a 50% the power which is needed for a given mass. For this reason, a well resolved computational study of *Aeschna juncea* is also included [114]. Indeed, it can be seen how the final HE, C for dragonflies is lower, less than half of the value obtained with the CH53 E Super Stallion.

Flyer Type	Mass [kg]	Surface [m ²]	HE, D [kg/W]	HE, C [$\frac{kgN^{1/2}}{Wm}$]
Dragonfly (<i>S. sanguineum</i>), quasi-steady [124]	0.000130	0.000320	0.0584	0.0372
Dragonfly (<i>Aeschna juncea</i>), CFD [114]	0.000754	0.00180	0.0272	0.0176
AeroVelo Atlas [66]	128	1300	0.174	0.0546
CH53 E Super Stallion [66]	33000	460	0.00449	0.0380

Table 1.1: Propeller system characteristics for hovering. HE = Hovering Efficiency, D = Dimensional, C = Corrected.

Based on the previous observation, it may seem that dragonflies are less efficient fliers than modern helicopters. However, it is important to mention that helicopters and dragonflies do not actuate at similar Re numbers, which is really important when assessing the lift to drag ratio L/D of the blades/wings. Lian *et al.* [63] determined that for lower Re the ratio L/D decreases due to a thicker boundary layer profile and sooner detachment of the flow (low energetic boundary layer). Dragonflies and Micro Air Vehicles (MAVs) in general tend to fly at much lower Re than helicopters. This lowers the aerodynamic efficiency L/D of conventional airfoil/blade configurations an order of magnitude [91]. The coefficient HE, C would also decrease an order of magnitude, as it is proportional to the aerodynamic efficiency in helicopters. Consequently, based on this preliminary study, at low Reynolds numbers which are characteristic of MAVs, flapping becomes a superior alternative to rotatory wings. In the literature other studies have been done comparing rotatory and flapping wings for low Reynolds numbers [11][135]. Overall there is consensus that flapping wings have a superior aerodynamic performance at sufficiently low Reynolds numbers ($Re < 10000$) and high lift coefficients ($Cl > 1$). Given that dragonflies fly at around ($Re \approx 1000$) and have really

high lift coefficients in hovering ($\bar{C}l = 2$ to 4) [124], flapping is the optimal flying strategy.

All in all, this indicates that dragonflies flapping technique and configuration are a serious candidate to improve current efficiency in near hovering manoeuvres for low Reynolds number regimes in MAVs.



(a) AeroVelo Atlas. [66]



(b) CH53 E Super Stallion. [53]

Figure 1-4: Analysis of hovering efficiencies of insects and actual propulsive systems.

Dragonflies flapping has been proved to be an efficient alternative to conventional propellers which are used for hovering. However, is this the same for example for other flying modes such as forward flight? The answer is that for sufficiently high speeds, fixed wings configurations with propfans are much more efficient than flapping [65]. The reason for this is that fixed wings can achieve flight at a constant and optimal angle of attack, with maximum aerodynamic efficiencies L/D . When flapping occurs, local angle of attack varies, and therefore the wings are not always flying at optimal conditions. On the other hand, for relatively slow flight conditions, steady aerodynamics is not sufficient, and unsteady flapping is needed to generate enough lift. At these flying conditions flapping becomes a much more viable alternative. Moreover, helicopters which are the other human-made alternative, do not behave properly in forward flight, because of the reverse flow region that is created inside of the disk, see Figure 1-5. On the other hand, dragonflies can avoid this by tuning the pitch angle of their wings to have optimal incidence angles at different speeds.

In summary, dragonflies display an outstanding agility and maneuverability, and at the same time are efficient flyers. Consequently, having analyzed the flight envelope and performance of dragonflies, it can be inferred that in slowly flying or hovering vehicles and at low Reynolds numbers, when there is not enough dynamic pressure to fly with steady aerodynamics, it might be a good idea to consider these insects in order to improve flight efficiency and manoeuvrability.

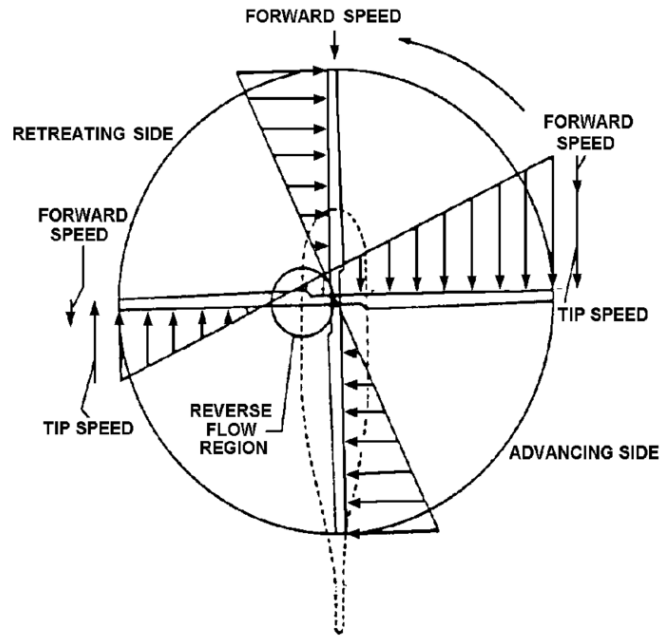


Figure 1-5: Reverse flow region in helicopter disk in forward flight.

[55]

Chapter 2

Literature Review

2.1 Flying mechanisms and kinematics

The first step when trying to study the aerodynamics of a dragonfly is understanding the kinematics that they follow. Once this is understood, then different aerodynamic phenomena can be identified. Dragonflies have four wings with several degrees of freedom in each wing. For this reason a formalism to identify these complex kinematics is going to be provided below.

In order to characterize the kinematics of the periodic movement of dragonfly wings, a Cartesian system \mathbf{X}_B is attached to the body of the dragonfly, with the \mathbf{x}_B axis aligned with the body pointing towards the tail, the \mathbf{z}_B axis defining the symmetry plane $\mathbf{x}_B - \mathbf{z}_B$ between the right and left wings, and the \mathbf{y}_B axis so as to have a right-hand-side-oriented Cartesian system, see Figure 2-1. The Cartesian system \mathbf{X}_B will be centered in the center of mass of the dragonfly body during its implementation in the Multibody solver, Appendix A. The body system \mathbf{X}_B is oriented with respect to the inertial reference system \mathbf{X}_0 following a 3-1-3 intrinsic Euler rotation: yaw ψ_B , pitch θ_B and roll ϕ_B . Then, a Cartesian system is attached to each wing of the dragonfly, \mathbf{X}_{W1} , \mathbf{X}_{W2} , \mathbf{X}_{W3} and \mathbf{X}_{W4} . These wings systems \mathbf{X}_W will be placed in the center of rotation of each wing in the Multibody solver implementation. The \mathbf{z}_W axis of each wing will be contained within the torsion axis (leading edge approximation in many cases due to stiffness of the veins), pointing outwards from the body to the wing tip for the right wings (right looking from behind of the insect tail), and inwards from the wing tip to the body for the left wings. Each wing \mathbf{x}_W axis will be defined so that the plane $\mathbf{x}_W - \mathbf{z}_W$ contains the wing (assuming flat plate wings, with no deformation), and is pointing towards the tail. The \mathbf{y}_W axis is oriented in each wing to have a right-hand-side-oriented Cartesian system, see Figure 2-2.

To orient the wings with respect to the body reference frame \mathbf{X}_B , the Euler angles will be used. In particular, following the literature [7] [8] [9], a 3-1-3 intrinsic rotation will be used, see Figure 2-2.

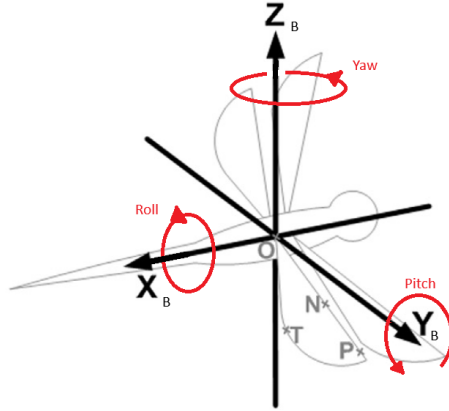


Figure 2-1: Yaw, pitch and roll, 3-1-3 intrinsic rotation for body reference system \mathbf{X}_B .

The wing reference system \mathbf{X}_W is initially oriented ($\psi = 0^\circ, \theta = \frac{\pi}{2}^\circ, \gamma = \frac{\pi}{2}^\circ$) with the \mathbf{x}_W axes of all wings aligned with the body \mathbf{x}_B body axis. Additionally, all wings will have the axis \mathbf{z}_W pointing in the same direction as \mathbf{y}_B for the initial position. First, starting from the initial position ($\psi = 0^\circ, \theta = \frac{\pi}{2}^\circ, \gamma = \frac{\pi}{2}^\circ$) a $\frac{\pi}{2} - \gamma$ rotation will be done around the \mathbf{z}_W axis. This rotation will define the stroke plane of both left and right wings. Second, a ψ rotation (the flapping angle) will be done around the \mathbf{x}_W axis for the right wing, and a $-\psi$ rotation for the left wings. The maximum amplitude of the flapping angle is denoted with Φ . Third, a $\frac{\pi}{2} - \theta$ rotation around the \mathbf{z}_W axis, that defines the feathering (pitch) angle for both right and left wings. With this, the full kinematics of the dragonfly are defined.

Dragonflies tend to fly following constant stroke plane angles $\gamma \approx 60^\circ$ [74] [100]. It is important to note that during this document the stroke plane (and other wing angles) are defined with respect to the body axis \mathbf{X}_B . In the literature the wing angles are sometimes referred to the inertial system \mathbf{X}_0 [123] [96], but in this case the stroke plane is not constant anymore [9]. The flapping angle follows a sinusoidal distribution, with maximum speed at the middle of the downstroke [115]. The amplitude of the flapping cycle varies slightly depending on the power requirements, while the frequency tends to be invariant [86]. Finally, dragonflies tune the feathering angle of their wings during the flapping cycle to control different aerodynamic phenomena that will be explained in more detail in section 2.2. It has been observed [115] [100] that dragonflies tend to vary the phases of the flapping cycles between each wing depending on the flying mode. In particular, counter-stroking or 180° phase between ipsilateral wings has been observed in hovering [26] [123]; near 90° phase or phased-stroking in forward flight [98] [123]; and 0° phase or synchronized-stroking in accelerated flight [98] [123] [26]. All the present literature on these flying modes, and in addition gliding and turning maneuvers will be reviewed in the following subsections subsection 2.1.1, subsection 2.1.2, subsection 2.1.3 and subsection 2.1.4.

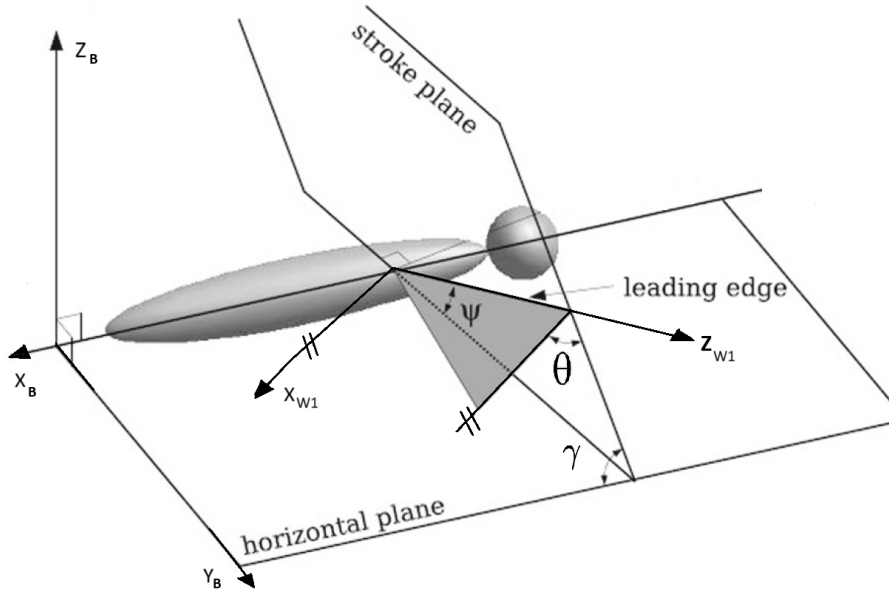


Figure 2-2: Chosen kinematic parameters of a generic dragonfly wing and body.

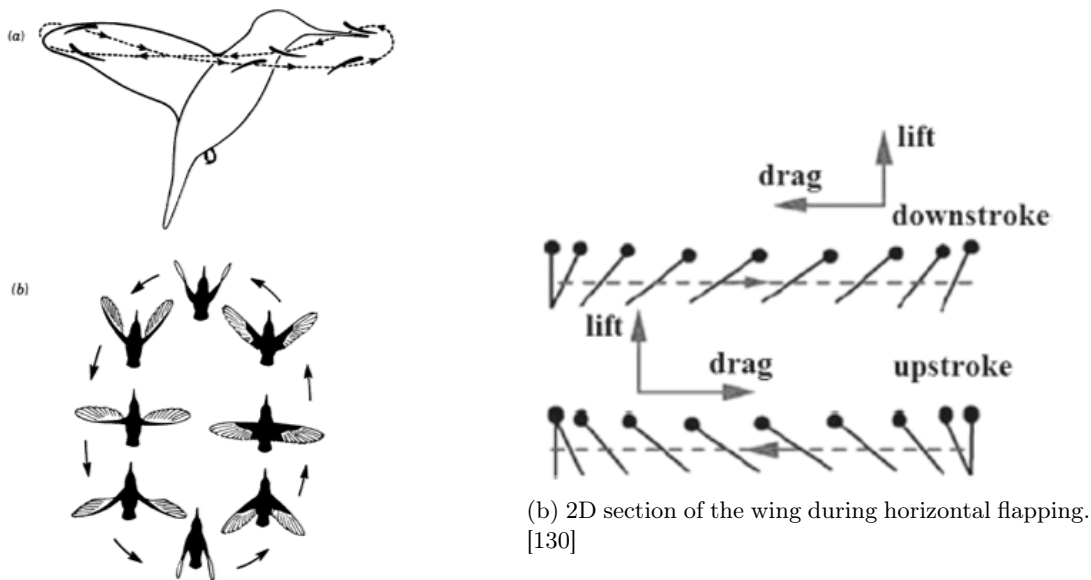
2.1.1 Counter-stroking, hovering

Hovering is the first step to understand flying insects. Once a stable force that is able to compensate weight is developed and understood, small changes on the applied direction of the force might achieve all kinds of different flight maneuvers. For this reason, hovering is going to be studied in more detail. First, general hovering strategies in animals are going to be considered, so as to have a good picture of insect hovering techniques. Second, dragonfly hovering is going to be studied in more detail.

Animals hovering

Animals can be classified into three types according to their hovering strategy [40]: horizontal stroke, inclined stroke and vertical stroke. This classification is based on the flapping stroke plane of the animal, which greatly defines the aerodynamic mechanisms that are being used.

First, the horizontal stroke is going to be analyzed. Weis-Fogh and Torkel [132] noted that this flapping strategy can be seen in animals such as hummingbirds. Moreover, Weis-Fogh and Torkel [133] discovered that most insects in nature use this flapping strategy. This hovering mechanism can be seen in Figure 2-3a, the bird claps its wings forwards and backwards, maintaining the leading edge in an horizontal plane. The main aerodynamic mechanism that makes this possible can be seen in Figure 2-3b. During the stroke from left to right the drag has the opposite sign compared to the other half of the cycle. Therefore the drag forces cancel, and the net force over the cycle is only vertical, allowing this way hovering. The aerodynamic cycle is quite similar to that of an helicopter, but this time the wings follow a translational motion instead of a circular one. Ellington [41] hypothesized that this translational flapping might have the advantage to recover part of the



(a) Horizontal flapping of a bird. Above, side-way view of the bird. Below, view of the bird from above. [40]

Figure 2-3: Horizontal stroke hovering.

wake energy released in the previous half stroke. During the first half of the cycle, when the wing is going from left to right, the wake has an induced component of velocity going also from left to right. When the flapping is reversed, the previously induced velocity gives an additional dynamic pressure to the wing that enhances lift. This is unique to translational flapping, and it is not used in an helicopter, where the wake is just propagated downstream following an helical path, without energy recovering.

Weis-Fogh and Torkel [133] also discovered an interesting aerodynamic phenomenon that enhanced lift production in horizontal flapping: clap and fling. The key of this mechanism is to avoid the well known "Wagner Effect", that is, to avoid the lift delay due to the vortex shed when there is a huge lift increase at the wing. First, looking at B in Figure 2-4 the two wings are approaching to each other. When the upper edges of both wings join, phase C, a kind of hinge is created that only allows air to go downwards. The rotation of the wings in the last phase of the clap expels downwards the air between both plates, phase E, and due to Newton action-reaction principle, a super-lift component is created. However, the most relevant part of the cycle in terms of lift is yet to come: the fling. The wings keep its rotation, and a huge space without air is created just above the plates, phase F, which creates a huge suction and therefore creates a down wash that tries to cover this void space. This of course generates an enormous lift during a short instant of time, due to this suction. The most relevant fact is that this down wash creates two opposite sign vortices attached to the top of each wing, see phase H. Due to Kelvin theorem, the net vorticity in the flow should

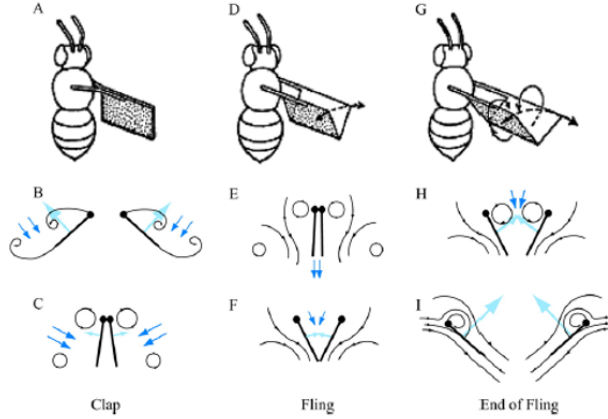


Figure 2-4: Sketch of the "clap and fling" technique.
[133]

remain constant. This implies that in normal flapping when a vortex is created that generates lift, another opposite sign vortex is shed downstream. However, this shed vortex diminishes the circulation attached to the wings, and produces the "Wagner Effect", which is a temporarily reduced lift that keeps later on recovers its intensity when the shed vortex is moving further downstream. On the other hand, with this "fling" mechanism, instead of having a shed vortex downstream, the opposite sign vorticity is attached to the other wing and is used in an effective way to produce lift. Moreover, a huge circulation is attached to both wings since the beginning of the horizontal stroke, see phase I, which implies great lift with no time lag, or no "Wagner Effect".

The "clap and fling" has been reported [132] to be a really useful way of producing unsteady forces, and has been implemented in most of the recently bio-inspired MAVs: DARPA's Hummingbird [57], FW-MAV [84], DelFly [34], RoboBee [134], etc. Weis-Fogh and Torkel [133] also realized that "clap and fling" was quite common in nature. However, Rüppell [96] only did observe a kind of "clap and fling" in 1 of the 16 cases studied in various dragonfly species. This tends to suggest that dragonflies rarely use this technique, and might be using other aerodynamic mechanisms. Rüppell hypothesized that the clapping phase might be damaging for the wings, and therefore the insects with largest life spans tend to avoid it.

The next type of hovering is the inclined stroke hovering. This is much more infrequent in nature than horizontal hovering [132]. It is done for example by small passerine birds [76], bats (Figure 2-5a) [75] and dragonflies [74]. These animals appear to generate relatively small forces on the upstroke. The dragonfly *Aeschna Juncea L.* [74] strongly supinates its wings on the upstroke, making the angle of attack near zero, and reducing the pressure drag. However, during the downstroke it uses large angles of attack to create a vertical force. In the horizontal flapping strategy drag was cancelled, and only lift was giving a net resultant across the cycle. On the other hand, due to the inclined flapping, drag also starts to be relevant and contributes greatly to lift during the downstroke, see

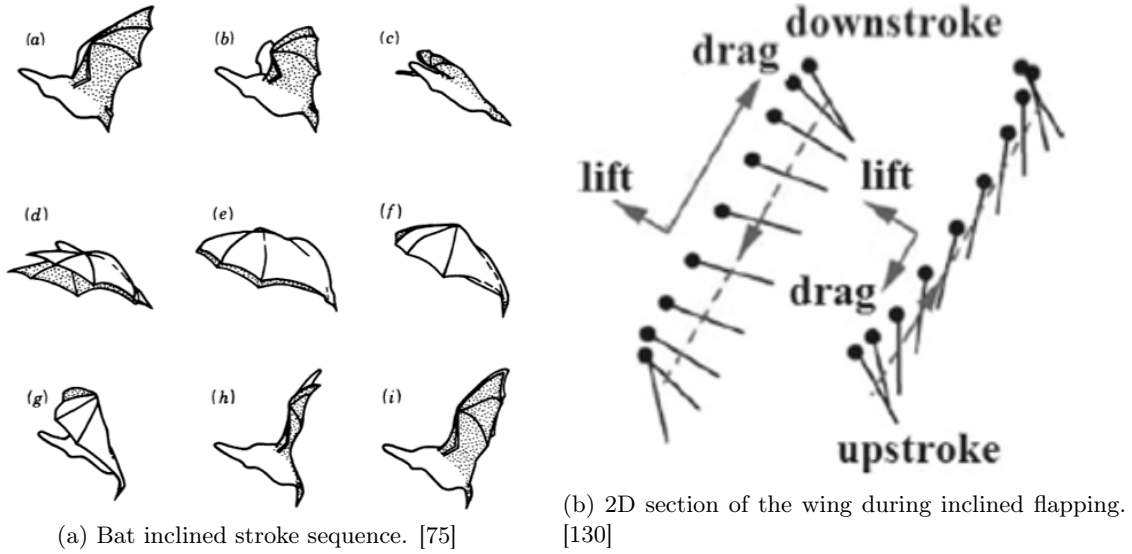


Figure 2-5: Inclined stroke hovering.

Figure 2-5b. This mechanism is completely different to horizontal flapping, and might be also the reason why dragonflies do not benefit so much from "clap and fling".

Finally, the third type of flapping observed in nature is vertical flapping. This is by far the less common stroke. The Large Cabbage White butterfly *Pieris brassicae* L was the only animal reported by Ellington and Porter [40] to do this. The main sustaining force is the pressure drag. The pressure drag during the downstroke is bigger than the skin friction of the upstroke, and consequently a net vertical force is produced. This asymmetry between the upstroke and downstroke are achieved by a greater supination that minimizes the angles of attack during the upstroke.

Dragonflies hovering

Norberg [74] was the first one to notice that dragonflies tend to vary the phase between ipsilateral wings between different maneuvers. He observed the dragonfly *Aeschna Juncea* L. during free flight and hovering, Figure 2-6. The position of the body was slightly pitching down: $\theta_B = -2^\circ$ and $\phi_B = 0^\circ$. The flapping frequency f in the three specimens was 36, 36 and 37 Hz. The stroke plane was defined as 59.8° with respect to the horizontal, which is equivalent to $\gamma_W = 57.8^\circ$ in body axis.

Norberg [74] and later other authors [8][9] stated that a sinusoidal representation of the flapping and feathering angle of the wing was able to capture quite accurately its kinematics. Norberg found the following approximation of the flapping angle kinematics in the stroke plane:

$$\psi_F = 5 + 30\sin(2\pi ft) \quad (2.1)$$

$$\psi_H = 15 + 30\sin(2\pi ft), \quad (2.2)$$

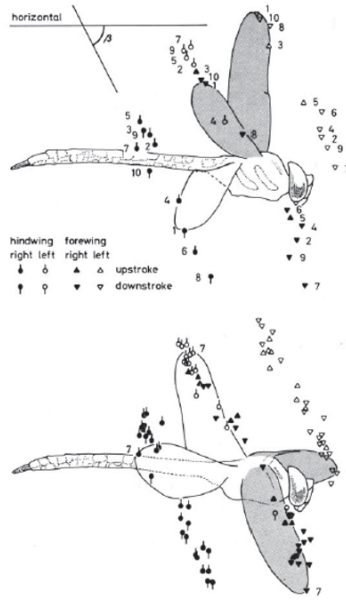


Figure 2-6: Kinematics of forewings and hindwings in dragonfly *Aeschna Juncea L.* during free flight and hovering. [74]

where ψ_F and ψ_H are the flapping angles of the forewings and hindwings respectively in degrees. Norberg facilitated the data from his research to Savage [103], and he further described the flapping cycle in a more precise manner, see Figure 2-7.

Nevertheless, Norberg [74] was not able to quantify the feathering angle θ_W of the wings, although he observed a strong rotation and supination at the end of the downstroke and upstroke. The particular feature of hovering was the phase between ipsilateral hindwings: the hindwings led the forewings by almost 180° . This phase is convenient to achieve a more uniform lift with smaller force fluctuations [131] and it is also appropriate to extract energy [94] from forewing-hindwing interaction.

Despite a good description of the stroke plane and flapping angles, the feathering angles during hovering of dragonflies in free flight have been reported in literature in a limited way. Ruppell [96] did an extensive study of dragonfly and damselfly kinematics for several species. Of all his 16 study cases, only one case was associated with pure hovering: dragonfly *Aeshna Cyanea*. The main relevant properties of this hovering case can be found in Figure 2-8. Flapping frequencies are identical to those measured by Norberg. Stroke plane with respect to the horizontal is also quite similar, 50° . Ruppell reported different and slightly higher stroke amplitudes for the hindwing and forewing, but this could be perfectly explained by the different species. The major and most remarkable difference is that in this hovering case the phase shift was 72° , far away from the 180° case reported by Norberg. This phase is more characteristic from the cases reported for forward flight, and might indicate that dragonflies can also hover within a wide range of out-of-phase flapping configurations. What is more interesting from Ruppell results, is that he provides the angle of attack

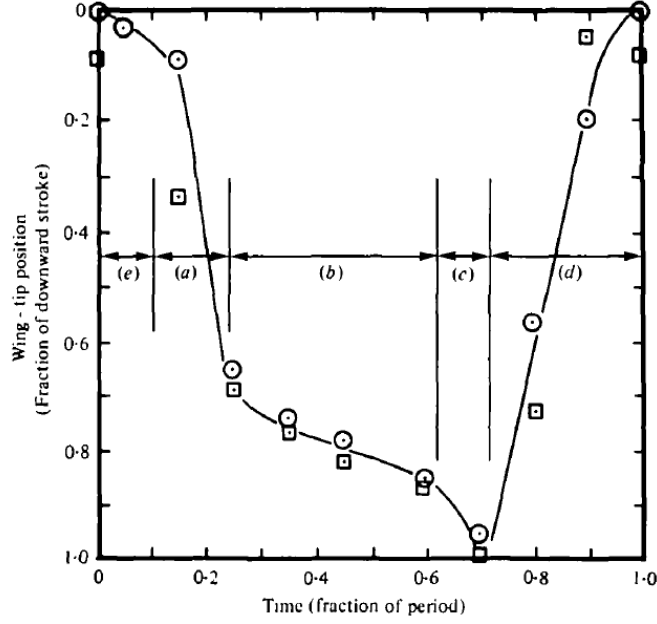


Figure 2-7: Detailed flapping kinematics of *Aeschna Juncea L.*
[103]

α at the middle of the downstroke and upstroke for both, the forewing and hindwing, see Figure 2-8. This can be converted to pitch angle of the wing plane relative to the horizontal plane as follows (assuming flapping contained in stroke plane):

$$\theta_0^D = \alpha_W^D - \gamma_W \quad (2.3)$$

$$\theta_0^U = \pi - \alpha_W^U - \gamma_W, \quad (2.4)$$

where U and D stand for the upstroke and downstroke respectively. Using the previous expression the following pitch angles relative to the horizontal plane are found:

$$\theta_f^D = -5^\circ \quad (2.5)$$

$$\theta_h^D = -10^\circ \quad (2.6)$$

$$\theta_f^U = 65^\circ \quad (2.7)$$

$$\theta_h^U = 65^\circ. \quad (2.8)$$

Now it can be devised the coordination between the stroke plane and the angle of attack. During the downstroke dragonflies tend to maintain almost an horizontal wing to maximize the vertical force. However, during the upstroke the wing has to be placed with a near 90° pitch to minimize

		Number of bodies	Number of flights	Mass (mg)	Wing length (fore-) (mm)	Wing area (mm ²)	Wing loading (mg mm ⁻²)	(N m ⁻²)	Wingbeat frequency (Hz)	Max. speed (cm s ⁻¹)	Acceleration take-off-0.1 s (m s ⁻²)	Acceleration 0.1-0.2 s (m s ⁻²)	
<i>Anisoptera</i> <i>Aeshnidae</i> <i>Aeshna cyanea</i> (<i>A.c.</i>)		♂	25	5	727.3 (41.2)	45.1 (1.1)	1870 (125)	0.39 (0.024)	3.8	36	1000	13	10

Advance ratio	Stroke amplitude (degrees)	Angle of stroke plane (degrees)		Angle of attack (all +) (degrees)		Phase shift (degrees)	Parallel stroking (%)	Stroke ratio up:down	f: forewing h: hindwing
		f	h	up	down				
	f 73 h 84	f -50 h -60	65f 55h	45 50	72	53	f 1:1.3 h 1:1.5		

Figure 2-8: Summary of *Aeshna Cyanea* properties in pure hovering. [96]

pressure drag that gives negative vertical force. It is interesting to see that the studied dragonfly does not reach the 90° during the upstroke. This might be due to the induced velocities in the flow field during consecutive flapping cycles, that modify the relative velocities that sees the wing. It may also be due to other unknown aerodynamic effects, or just physiological limitations. This will be inspected in more detail in section 2.2.

Rüppell [96] was the only case in the literature where the feathering angles were provided during pure hovering. Despite the limited information provided by Ruppel (only mid stroke feathering angles), assuming periodical movements a first approximation can be obtained for the missing feathering angles. More studies were done with free flight dragonflies [8] [9] [26] [123], however, in all these cases dragonflies were moving with accelerated, forward and turning maneuvers. Apparently it is quite difficult to film dragonflies during pure hovering. From all the 16 cases filmed in [96] only one was pure hovering. Azuma *et al.* did not film one single case in pure hovering. This might indicate that dragonflies do not frequently use hovering. The explanation for this could be that dragonflies invest much more energy for pure hovering than for flying at slow speeds, see Figure 2-9. For example, *Anax Parthenope* invests two times more energy for hovering than for uniform flight at 1.5 m/s. Therefore it makes sense that dragonflies tend to avoid the most energy demanding modes, unless it is strictly necessary.

Additionally to free flight, studies have been done with tethered dragonflies [131], but in these cases dragonflies tend to escape with much more brusque maneuvers and kinematics resembling those of accelerated and forward flight, so they might not follow the desired hovering regime. For example, Wang and Russell [131] were able to reconstruct both the feathering and flapping angle in *Libellula Pulchella* (Figure 2-10a), however, the phase between wings was almost the one associated with accelerated flight and ascending flight [123]. On the other hand, stroke plane (53° for the forewing and 44° for the hindwing) and frequencies (33.4 Hz) are similar to those reported by Norberg [74] and Azuma *et al.* [9], so despite the different phase, their 3D kinematic reconstruction might contain

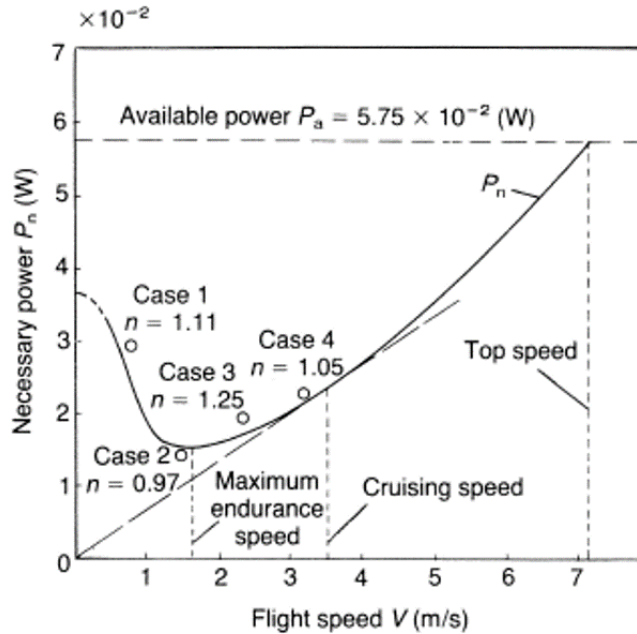


Figure 2-9: Power consumption at different flight speeds of dragonfly *Anax Parthenope*. [9]

useful information to recreate hovering flight.

A summary of the pure hovering kinematics detected in dragonflies are shown in Table 2.1. Due to the lack of information of actual dragonfly kinematics, several strategies have been followed in various computational and experimental studies to model hovering flight. A review of the techniques used to model the kinematics in the literature can be seen in Table 2.2.

First, it can be seen that all the modeled stroke frequencies oscillate between 27.5° and 40° . The most common flapping frequency is the one described by Norberg [74] and Rüppell [96]: $36Hz$.

There is also a quite good agreement on the established stroke plane, 60° , which was the one described by Norberg [74] with respect to the horizontal reference frame.

Most of the flapping angles follow a sinusoidal distribution, with the values described by Norberg [74]. Sun *et al.* [114] also have a sinusoidal distribution but with a slightly higher amplitude than the one observed by Norberg [74]. Savage [103] is the only one that refines more the flapping trajectory. Thanks to Norberg, Savage [103] obtained more detailed data of the flapping trajectory published in [74].

Finally, the least described parameter, the feathering angle θ , is the one that presents more discrepancies. Given the limited data available, some authors [129] [109] [52] [70] opted to reconstruct the feathering angle with a sinusoidal distribution, taking the values from Rüppell [96]. Other authors [114] [103] [67] decided to maintain a constant feathering angle during the downstroke and upstroke, with rotation only during supination and pronation phases. Finally, Hu *et al.* chose to

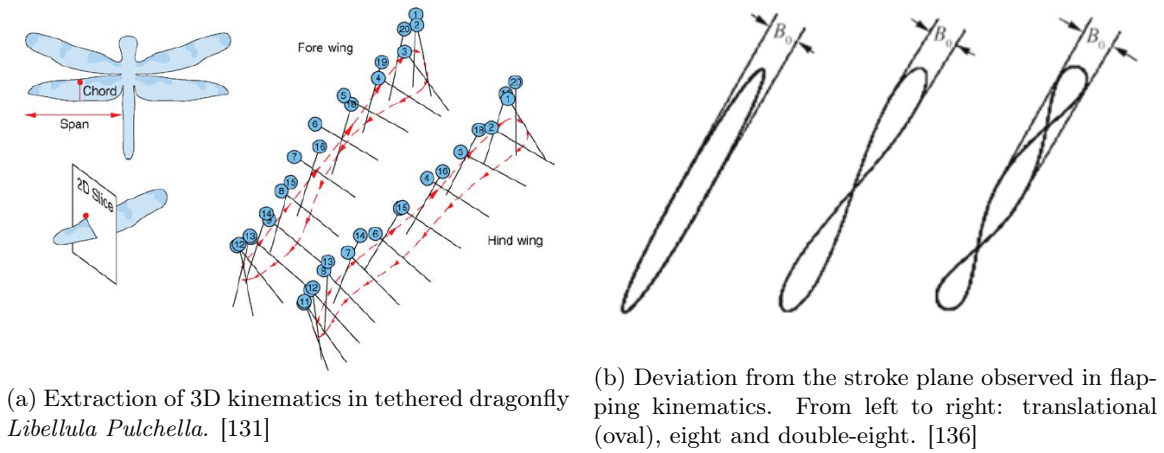


Figure 2-10: Actual wing kinematics reported during dragonfly flight.

Type	Species	Author	Hz	Stroke Plane	Flapping Angle	Feathering Angle	Phase Ipsilateral
Free Flight, pure hovering	<i>Aeshna Juncea L.</i>	Norberg [74]	36	57.8°	Yes, 1 <i>sin</i> mode	No	180°
Free Flight, pure hovering	<i>Aeshna Cyanea</i>	Rüppell [96]	36	50° F, 60° H	Yes, 1 <i>sin</i> mode	Only mid stroke	72°
Tethered, ¿pure hovering?	<i>Libellula Pulchella</i>	Wang and Russell [131]	33.4	53° F, 44° H	Yes, detailed flapping	Yes, detailed feathering	22°
Tethered, ¿pure hovering?	<i>Libellula Luctuosa</i>	Somps and Luttges [112]	28	55°	Yes, 1 <i>sin</i> mode	-10° to 0° downstroke, 90° to 100° upstroke,	50° to 100°

Table 2.1: Kinematics reported of living dragonflies in nature during hovering.

implement a higher order Fourier series described by Azuma [8] for free flight dragonflies without pure hovering. Azuma asserted that only one Fourier mode was not sufficient to capture the feathering angle kinematics, and therefore, Hu *et al.* decided to implement a higher order Fourier series, despite the data being measured in a slow forward flight.

Until now, most of the computational and numerical studies done in the literature consider flapping contained within the stroke plane, see Table 2.2. However, it has been reported [131] that dragonflies deviate their stroke slightly from the stroke plane (Figure 2-10a). A few different patterns have been observed: translational (oval), eight figure and double-eight figure, see Figure 2-10b. Xu *et al.* [136] noticed that the eight figure produces slightly higher lift force as well as thrust. Little attention has been paid to this topic and most studies (Table 2.2) have simplified the kinematics assuming a constant stroke plane, as initially described by Norberg [74].

Overall dragonflies have several degrees of freedom in each wing, and they can control them independently [138]. In particular, dragonflies and bigger flies are the only insect that have three independent degrees of freedom per wing [116]: flapping within stroke plane, feathering and normal movement with respect to the flapping plane. This is achieved by a complex combination of direct and indirect muscles. For example, the periodic contraction and relaxation of Dorso Ventral and Bassaral muscles (Figure 2-11a) work as a lever that produces the flapping movement of the wings. All these muscles are connected to the first, second and third axillaries, which are the joints between the wing and torax, see Figure 2-11b. Wang [128] suggested that feathering is achieved passively by the inertia and loads on the wing. Nevertheless, dragonflies have muscles that control feathering angles [35], and even though they may be helped by passive rotation during pronation and supination, they certainly adjust their pitch angle depending on each maneuver [8]. Most of the state of the art bio-inspired MAVs, such as Delfly II [34] or Robobee [134], use passive feathering and do not have an active way to control pitch. On the one hand, this might be beneficial in terms of weight as they do not have to carry additional mechanisms to allow active feathering, but on the other hand they are incapable of controlling in more detail the aerodynamics of each stroke (Dynamic Stall, Leading Edge Vortex growth, Vortex Interaction, etc.) The fact that heavier insects (dragonflies and bigger flies) and most birds [116] have active control of feathering angle might indicate that for heavy enough vehicles, the benefit of a more controlled flapping might overshadow the extra weight required.

Type	Author	Frequency	Stroke Plane	Flapping Angle	Feathering Angle	Phase Feathering-Flapping	Phase Ipsi-lateral
2D Num	Wang [129]	40 Hz	60°	1 <i>sin</i> mode	1 <i>sin</i> mode, 0° to 90°	90°	None, 1 wing
2D Num	Shilong & Mao [109]	27.45 to 34.15 Hz	60°	1 <i>sin</i> mode	1 <i>sin</i> mode, 0° to 90°	90°	0°, 90°, 180°
2D Num	Hsieh <i>et al.</i> [52]	40 Hz	60°	1 <i>sin</i> mode	1 <i>sin</i> mode, 0° to 90°	54°, 90°, 126°	0°, 90°, 180°
3D Num	Sun <i>et al.</i> [114]	36 Hz	60°	1 <i>sin</i> mode, $\Phi = 69^\circ$	0° constant downwash, 90° constant upwash	90°	180°
3D Exp	Maybury & Lehmann [70]	40 Hz	60°	1 <i>sin</i> mode	1 <i>sin</i> mode, 0° to 90°	90°	0°, 90°, 180°
3D Exp	Savage [103]	36 Hz	60°	Detailed Norberg flapping. See Figure 2-7	0° downwash, 90° upwash	Only rotation at supination and pronation	None, 1 wing
3D Exp	Lu <i>et al.</i> [67]	36 Hz	60°	1 <i>sin</i> mode, Norberg [74]	Specific function, 0° mid downwash, 90° mid upwash	90°	180°
3D Exp	Hu and Deng [54]	36 Hz	60°	1 <i>sin</i> mode, Norberg [74]	3 <i>cos</i> modes, Azuma [8]	54° first <i>cos</i> mode	0°, 180°

Table 2.2: Kinematics implemented in computational and experimental studies of hovering dragonflies. Wing angles are described with respect to the inertial (horizontal) reference frame.

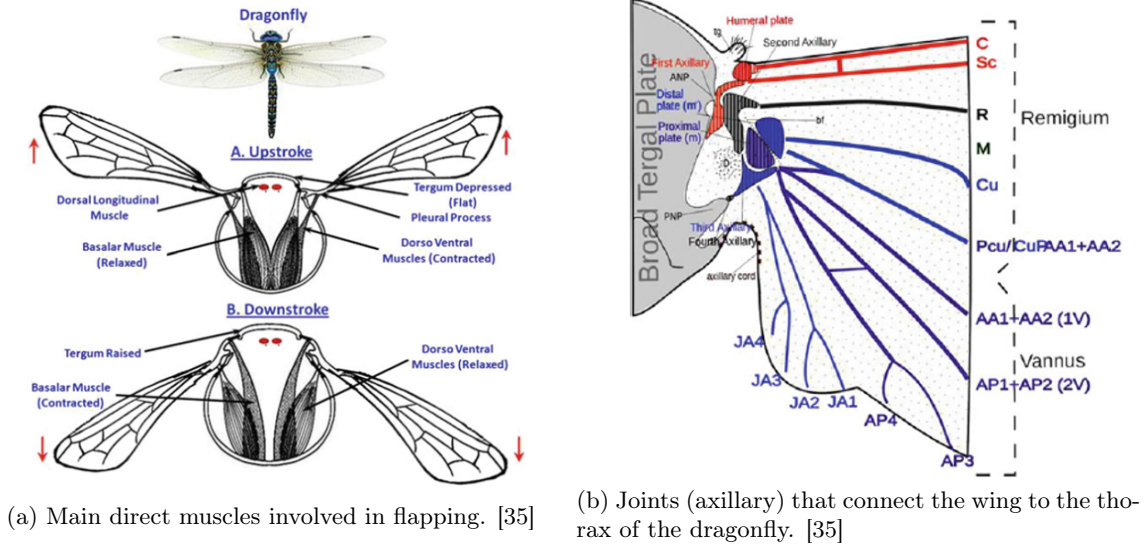


Figure 2-11: Dragonfly morphology of wing muscles and joints.

2.1.2 Phased-stroking, forward flight

The kinematics in forward flight of dragonflies have been reported in much more detail in the literature [8] [9] [99][123] [125] than pure hovering, see Figure 2-12. Several analysis that include a detailed description of both, the flapping and feathering angle, were done by several authors.

When dragonflies fly forwards they shift the phase between forewing and hindwings to angles between 54° and 100° [125]. The reason why this shift occurs is believed to be the vortex interaction between forewing and hindwing [126]. This will be inspected in more detail in section 2.3.

Azuma and Watanabe [8] studied in detail the flapping and feathering angles of dragonfly *Symptetrum frequens* in forward flight, $V = 0.54 \text{ ms}^{-1}$. They explained that the flapping motion was included within a stroke plane θ_W of 50° and 40° with respect to body axis and the horizontal respectively ($\theta_B = 10^\circ$). The beating frequency was $f = 41.5 \text{ Hz}$. Azuma and Watanabe considered that Fourier series with only one term was sufficient to fully described the flapping kinematics:

$$\psi_f = -3 - 43\cos(2\pi ft) \quad (2.9)$$

$$\psi_h = 2 - 47\cos(2\pi ft + 77),$$

where both expressions are in degrees, and ψ_f is forewing ψ_h hindwing. Note how the hindwing leads the forewing by 77° .

However, Azuma and Watanabe observed that only one Fourier mode was not sufficient to capture

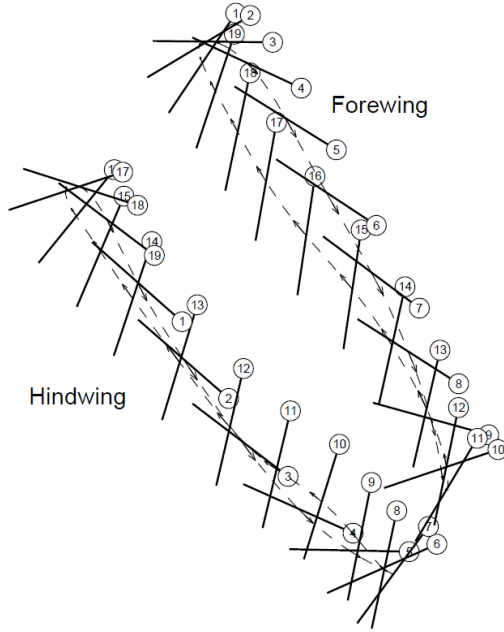


Figure 2-12: Wings kinematics in forward flight for *Libellula Pulchella*.
[99]

the complexity of the feathering angle, and for this reason they used a three term Fourier series:

$$\theta_f = 98 - 77\cos(2\pi ft - 49) - 3\cos(4\pi ft + 67) - 8\cos(6\pi ft + 29) \quad (2.10)$$

$$\theta_h = 93 - 65\cos(2\pi ft + 18) + 8\cos(4\pi ft + 74) + 8\cos(6\pi ft + 28).$$

It is also probable that this complex feathering pattern is observed during pure hovering. Nevertheless, only one single feathering mode was reported in free hovering flight, see subsection 2.1.1, so this might be a clear limitation.

Azuma and Watanabe [9] continued their analysis of dragonflies in forward flight. This time they studied two specimens (A and B) of dragonfly *Anax parthenope Julius* at four different velocities: $V = 0.7, 1.5, 2.3, 3.2 \text{ ms}^{-1}$. They discovered that the phase difference between ipsilateral wings tended to increase at higher speeds, see Figure 2-13. Moreover, the stroke plane angle γ measured from horizontal line is increased in faster forward flight. Note how the stroke plane with respect to body axis is maintained more or less constant. Dragonflies tend to swing their wings always within the same stroke plane angle relative to their bodies, because their muscles are designed to work in a specific range of angles. This is the reason why in this document the angles are defined with respect to body axis, see Figure 2-2. However, when they increase flight speed, they incline their body

Dragonfly Experiment		A 1	A 2	A 3	B 4
Velocity	V (m s ⁻¹)	0.7	1.5	2.3	3.2
Flight angle	Γ (degrees)	-12	-1.1	4.8	0
Body attitude	Θ (degrees)	20	12	4	2.0
Beating frequency	f (Hz)	26.5	28.1	29.0	27.0
Stroke plane inclination					
measured from horizontal line					
forewing	γ ^f (degrees)	40	55	58	63
hindwing	γ ^h (degrees)	38	48	52	68
measured from body axis					
forewing	γ ^f + Θ (degrees)	60	67	62	65
hindwing	γ ^h + Θ (degrees)	58	60	56	70
Flapping amplitude					
forewing	ψ ^f (degrees)	36	25	25	38
hindwing	ψ ^h (degrees)	26	26	26	34
Phase difference of flapping motion between forewing and hindwing					
	δ ^h (degrees)	51	61	61	93
Phase difference between flapping and feathering					
forewing	φ _{1,0.75R} ^h	89	93	91	89
hindwing	δ ₁ - φ _{1,0.75R} ^h	102	92	95	81
Calculated load factor	n	1.1	0.97	1.25	1.05

Figure 2-13: Main kinematic parameters of dragonfly *Anax Parthenope Julius*. 4 experiments performed, 3 with specimen A, and 1 with specimen B.

[9]

forwards, reducing the body pitch angle θ_B . This way they align their body with the horizontal at higher flight speeds and reduce drag [9]. On the other hand, at low speed and hovering having a high body pitch angle θ_B has been suggested to be beneficial in terms of stability, due to passive pendulum stability [93].

Another important aspect is that Azuma and Watanabe [9] did notice that dragonflies tend to increase the amplitude of their flapping when they need more thrust. On the other hand, the frequency remained almost constant in these situations. Further studies have hypothesized that this is due to limited speed of insect flapping reflexes [116]. Azuma and Watanabe [9] also provided an analytic expression for the flapping angle with only one Fourier mode:

$$\psi = \psi_0 + \psi_1 \cos(2\pi ft + \delta_\psi), \quad (2.11)$$

where the coefficients can be obtained from Figure 2-13 for each case. The experimental data and the analytical model can be seen in Figure 2-14 for each experiment. For the feathering angle, once again it was considered that 1 Fourier mode was not enough, so they provided the a Fourier series with 4 terms:

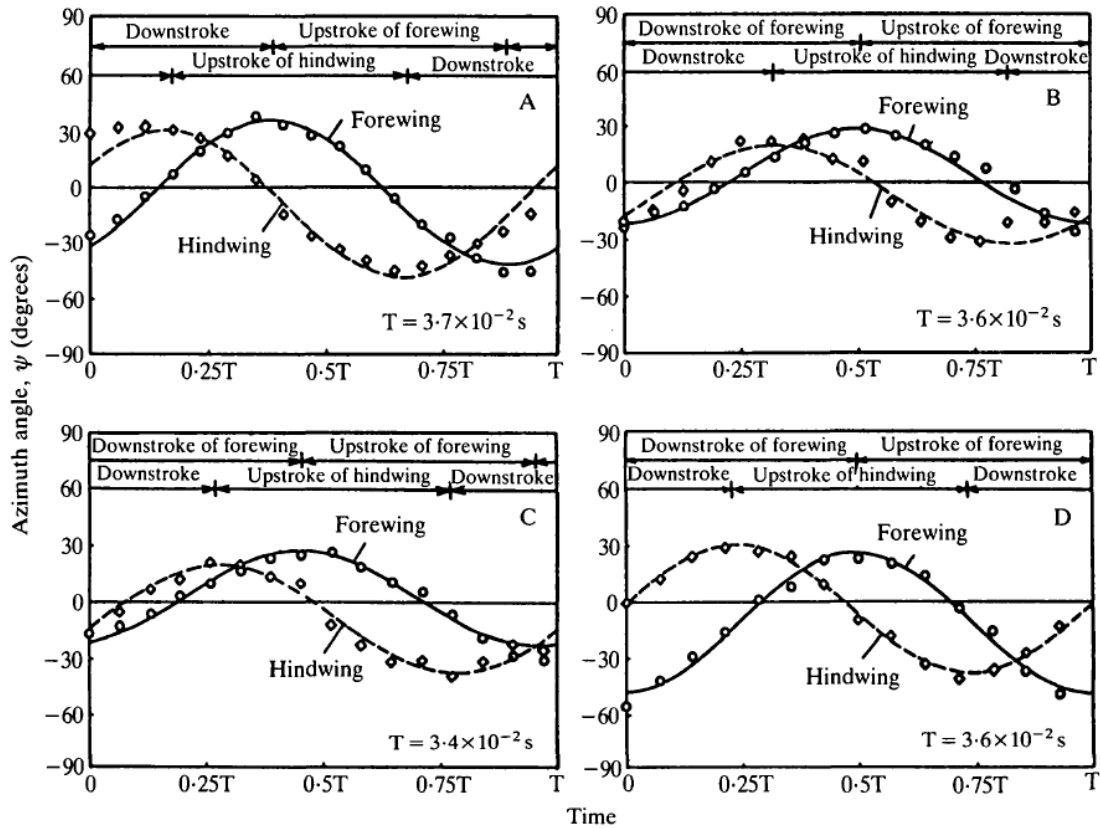


Figure 2-14: Flapping angle ψ within the stroke plane. \circ , forewing; \diamond , hindwing. (A) Experiment 1 ($V = 0.7 \text{ ms}^{-1}$); (B) Experiment 2 ($V = 1.5 \text{ ms}^{-1}$); (C) Experiment 3 ($V = 2.3 \text{ ms}^{-1}$); (D) Experiment 4 ($V = 3.2 \text{ ms}^{-1}$).

[9]

$$\theta = \theta_0 + \sum_{n=1}^4 \theta_n \cos(2n\pi t + \delta_\theta), \quad (2.12)$$

where the specific coefficients for each case can be found in [9].

Wakeling and Ellington [123] did a similar analysis for dragonfly *Sympetrum sanguineum*, but this time they included a difference: they did not only consider flapping within the stroke plane, they also reported the elevation angle of the wing over and under the stroke plane. This way they confirmed that dragonflies used both translational and double-eight flapping figures, see Figure 2-10b. They also provided the coefficients for 5 terms Fourier series that described in detailed the flapping angle and deviations from the stroke plane. On the other hand, Wakeling and Ellington only did focus on the flapping and did not report feathering. Larger body pitch angles were reported and a higher flapping frequency variation. It was also confirmed the previous findings by Azuma and Watanabe [9], such as fixed stroke plane with respect to body axis.

Finally, Russell [99] did an analysis of tethered dragonflies in a wind tunnel. He reported in detail (only graphs, no Fourier series) flapping angle, out of stroke plane deviations and feathering angles, see Figure 2-12. No new relevant findings were added with respect to the previously mentioned kinematics.

2.1.3 Synchronized and non-symmetric stroking, accelerated flight and turning maneuvers

Dragonflies tend to synchronize the flapping of ipsilateral wings when they want to accelerate [115], see Figure 2-16. This way they get a huge peak of acceleration in a short period of time. They also tend to maintain a constant flapping frequency and increase the amplitude of the stroke [9].

Wakeling and Ellington [123] were the first to measure dragonflies in different maneuvers that required acceleration. They detailed the flapping angles and the elevation of the wing over the stroke plane, but not the feathering angles. They provided a fifth order Fourier series for the flapping and elevation angle. Almost all dragonflies *Sympetrum sanguineum* with high accelerations had a near synchronous flapping. Figures of eight (Figure 2-10b) and ovals were observed during acceleration strokes.

Wang *et al.* reported accelerated flight during a turning manoeuvre. This kinematics had the peculiarity of an asymmetry between left and right wings: the flapping amplitude and angles of attack during the downstroke of the outer wings were bigger. This asymmetry provided a yawing and rolling torque that was enough for making the turn. As previously done by Azuma and Watanabe [9], the flapping angles were considered simple enough to be described by only one Fourier mode, see Figure 2-17a. However, the feathering angle was described by a Fourier series with 3 terms, see

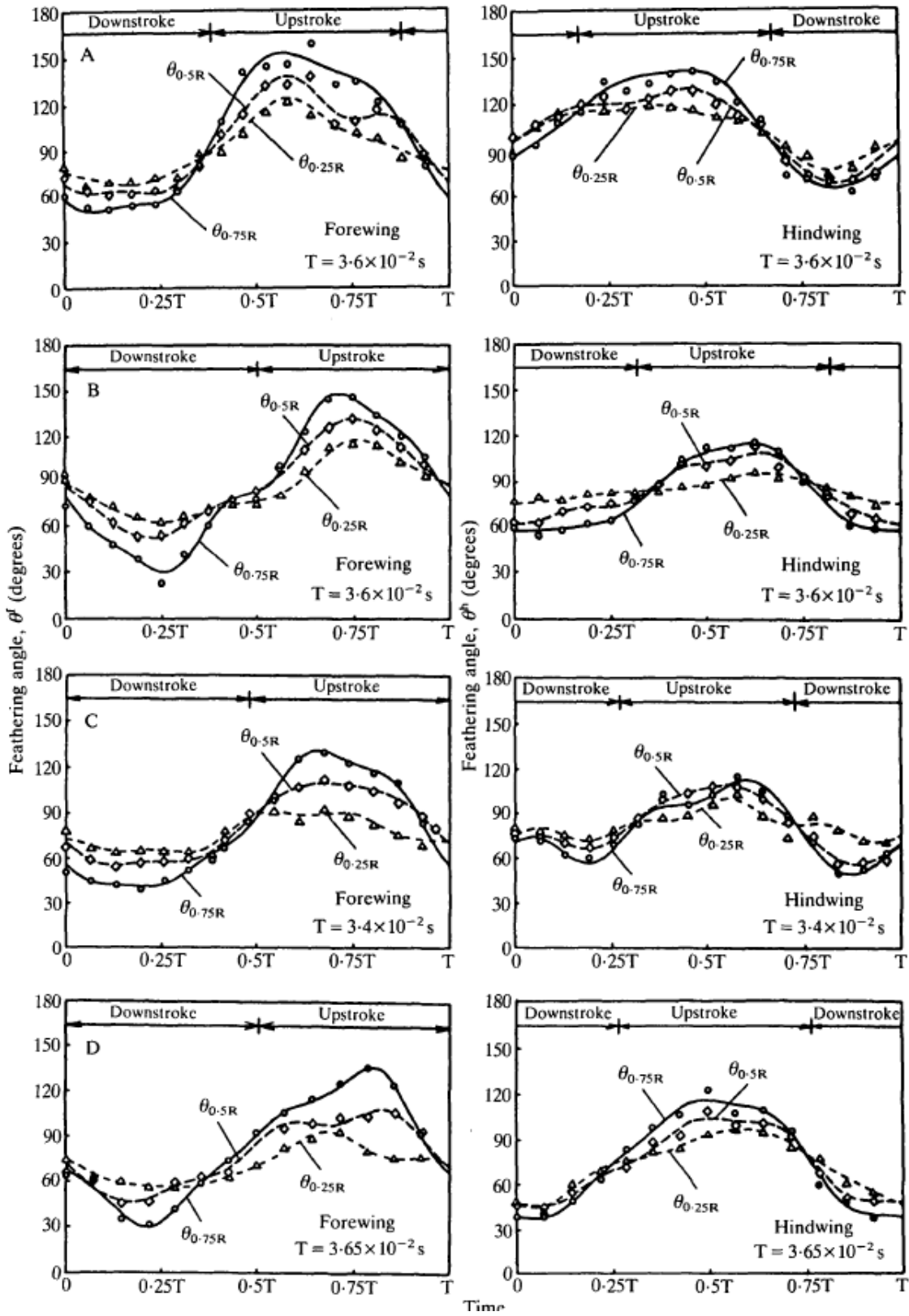


Figure 2-15: Flapping angle ψ with respect to the stroke plane. Span position, \circ , $0.75R$; \diamond , $0.50R$; \triangle , $0.25R$. (A) Experiment 1 ($V = 0.7 \text{ ms}^{-1}$); (B) Experiment 2 ($V = 1.5 \text{ ms}^{-1}$); (C) Experiment 3 ($V = 2.3 \text{ ms}^{-1}$); (D) Experiment 4 ($V = 3.2 \text{ ms}^{-1}$). [9]

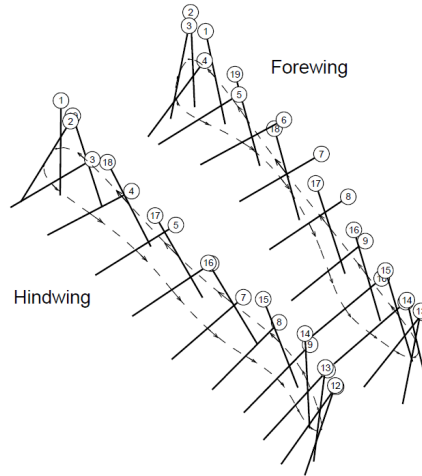


Figure 2-16: Wings kinematics of dragonfly *Libellula pulchella* in accelerated flight. [99]

Figure 2-17b. Frequencies were not modified during the turning maneuvers, just the amplitude of the strokes.

Alexander [5] also studied the turn of dragonflies and discovered two possible maneuvers:

1. Conventional: increase amplitude (more common) and/or angle of attack of outer wings during the turn. This causes a roll into a bank. Then the lift vector points sideways and allows the turn. This maneuver is typical in fast forward flight, and it is the same mechanism used by conventional aircraft during turns.
2. Yaw turn: at slow speeds dragonflies can turn using the drag of their wings in a similar fashion as a turn in a kayak by rowing. This causes a yaw turn without roll.

More recently, Li and Dong [62] tracked the wing kinematics of dragonfly *Erythemis Simplicicollis* with high frame-rate cameras. A detailed description of one turning maneuver was provided, with the wing kinematics of each wing. No Fourier series was given, only the graphs and plots of the kinematics.

2.1.4 Free flight, gliding

Dragonflies have been considered to have the best gliding performance of all insects [122]. They are capable of gliding 40 chord lengths in one complete wing beat and they use gliding in hot weather to dissipate the accumulated heat in their body, and therefore avoid overheating [115].

Wakeling and Ellington [122] measured the gliding performance of real dragonflies. This was done by considering the descent slope during gliding. In Figure 2-18, the polar of three specimens of dragonfly *S. sanguineum* can be seen. They compared this with the reported polars of many other

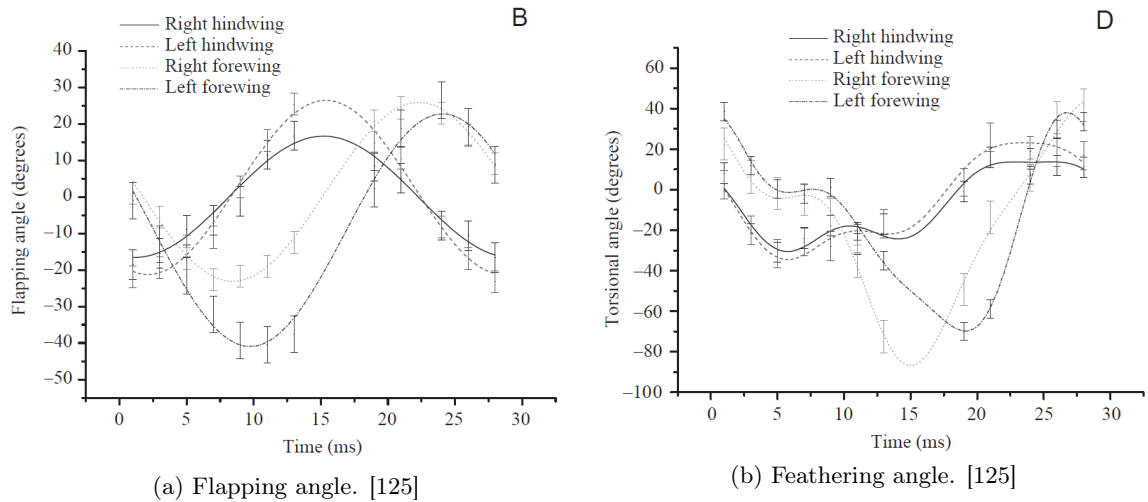


Figure 2-17: Kinematics of dragonfly *Polycanthagyna melanictera Selys* during a turning maneuver.

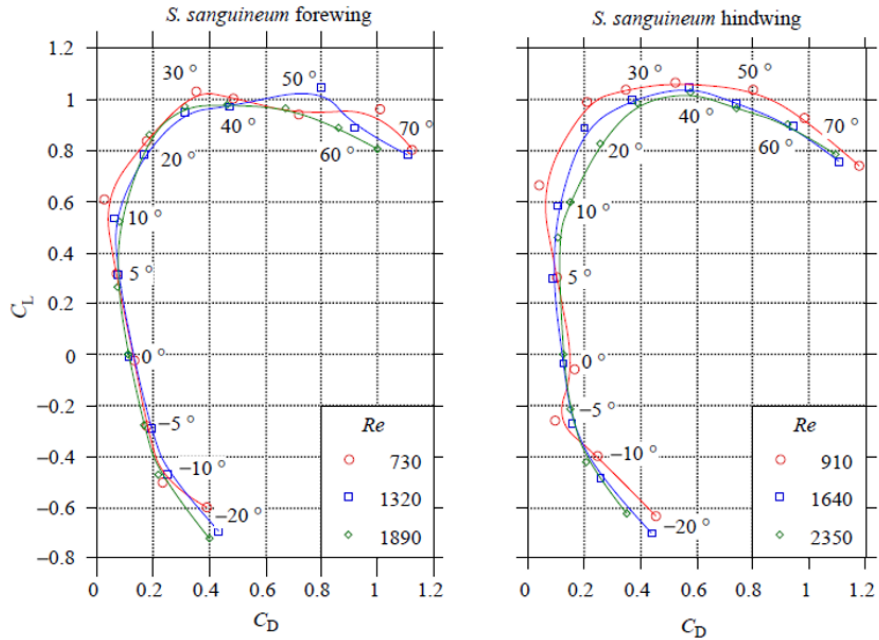


Figure 2-18: Experimentally measured polar of three specimens of dragonfly *S. sanguineum* forewing and hindwing.

[122]

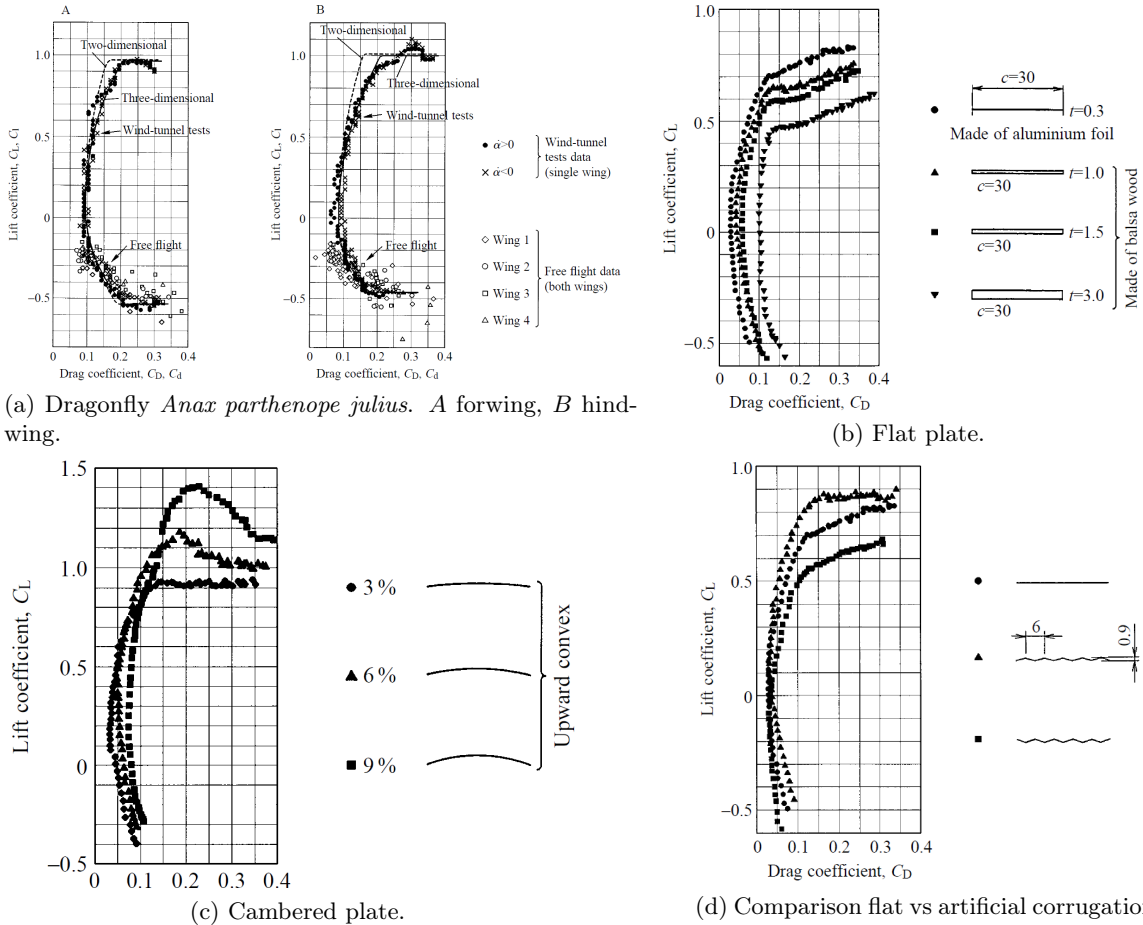


Figure 2-19: Lift vs drag coefficient for different airfoils. $Re = 2 \times 10^4$. [80]

insects, and the aerodynamic efficiency L/D was higher than the ones measured in many other insect species. More importantly, looking closer at the polars it can be seen that for large angles of attack lift is maintained almost constant. This is something quite peculiar which is not observed in conventional airfoils, which have a steep stall and a dramatic lift decrease. Corrugation and specific wings geometry is the secret after this, and it will be inspected in more detail in section 2.4.

A similar study was done by Okamoto *et al.* [80], where they compared the gliding performance of dragonfly wings, flat and cambered plates. They discovered that dragonfly corrugated wings (Figure 2-19a) had a better performance than flat plates, specially at high angles of attack. Moreover, they realized that it was better to have thin airfoils, than thick ones (Figure 2-19b). Cambered plates (Figure 2-19c) were the only ones that showed a better performance than dragonfly wings. In fact, it has been detected [115] that dragonflies camber their wings due to inertia and aerodynamic forces, especially next to the wing tip, so they might be benefiting from this aerodynamic feature. Finally, it was observed that not all types of corrugation were beneficial. In Figure 2-19d, it can be seen that one corrugation pattern outperforms the flat plate, while the other one does not.

2.2 Aerodynamics and lift generation

In the previous section, section 2.1, the kinematics of dragonflies were analyzed, with special attention to hovering. Now, we are going to decipher the aerodynamics behind those strategic flapping strategies. In this section only the aerodynamic mechanisms of one single flapping wing are going to be inspected. Once this is understood, interaction between two ipsilateral wings will be studied in section 2.3.

First, the quasi-steady approximation is going to be explained in subsection 2.2.1. Then, unsteady aerodynamics (subsection 2.2.2) are going to be studied in more detail, including several topics observed in dragonfly aerodynamics, such as dynamic stall, leading edge vortex (LEV), vortex interaction, etc.

2.2.1 Quasi-steady approximation and wake models

The quasi-steady approximation was used in the first aerodynamic studies of dragonflies. Weis-Fogh [132] and Ellington [41] included several approximations within their quasi-steady analysis. First, they assumed incompressible and inviscid flow, which led to the formulation of Navier Stokes in terms of a potential function. Additionally, in the quasi-steady approximation they assumed that the wing is following a succession of steady steady state solutions, in which the history of events is not considered. Finally a 2D approximation of a flat plate was considered. With these assumptions the circulation around the flat plate Γ is given by [41]:

$$\Gamma = \pi c U \sin \alpha + \pi \omega c^2 \left(\frac{3}{4} - x_0 \right), \quad (2.13)$$

where c is the chord of the airfoil, U the translating velocity, ω the angular velocity and X_0 the non-dimensional coordinate where the translation is done. This theoretical framework was developed by Glauert [48], who proposed a quasi-steady model and predicted that the critical point (rotation axis that gives 0 lift) resides at a distance of 3/4 chord lengths from the leading edge. The critical point in a flat plate is going to be relevant when analyzing pronation and supination of the wing, at the end of the upstroke and downstroke respectively.

Additionally, the Kutta–Joukowski theorem theorem has to be included to obtain the resulting lift L from the circulation Γ , velocity U and density ρ :

$$L = \rho \Gamma U. \quad (2.14)$$

Using the previously defined quasi-steady model, Weis-Fogh [132] found maximum lift coefficients

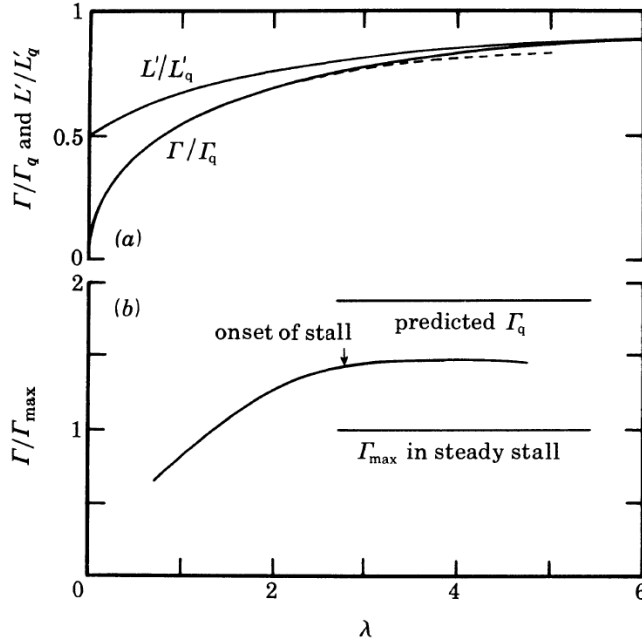
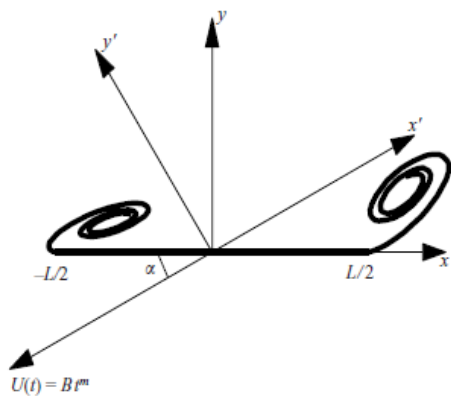


Figure 2-20: Above, ratio of quasi-steady circulation Γ_q to instantaneous circulation Γ , and quasi-steady lift and instantaneous lift. Below, ratio of quasi-steady lift and instantaneous lift. Flat plate suddenly set into transitional motion. λ is the number of chords covered by the flat plate.

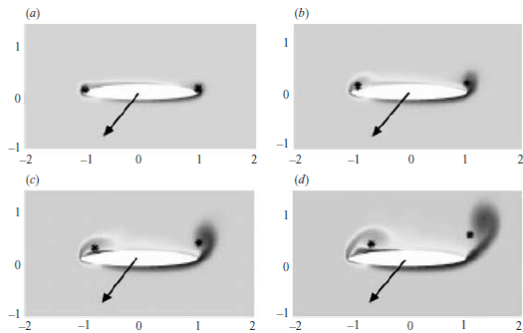
[41]

in dragonflies of 1 (see lift coefficients of steady flight in gliding, Figure 2-19a). However, Ellington [40] reported that during his measurements of dragonflies in free flight, lift coefficients between 2 and 6 were found. Ellington suggested that this was due to the strong unsteadiness of the flow. Therefore, the quasi-steady approximation was no longer valid.

To solve this without solving the whole Navier Stokes equations, several approximations have been done. The main idea is to assume incompressible and inviscid flow, which seems to be a quite accurate approximation given the Reynolds numbers observed in dragonflies, $Re \approx 1000$ [49]. Sane [102] suggested a refined quasi-steady model for 3D wings. He did the weighted average across the 2D section along the span and included the lift and drag data of dragonfly wings that was measured experimentally by Wakeling and Ellington [123]. Additionally, Sane also included the added mass effect to model the acceleration of the surrounding fluid. He obtained decent results, but he noted that it was important to consider the effect of the wake, which was neglected in the quasi-steady model. In Figure 2-20 the effect of the wake can be seen in a flat plate suddenly set into transitional motion. The quasi-steady circulation around this plate is not the one predicted by the quasi-steady model, because the vortices shed at the wake are modifying the circulation at the flat plate. Only after the shed vortices are far away enough downstream, the vorticity at the flat plate approaches the quasi-steady values. This was the so called Wagner effect that was mentioned in section 2.1.1, and the reason why "Clap and Fling" was found to be so efficient in horizontal flapping.



(a) Sketch of modelled vortex. [87]



(b) Vorticity field of inviscid Navier-Stokes solution. The dot shows the position of the vortex within the approximated solution. [87]

Figure 2-21: Modelling wake vorticity.

To model the wake, which was missing in the previously mentioned approximations, the Kelvin theorem has to be applied: the net circulation does not vary in an inviscid flow. Therefore, the vortices that are shed at the wake are caused by variations of vorticity around the airfoil. Pullin and Wang [87] used this theorem to calculate the vorticity which was shed into the wake. Then, they added a model to advect the vorticity at the wake, and additionally they considered vortex growth. In Figure 2-21b the results of their model can be seen. The black dot represents the position of the vortex in their model, and it is superimposed over the discrete solution of the vorticity equation. The position of the shed vortex follows quite accurately the numerical solution, and they obtained quite reasonable results with their approximation. Their prediction outperformed the results from Theodorsen theory and Wagner effect, mainly because these theories only consider vortex shedding at the trailing edge. However, they modeled both, vortex shedding at the leading and trailing edge, see Figure 2-21a. This approximation was much more accurate in insect wings: the leading edge vortex (LEV) clear breaks up due to sharp leading edge of insect wings at relatively small angles of attack [90]. Therefore, by considering a discrete LEV and trailing edge vortex (TEV) and their advection, a quite good approximation of the wake influence can be achieved.

In summary, unsteady effects are vital due to the high flapping frequency of dragonflies. A quasi-steady approximation with the added mass effect still lacks the influence of the wake. Approximations to model the wake influence can be done by advecting the vortices which are shed at the wing due to the Kelvin theorem. In particular, it is key to model both, the LEV and TEV.

2.2.2 Unsteady methods

The lack of accuracy of the quasi-steady methods for dragonfly hovering has led many authors [112] [40] [44] to suggest that unsteady effects are key in the aerodynamics of the insect. In the previous section, subsection 2.2.1, the main unsteady mechanisms were identified: added mass effect and wake

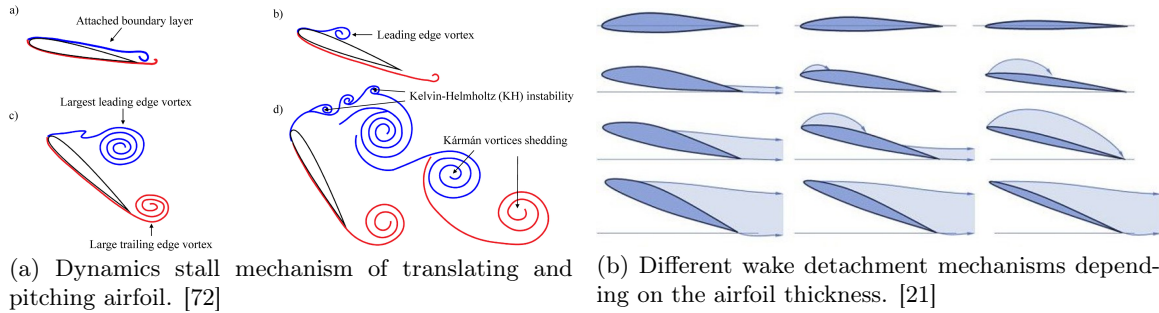


Figure 2-22: Modelling wake vorticity.

effect. These phenomena could be modeled with simplistic models that capture the data observed experimentally. However, its application is limited and inaccurate when the wake becomes really complex (accumulation of vortices in hovering at the same spot) and does not model dissipation for really large times. In this section a more in depth approach of all the unsteady aerodynamics governing dragonfly flight is going to be taken. The aim here is to understand the essence of the most important factors that define dragonfly aerodynamics during hovering. For this, fully resolved Navier-Stokes simulations and experiments are going to be considered.

Dynamic stall

It was seen in subsection 2.2.1 that a TEV and LEV were generated during the flapping motion of a 2D flat plate. This mechanism is known as dynamic stall, and occurs when the flow cannot be attached anymore to the airfoil. First, a shear layer is created due to the velocity difference between the flow attached to the airfoil and the upper flow, see *a*) in Figure 2-22a. Then this shear layer rolls up forming a pair of LEV and TEV, *b*) in Figure 2-22a. The rollers continue to grow with time *c*) in Figure 2-22a, and eventually they are shed downstream *d*) in Figure 2-22a.

There is substantial difference in the formation mechanism of dynamics stall depending on the thickness of the airfoil, Figure 2-22b. Particularly for thick airfoils, detachment occurs first at the trailing edge, creating a trailing edge shear layer that propagates towards the leading edge while rolling up due to the Kelvin-Helmholtz instability. However, for thin airfoils, the leading is so sharp that the flow immediately detaches for low angles of attack, when the stagnation point leaves the leading edge [90]. This causes a more sudden recirculating bubble at the leading edge, that evolves and grows to form a LEV. This LEV keeps growing until it is detached. Note that dragonfly wings are quite thin and have sharp leading edges, so this second mechanism is found in their flapping.

Once the thickness of the airfoil has been considered, there are two other non-dimensional parameters that govern dynamic stall during flapping: the rate between rotation (pitch) and translation (plunge); and the Reynolds-number.

Ol *et al.* compared pure plunge to pitch-plunge, and realized that with conveniently chosen pitch

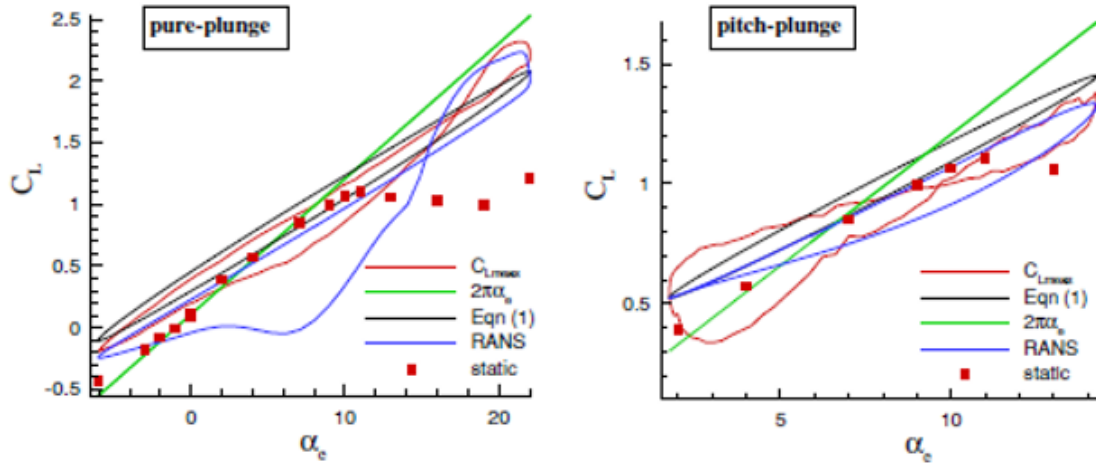


Figure 2-23: Comparison of lift coefficients for pure-plunge and pitch-plunge. [81]

angles, dynamic stall could be postponed during flapping. In Figure 2-23 it can be seen that the lift coefficient during pure plunge reach higher values, however they also have a large hysteresis effect because of the deep stall. With pitch-plunge, deep dynamic stall could be controlled, achieving a slightly higher average lift coefficient across the cycle. For better understanding, the vorticity plots of PIV and numerical results are shown in Figure 2-24. Indeed, in the pitch-plunge case the flow is slightly detached, however, the pitch controls the growth of the LEV. On the other hand, for pure plunge, the flow is completely detached and a LEV appears and grows. When the LEV is big enough, it can not be maintained attached anymore, and it is shed. This causes a huge decrease in lift, and it takes some time before it recovers the previous lift values (deep dynamic stall). Based on this, it can be inferred that it is crucial to avoid at all cost the shedding of the LEV. Moreover, using pitch to reduce effective angle of attack (the so called Kramer effect) can be used to control the size of the LEV and its shedding.

Finally, the Reynolds number effect is going to be considered. Ol *et al.* visualized the flow field around a thin airfoil at different Reynolds numbers (Figure 2-25). They observed that dynamic stall displayed a quite different behaviour depending on the Reynolds number. For smaller Reynolds numbers, the flow suffered Kelvin-Helmholtz instabilities, and was greatly detached from the upper surface. However, for higher Reynolds numbers, the boundary layer displayed a much more energetic behaviour and the flow was attached close to the upper surface. They also noted that the rollers caused by the Kelvin-Helmholtz instability were much smaller in size at high Reynolds numbers. The LEV only grows in a limited way for $Re = 10K, 20K$. For these cases, the flow had big enough rollers and was sufficiently detached to form a clearly visible LEV.

Visbal *et al.* also analyzed dynamic stall for different Reynolds numbers. In particular, they noted a quite interesting fact. If the flapping frequency is high enough, the LEV does not have time

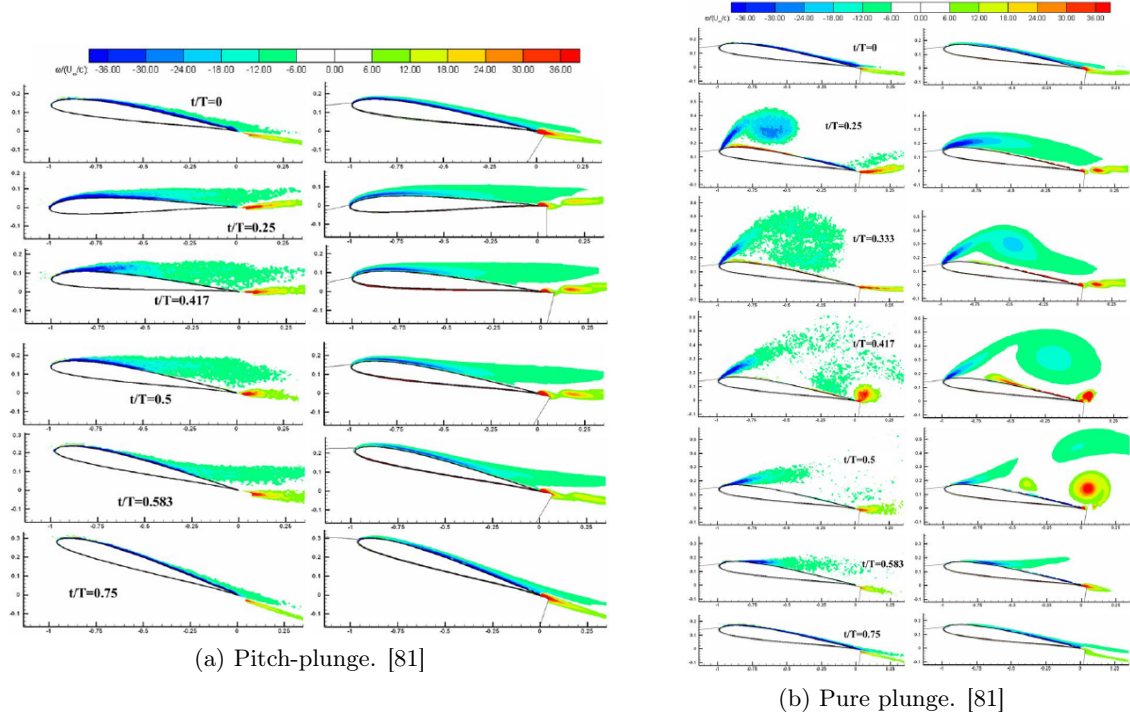


Figure 2-24: Vorticity contours. Left, PIV measurements. Right, CFD simulation.

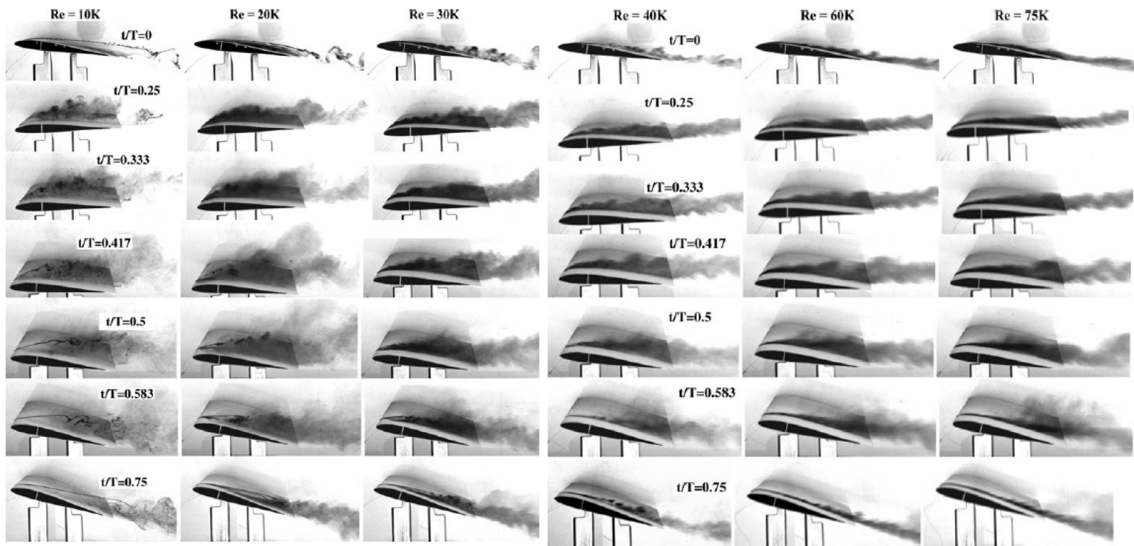


Figure 2-25: Reynolds number effect during pitch-plunge mode. Smoke visualization. [81]

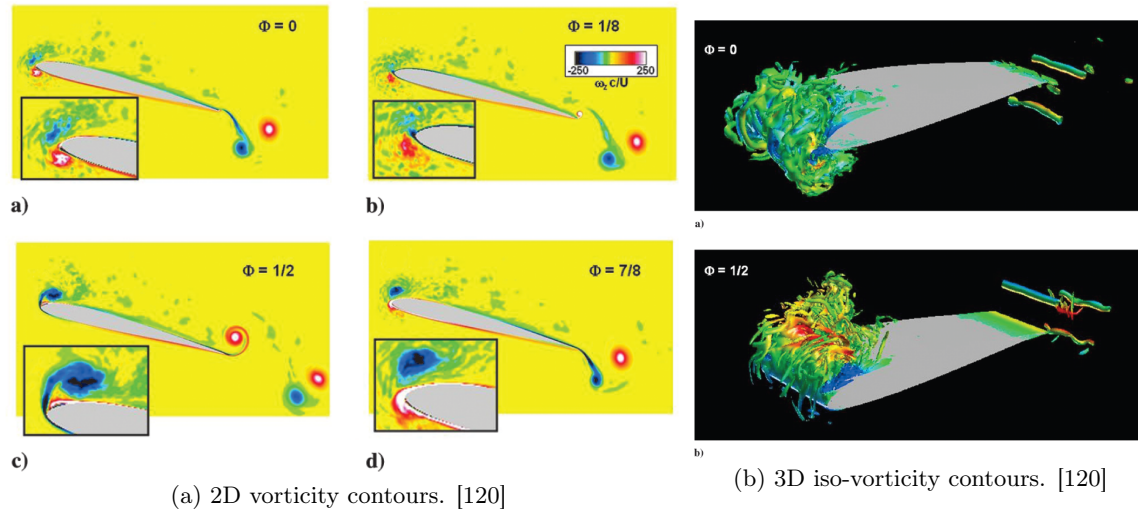


Figure 2-26: Dynamic stall. 3D numerical simulation. $Re = 10K$. High frequency, small amplitude during pure plunge.

enough to grow and be shed. Therefore, in every cycle a new LEV is created and adds up to the previous series of LEV that did not have time to be shed. This creates an extremely complex vortex structure, see Figure 2-26b. This convoluted structure is not beneficial for lift, as a lot of energy is wasted in random vorticity that does not contribute to the vertical momentum component.

In conclusion, dragonflies sharp leading edge causes leading edge dynamic stall when they are flapping. This leads to a roll-up of vorticity and the creation of a LEV. The growth of the LEV can be controlled combining pitch-plunge motion to adjust the angle of attack. Additionally, high Reynolds number withstand higher effective angles of attack before the roll-up and creation of the LEV. Finally, it is important to let the LEV grow in a *clean* upstream flow, to have a coherent structure that maximizes lift production. For this, it is necessary to get rid of the LEV created in the previous cycle.

2.2.3 Leading edge vortex stability and 3D structure

In previous sections a 2D LEV was identified, and the mechanism that creates it, dynamic stall, was studied. This LEV is extremely relevant for lift production according to the Kutta–Joukowski theorem. For this reason, the 3D structure of the vortex is going to be studied in more detail. Thomas *et al.* studied the critical points of the 3D LEV generated during the downstroke of a dragonfly and identified that it had a *U* shape. They used smoke visualization with a tethered dragonfly, see Figure 2-27. Moreover, they confirmed that it was caused due to dynamic stall.

Similar LEV structures caused by dynamic stall have been identified in other insects in nature, see Figure 2-28b. Dragonflies have the peculiarity that they maintain the structure of the LEV above their thorax, connecting this way the LEV from both wings. This does not happen in other

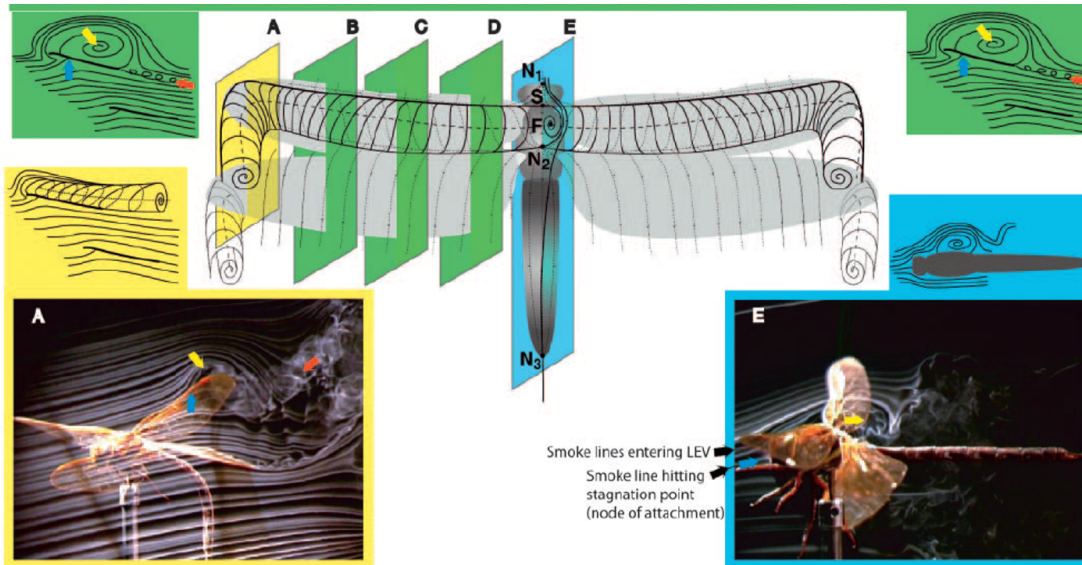


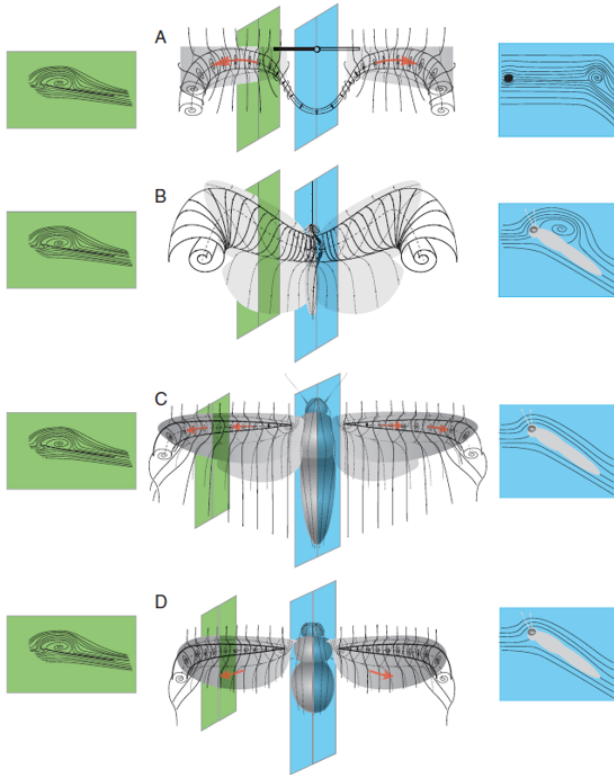
Figure 2-27: Characteristic smoke patterns associated with the forewing downstroke in normal counterstroking flight. The video images show a tethered hawkmoth *Aeshna grandis*. Visualizations are shown for 5 spanwise stations along the wing (A–E), marked by colour-coded slices in the figure. [117]

insects, see Figure 2-28a, and it seems to be beneficial in terms of additional lift at the thorax and a more stable vortex.

Ellington [39] also studied the structure of the LEV in dragonflies. He used smoke visualization of dragonflies and a self-made flapping device. He also confirms the findings by Thomas *et al.* [117]: 3D U vortex shape caused by leading edge dynamic stall.

On top of the 3D LEV structure a more detailed interpretation of the vortex elements was provided by Fujita *et al.* [46]. A vortex beneath the main LEV was identified, see Figure 2-28b. This vortex, the so called *lambda vortex*, had a counterclockwise vorticity. Ellington [39] and Thomas [117] were not able to identify it with smoke visualization because it was surrounded by the clockwise LEV. The lambda vortex induces velocity in vortex 1 away from the flat plate, and this means that it favors LEV detachment. This was seen in section 2.2.2 to be negative, as it suddenly decreases the enhanced lift, entering into deep dynamic stall.

Despite, the existence of a lambda vortex that favors LEV detachment, Ellington [39] and Thomas *et al.* observed that dragonflies maintain their LEV attached during the whole downstroke, and it is only shed during supination. This phenomenon was quite surprising, as dragonflies flap their wings with really high angles of attack during the downstroke (45 to 60°), and the shedding of the LEV was supposed to occur at much smaller angles of attack [120]. Ellington [39] provided a possible explanation for this phenomenon. He realized that dragonflies had axial flow (from wing root to tip) during its flapping (Figure 2-30b). The LEV is only shed once it is so big that it can no longer be maintained attached. Consequently, Ellington [39] hypothesized that the spanwise



(a) Sketch of LEV observed for several insects. [117]



(b) Smoke visualization (blue) of the LEV in a tethered dragonfly. [39]

Figure 2-28: Different 3D LEV structures.

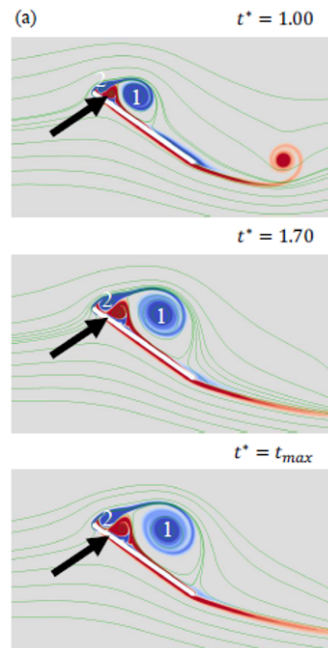
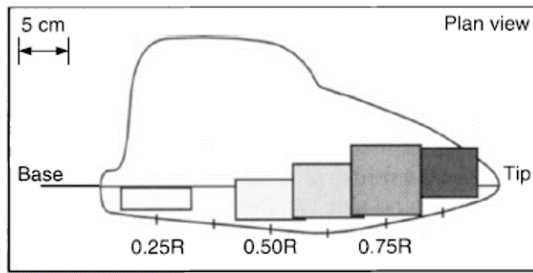
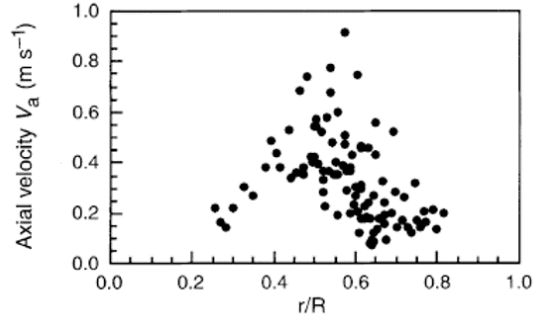


Figure 2-29: Creation of a secondary vortex structure that has opposite circulation: the lambda vortex (colored in red).

[46]

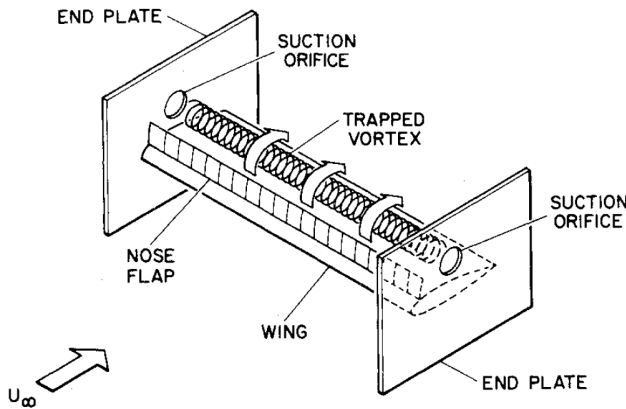


(a) Upper view of the wing. Circulation intensity of the LEV across the span. [39]

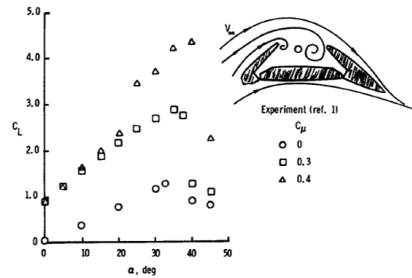


(b) Measured axial velocity (from root to tip) across the span. [39]

Figure 2-30: 3D LEV structure.



(a) Sketch of the experiment with a trapped vortex. [95]



(b) Experiment. Active spanwise suction to generate super lift. [42]

Figure 2-31: Stabilizing the LEV. Spanwise blowing.

flow was advecting vorticity away from the wing to control the growth of the LEV, and avoid this way detachment. This way he justified the conical LEV structure that he measured (Figure 2-30a), growing in size towards the tip, and advecting vorticity in the spanwise direction. These attached vortices stabilized by spanwise blowing have also been observed in swept wings at high angles of attack in forward flight [12], for example in birds such as swallows or delta wings.

The stabilization of vorticity by axial flow is a concept that has been proved in literature. Cornish [33] stated that vortices are prone to develop 3D structures, as it is a more stable form. He observed this in a Karman vortex street, that naturally tended to develop 3D conical structures. Rossow [95] proved experimentally that a vortex could be trapped using axial flow, see Figure 2-31a. He demonstrated that incredibly high lift coefficient of up to 8 were achievable thanks to this mechanism. Erickson [42] did a similar experiment: he created a trapped vortex with two movable flaps, and stabilized it with axial flow. In Figure 2-31b it can be seen how with increasing axial flows more intense vortices (that lead to higher lift coefficients) can be stabilized.

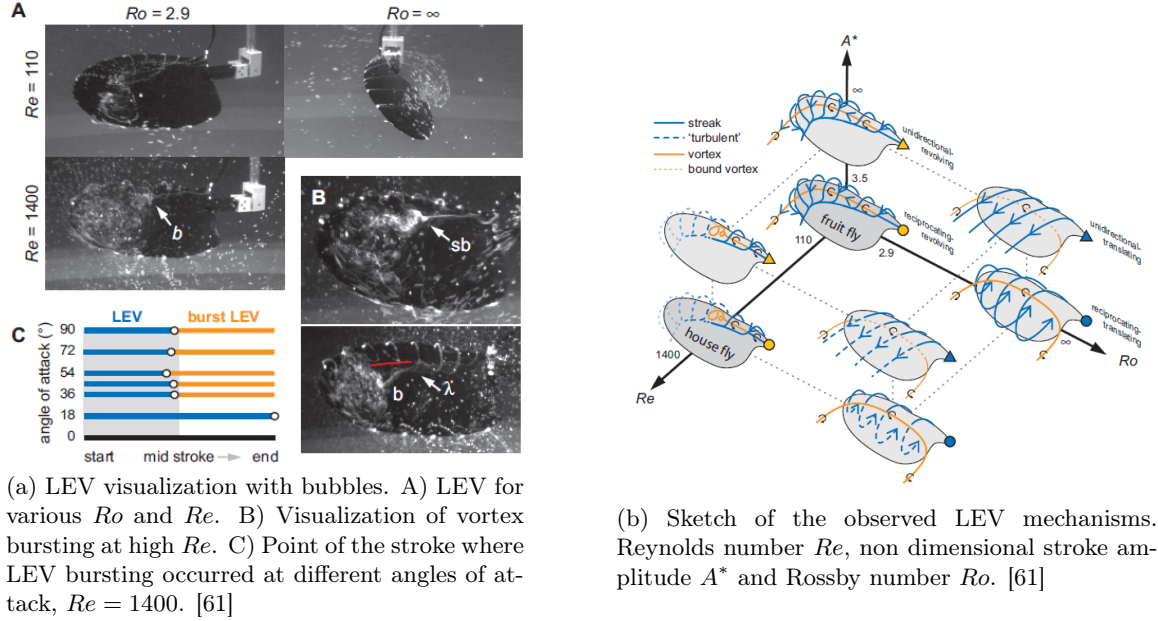


Figure 2-32: LEV dependence with Rossby and Reynolds numbers.

Even though vortex stabilization by axial blowing has been demonstrated, the hypothesis made by Ellington [39] has been questioned in the literature, in experiments [13] [15] [27] and simulations [111]. It is agreed that around Reynolds number around 100 axial flow intensity is non-enough to stabilize the LEV by vorticity convection. On the other hand, Birch *et al.* [15] and Shyy *et al.* [111] detected that spanwise flows starts to be important and dominate LEV at Reynolds number 1000. More importantly, despite the differences of spanwise flow at various Reynolds numbers, in all cases the LEV was found to be stable. Lentink and Dickinson [61] were able to find an explanation that justified LEV attachment for lower Reynolds numbers, without the existence of axial flow. They argued that in this viscous regimes, the boundary layer had an Eckman distribution, which allowed for Eckman pumping. This phenomenon was able to attach the LEV to the flat plate, and avoided vorticity shedding. They also noted that for higher Reynolds numbers vorticity advection was able to stabilize the LEV, as at this regime spanwise flow was relevant.

Apart from the Reynolds number dependence Lentink and Dickinson [61] also realized that LEV stability was strongly related to the ratio between Coriolis and inertial forces, the so called Rossby (Ro) number:

$$Ro = \frac{U^2}{\Omega U} = \frac{U^2}{\frac{U}{R_g} U} = \frac{R_g}{c}, \quad (2.15)$$

where R_g is the rotation radius, and c the chord of the airfoil. In a 3D flapping wing the rotation section of each 2D section changes. For this reason Lentink and Dickinson [61] decided to

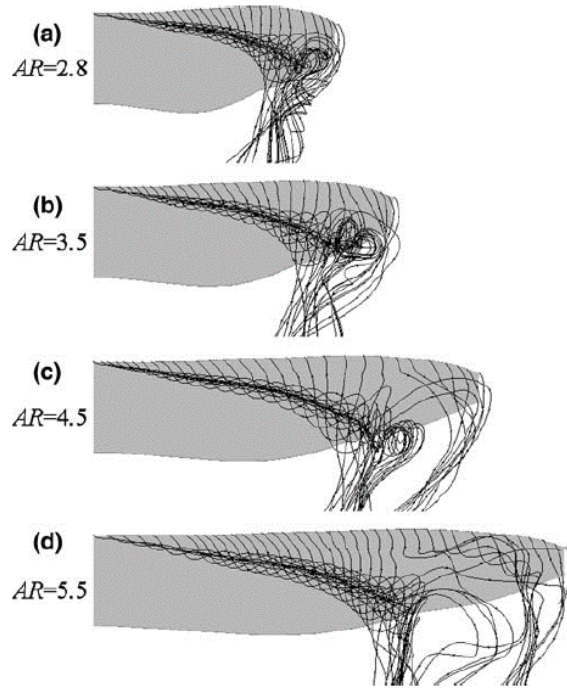


Figure 2-33: LEV vortex stability with higher aspect ratios AR.[68]

consider the tip radius to characterize each rotating wing, being therefore the Rossby number equal to the aspect ratio of the wing. Several additional conclusions can be extracted from Lentink and Dickinson's work [61] that help to better understand vortex stability, Figure 2-32b:

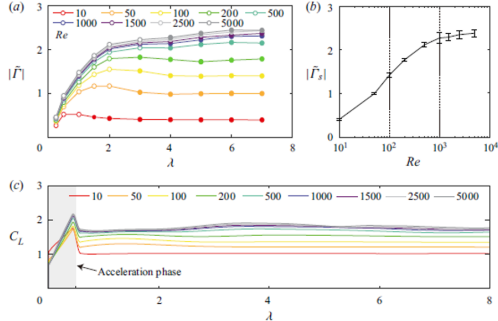
1. For higher Ro numbers (higher aspect ratio wings) the LEV was more unstable. In pure translational movement ($Ro = \infty$) neither low Re (Eckman pumping) nor high Re mechanisms (spanwise vorticity advection) were able to stabilize the LEV. In particular, Luo *et al.* [68] verified this behaviour computationally. See in Figure 2-33 how for larger aspect ratio wings the LEV is no longer stable near the tip. Note that the LEV becomes unstable in their study at the span length $\frac{y}{c} = 3$, which is equivalent to $Ro = 3$.
2. The larger the stroke amplitude A^* the more time the vortex had to grow. This is specially relevant in cases where the LEV vorticity is not removed: high Ro . Therefore, the LEV keeps growing and reaches a point where it is so big that it can no longer remain attached.
3. At low Re the vortex remained laminar. However, at around $Re = 1400$ vortex bursting was observed near the wing tip, Figure 2-32a. The closer to the tip the higher the velocity, so it makes sense that some sections may be experiencing transition. However, despite vortex bursting, lift and vortex structure were preserved. When bursting occurs the flow transitions, but the vortex remains attached to the leading edge. Himmelskamp effect [59] could be a possible explanation for this phenomenon.

Lentink and Dickinson [61] were not able to explain why did the spanwise flow towards the tip occurred. Aono *et al.* [6] visualized the pressure field near a rotating wing and he discovered that there was an adverse pressure gradient towards the wing tip. He reasoned that the increasing strength of the LEV from the base toward the tip (higher effective velocity towards the tip) was the reason for this pressure suction. The question now is, why does at lower Re number decrease the spanwise flow? This was not mentioned in Aono *et al.* work, but here it is hypothesized that at lower Re circulation is less intense due to viscous diffusion, causing this way less suction difference towards the wing tip. For example, in Stokes regime ($Re > 1$) it is known [56] that an airfoil loses almost all circulation. However, it was already observed negligible spanwise flow already at $Re = 100$ [13] [15] [27] [111], far away from creeping flow regime, so there might be another possible explanation. Recent numerical simulations [23] have shown that circulation in a revolving wing is indeed highly dependent on Re number, see Figure 2-34a. For $Re = 10$ circulation is almost negligible, so it seems that way above $Re = 1$ the wing displays a typical creeping flow behaviour. $Re = 500$ is the critical point where viscous effect start to be negligible. These results agree with Aono *et al.* pressure gradient hypothesis, and the observations at $Re = 100$ [13] [15] [27] [111] and $Re = 1400$ [15] [111].

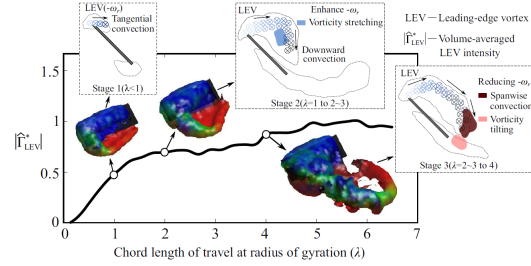
As noted first by Lentink and Dickinson [61] LEV intensity is also highly dependent on the stage of the stroke. The stroke is usually quantified in literature with the number of chords covered by the wing tip: $\lambda = \frac{s}{c}$. At the beginning of the stroke circulation is really weak and non-stationary forces dominate due to the added mass effect of the surrounding fluid, see Figure 2-34a. When the wing tip covers a larger distance, more circulation is accumulated at the leading edge and this enhances lift enormously. Nevertheless, in revolving wings vorticity reaches a point after approximately $4c$ of travel where it achieves stationary state [24], although in low Re regimes the maximum vorticity is reached before, as less circulation is allowed in the steady state due to viscous diffusion. It was also observed in literature [25] that the sooner the maximum stroke velocity is reached, the sooner the steady state vortex is achieved, being the limit around 2.5 chords with an almost impulsively accelerated stroke.

Chen *et al.* [24] were able to give a comprehensive understanding of the vortex dynamics. They divided LEV development into three different stages (Figure 2-34b):

1. Initial LEV vortex begins to grow, while it is advected downstream.
2. LEV vortex continues to grow. Vortex starts to roll up and vorticity is advected towards the wing due to vortex self induction. This limits vortex growth, and at the same time vorticity stretching increases LEV strength.
3. In the final stage vortex reaches a steady state. Steady equilibrium is reached when spanwise vorticity destruction is equal to production. Apart from the conventional spanwise vorticity advection, another key destruction mechanisms has been identified in literature [23]: vorticity



(a) Circulation and lift coefficient variation with Reynolds number. [23]



(b) Circulation increase with time in a revolving wing. Contours of vorticity and sketches display the three different stages in the formation process of a LEV. [24]

Figure 2-34: Stable LEV in a revolving wing.

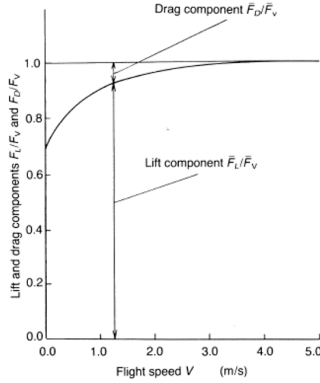
tilting due to non-inertial reference frame. Spanwise vorticity (LEV) is converted into downstream vorticity, and tangential vorticity (tip vortex) is rotated to negative spanwise vorticity, subtracting this way circulation from the LEV. This establishes a dynamic exchange of LEV and tip vortex vorticity that controls the growth of the LEV.

In summary, a stable and attached LEV caused by dynamic stall is observed in insects. This vortex enhances force production and in dragonflies it has been observed to continue across the thorax, connecting both wings LEV. Dragonflies typically have $Re \approx 1000$, which means that according to Chen *et al.* [23] they are able to develop the maximum possible non-dimensional circulation, as they do not suffer viscous diffusion that diminished the intensity of their LEV. Moreover, according to Chen *et al.* [25] and observing typical dragonfly aspect ratios ($AR \approx 6$ [40]) maximum vortex size is achieved around half of the stroke in dragonflies. Rossby numbers of dragonflies are typically around 6, which according to Lentink and Dickinson [61] should guarantee vortex stability at all Re numbers. In particular, at dragonflies Reynolds numbers stability of LEV is achieved mainly due to vortex spanwise advection and vortex tilting [23]. At this Re numbers vortex bursting around half of the wing is also expected according to Lentink and Dickinson [61] observations. Note that actual dragonflies have corrugated wings and previous studies have been done with flat plates, so there could be slight differences in the LEV structure, see section 2.4.

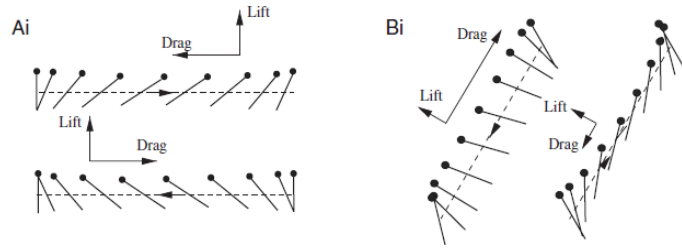
2.2.4 Drag as a vertical force

The separation of lift and drag was convenient for an airfoil for at least two reasons. First, at a small angle of attack, the lift is many times the drag. Second, in steady forward flight, the efficiency is measured by the lift-to-drag ratio. Neither of these applies to a hovering insect, so a completely new approach has to be followed to understand dragonfly aerodynamics.

The first studies of dragonflies already observed that steady aerodynamics were not sufficient to explain the high lift coefficients of dragonflies. Unsteady phenomena, such as added mass effect or



(a) Drag vs lift usage at different flight regimes in dragonflies. [7]



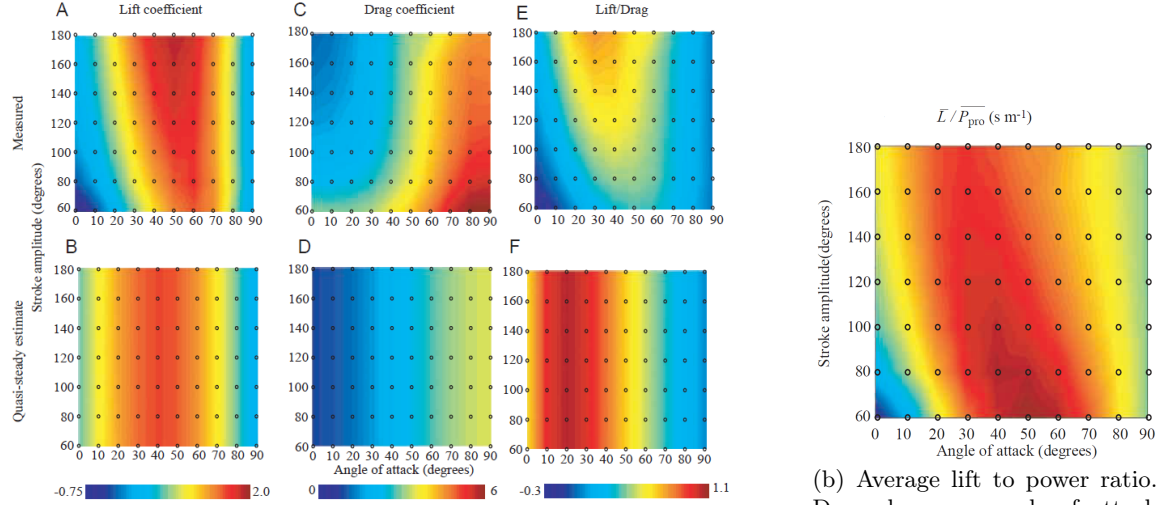
(b) Ai) horizontal stroke observed in most insects. Bi) inclined stroke observed in dragonflies. [130]

Figure 2-35: Drag role during dragonflies hovering.

LEV were then considered to address these discrepancies. However, only lift component (normal to the stroke path) was considered in the first estimates of Ellington [40] [39] and Weis-Fogh [132] [133]. Azuma *et al.* [7] were the first to realize that drag also played a crucial role in the production of vertical force in insects. They observed that drag importance increased at low flight speed, see Figure 2-35a. During pure hovering almost 40% of the total vertical force was produced by drag. Wang *et al.* [130] numerically studied the importance of drag in the typical inclined stroke of dragonflies. Due to the high angles of attack drag was relevant specially during the downstroke, where drag could support about 76 % of the dragonfly weight. Therefore, it can be seen that in pure hovering the lift-to-drag ratio is not a good indicator of the hovering performance. Wang *et al.* [130] explained that this could also be a possible explanation for the high lift coefficients derived in the free flying dragonflies. Unsteady aerodynamics was not the only explanation, drag was also missing. Dynamic stall (unsteady effects) can increase C_L to 2, but not to 4. Here drag plays a role.

In section 2.1.1 it was seen that the three existing flapping strategies observed in nature are horizontal, inclined and vertical stroke. In horizontal stroke, Figure 2-35b Ai, vertical force production can only be produced via lift. Therefore, drag is not desired and is a waste of energy. Given that at insect flying regimes lift-to-drag ratios are quite low (around 2 - 5 [9]), flapping efficiency in horizontal stroke is low. On the other hand, in the typical inclined stroke of dragonflies (stroke plane of $\approx 60^\circ$, see notation section 2.1) used by dragonflies, Figure 2-35b Bi, both drag and lift can be used to produce vertical force. This means that drag is now desired and can in fact maximize total vertical force production. This is a novel approach of producing vertical force, and makes sense at low Re such as the ones observed in insects. As it is commonly said: *if you can not beat them, join them.*

An important concept should be noted before we proceed with the discussion. Let's define the vertical force coefficient as: $C_F = \frac{\sqrt{L^2 + D^2}}{\frac{1}{2} \rho \omega^2 R_g^2 S}$, where S is the wing surface, ω the angular velocity, R_g



(a) Dependence of stroke-averaged coefficients with the angle of attack and stroke amplitude. First row, actual measurements during the experiment. Second row, coefficients obtained with quasi-steady model. First, second and third columns, lift, drag and lift/drag respectively. [101]

(b) Average lift to power ratio. Dependence on angle of attack and stroke amplitude. [101]

Figure 2-36: Experimental flapping of a flat plate.

the radius of gyration and L and D the lift and drag. Note that lift and drag should be oriented such as the resultant points in the vertical direction. Then, the ratio of force to power is defined as the Figure of Merit FM , $FM = \frac{F}{P} \approx \frac{1}{\omega R_g}$. Operating the previous expressions the following is obtained:

$$W = F = C_F \frac{1}{2} \rho \omega^2 R_g^2 S \approx C_F \frac{1}{2} \rho \frac{1}{FM^2} S \rightarrow FM = \sqrt{\frac{C_F \rho S}{2W}}. \quad (2.16)$$

What is important from the previous expression is that in order to maximize the force to power ratio FM for a given insect of weight W and wing surface S , the force coefficient C_F should be maximized. This is the reason why inclined flapping is beneficial in dragonflies: drag can be effectively used on top of lift to maximize the total force production. Inclined stroke plane is just an strategy to redirect the total force vector in the vertical direction.

The question now is, how can force production be maximized? In this section only the downstroke and upstroke are going to be studied. Rotation phenomena during pronation and supination will be studied in a separate section, subsection 2.2.5, as it involves slightly different aerodynamic phenomena.

First, the dependence of stroke-averaged coefficients with the angle of attack is going to be considered. Sane *et al.* [101] studied strokes with different angles of attack, and experimentally measured the averaged lift and drag coefficients, see Figure 2-36a. Maximum averaged lift coefficients

were observed with angles of attack of 60° . On the other hand, drag coefficients reached maximum values around 80° . However, in this experiment they used an horizontal stroke, so only lift is useful, drag is just a waste of energy. For this reason the maximum efficiency $\frac{\bar{L}}{\bar{P}}$ is achieved around 50° with maximum lift coefficients, as it is seen in Figure 2-36b. Moreover, they also noted that strokes with amplitudes around 60° were more energetically efficient. Dickinson *et al.* [36] did a similar experiment and provided a numerical approximation for the averaged coefficients during a revolving stroke with a flat plate:

$$C_L = 0.225 + 1.58\sin(2.13\alpha - 7.2) \quad (2.17)$$

$$C_D = 1.92 - 1.55\cos(2.04\alpha - 9.82), \quad (2.18)$$

where α is the stroke angle of attack in degrees. The numerical regression and the experimental data can be seen in Figure 2-37a. From the analysis done before, $\sqrt{C_L^2 + C_D^2}$ should be maximum during an inclined downstroke to optimize the Figure of Merit FM . Using Dickinson *et al.* data, an optimal stroke angle of attack during the downstroke of $\approx 85^\circ$ is obtained. Moreover, the stroke plane angle should be $\approx 70^\circ$ to direct the total force into the vertical direction. This stroke value is close to the observations of Norberg [74], 60° , and shows that dragonflies indeed use drag as the main component to hover during the downstroke.

In subsection 2.2.3 it was seen that the LEV plays a crucial role in the development of lift force. However, now it has been seen that drag is also relevant, so the following question follows: is the LEV also beneficial for drag? The answer is yes. Dickinson *et al.* [36] showed that for pure translational flapping (Rossby number is ∞), where no spanwise vorticity blowing nor vortex tilting occur, the LEV is detached. However, when revolving wings were used, a stable LEV was obtained, see Figure 2-32b. Lentink *et al.* [61] saw that indeed in revolving wings (LEV attached) both lift and drag were much higher, Figure 2-37b, compared to a translational wing (LEV detached). This answers the question that was posed before. LEV enhances lift as well as drag production.

Summarizing, dragonflies orient their stroke plane to direct the resultant force of both lift and drag in the desired direction. This way by using drag during the downstroke they are able to reach much higher force coefficients. According to the Figure of Merit that was studied, this minimizes the power consumption for hovering for a given mass. Finally, the LEV is crucial as it maximizes the production of lift and drag, and therefore allows to reach a much more efficient hovering.

2.2.5 Rotational force and wake capture

Until now only translation and revolving wings during downstroke and upstroke have been studied. It has been seen the importance of dynamic stall and a stable LEV to maximize force production.

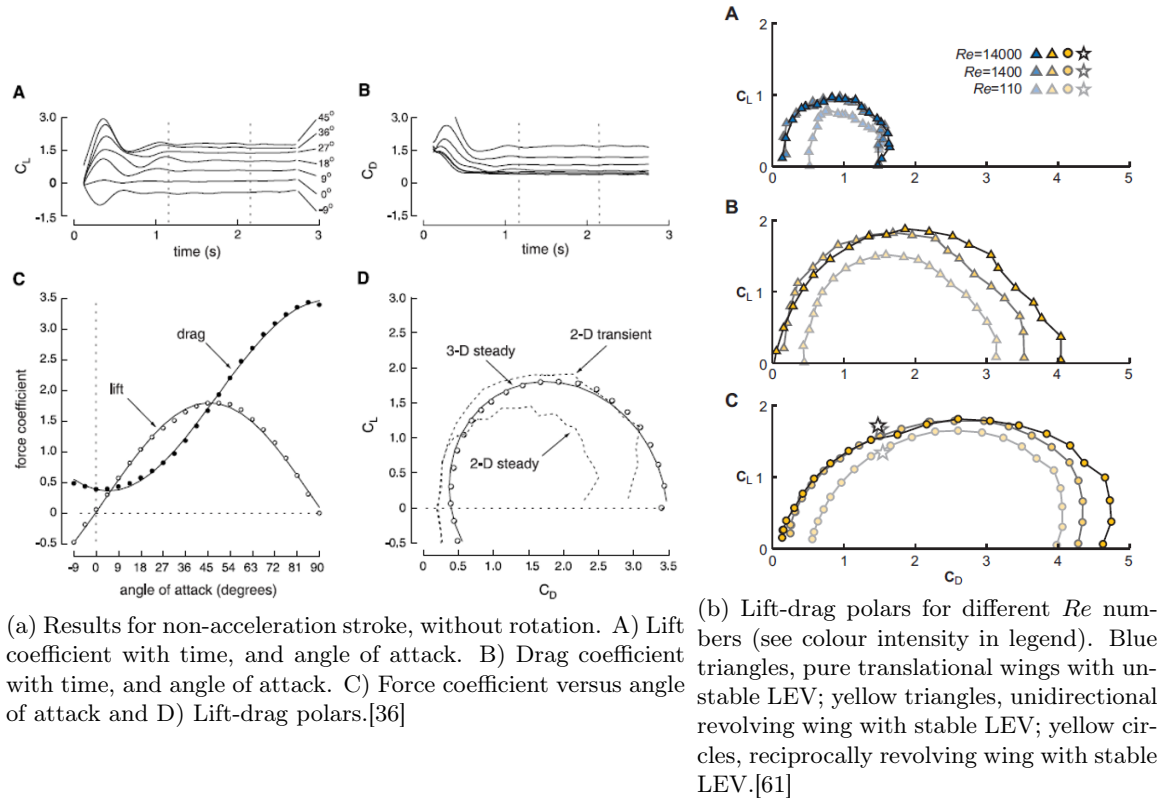


Figure 2-37: Flapping of a flat plate. Experimental results.

However, flapping aerodynamics also has an important stage that has not been addressed: pronation and supination of the wings. At the end of each upstroke and downstroke, insect wings are rotated to start the next stroke. This rotation has been proven to contribute significantly to the average vertical force during a flapping cycle. For example, rotation phases contribute to 35 % lift in *Drosophila* [36]. Ellington studied the importance of rotational lift using linear potential theory [41]. This approximation gives an idea of the forces per unit of length contributing during rotation:

$$L_{unsteady} \approx \frac{1}{4} \rho \pi c^2 \left[\frac{d^2 z}{dt^2} - \frac{d\omega}{dt} c \left(\hat{x}_0 - \frac{1}{2} \right) + \omega U \right] \quad (2.19)$$

$$L_{steady} \approx \pi \rho U \omega c^2 \left(\frac{3}{4} - \hat{x}_0 \right) + \pi \rho U^2 c \alpha. \quad (2.20)$$

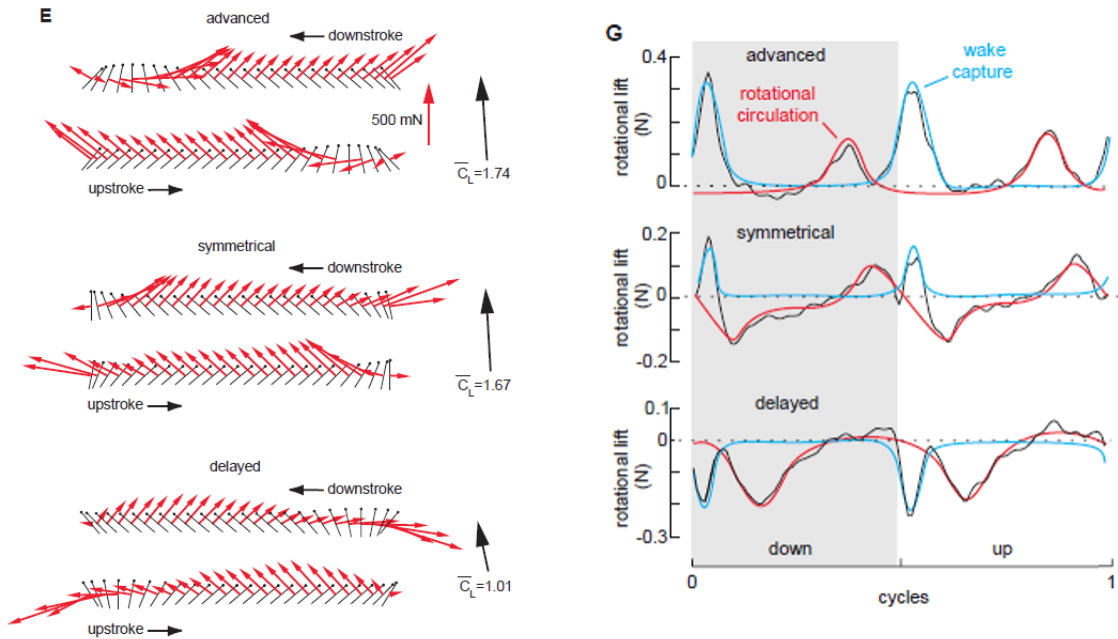
\hat{x}_0 is the non-dimensional (with the chord c) point of rotation measured from the flat plate leading edge, ω the rotation speed, z the vertical displacement, α the angle of attack, ρ the density and U the upstream velocity. $L_{unsteady}$ includes the added mass effect due to translational acceleration $\frac{1}{4} \rho \pi c^2 \frac{d^2 z}{dt^2}$ and rotational acceleration $-\frac{1}{4} \rho \pi c^3 \frac{d\omega}{dt} \left(\hat{x}_0 - \frac{1}{2} \right)$. Note how rotational acceleration scales with c^3 , so rotational forces would contribute more to low aspect ratio wings. The term $\frac{1}{4} \rho \pi c^2 \omega U$ is the added mass effect caused by the rotation of the surrounding flow at speed U , and could be

regarded as a Coriolis force.

L_{steady} refers to the circulatory lift. The second steady lift term, $\pi\rho U^2 c\alpha$ refers to the classical circulatory lift found during pure translation. The first component can be referred as the Magnus effect [107], $\pi\rho U\omega c^2 (\frac{3}{4} - \hat{x}_0)$. Dickinson *et al.* [36] were able to prove the importance of Magnus effect during the rotation phase of wings. They considered an experimental set up with a flat plate that was able to translate and rotate independently. They studied three different rotation schemes with respect to the translational stroke, see Figure 2-38a: advanced, symmetrical and delayed rotation. They noticed that with advanced rotation ($U > 0, \omega > 0$), Magnus effect (called rotational circulation in red in Figure 2-38b) contributed effectively to positive vertical forces, while delayed rotation gave a negative vertical component ($U < 0, \omega > 0$). This aligns perfectly with the predictions of linear potential theory (Coriolis and Magnus terms, $\frac{1}{4}\rho\pi c^2\omega U$ and $\pi\rho U\omega c^2 (\frac{3}{4} - \hat{x}_0)$ respectively). Consequently, using potential theory it can be estimated for example that during supination (rotation at the end of the downstroke) advanced rotation is desired, to make sure ω and U have the same sign, and contribute to a positive Coriolis term $\frac{1}{4}\rho\pi c^2\omega U$. Moreover, Dickinson *et al.* [36] proved that the rotational axis, which is exactly 0.75 for linear inviscid potential flow with a flat plate [41], can be extended with good agreement for viscous flows ($Re \approx 1000$) and non-linear oscillations, see Figure 2-39a. This is useful because during supination (non-linear rotation), it can also be inferred that the position of the axis of rotation should be placed close to the leading edge $\hat{x}_0 \approx 0$ to produce vertical force via Magnus term $\pi\rho U\omega c^2 (\frac{3}{4} - \hat{x}_0)$.

Flapping wings follow a periodical stroke. This means that the wings faces the flow history from previous strokes. Consequently, flow history and wake capture is also important, and was not included in the previous model. Dickinson *et al.* [36] and James M. Birch *et al.* [14] observed experimentally that correctly tuning wing rotation phase has a great impact in terms of vertical force production. Figure 2-39b shows three rotation strategies at the end of an horizontal stroke. The wing was coming from the left, so it has a wake with an induced velocity going from left to right. Then it turned around and in the figure is shown at the beginning of the next stroke, going from right to left. Depending on the pitch angle of the airfoil during the beginning of the next stroke, this horizontal induced flow can be pushed downwards (advanced) or upwards (delayed). Therefore, advanced rotation produces positive vertical force, and vice versa. This is what they called wake capturing. Lentink *et al.* [61] also observed the explained phenomenon in revolving wings, see Figure 2-37b. Between concurrently revolving wings (periodical strokes) and unidirectional revolving wings (no direction reversal), it was seen that the overall forces (especially the drag) were higher in the wing that had periodical strokes, as the wing perceived a higher dynamic pressure due to the wake induced in the previous half stroke.

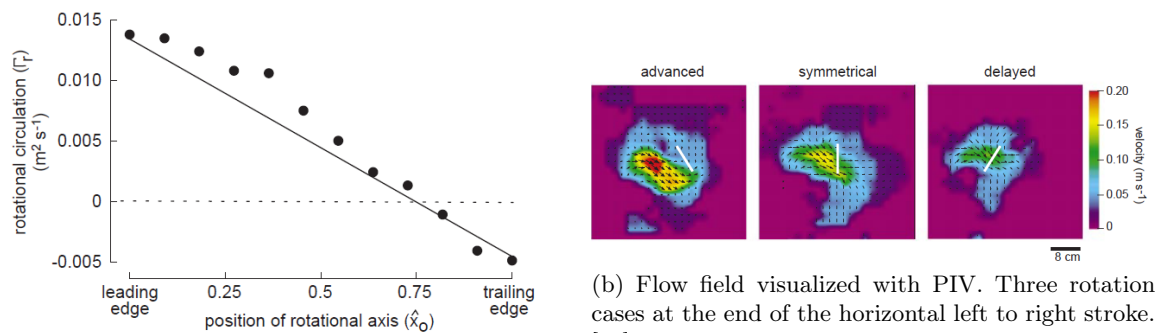
In conclusion, the rotational phase contributes to a great percentage of the average forces during the flapping cycle. Added mass effects can be due to translation, rotation or Coriolis accelerations.



(a) Stroke trajectory and forces on the flat plate. Three rotation cases: advanced, symmetrical and delayed. [36]

(b) Isolated vertical force associated with pure rotation. Two phenomena can be distinguished: wake capture and rotation circulation. [36]

Figure 2-38: Vertical forces in hovering depending on point of the stroke where rotation is started.



(a) Circulation measured in actual flat plate depending on the axis of rotation. [36]

(b) Flow field visualized with PIV. Three rotation cases at the end of the horizontal left to right stroke. [36]

Figure 2-39: Wake capture and dependence of circulation with rotational axis.

With flapping and pitching phase, Magnus effect and Coriolis added mass effect can be tuned to enhance vertical force production during wing pronation and supination. Additionally, wake capture is important to improve flying efficiency. The idea is basically to convert kinetic energy from the previous stroke into useful force production.

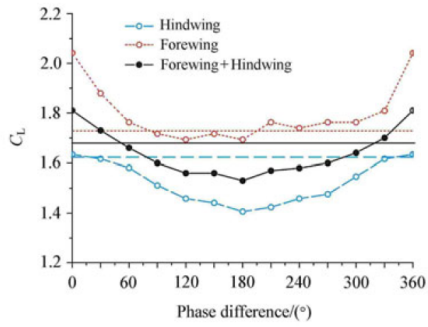
2.3 Wings interaction

Until now the aerodynamics of one ipsilateral single flapping wing has been studied. However, dragonflies have two pairs of wings. Is this really beneficial? This is the question that is going to be inspected in this section.

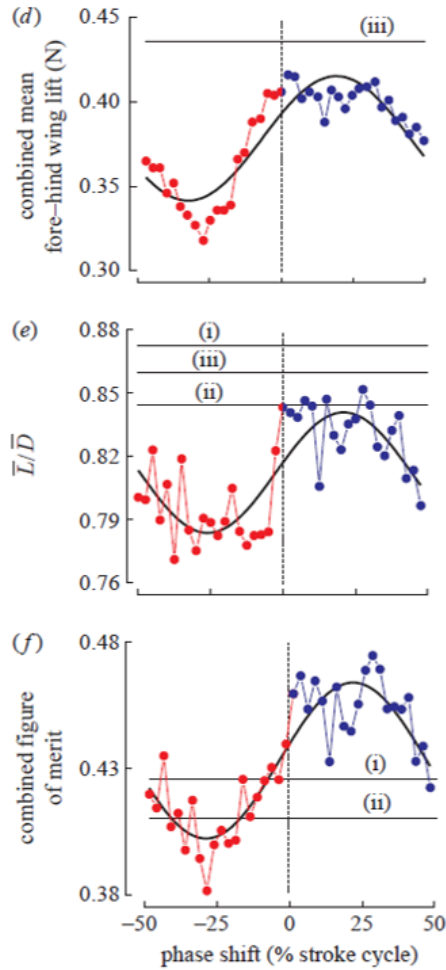
Platzer *et al.* [86] discovered that if an steady airfoil (2D) was placed rearward of an oscillatory airfoil, propulsive efficiency of such a configuration is close to 100 percent and is nearly independent of the reduced frequency. The key is that the energy carried away in vortices within the wake of the first oscillatory airfoil, is being converted into thrust by the second steady airfoil, instead of being swept away with the flow. Based on this observation they suggested that the wing-vortex interactions generated by the dragonfly are a way of trapping with the hindwings the energy from the free vortices shed by forewing, and this enhances lift.

Hu *et al.* [54] studied more in detail the interaction between the hindwings and forewings. They measured the forces experimentally and determined that there was a huge dependence on the phase shift between ipsilateral wings. They concluded that in-phase flapping gave a higher lift coefficient (averaged through stroke cycle), Figure 2-40a. This agreed with observations from Ellington [40] and Weis-Fogh [133], as dragonflies used in phase flapping for accelerated maneuvers, where a higher lift coefficient was required. On the other hand, Usherwood and Fritz-Olaf *et al.* [118] did a similar experiment, but they measured a higher average lift of both wings combined (Figure 2-40b), with the hindwing leading the forewing by 25° .

These previous results clearly disagree with each other. To further clarify these results flow visualization are going to be studied. Broering and Lian [19] studied wings interaction with a 2D simulation. Even though it was seen in subsection 2.2.3 that 2D simulations do not correctly represent the physics of 3D LEV, their analysis provides useful information to clarify previous disagreements. Broering and Lian modelled wing flapping at different phase shifts and with different horizontal spacing. They discovered that what really matters is the interaction of the wake of the forewing with the hindwing. In Figure 2-41a they simulated a scenario where the phase shift and spacing was different, however, it can be seen how the wake of the forewing interacts with the hindwing a really similar way. More importantly, when they computed the force coefficient of this scenario in Figure 2-41b they realized that they were almost identical if the forewing wake-hindwing interaction was replicated. This is probably the main reason why Hu *et al.* [54] and Usherwood

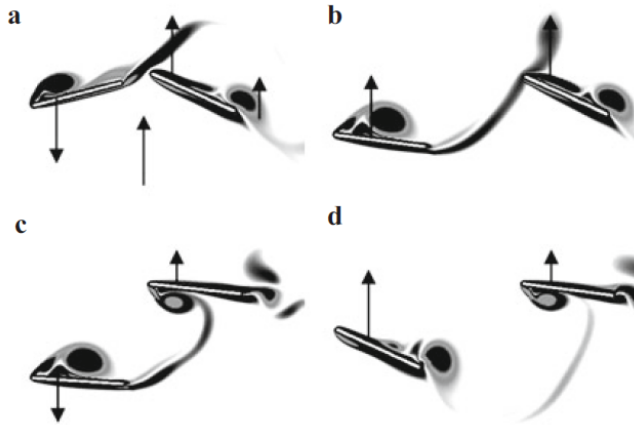


(a) Lift coefficient with phase difference. Experimental results for hindwing and forewing. [54]

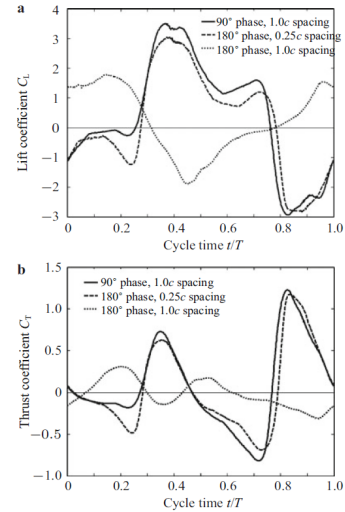


(b) A) Combined lift force [N]. B) Average lift to drag ratio. C) Combined figure of merit FM. [118]

Figure 2-40: Performance dependence with phase shift between forewing and hindwing.



(a) Vorticity plot. a) and c) have 180° phase difference and $0.25c$ spacing. b) and d) have 90° phase difference and $1c$ spacing. [19]



(b) Lift and thrust coefficient during the stroke cycle. Three different phases and spacings are studied. [19]

Figure 2-41: Advection of vorticity in the wake is what really conditions the forces. This depends on phase and distance between ipsilateral hindwinds.

and Fritz-Olaf *et al.* [118] results did not agree. They used a different spacing between their wings in their experiments. Therefore, it can be concluded that there is no universal phase shift that optimizes flapping properties. All depends on the actual relative position between the wings, and for this a detailed study of wake advection is required.

However, there is still the unknown of how vorticity shed into the wake affects each wing. For example, in Figure 2-40a it can be seen how the lift performance of the hindwing decreases, while on the other hand the forewing increases. To answer this question the flow field induced at the wake is going to be seen in more detail. Hu *et al.* were able to measure with PIV the flow field of two wings following Norberg's [74] kinematics. In Figure 2-42a it can be seen the flow field generated at the wake during the downstroke. The wake has an induced downward velocity, the blue area sketched in Figure 2-42b. On the other hand, the LEV area has local velocity going upwards due to the circulation. Now let's imagine that the represented wing in Figure 2-42b is the hindwing, therefore, the forewing sweeping plane would be to the right, next to the LEV region. In this region the forewing during the downstroke will find an induced upwash (due to the hindwing LEV) that goes against its movement, and that increases the dynamic pressure. This is the reason why lift coefficients are increased so much when the hindwing is more or less in phase with the forewing in Figure 2-40a and Figure 2-40b. On the other hand, if we consider that the flat plate in Figure 2-42b is the forewing, then the hindwing would be placed to the left of the sketch. In theory if the hindwing and forewing strokes are parallel, it seem that they should not interfere. However, the blue region of the forewing is advected downwards following the streamline indicated in black, and enters in the

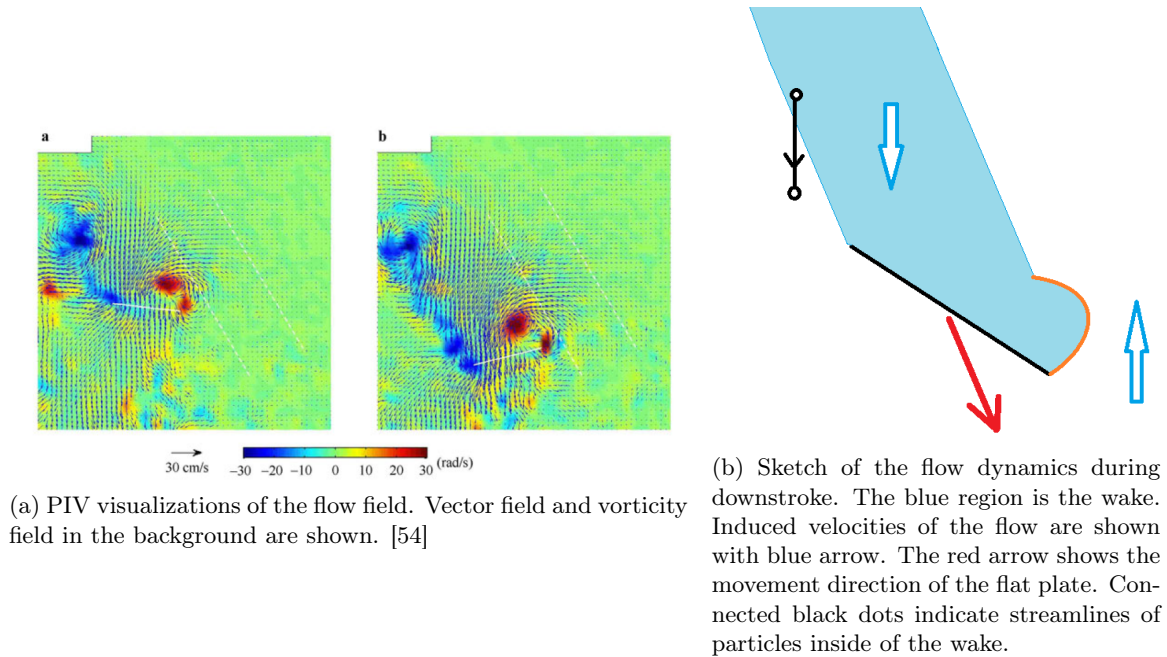


Figure 2-42: Velocity field in the wake of a flapping plate.

path of the hindwing. This downwash decreases the effective angle of attack of the hindwing and its dynamics pressure (less relative velocity of the hindwing during the downstroke when most of lift production happens), and is the reason why the hindwing suffers a decrease in lift relative to the forewing, see Figure 2-40a.

In the previous scenarios it was seen that depending on the interaction, the relative velocity of the flow field to the flat plate can be increased or decreased. Moreover, there is also a really important phenomenon that was not mentioned before: the LEV growth and shedding. Varying incoming flow speed can have a great effect and modify completely the dynamics of the LEV. For example, in Figure 2-43 see how the wake greatly increases the LEV in j) (in-phase flapping), while in k) (90° phase) and l) (180° phase) the LEV is diminished.

Nevertheless, in hovering there is an added difficulty: vortices are accumulated near the stroke planes of the hindwing and forewing in successive strokes. Given dragonflies Reynolds numbers, this vortices take some time to dissipate. Moreover, there is no U_∞ velocity to advect this vortices. As a consequence, vortex structures are accumulated as shown in Figure 2-44. Having a coherent vortex structure is an opportunity for energy extraction and optimization. However, if the wake gets too chaotic, this may start to be negative. To solve this Jane Wang [129] devised a mechanism to shed vorticity: dipoles. Dipoles induce each other a velocity in the same direction. This causes automatically the advection of the structures away from the stroke plane if they are oriented in the right way, see Figure 2-45. It is important to highlight once again that some of these results, such as dipole advection, were done in 2D. It is already known that 3D mechanisms are completely different

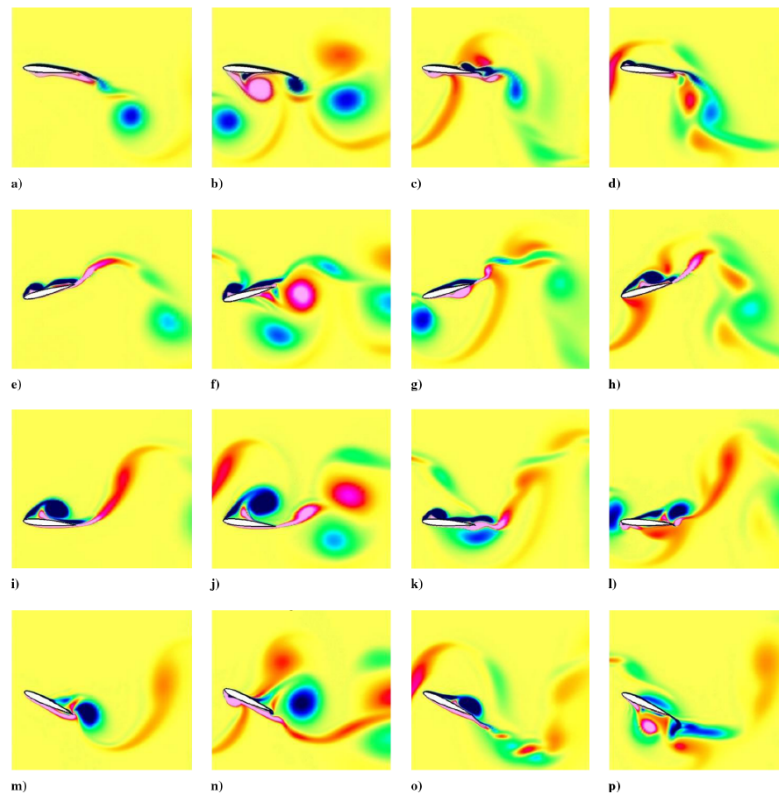


Figure 2-43: Vorticity contours of 2D numerical simulations. Blue indicates clock-wise vorticity and red counter-clock-wise vorticity. First column: single airfoil. Second column: in phase flapping, 0° . Third column: phased stroking, 90° . Fourth column: counter stroking, 180° . Each row contains the exact same point of the stroke of the hindwing. [20]

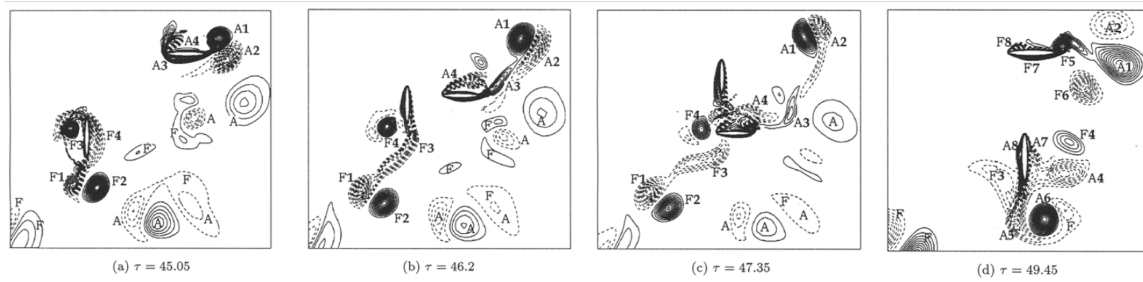


Figure 2-44: 2D numerical simulation. LEV accumulation during hovering. [109]

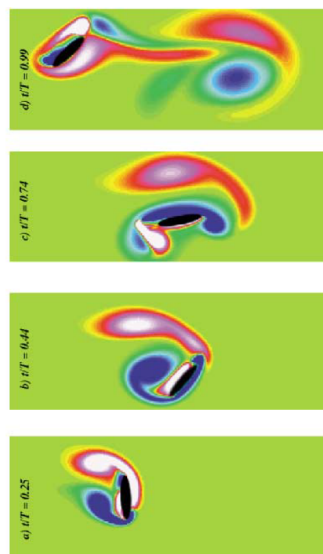


Figure 2-45: Dipole self induction as a mechanism of vortex shedding. [129]

(non-inertial rotational effects in revolving wings, spanwise blowing ...), so this may not be valid anymore.

In summary, wake interaction presents at the same time a challenge and opportunity for flapping optimization. The most relevant parameter is the relative distance between a wing's wake and another wing. Stroke phasing and wing spacing are two possible ways of controlling this relative distance. This allows to orient every wing in an efficient way regarding the incoming wakes. Moreover, it was seen that the two main mechanisms that lead to force modification during wing-wing interaction are variations of relative velocity and modification of LEV dynamics. Finally, in order to control vortex accumulation during hovering, dipoles self-induction may be a good solution, although its effectiveness has to be verified in 3 dimensional flows.

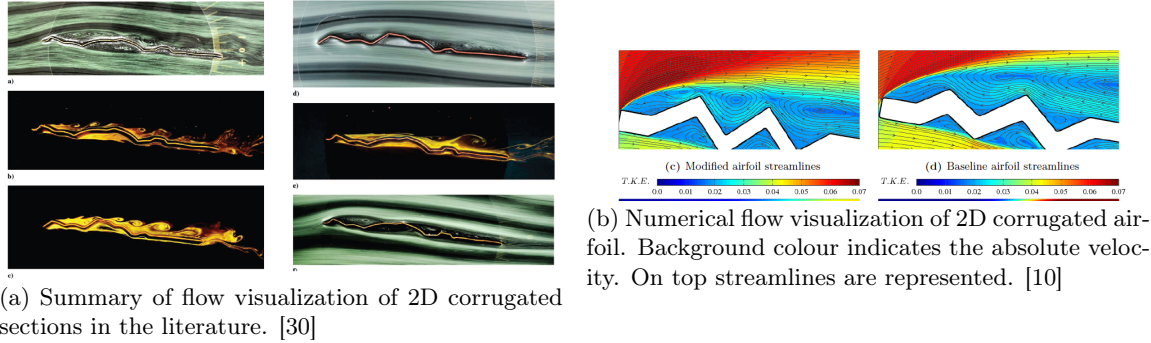


Figure 2-46: Flow visualization around corrugated wings.

2.4 Corrugation

Most of the studies that have been done in literature used a simplified model of the wing. Normally, a flat plate is the chosen alternative. Nevertheless, actual insects and in particular dragonflies have corrugated wings. However, a question arises here: are all the conclusions and observations regarding wing flapping (LEV stability, LEV structure, vorticity shedding, etc) still valid with corrugated wings? In this section the current understanding of corrugation effects is going to be assessed.

2.4.1 Steady analysis

First, steady analysis of flow around a corrugated airfoil is going to be considered. Overall, experimental [78] [92] and numerical [30] [10] [119] studies agree that in steady flight, a profiled airfoil around the corrugation is created, see Figure 2-46a. In particular, the profiled airfoil has a higher camber and thickness, and this increases the lift coefficient [10] [119], when compared to a flat plate. Within the corrugation valleys recirculation areas are created. Therefore, corrugation seems to trap vortices around the airfoil, and also increases effective thickness due to these trapped structures. Moreover, corrugation profile is not something random. Barnes *et al.* [10] showed numerically that varying slightly the corrugation shape can have a huge effect in the overall aerodynamic behavior of the wing. For example, in Figure 2-46b it can be seen how in the geometry from the left, a stable vortex is created in the second valley (consider leading edge as first valley) of the upper side of the wing. This vortex pushes the flow that has passed the second valley towards the airfoil, and therefore maintains attached the flow. However, in the corrugation pattern from the right, there is no stable vortex in the second valley. Therefore, the flow is detached, and the effective camber increases much more. Consequently, it can be concluded that trapped vortices can help to maintain attached the flow. Nevertheless, the geometry has to be specially tuned for each angle of attack. It is uncertain if this behavior will remain over a wide range of angles of attack for a fixed geometry.

Trapped vortices can also be understood as *wheels* that push smoothly outer streamlines. See in Figure 2-47a how a clear profiled airfoil is created, and how in each valley the recirculation zones

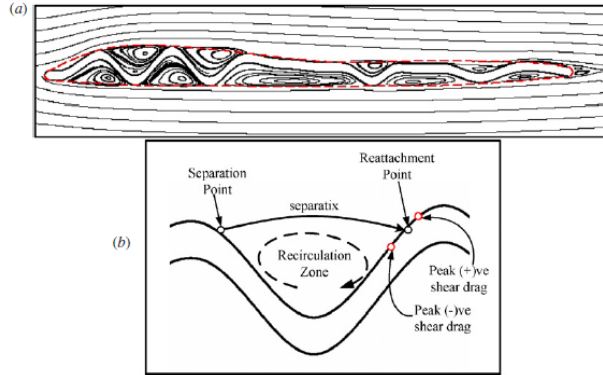
act like a kind of wheel pushing the flow downstream. In fact, due to these recirculation regions it can be seen in Figure 2-47b how at some points of the airfoil negative skin friction coefficients are reached [119]. Additionally, in Figure 2-47b Vargas *et al.* [119] compared an airfoil that had the same profile as the profiled corrugated airfoil. It is really interesting to see how indeed the recirculation regions are able to decrease the global skin friction, while maintaining similar lift coefficient. Note that the non corrugated airfoil was designed to have the same profile, so it has similar streamlines, which mean similar lift coefficient. The trick here is that drag is not only skin friction, there is also pressure drag. However, quite surprisingly, Vargas *et al.* computations demonstrate that even though pressure drag increases slightly in the corrugated airfoil, there is an overall drag reduction.

It has been seen that corrugation may be a promising alternative in terms of postponing flow detachment and drag reduction. However, until now only 2D man-made corrugation has been analyzed. Actual 3D corrugation patterns of insects might unveil some optimization that could be useful to understand. There are very few papers in the literature that have regarded this. Chitsaz *et al.* [29] did an experiment with an actual 3D dragonfly wing. However, they were not able to resolve the vortices scales around the airfoil due to PIV resolution. Despite this, they observed that a Karman vortex street appeared, which was created by the wake oscillations generated by the unstable shear layer. Based on this they hypothesized that the laminar trapped vortex intensity oscillated in time, due to the instability of the shear layer of the profiled airfoil, and after leaving the leading edge leads to the Karman vortex street. This agrees with the drag time-dependent oscillations that Vargas *et al.* [119] observed in the friction coefficient.

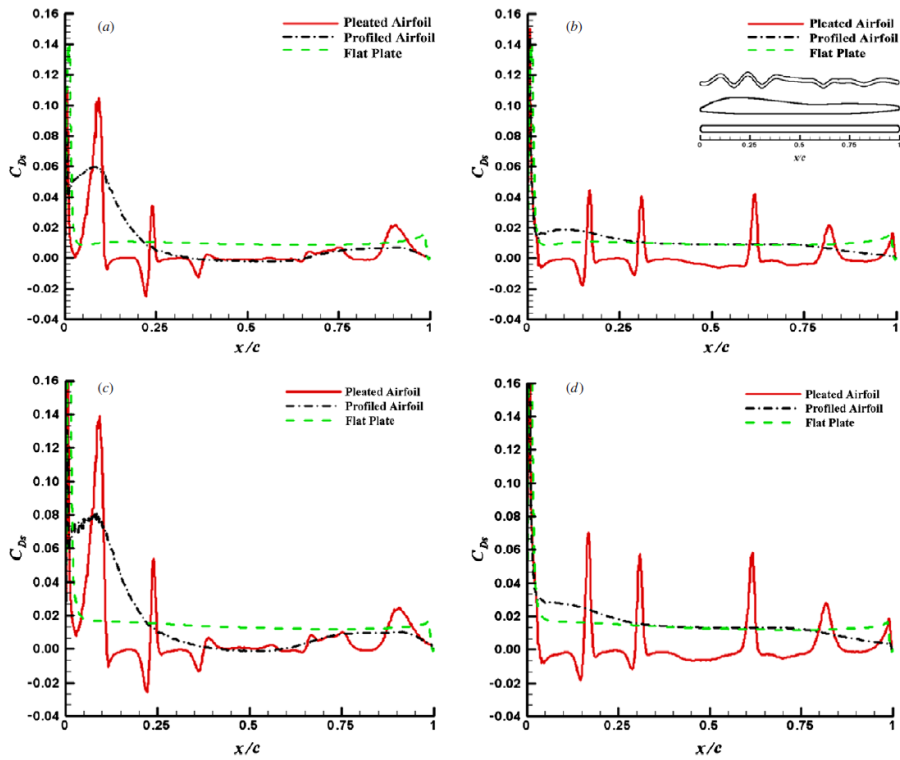
Additionally, a numerical study [30] with the same actual geometry as Chitsaz *et al.* [29] was done. They observed (Figure 2-48a) a complex vortex structure that interacted in a three dimensional way depending on the spanwise evolution of corrugation. Therefore, they realized that 2D simplification were lacking a lot of complex phenomena, such as spanwise vortex interaction. In particular, the 3D spanwise corrugation acted as channels that advected streamlines from the root to the tip. This channels might be related to the 3D spanwise vorticity, which was key in the leading edge vortex stability (subsection 2.2.3), see Figure 2-48a. Finally, it is interesting to mention that their numerical simulations gave higher lift and drag for the corrugated wing, see Figure 2-48b. This means that corrugation interacts more strongly with the surrounding flow. It was derived in subsection 2.2.4 that in flapping it is desired a higher force coefficient, so that the same force can be obtained with less energy. Consequently, corrugation is clearly beneficial for this purpose.

2.4.2 Unsteady analysis

In previous section steady analysis were done of corrugated wings. However, as is has been seen, unsteady effects are clearly dominant in flapping wing aerodynamics. In this section the effects of corrugation for the unsteady case are going to be investigated.

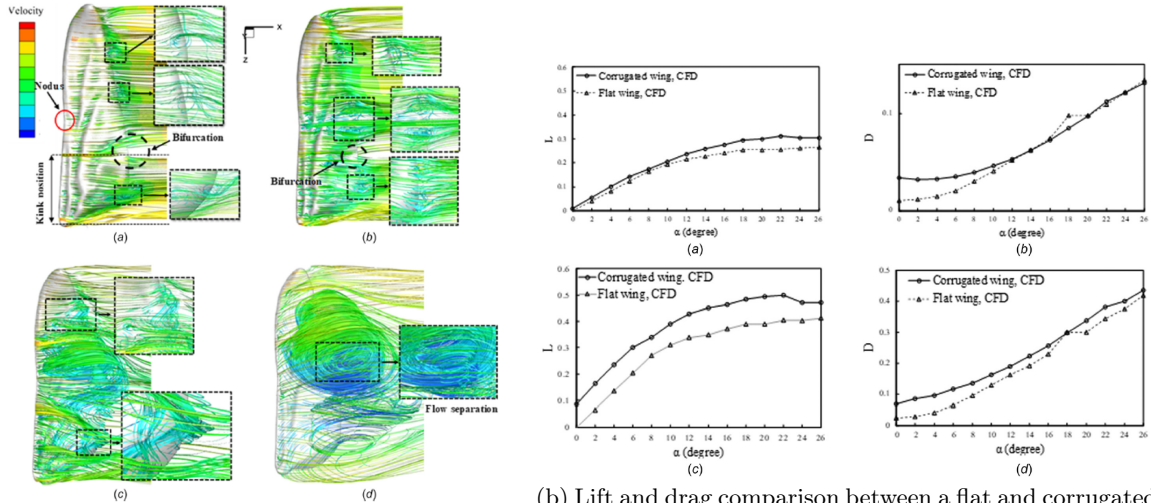


(a) a) Streamlines around a corrugated 2D section. b) Sketch of recirculation region in the corrugation valleys acting like a "wheel". [119]



(b) Skin friction coefficient at different Reynolds numbers. a) and c) suction surface; b) and d) pressure surface. a) and b) $Re = 10000$; c) and d) $Re = 5000$. [119]

Figure 2-47: Understanding the vortex dynamics within the corrugated valleys.



(a) Numerical simulation of actual dragonfly 3D geometry. Steady forward flight (no flapping). Streamlines are coloured with velocity norm. a) $\alpha = 5^\circ$ b) $\alpha = 10^\circ$ c) $\alpha = 20^\circ$ d) $\alpha = 40^\circ$. [30]

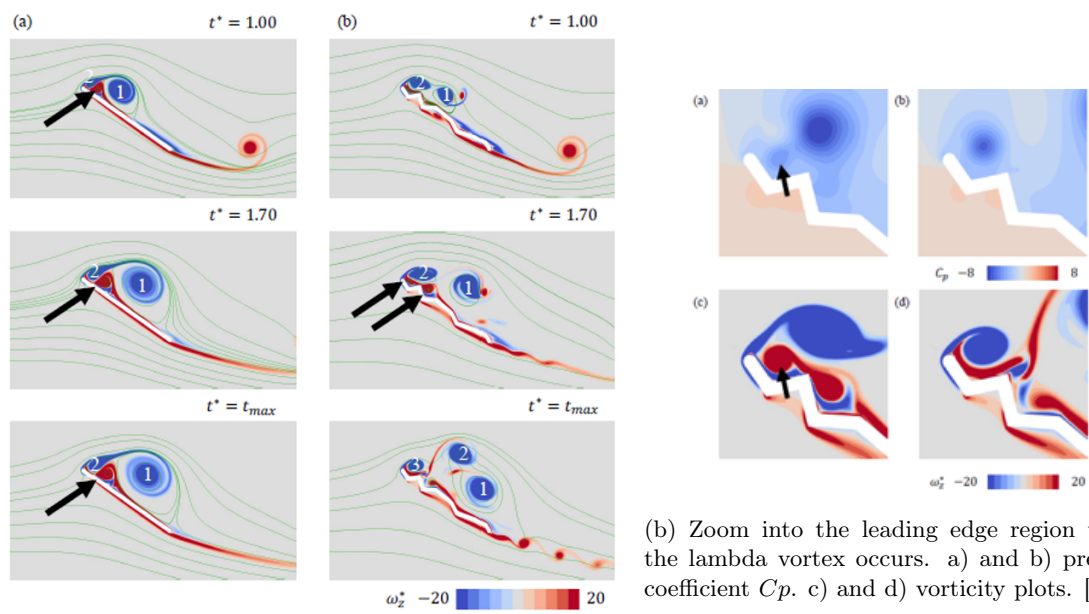
(b) Lift and drag comparison between a flat and corrugated wing. Wing corrugation was obtained with micro-CT from actual dragonflies. [30]

Figure 2-48: Numerical simulation of 3D corrugated wing.

Fujita and Iima [45] studied the unsteady effects in a corrugated airfoil with a 2D simulation. They realized that corrugation could greatly affect the LEV evolution: it could be shattered into smaller components of vorticity, and also trapped within the corrugation valleys, see Figure 2-49a. Moreover, the vortices that were shattered could interact with each other. In Figure 2-49a vortex 1 is being pushed towards the airfoil by vortex 2, while vortex 2 is being thrown away by vortex 1. Therefore, some vortex can remain attached for larger periods while others are shed almost instantly.

Eldredge *et al.* [38] reported a secondary structure next to the LEV, the so called lambda vortex. This lambda vortex had opposite vorticity to the leading edge, and was associated with its detachment. Fujita and Iima [45] also realized that this lambda vortex could be modified thanks to corrugation. See in Figure 2-49b c) how the lambda vortex is trapped between corrugation valleys, and was also shattered. Fujita and Iima [45] hypothesized that this effect could be tuned to delay the shedding of the LEV.

Unfortunately, there are almost no studies exploring corrugation effects in unsteady flow. The 2D results are limited as it was shown in subsection 2.2.3, because 2D profiles do not include effects like 3D spanwise advection that allow to stabilize the LEV. Therefore, the LEV shedding observed by Fujita and Iima [45] will probably not occur in 3D. This means that LEV shattering by corrugation probably has a completely different behavior.



(a) Snapshots of vorticity at different points of the stroke. Blue clockwise, red counter-clockwise. [45]

(b) Zoom into the leading edge region where the lambda vortex occurs. a) and b) pressure coefficient C_p . c) and d) vorticity plots. [45]

Figure 2-49: Numerical simulation of a 2D flapping wing. Comparison between corrugated and flat plate.

2.5 Conclusions and summary of literature review

Dragonfly kinematics are reported in the literature in a limited way, specially for hovering. There is a good description of the flapping angles, stroke plane angles and frequencies, but the feathering angle data is not sufficient. This implies that bio-inspired flapping dynamics can not be fully modelled and therefore understood using solely insect data.

Based on this, another approach has to be followed to understand how wings should be flapped to have efficient hovering. For this, a good understanding of the key known aerodynamic phenomena of flapping is required. Once the simple *building blocks* that characterize flapping aerodynamics are available, it is possible to understand how to properly combine them to have an efficient stroke. That is the reason why in the literature review a thoroughly investigation of these *building blocks* was done. The main identified *building blocks* were the following ones:

1. **Dynamic Stall**, see section 2.2.2.
2. **Leading Edge Vortex**, see subsection 2.2.3.
3. **Drag as Vertical Force**, see subsection 2.2.4.
4. **Wing Rotation**, see subsection 2.2.5.
5. **Wake Capture**, only one wing, subsection 2.2.5; two wings, section 2.3.
6. **Corrugation**, see section 2.4.

Dynamics Stall is well understood and described in the literature. The initial shear layer caused by dynamic stall rolls-up to create a stable and attached 3D **Leading Edge Vortex**. The **Leading Edge Vortex** is really interesting because it provides a huge amount of lift and drag while it remains attached. The key point is, how can it remain attached? The literature has brought some light to this issue. Several hypothesis have been suggested, such as axial flow, Coriolis effect, Eckman pumping and vorticity tilting. The reality seems to be a combination of all these factors, that varies with the Reynolds and Rossby numbers, but there is still much more work to be done to clarify the dependencies.

Another important concept is that flapping is quite unconventional, it uses **Drag as Vertical Force**. This a key mechanism that has been widely overlooked in the literature. All literature was focused on unsteady lift effects until only a few years ago. However, it is now known that most of the vertical force during the downstroke comes from drag. The limited dragonfly kinematics data seems to confirm this.

During a periodical stroke flapping wings have to turn around at some point. Thanks to classical lift theory, recent numerical simulations and experiments, **Wing Rotation** is well understood. Added mass effects, classical circulatory lift, and Magnus effect define the forces during the rotation

of the wing. The axis of rotation and point of rotation within the stroke cycle, have to be tuned according to these components to maximize force production in the desired direction.

The advantage of having periodical strokes is that it is possible to use in an efficient way the wasted energy shed into the wake during previous cycles, the **Wake Capture**. Early in the literature it was pointed that dragonflies have different phases between ipsilateral wings depending on the maneuver. Therefore, researchers started to replicate these different phases to see what was the optimal one. However, there are two main problems with this: each research group had their own experimental or numerical set up; and they only looked at the results that were interesting to them, in most cases the forces. These leads to several papers pointing to different optimal phasing and flapping strategies. The main problem here is that by using a slightly different set up, the underlying physics change completely and give different results. Initially it was thought that the main factor for wake capture was phasing (what they observed in the insects), however, what is important is the detailed wake vortices interaction with each wing. These interactions depend indeed on phasing, but also depend on other geometrical factors of the flapping system (distance between wings, frequency of flapping, etc), which were varied between most research papers. Recent papers have tried to solve this by looking at the detailed flow field and wake interactions with numerical simulations. The problem here is that for simplicity they tend to use 2D simulations. Nevertheless, while inspecting the **Leading Edge Vortex** stability it was seen that it changes dramatically between 2D (unstable) and 3D (stable). Consequently, most of the literature conclusions cannot be applied to three dimensional systems.

Corrugation was the last *building block* that was analyzed. Corrugation has been widely overlooked in the literature. Most previous *building blocks* were analyzed using flat plates. There are some results of steady corrugated airfoils in 2D and 3D. However, these papers only provide steady aerodynamic coefficients, and it is known that most force comes from unsteady flow. It has only been reported one 2D case of unsteady corrugated flapping. As it is in 2D it also does not capture the three dimensional non-inertial effects that completely change vortex dynamics. It may be that insects only use corrugation to improve bending stiffness, without any aerodynamics effects, but this has not been proved up to date.

Finally, the relationship between all *building blocks* is by far the less researched topic in the literature. Typically a paper only analyzes some effects within one of the *building blocks*. However, a flapping system should be regarded as a mixture of *building blocks* where all elements have some relevance. For example, at what point of the growth of the **Leading Edge Vortex** growth should **Wake Capture** start? Is the **Leading Edge Vortex** stability affected by **Wing Capture**? What is the desired **Wing Rotation** to shed vortices adequately and have **Wake Capture**? Can a certain **Corrugation** pattern increase the stability of the **Leading Edge Vortex**? These issues have not been answered in the literature, and are certainly relevant to understand and improve flapping.

Overall all these questions are equivalent to trying to optimize the flapping stroke during hovering. This is going to be the main topic of the thesis. Moreover, to deal with the optimal stroke a good understanding of each *building block* is required. Therefore, the focus will be placed on improving the understanding of the less well known *building blocks*, specially **Wake Capture**, **Corrugation**, **Drag as Vertical Force** and **Leading Edge Vortex** stability. In particular, numerical simulations and experiments of a single flapping wing will be first used to delve into the concepts of **Drag as Vertical Force** and **Leading Edge Vortex** stability. Later on, **Corrugation** effects will be inspected with simulations of an actual dragonfly wing. Finally, all *building blocks* will be placed together in a whole dragonfly flying in hovering mode.

Chapter 3

Methodology

To delve into the challenges posed in the literature review chapter 2 two approaches will be followed: numerical simulations and experiments. The goal is to reinforce the validity of the claims by comparing each method when possible. Numerical simulations will be used alone in cases where the experiment was not possible to be conducted due to technical or time constraints.

3.1 Numerical formulation

To simulate aerodynamic phenomena a model for the fluid-solid interaction is required. In particular, given the low flapping speeds the fluid model will be the incompressible Navier Stokes equations:

$$\frac{\partial u_i}{\partial t} + \frac{\partial(u_i u_j)}{\partial x_j} = -\frac{\partial P}{\partial x_i} + \frac{1}{Re} \frac{\partial^2 u_i}{\partial x_j^2} \quad (3.1)$$

$$\frac{\partial u_i}{\partial x_i} = 0. \quad (3.2)$$

To discretize the equations a finite volume approach implemented in INCA [4] is implemented. A staggered grid is used to avoid pressure-velocity decoupling. A second order centered discretization is used. Time stepping is done with a explicit RK3 scheme. Incompressibility is imposed in every step by solving the Poisson equation with a Krylov-Poisson solver (BiCGstab with Strong Implicit Procedure preconditioner [85]). To impose the boundary conditions at the object surface a conservative cut-cell immersed boundary method is used. In particular, to avoid CFL restrictions with small cells created by geometry intersection, a merging procedure is used [83]. The fluid solver was coupled to a Multibody Solver that was specifically developed for these simulations. For brevity, the detailed description of the Multibody Solver and all the verification cases are included in Appendix A.

3.1.1 Verification cases

Fixed 2D cylinder

The first case is going to be a fixed cylinder immersed in a uniform flow in two dimensions. The fluid problem is non-dimensionalized with the cylinder diameter D , the uniform upstream velocity U and the kinematic viscosity ν . The Reynolds number is based on the diameter of the cylinder: $Re = \frac{UD}{\nu} = 100$.

The domain dimensions are $[-20, 30] \times [-20, 20]$. A structured and staggered grid is used to discretize the domain. Adaptive mesh refinement (AMR) is used in both x and y directions, refining towards the cylinder, see Figure 3-1a.

The slip boundary conditions are enforced at the upper and lower surfaces. Upstream a uniform velocity $U = 1$ is given (non-dimensionalized parameter). Downstream, constant total pressure is enforced. At the cylinder surface a no-slip boundary condition is applied.

First, grid independence is achieved with a grid refinement study, see Table 3.1. n is defined as the number of cells projected along the x direction of the cylinder. The parameters which are studied for grid convergence are the average lift and drag coefficients $\overline{C_L}$ and $\overline{C_D}$; the semi-amplitude of the lift oscillations $\widetilde{C_L} = \frac{C_L^{max} - C_L^{min}}{2}$; and the Strouhal number (based on the period of lift oscillations, T) $St = \frac{D}{TV}$.

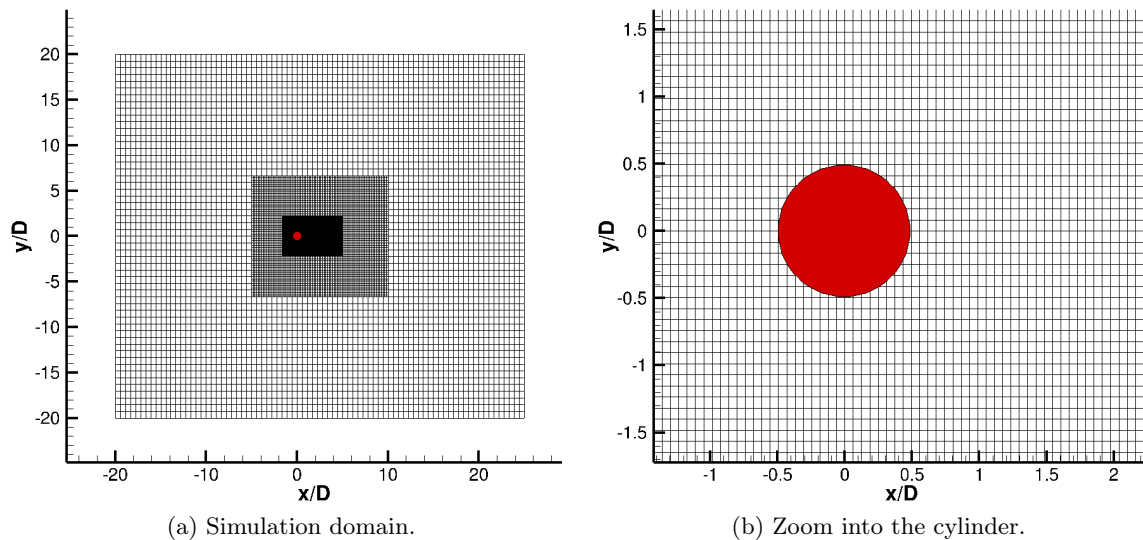


Figure 3-1: Structured grid, with AMR ($n = 16$).

n	$\overline{C_D}$	$\overline{C_L}$	$\widetilde{C_L}$	St
16	0.98	-0.21	0.096	0.157
32	1.46	0.19	0.43	0.163
64	1.39	0.029	0.36	0.166
128	1.38	0.0026	0.35	0.166

Table 3.1: Grid convergence of the 2D cylinder simulation. $Re = 100$.

Note how the semi-amplitude of the lift oscillations $\widetilde{C_L}$ is not exactly zero in Table 3.1. In theory $\widetilde{C_L}$ should be exactly zero due to the symmetry of the problem, so it can be seen as an indicator of the error in the solution (statistics where converged through a long enough period). For the two coarser grids the convergence in $\widetilde{C_L}$ is non-monotonic due to the non-linearity of the equations and the fact that the grid is too coarse. However, for $32 \leq n$ monotonic convergence of all the parameters is observed. For $n = 128$ errors of order 10^{-3} are achieved. This grid resolution is going to be considered as enough to provide grid independence, given the typical modeling errors observed in the literature, Table 3.2.

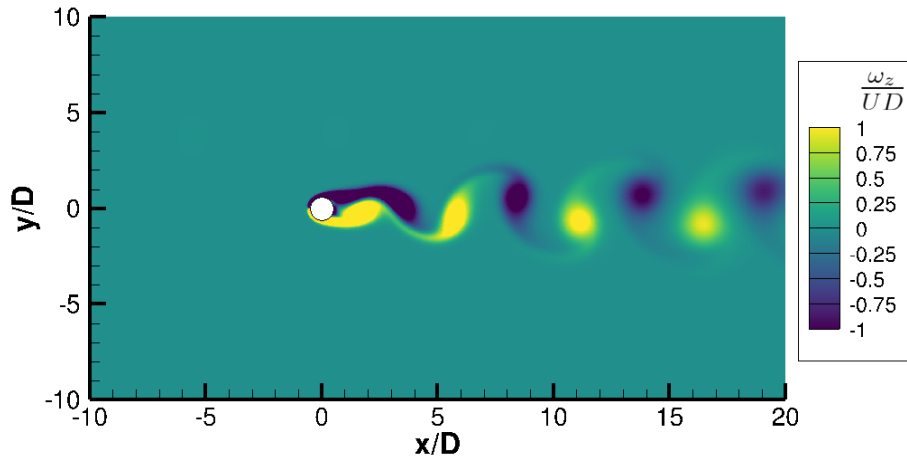


Figure 3-2: Snapshot of the instantaneous vorticity field in the 2D cylinder simulation. $Re = 100$. $n = 128$.

A snapshot of the instantaneous vorticity field of the grid-independent solution is shown in Figure 3-2. See how the expected vortex shedding occurs in the wake of the cylinder.

Finally, the grid-independent solution is compared with other results of the same problem found in the literature, see Table 3.2. A quite good agreement can be seen.

Reference	$\overline{C_D}$	$\widetilde{C_L}$	St
Experiment [51]	1.3	-	-
Experiment [43]	-	-	0.165
Numerical [97]	1.38	0.300	0.169
Numerical [64]	1.35	0.344	0.164
Numerical [17]	1.36	0.25	-
Present, numerical ($n = 128$)	1.38	0.35	0.166

Table 3.2: Comparison of present results with the literature. $Re = 100$.

3D rotating sphere

A 3D rotating sphere with a uniform upstream flow is assessed in this section. Rotation occurs with uniform non-dimensional angular speed $\Omega^* = \frac{D\omega}{2U_\infty}$, where D is the sphere diameter, ω the angular speed around the y axis, and U_∞ the upstream flow at infinity aligned with the x axis direction, see Figure 3-3. In particular, two rotation speeds are inspected, $\Omega^* = 0$ and $\Omega^* = 0.25$. The Reynolds number is $Re = \frac{U_\infty D}{\nu} = 100$, where ν is the kinematic viscosity of the fluid. First, it should be mentioned that the wake remains steady over the range of Ω^* considered. The steady structure of the wake can be seen in Figure 3-3 and Figure 3-5a. A comparison of the streamlines with the results from Niazmand and Renksizbulut [73] can be seen in Figure 3-5b. As it can be appreciated, the topology of the streamlines matches perfectly the reference.

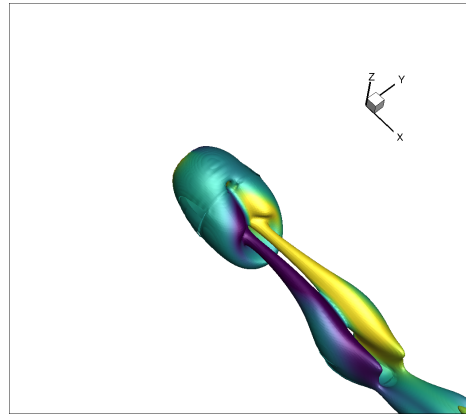


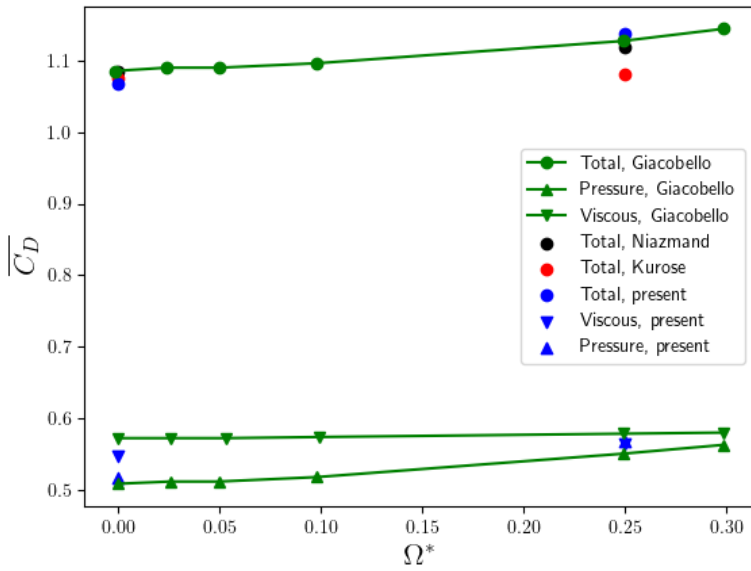
Figure 3-3: $Re = 100$. $\Omega^* = 0.25$. Q criterion isocontours coloured by streamwise vorticity (ω_x). Yellow, downstream vorticity orientation; purple, upstream vorticity orientation.

Next, the mean drag and lift coefficient in the vertical direction are defined as:

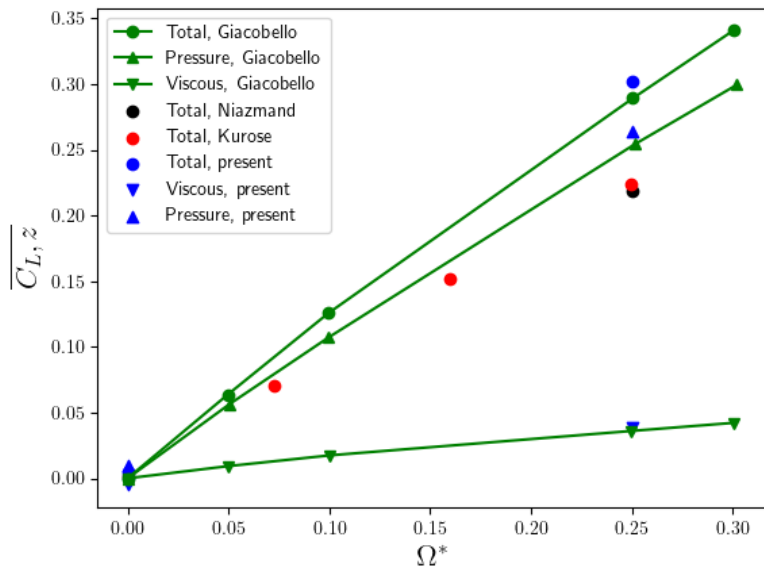
$$\overline{C_D} = \frac{\overline{F_x}}{\frac{1}{2}\rho_\infty U_\infty^2 \pi \frac{D^2}{4}}$$

$$\overline{C_{L,z}} = \frac{\overline{F_z}}{\frac{1}{2}\rho_\infty U_\infty^2 \pi \frac{D^2}{4}}.$$

The total forces can also be decomposed into the pressure and viscous components. These are plotted in Figure 3-4a and Figure 3-4b. A good agreement is observed with the literature, specially with the results from Giacobello *et. al* [47].



(a) Averaged drag coefficient.



(b) Averaged lift coefficient in z direction.

Figure 3-4: Comparison of lift and drag coefficient for different non-dimensional rotation speeds Ω^* . $Re = 100$. References used: Giacobello [47], Kurose [60] and Niazmand [73]

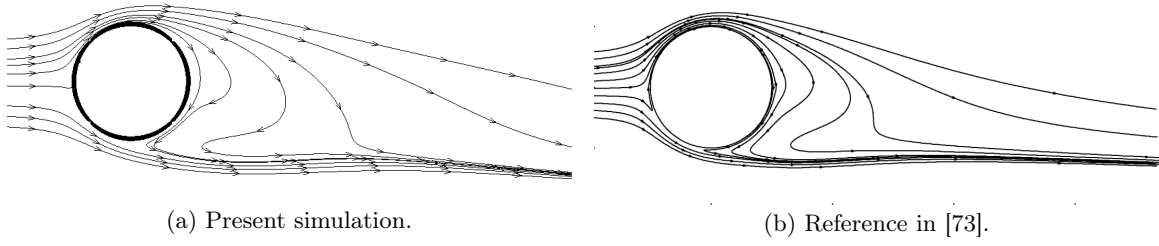


Figure 3-5: Comparison of streamlines contained on the $x - z$ plane (only considering u and v components), see axis system Figure 3-3. $Re = 100$. $\Omega^* = 0.25$.

Single 2D pendulum immersed in a fluid

Finally, a 2D pendulum in free fall immersed in a fluid flow is considered. The fluid solver is coupled to a Multibody Solver to allow for the fluid-solid dynamics interaction. For brevity, the detailed description of the Multibody Solver and all the verification cases are included in Appendix A. The results from [71] are considered, in particular, the test case with pendulum mass $m = 5000 \text{ kg}$ and pendulum's bob radius $r = 0.015 \text{ m}$ is used. Other relevant parameters defined in the reference for the simulation are: pendulum length $L = 0.2 \text{ m}$, fluid density $\rho = 1000 \text{ kg/m}^3$, fluid dynamic viscosity 0.01 kg/(m s) , gravitational acceleration $g = 9.81 \text{ m/s}^2$ and initial angular displacement $\theta_0 = -\frac{3\pi}{10} \text{ rad}$.

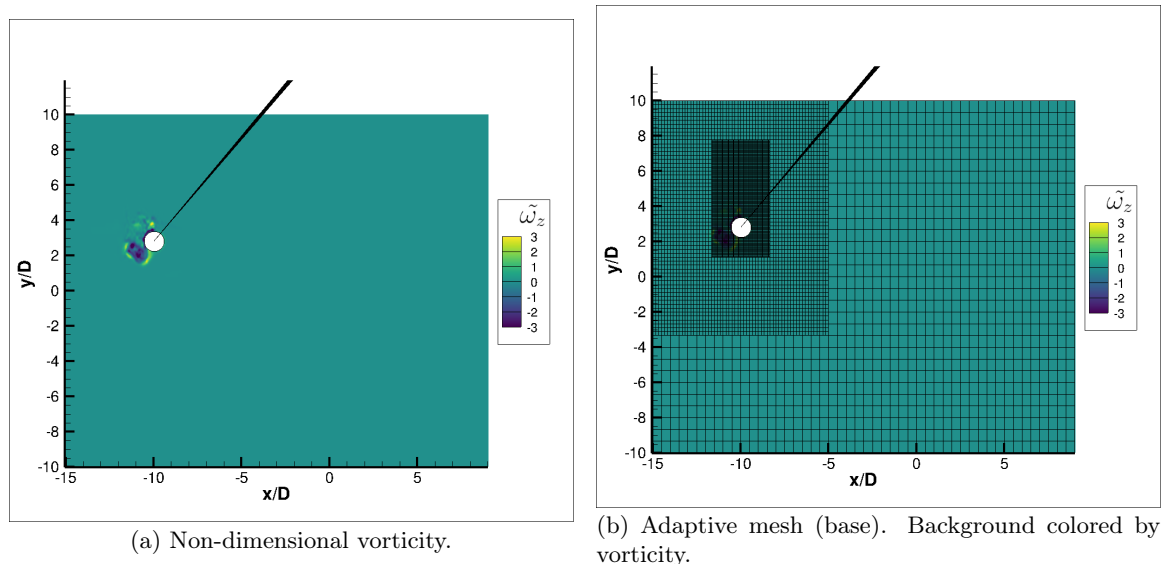


Figure 3-6: Present results in test case selected from. [71]

To study mesh convergence three levels of adaptive mesh refinement are compared with the reference. Once again to compare the level of refinement, n is defined as the number of cells projected along the x direction of the pendulum's bob. The coarse mesh has $n = 16$, the base mesh has $n = 32$ and the fine mesh $n = 64$. Results for the three refinement levels are shown in Figure 3-7. It can be concluded that the results from the present fluid solver with the coupled multibody solver converge to the reference values.

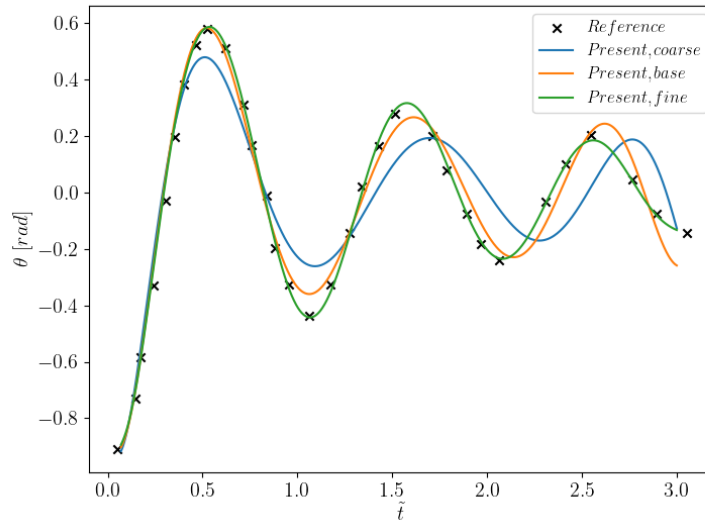


Figure 3-7: Convergence of pendulum trajectory with mesh refinement. Reference from [71].

3.2 Experiment design

The experiment that will be described next was conducted thanks to California Institute of Technology facilities and resources. The goal of this experiment is to provide a physically relevant case that can contribute to answer the questions of the literature review. In particular, a single flapping plate has been chosen, as it was feasible with the time and resources available, while it can also illustrate many of the most relevant phenomena explored in the literature review.

The experiment was designed to have one degree of freedom, rotation around the z axis. The z axis rotation was achieved with a servo-motor that moved a shaft connected to the flat plate. In Figure 3-8a the CAD design and the actual experiment can be seen in more detail. The tank was filled with distilled water at $20^{\circ}C$, $\nu = 10^{-6}[m^2/s]$. The vertical force (lift) was measured with two 1D load cells (in red in Figure 3-8a). Each load cell connects the edges of the beam to the two support structures in each side of the tank. The torque (drag torque) was measured with a reaction torque sensor, in yellow in Figure 3-8a and Figure 3-9a.

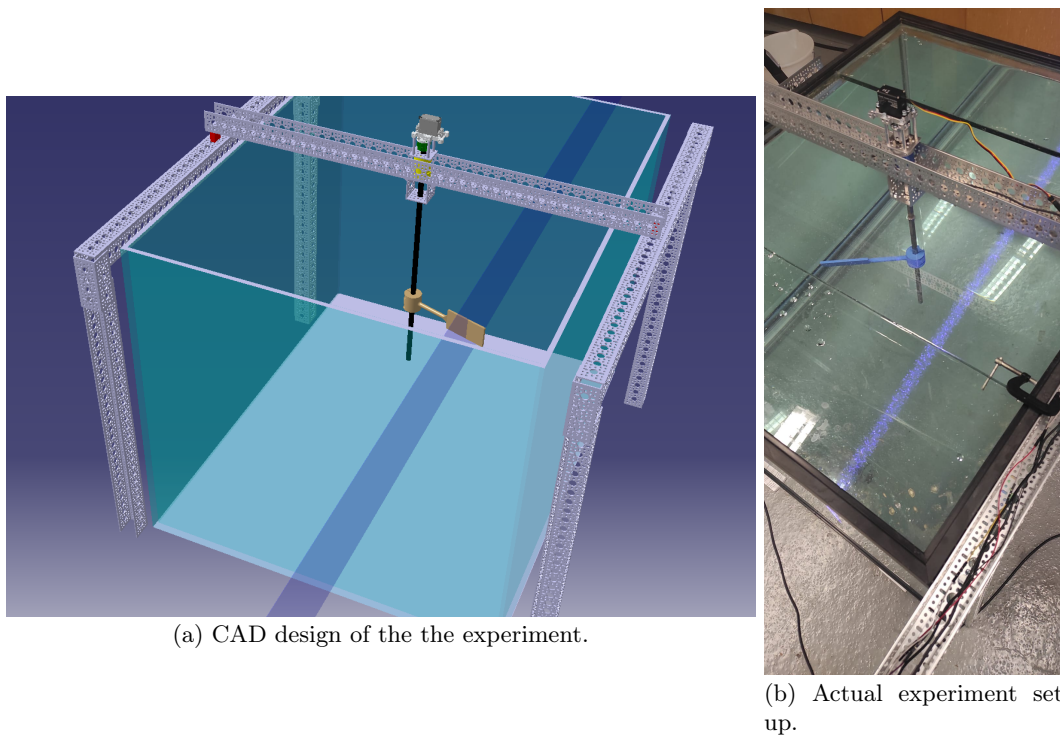


Figure 3-8: Experiment design. The laser sheet for PIV (blue) is active in both pictures.

A more detailed view of the CAD design can be seen in Figure 3-9a. The servo-motor (dark grey, top of the image) was connected via four separators to a torque sensor (in yellow). Then, this torque sensor was attached to a fixed support (aluminium beam). The shaft (in black) is connected to the servo motor via a coupling, colored in green. Also note that the shaft goes across the hole-through torque sensor, that has a bigger inner diameter (14 mm) than the outer diameter of the shaft (12

mm). At the bottom of Figure 3-9b, the shaft passes through a bearing to remove the radial loads from the torque sensor and improve the stability of the system.

Note that all the torque caused by the fluid forces goes up through the shaft, then reaches the coupling, next the servo-motor, and finally the torque sensor that is fixed to the beam. It is important to highlight that the torque sensor is measuring both, fluid and inertia torque. To remove the inertia forces, all experiments were done twice, once with the tank full of water, and another one with an empty tank. Neglecting the fluid forces caused by air (around a thousand times smaller than in water), the measurements in air represent solely the inertia forces of the system. Therefore, subtracting both cases, the torque caused by the fluid can be isolated as:

$$T_{fluid} = T_{water} - T_{air}. \quad (3.3)$$

Additionally, the load cells measure the forces of all the elements on the beam, however, all the elements are passive and only the fluid forces produce a varying vertical force in time.

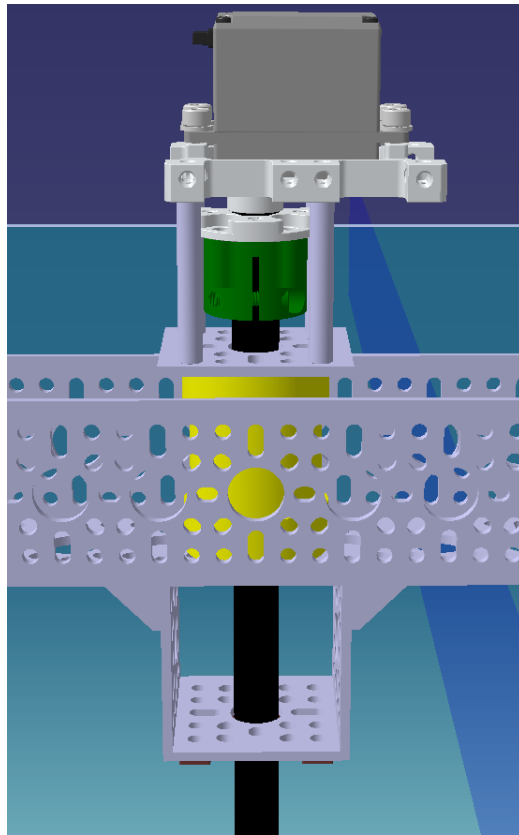
The flat plates were 3D printed using California Institute of Technology facilities, see Figure 3-10. Five different wing designs were tested, each of them with a different angle of attack (AoA): 10° , 25° , 45° , 70° and 90° . The radius of gyration of the root R_r of all flat plates was 50 mm . The span b , chord c and thickness t of the flat plates was 50 mm , 25 mm and 2.5 mm respectively.

To visualize and get a better understanding of the LEV dynamics, planar PIV was implemented, see Figure 3-11. A 445 nm blue laser with a maximum power of 20 watts was used. The laser power was tuned as the minimum possible to not be exposure limited by the camera. A convergent lens was selected to create a laser sheet. A camera with 1936×1216 pixel resolution was placed perpendicular to the laser sheet. Flow fields were reconstructed using cross-correlation with a Gaussian regression to get subpixel resolution. All PIV results presented in this document are taken when the wing is perpendicular to the laser sheet. To assess the evolution of the LEV, the same flapping trajectories were repeated but each time, starting at a different initial angle ψ_0 from the perpendicular position to the laser sheet (PIV measurement point), see Figure 3-12a and Figure 3-12b. This way when the flat plate arrives to the measurement point (perpendicular to the laser sheet), the LEV would have been developing for different distances depending on the initial ψ_0 .

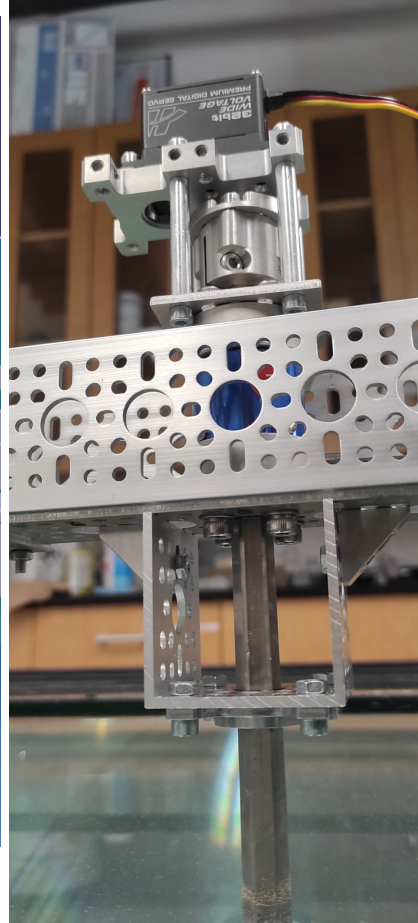
3.2.1 Error analysis

3.2.2 Servo-motor

The servo-motor has a deadband width of $1\ \mu\text{s}$. The PWM signal oscillates between 1000 and 2000 μs , and the amplitude of oscillations is 190° . Consequently, the angular resolution in the trajectories is:



(a) CAD design. Yellow, hole-through torque sensor; dark grey (top), servo-motor; green, coupling; light grey, support beam; black, shaft.



(b) Actual experiment set up.

Figure 3-9: Zoom into the experiment set up.

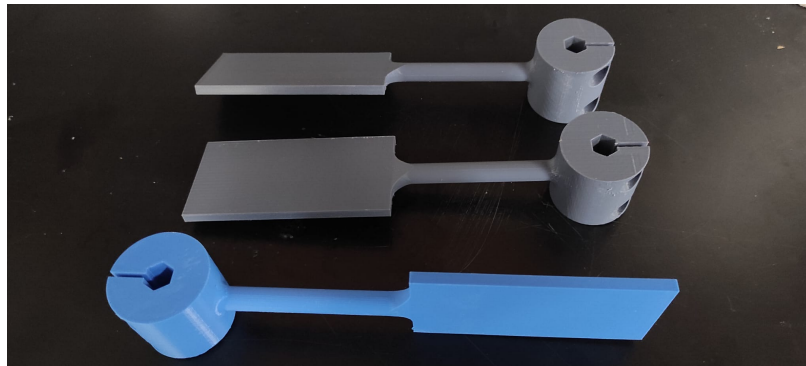


Figure 3-10: 3D printed wings with different angles of attack. Blue bottom, 90°; grey middle, 10°; grey top, 25°.

$$\Delta\psi = \frac{1}{1000}190 = 0.19^\circ. \quad (3.4)$$

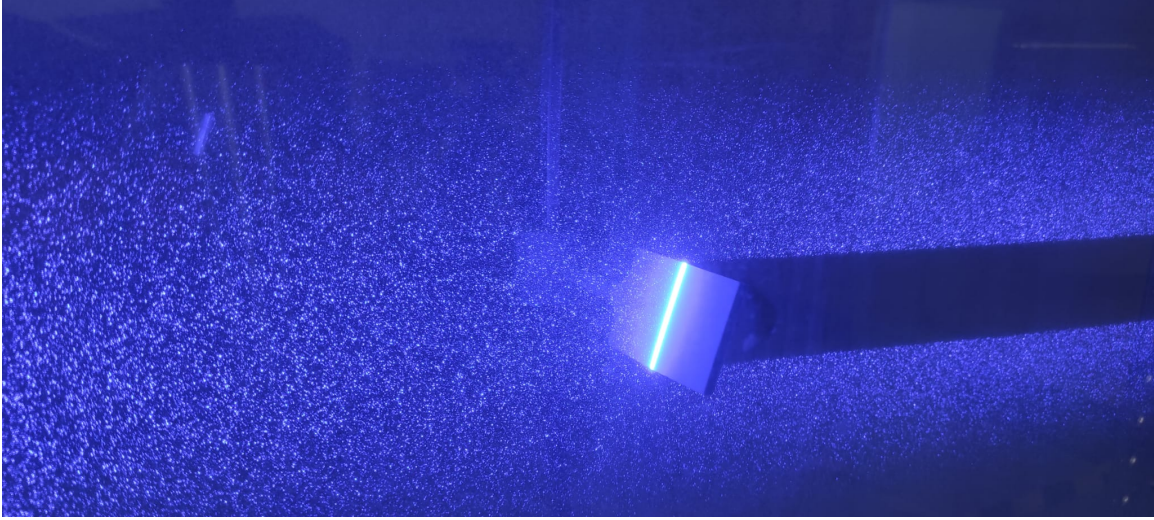


Figure 3-11: Photo of the planar PIV laser sheet with the flat plate at $\psi_0 = 0^\circ$. Note that the photo was not taken neither with the camera used for PIV, nor from the position of the PIV camera.

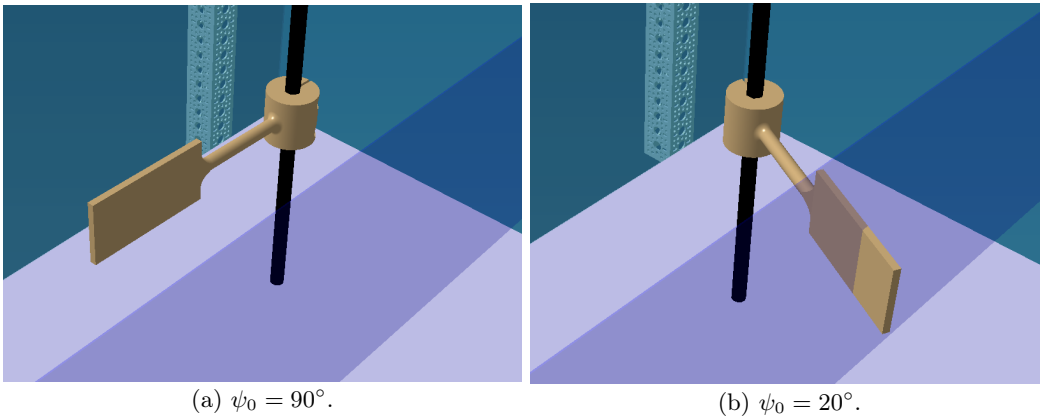


Figure 3-12: CAD of the 90° AoA flat plate at two different initial positions ψ_0 . For reference, $\psi_0 = 0^\circ$ is the position of the flat plate perpendicular to the depicted blue laser sheet.

The temporal resolution is limited by the bandwidth of one cycle of the PWM signal:

$$\Delta t = 20000\mu s = 0.02s. \quad (3.5)$$

3.2.3 PIV

Using the first order term from a Taylor series the uncertainty can be estimated as [31]:

$$\epsilon_U = \sqrt{\left(\frac{\partial U}{\partial \Delta t} \epsilon_{\Delta t}\right)^2 + \left(\frac{\partial U}{\partial \Delta x} \epsilon_{\Delta x}\right)^2} \rightarrow \frac{\epsilon_U}{U} = \sqrt{\frac{\epsilon_{\Delta t}}{\Delta t} + \frac{\epsilon_{\Delta x}}{\Delta x}}. \quad (3.6)$$

After pre-processing the images, the particles move around 4 pixels every image, $\Delta_x \approx 4px$. Additionally, the value of ϵ_x with Gaussian correlation is usually around $0.1 px$ [105]. ϵ_{Δ_t} is given by the exposure time of the camera, which was $498\mu s$. On the other hand, Δ_t is given by the frame rate of the camera, $f = 100Hz$. With these values the estimated error bound is:

$$\frac{\epsilon_U}{U} = \sqrt{\frac{\epsilon_{\Delta t}}{\Delta_t} + \frac{\epsilon_{\Delta x}}{\Delta_x}} = 5\%. \quad (3.7)$$

Finally, also comment on the importance of having an adequate particle displacement within two frames. Literature indicates that a $1/4$ interrogating window displacement is optimal for PIV [105], see Figure 3-13a. As indicated $\Delta_x \approx 4px$, which means that $16 px$ is the optimal size for the interrogating windows. Also the seeding density was adjusted to have around 6 particles per interrogating window, so that a good correlation factor is obtained [105].

More importantly, in flapping wings a huge component of the noise in the planar PIV measurements is going to come from the out of plane displacement of particles, see Figure 3-13b. The laser thickness Δz was $14px$. Assuming a quite pessimistic scenario, in which all particles are orthogonal to the laser sheet, it gives $\Delta_x/\Delta z = 4/14 = 2/7$ displacement between frames. This is a reasonable value as most of the particles will remain within the laser sheet between two frames, giving this way a good correlation [105].

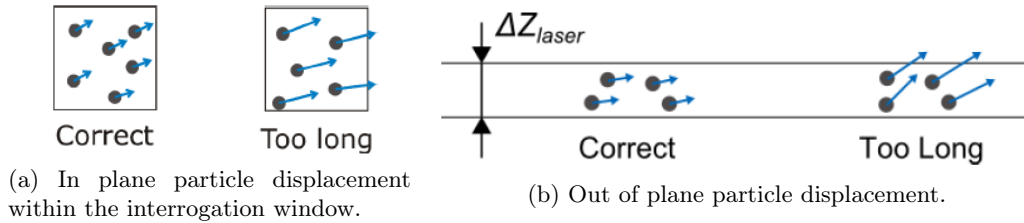


Figure 3-13: Selection of image sampling rate for PIV and analysis of out of place displacement. [106]

Chapter 4

Experimental and numerical analysis of a single flapping wing

4.1 Comparison between experiments and numerical simulations

In this section the results for a flat plate flapping at a uniform velocity ω are inspected (instantaneous acceleration). The angle of attack of the flat is $\alpha = 70^\circ$, which is similar to the angle of attack of insect wings like dragonflies during the downstroke [39]. Also remark that the typical flapping angle amplitude of dragonflies is around $\psi = 60^\circ$, see section 2.1, so only this range of flapping angles is going to be inspected. The Reynolds number is defined based on the radius of gyration at the tip of the flat plate ($R_g = R_r + b$), and the chord length c (see section 3.2 for more details of the wing geometry):

$$Re = \frac{\omega R_g c}{\nu}, \quad (4.1)$$

where $\nu = 10^{-6} m^2/s$ is the kinematic viscosity of water at $20^\circ C$.

Remark that the Strouhal number, given a certain non-dimensional flapping trajectory, is always the same independent of characteristic length of the wing R and flapping frequency scaling f :

1. Unsteady term $\approx \frac{U}{t} \approx f^2 R$
2. Advection term $\approx \frac{U^2}{R} \approx f^2 R$,

where U is the characteristic flow speed and t the characteristic time.

Finally, comment that experiments did have force and torque measurements. However, these measurements were only valid when flapping was fast enough, so that forces can be clearly distinguished from measurement noise (note that force signal scales with the velocity squared). This was practical for $Re > 20000$ for the present set up. This is a regime where dragonflies and most insects do not fly. Additionally, doing DNS at this regime is not possible with the computational resources available for this thesis. Therefore, it was decided to only use PIV which works well for slower flapping regimes (the ones observed in insects) and compare with DNS that can be fully resolved in these lower Reynolds numbers.

4.1.1 3D structure of the LEV

The LEV of a flapping wing presents a complex 3D structure [22]. This will be inspected in this section via experiments and numerical simulations. In particular, 2D slices of the flow field are going to be inspected and latter on, 3D structures will be visualized in the numerical simulations.

First, looking at the flapping angle $\psi_0 = 20^\circ$, Figure 4-1, when the LEV starts to grow, it can be seen that at $0.75b$, the flow field has higher velocity magnitude. This makes sense, as towards the tip

velocity is higher. Therefore, due to the higher velocity towards the tip, circulation of the LEV and TEV grow faster for the same flapping angle. This can be appreciated looking at the streamlines that define the recirculation regions of the flow. A quite good agreement in both the experiment and simulation can be seen, specially for the $0.25b$ slice. It will be seen later on that the flow in the numerical simulations and experiments transitions to turbulence at the tip. Therefore, due to the chaotic nature of turbulence it is expected that exact instant correlation between experiment and simulation are worse close to the tip.

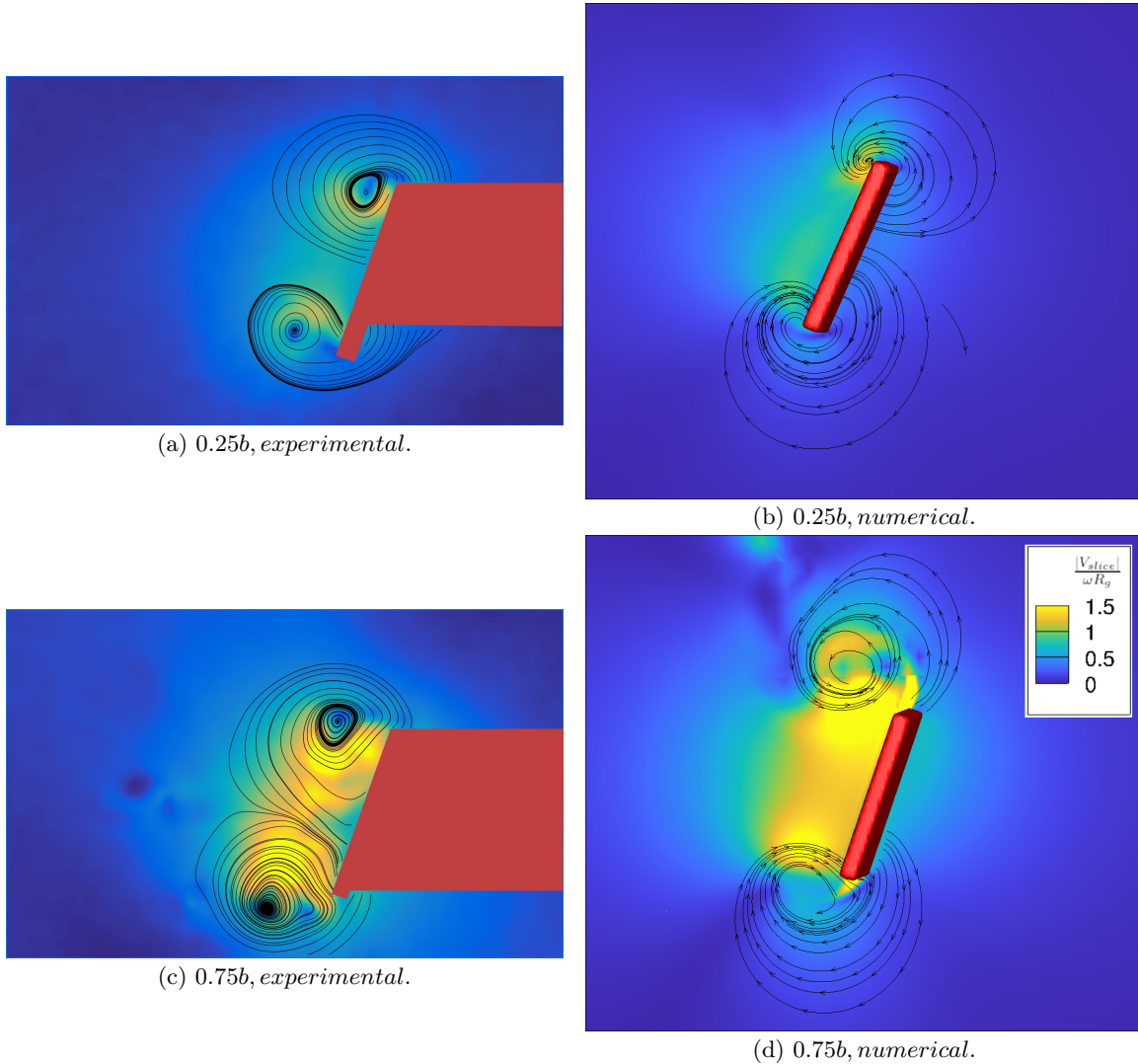


Figure 4-1: $\psi_0 = 20^\circ$. Streamlines colored by velocity magnitude of the flow field at different span section. Flat plate flapping to the right. Shadow region colored in red. $Re = 392.7$. Instantaneously accelerated plate, constant ω . $\alpha = 70^\circ$.

Next, at $\psi_0 = 40^\circ$, Figure 4-2, the LEV remains closely attached to the flat plate at $0.5b$ in the experiment, while in the numerical simulation it is still attached but it is shifted slightly upwards. On the other hand, the LEV is more separated close to the tip at $0.75b$, in both the experiment and the

simulation, due mainly to the faster circulation growth in this region. Also note the chaotic nature of the flow in both experiment and simulation for this section. As mentioned before transition close to the tip occurred, and for this reason the section closer to the tip is starting to depict a chaotic behavior. Moreover, the TEV is starting to be detached. The reason for this detachment is the following: LEV and TEV create a jet of momentum downwards and to the right (generates huge lift and drag, in the opposite direction of the jet). Then, this jet cuts the circulation of the TEV and detaches it from the flat plate. This is the reason why the TEV is usually detached much faster than the LEV in flapping wings. Also note that this is beneficial as the TEV contributes to negative lift (Kutta-Joukowski theorem), so getting rid of it would enhance lift production.

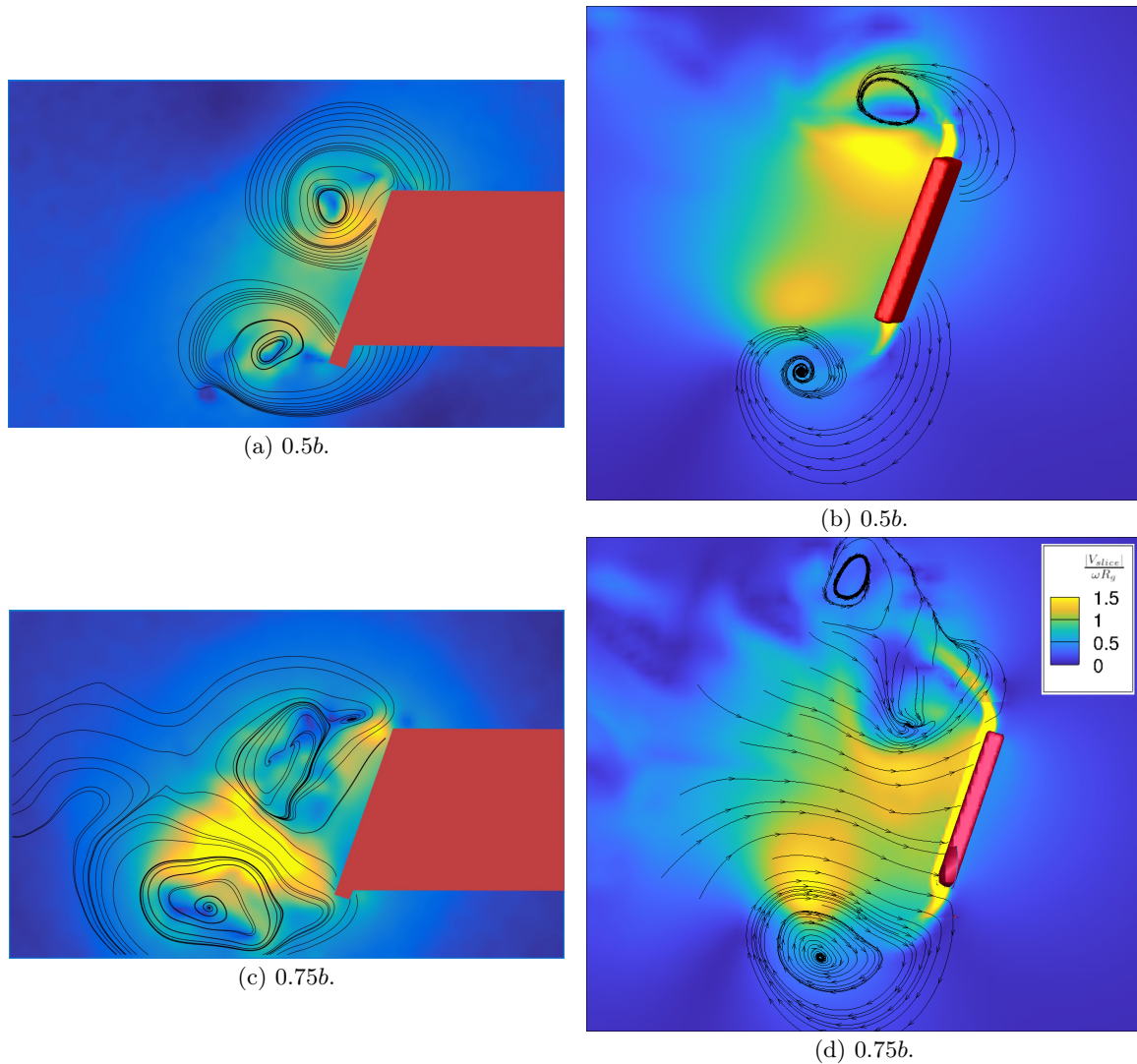


Figure 4-2: $\psi_0 = 40^\circ$. Streamlines colored by velocity magnitude of the flow field at different span section. Flat plate flapping to the right. $Re = 392.7$. Instantaneously accelerated plate, constant ω . $\alpha = 70^\circ$.

To better understand the 3D structure of the LEV, the Q-criterion isocontours of the numerical

simulation at a flapping angle $\psi = 40^\circ$ are shown in Figure 4-3. See how the LEV is attached and grows towards the tip, due to the faster spinning velocity. Additionally, observe how the LEV structure becomes more complicated and transitions close to the tip. This was also noticed in previous experiments, for example in the mechanical flapping done in [61], see Figure 2-32a. They observed at a slightly higher Reynolds number with hydrogen bubbles how the LEV structure transitions at half the span, quite similar to what happened here. Also note how for high Reynolds numbers, circulation shedding occurs due to transition (see the structures at the wake of the flat plate coming from the LEV), which controls the size of the LEV.

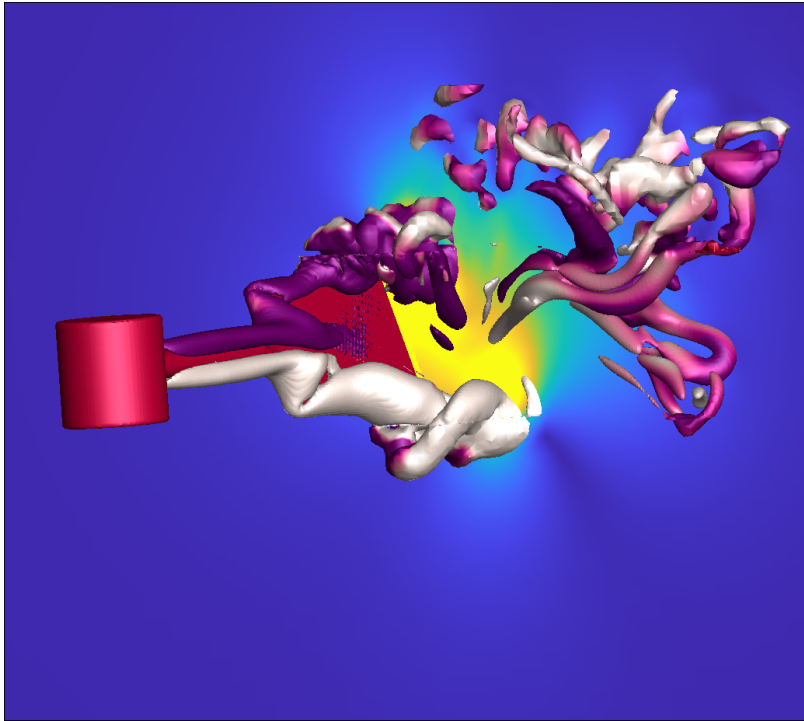


Figure 4-3: $\psi = 40^\circ$. Q-criterion isorcontours colored by background vorticity. Slice colored by velocity magnitude. $Re = 392.7$. $\alpha = 70^\circ$.

Finally, in Figure 4-4 special attention is placed to the LEV structure and spanwise blowing. First, note how the streamlines projected on the LEV go towards the tip. This spanwise blowing is what is known as Coriolis spanwise blowing, and controls the growing (and therefore stabilizes) the LEV structure close to the root. Also note that at around half of the span of the flat plate the LEV is suddenly separated from the flat plate surface. The reason for this is the collision of two spanwise flows going in opposite directions, one coming from the root vortex and the other from the tip vortex. This causes ejection of mass away from the flat plate and contributes to the LEV detachment. This will be inspected in more detail in section 4.3.

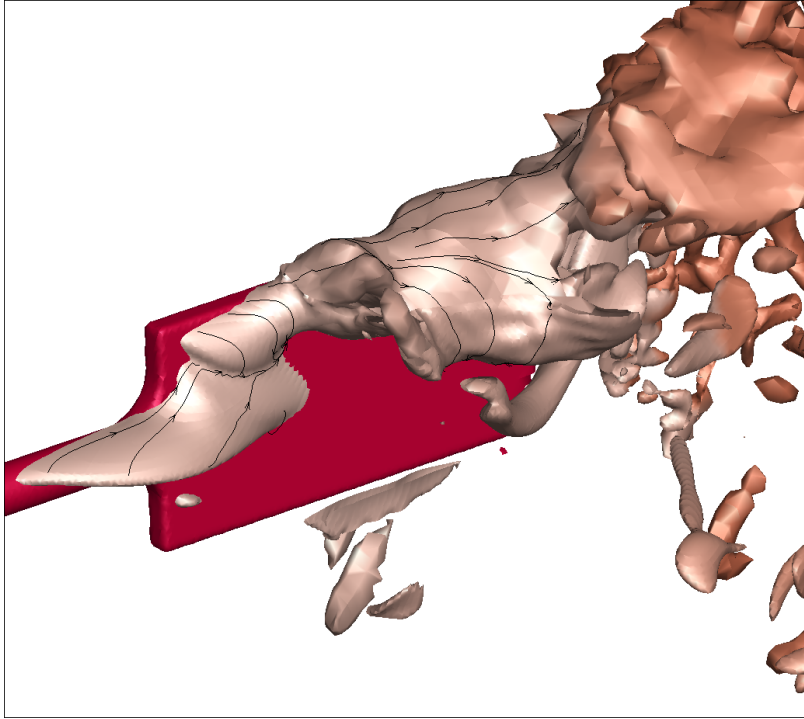
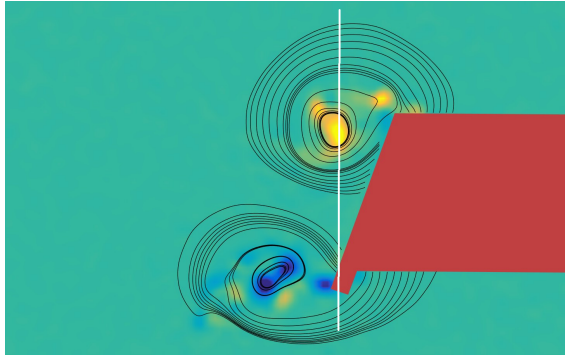


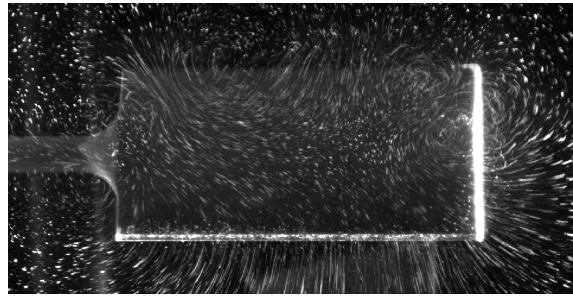
Figure 4-4: $\psi = 40^\circ$. Vorticity isocontour colored by wall distance. Velocity streamlines projected on the isocontour. $Re = 392.7$. $\alpha = 70^\circ$.

4.1.2 Analysis of the wake

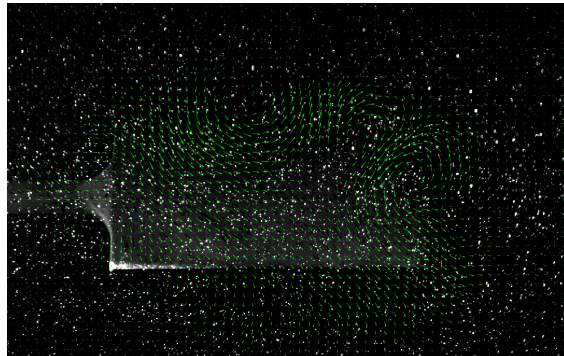
In this section the structure of the wake is going to be inspected in more detail. Once again experiments and numerical simulations are going to be compared. The wake is going to be studied through vertical slices taken once the flat plate has just passed, see Figure 4-5a where the location of the laser sheet is presented in white. In Figure 4-5b the superimposed PIV images depict the placement of the wing with respect to the slice, and in Figure 4-5c the resolved vector field is presented.



(a) PIV results with $\psi = 40^\circ$. Streamlines colored by vorticity. Mid span, $0.5b$. In white the location of the laser sheet used to inspect the wake with PIV.



(b) Superimposed snapshots of the PIV particles. Figure 4-5a looked from the left.



(c) Resolved PIV vector field.

Figure 4-5: $\psi_0 = 20^\circ$. Wake results for $Re = 392.7$. Instantaneously accelerated flat plate, $\alpha = 70^\circ$.

At the beginning of the flapping movement, $\psi = 20^\circ$, if the spanwise blowing component is inspected (Figure 4-6a and Figure 4-6b), it can be seen that two jets in opposite directions emerge: the LEV at the root (left part of the image) blows from left to right, while the LEV at the tip blows from right to left. These two jets collide at around $3/4$ of the span. Because the flow is incompressible, to preserve volume, a jet away from the flat plate is created. This creates a vertical blowing (and another blowing component outside of the image plane which is not shown) that pushes the LEV away from the flat plate and favors its detachment. This phenomenon can be seen in both the PIV and numerical results. In Figure 4-6a the estimated position of the vortex core is shown with a red line. Note how the upwards vertical blowing that occurs at around half of the span goes exactly

through the vortex core. For this reason at around half the span, the LEV suddenly separated when the 3D LEV structure was visualized in Figure 4-3. In the literature a lot of emphasis has been placed in spanwise blowing as the leading stabilizing effect [61]. However, here it is shown that it can also be a dangerous component that enhances detachment. This will be inspected in more detail in section 4.3.

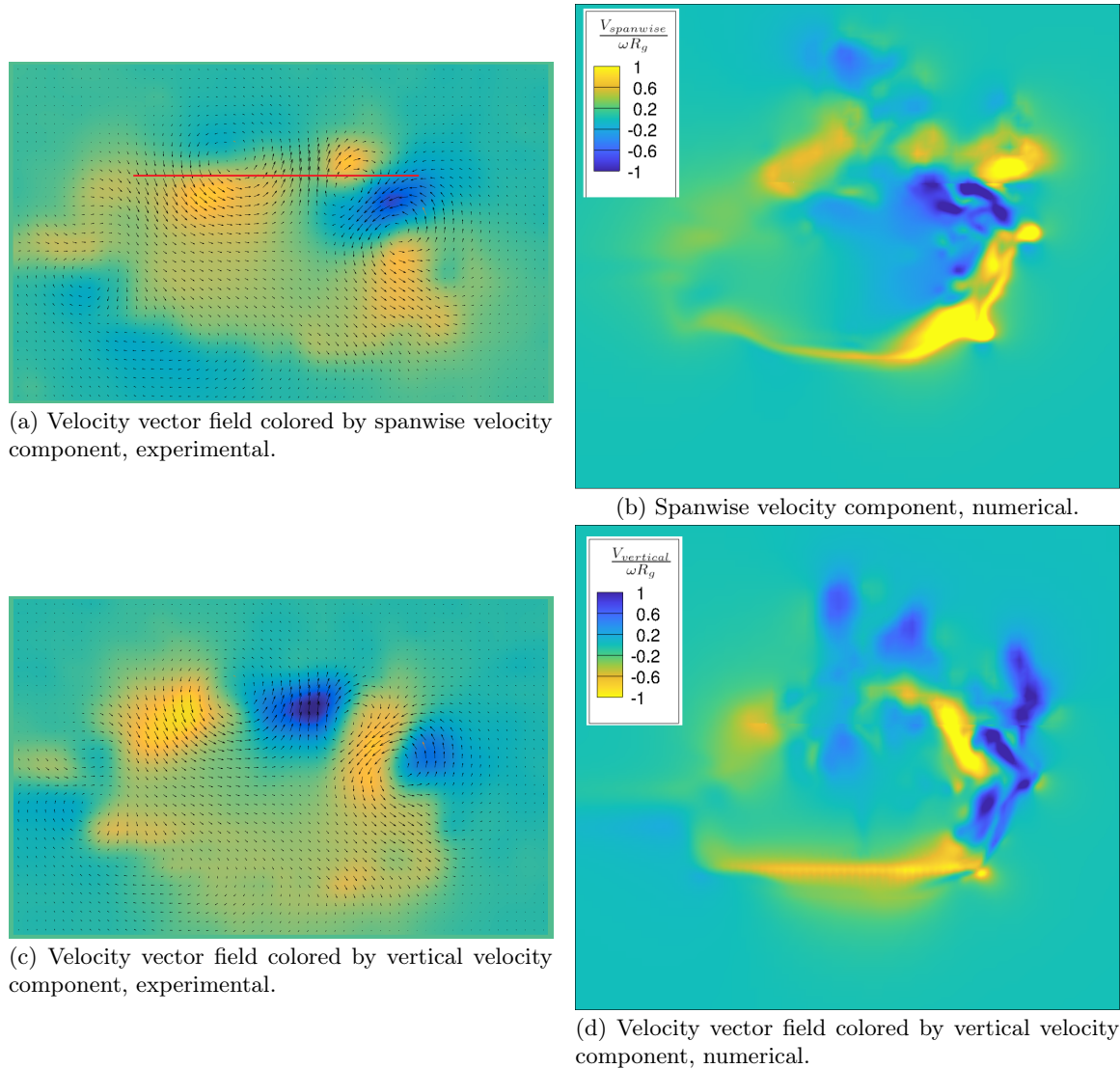


Figure 4-6: $\psi_0 = 20^\circ$. Wake results for $Re = 392.7$. Instantaneously accelerated flat plate, $\alpha = 70^\circ$.

Next, when the flapping angle keeps increasing (Figure 4-7a and Figure 4-7b) it is observed that vertical downwash blowing only happens close to the root, where the LEV was seen to be stable and well attached in Figure 4-3 and Figure 4-4. The stable LEV close to the root is responsible for a vertical downwash that will generate lift. Once the LEV is pushed further away from the flat plate at around half the span, the vertical downwash is no longer effective as seen for $\psi_0 = 40^\circ$ and $\psi_0 = 60^\circ$, which implies a lost of lift production.

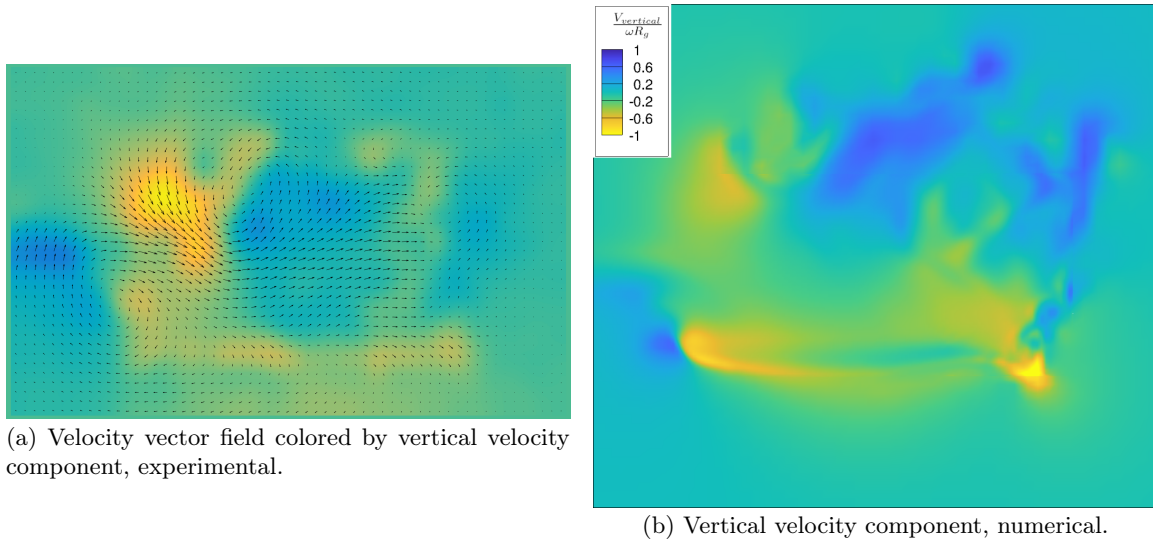


Figure 4-7: $\psi_0 = 40^\circ$. Wake results for $Re = 392.7$. Instantaneously accelerated flat plate, $\alpha = 70^\circ$.

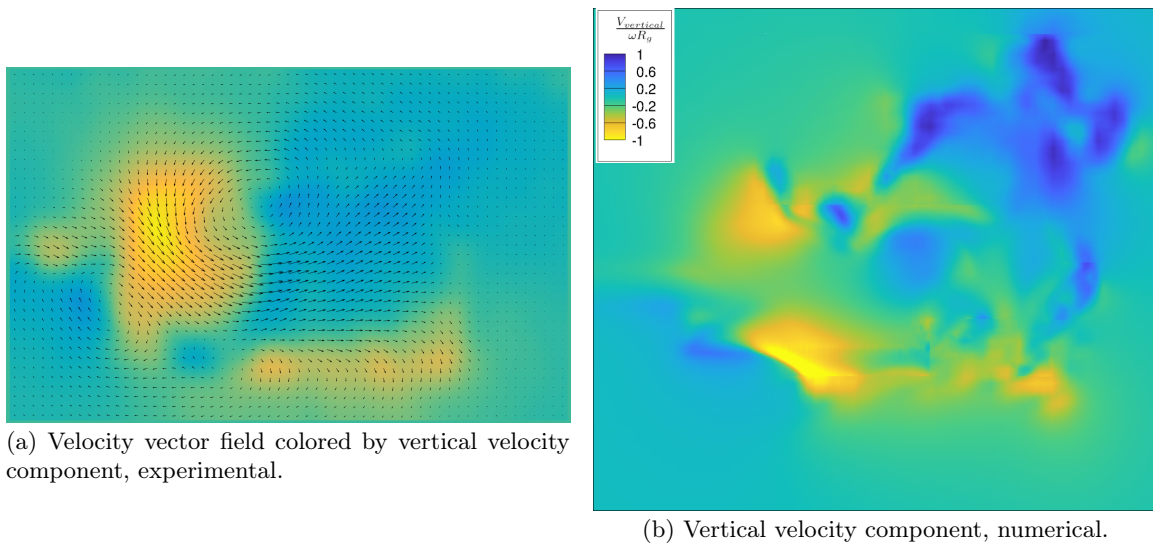


Figure 4-8: $\psi_0 = 60^\circ$. Wake results for $Re = 392.7$. Instantaneously accelerated flat plate, $\alpha = 70^\circ$.

Finally, the experimental spanwise blowing results are compared with those found in a paper published in Nature [13]. In the mentioned paper they were testing the effect of spanwise blowing on the stability of the LEV. To test this they placed the fins in two positions showed in Figure 4-10: at the LEV and at the TEV. They were expecting to find spanwise blowing at the height of the LEV, case a), so placing the fins there should disrupt the stability of the mentioned structure. However, they saw that with the fins near the trailing edge, the decrease in vorticity and force production was much higher, a 25% drop in net force. Additionally, with the fences at the leading edge, they did not alter force generation relative to the fenceless wing. The authors were shocked by this results as they expected spanwise flow to be blowing through the leading edge, and removing vorticity (similar

to a delta wing of the Concorde), and they were not able to explain these findings. Based on the current results, now it is clear why this happened. In Figure 4-9 it can be seen how the spanwise flow was close to the leading edge at the root, however, it fell back to the trailing edge pretty soon, due to the tip vortex jet. For this reason when they placed the fins at the trailing edge it affected much more the spanwise blowing. By doing this they removed the Coriolis advection close to the trailing edge (where it was dominant). To preserve mass a jet was generated outwards from the flat plate when the spanwise blowing met the fin, and this probably caused the LEV separation from the wing at the root. The most important lesson from this is that Coriolis spanwise blowing is responsible for mass removal, and not always for vorticity removal. In fact, what it is desired is to control mass accumulation between the LEV and the flat plate, as this would push the LEV away from the flat plate and cause its separation. However, there is no need to remove this mass just when it has already arrived at the LEV core. Note that the flow circulates around the outer part of the LEV before arriving to the region between the vortex core and flat plate. Therefore, mass removal could occur anywhere along this trajectory, not just at the vortex core. In particular, it is seen that this mass removal starts to occur mainly downwards from the LEV structure, not allowing it to reach the vortex core. Due to this, mass has already been removed before arriving at the vortex core, and there is no need for further spanwise blowing at the LEV core to control its size.

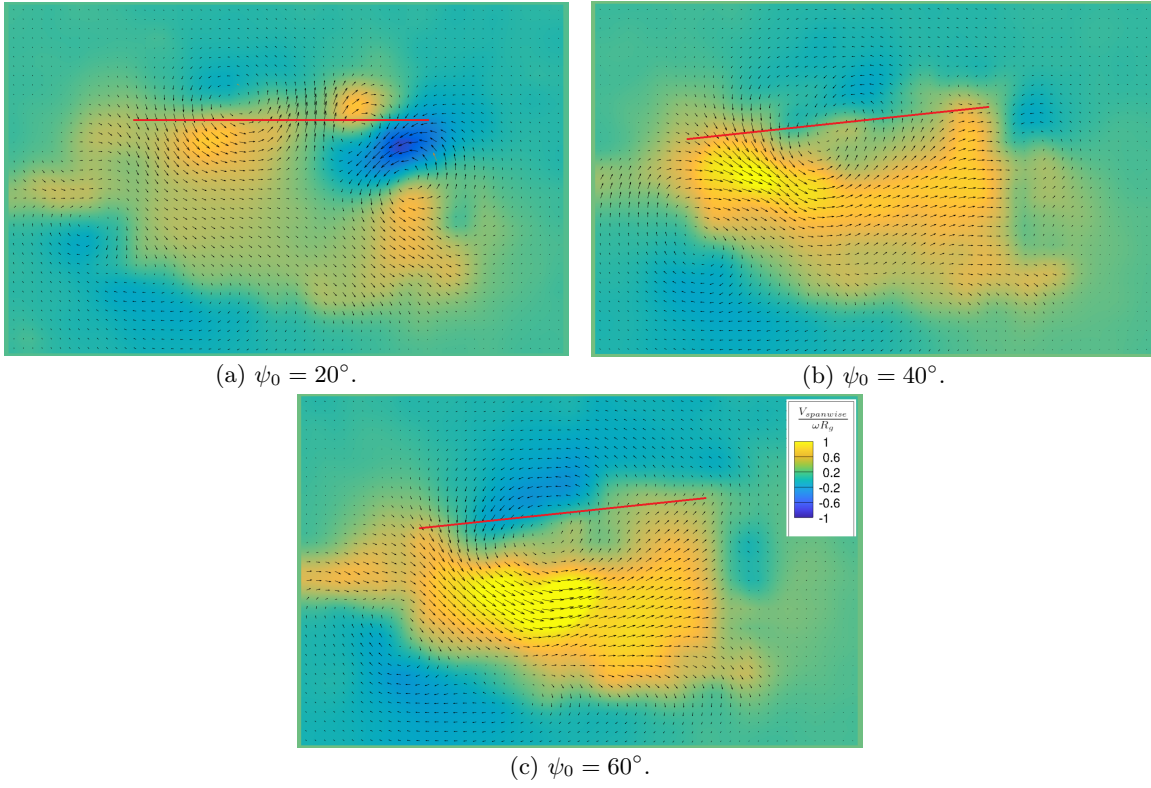


Figure 4-9: PIV resolved spanwise velocity component. Wake results for $Re = 392.7$. Instantaneously accelerated flat plate, $\alpha = 70^\circ$. Approximated position of the LEV core indicated with a red line.

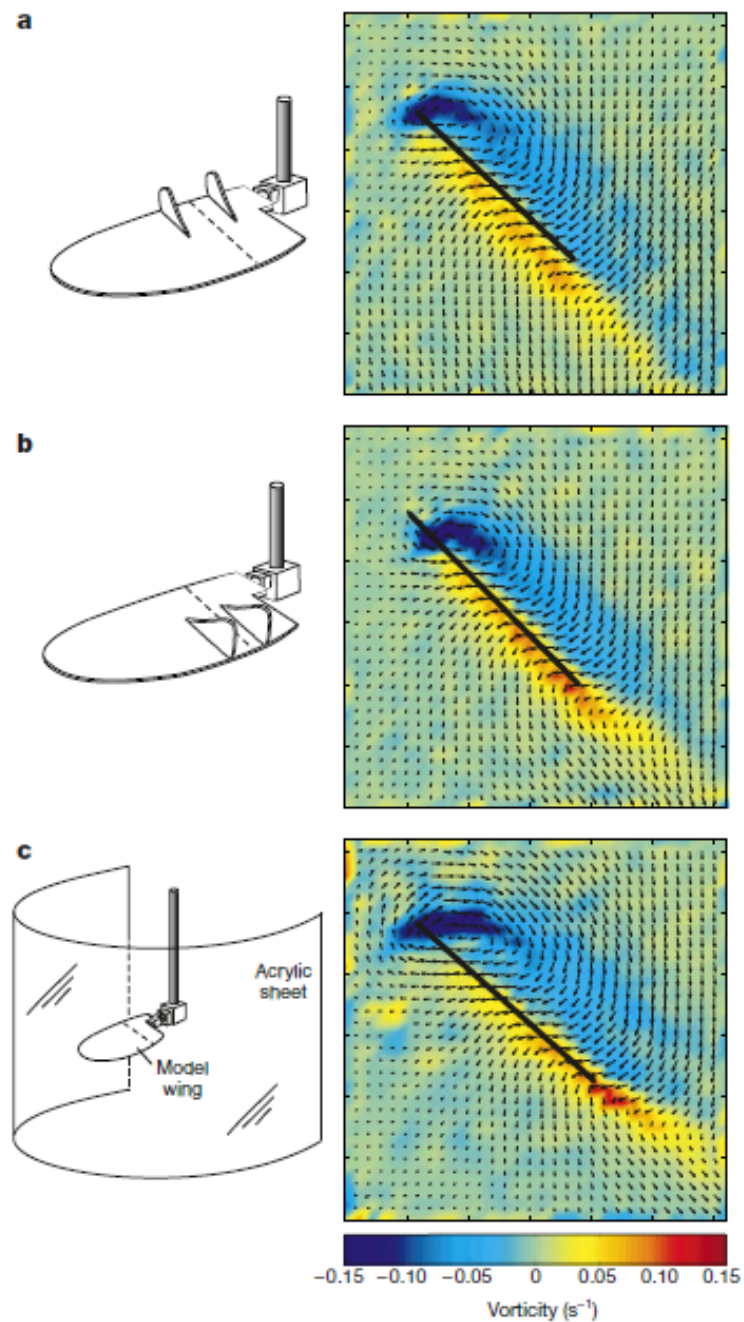


Figure 2 The leading edge vortex (LEV) remains attached despite experimental manipulation. Left column shows wing morphology, dotted line is position $(0.48R)$ of vorticity plots (right column). **a**, Forward-pointing fences. **b**, Rearward-pointing fences. **c**, Wall. Compared to the two fence manipulations, the presence of a wall causes the LEV to enlarge and extend farther along the wing before detaching into a tip vortex.

Figure 4-10: Fins placement in experiment published in [13].

4.2 Reynolds number effect

Depending on the specific dragonfly species, they can fly at a very different Reynolds number. For reference, smaller dragonflies have a characteristic Reynolds number of the order of a 100, while bigger dragonflies can have Reynolds numbers up to 10000 [2]. This gives a great range of possible flow regimes, and it will be seen in this section that this affects the stability and structure of the LEV. The Reynolds number is defined as in the previous experiment, see Equation 4.1.

First, the evolution of the LEV and TEV is presented after 20° and 40° of flapping, in Figure 4-11 and Figure 4-12. The first remarkable difference is that around $Re = 196.35$, the LEV near the wing tip starts to become unstable and is lifted upwards. For higher Reynolds numbers, it can be seen how the tip becomes completely unstable and a group of smaller vorticity structures emerge. The range of Reynolds numbers where the turbulent and laminar LEV structure are present agrees with the experiments in [61] (see Figure 2-32a). For $Re = 392.7$, the Reynolds number of the present experiment, the tip vortex is completely unstable, as it was observed in the PIV measurements. For this reason exact correlations between structures in the PIV and simulation could not be expected.

It is important to mention the different mechanisms to control the amount of circulation in the LEV at different Reynolds numbers. As a remainder, the amount of circulation was crucial as it is generally agreed that when the LEV grows too much the structure can no longer be adhered and is detached. For high Reynolds numbers, when the flow transitions, vortex shedding occurs specially close to the tip. This can be observed in the simulations as the main mechanism to control LEV size. Note how for example at $Re = 392.7$ the LEV core is still attached, but there is a substantial amount of vorticity that was shed away due to the instability at the tip. On the other hand, for low Reynolds numbers a completely different mechanism occurs. In Figure 4-11 and Figure 4-12 two Q-criterion isocontours were visualized, the same two for all figures. The transparent Q-criterion isocontour has a value of an order of magnitude less than the solid one. Q-criterion aims to represent the strength of a vortex, therefore, the solid vortex core indicates the presence of a strong vortex, while the transparent isocontour shows a much weaker vortex core. For higher Reynolds number it can be seen that both isocontours are almost identical. This means that the vortex core is contained within a certain spatial location, and its vorticity is not spread away due to diffusion. However, for the lower Reynolds numbers, it can be seen that vorticity is diffused quite rapidly away from the vortex core. This is another way of removing vorticity for low Reynolds numbers. Most studies inspected in the literature review only look at 2D flapping. The vorticity removal in low Reynolds numbers should be similar in 2D and 3D flows. On the other hand, turbulence transition occurs due to vortex stretching, which is specific of 3D flows.

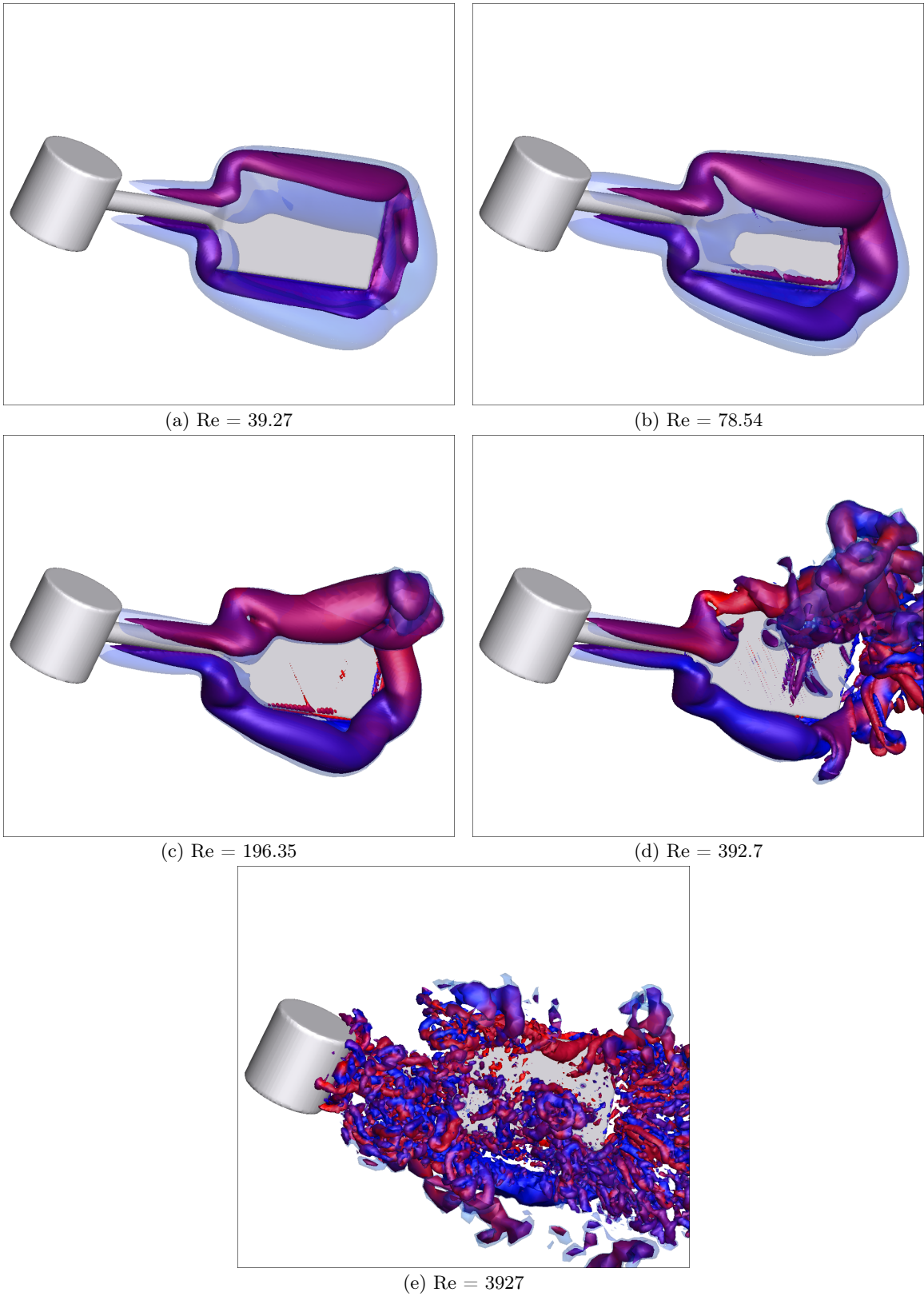


Figure 4-11: $\psi_0 = 20^\circ$. Q-criterion isocontours colored by spanwise vorticity for different Reynolds numbers. Instantaneously accelerated flat plate, $\alpha = 70^\circ$.

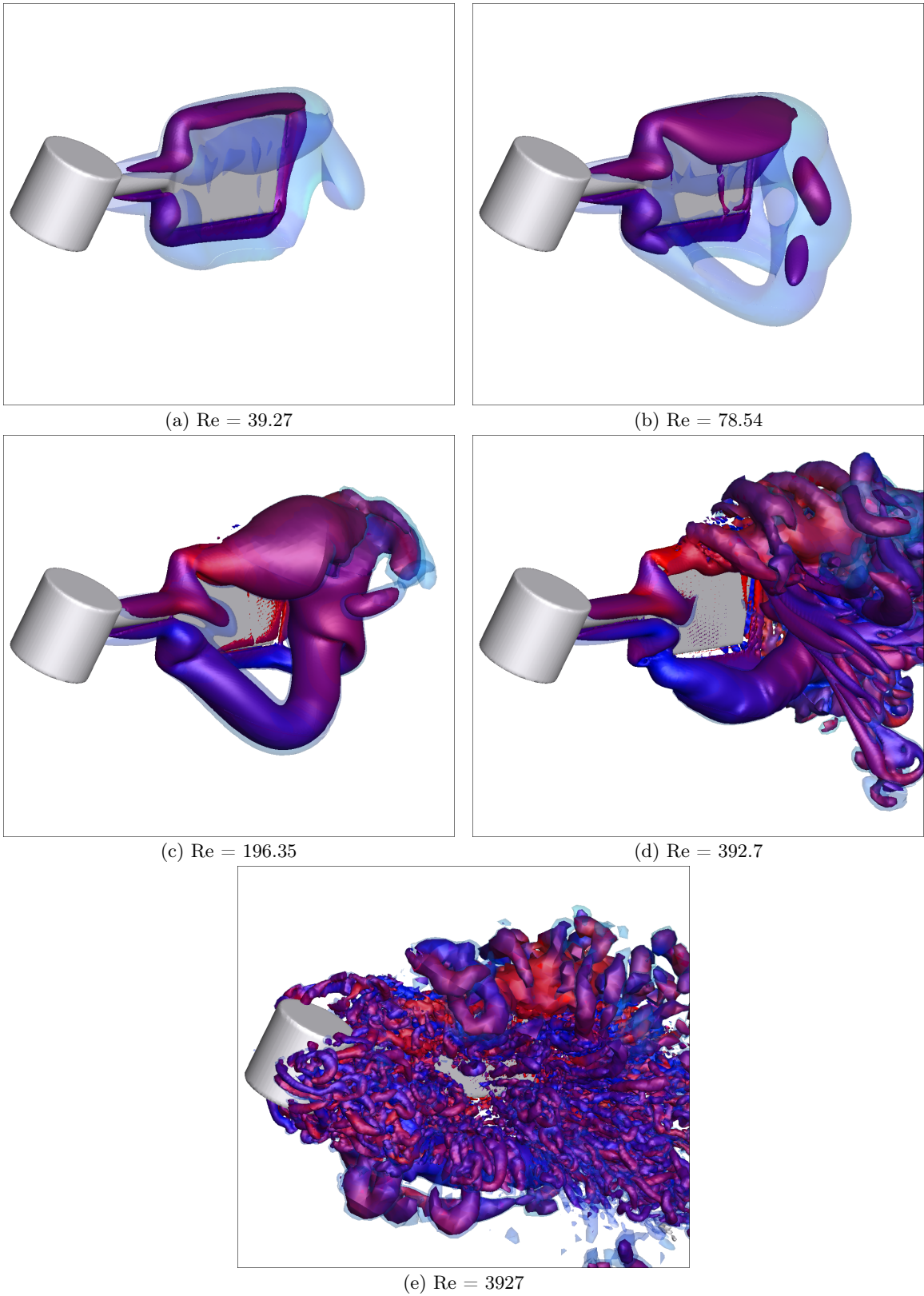


Figure 4-12: $\psi_0 = 40^\circ$. Q-criterion isocontours colored by spanwise vorticity for different Reynolds numbers. Instantaneously accelerated flat plate, $\alpha = 70^\circ$.

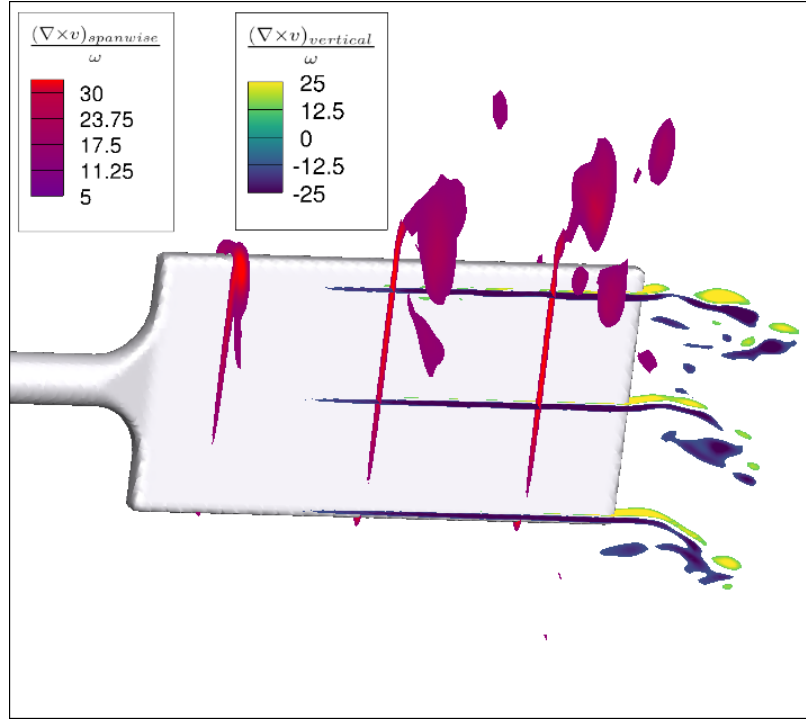


Figure 4-13: $\psi_0 = 20^\circ$. $Re = 392.7$. Violet and red: slices at different spanwise distances, colored by spanwise vorticity. Yellow and blue: slices parallel to the flapping plane colored by vorticity normal to the flapping plane. Instantaneously accelerated flat plate, $\alpha = 70^\circ$.

It was seen that around $Re = 196.35$ an instability occurred. To visualize this, slices of the spanwise and tip vorticity are shown in Figure 4-13. First, it can be clearly seen the mechanism of vortex shedding at the LEV and at high Reynolds numbers. Second, at the tip the vorticity component normal slice is shown. See how a Kelvin Helmholtz type instability occurs in the sharp shear layer of the tip vortex. This also occurs for example in the wake of a cylinder, the Von-Karman vortex street: periodic opposite sign vorticity shedding. The reason why this begins at the tip is the higher flow velocity in this region.

Finally, to better understand the structure and importance of the LEV, slices of the spanwise vorticity and vertical downwash velocity are shown in Figure 4-14. It can be noticed that for low Reynolds numbers the LEV remains as a coherent structure well attached to the leading edge. However, for higher Reynolds numbers, transition occurs, and vorticity shedding is responsible for controlling the circulation in the LEV structure. Remark that just by looking at the LEV core, the circulation (surface integral in the slice of vorticity) is larger for the high Reynolds number cases. This was observed before in the literature, see Figure 2-34a from [23]. When increasing the Reynolds numbers the LEV loses less circulation from its core due to vorticity diffusion and dissipation. Therefore, circulation keeps increasing until around $Re = 500$ as observed by [23]. At this point circulation starts to be controlled by the vortex shedding mechanism and reaches a

maximum. On the other hand, the vertical downwash is correlated with lift production: Newton's third law, action reaction principle. For lower Reynolds numbers the downwash is clearly smaller, and keeps increasing with the Reynolds number until the vorticity shedding mechanism starts. Point out as seen in the literature review that lift is also correlated with the circulation of the LEV, according to Kutta–Joukowski theorem, see Equation 2.14. In Figure 4-15 the reader can verify that indeed for the higher Reynolds number regimes, when the circulation is higher, the lift coefficient is higher. This agrees with the previously justified correlation between the three components: circulation of the LEV, vertical downwash and lift. Observe how the lift coefficient starts oscillating when the LEV transitions and the flow becomes turbulent. The lift coefficient is defined for all other plots analyzing the flat plate as:

$$C_L = \frac{F_z}{\frac{1}{2}\rho(\omega R)^2 S}, \quad (4.2)$$

where $R = R_r + b$ (see section 4.1) is the tip distance to the center of rotation, F_z the vertical force, ω the angular velocity, ρ the density and S the area of the flat plate.

Based on this analysis it may seem clear that a dragonfly should fly in higher Reynolds regimes, to maximize lift production. However, animals want to minimize the power requirements when doing a task, for example hovering. Therefore, the quantity of interest is not the lift coefficient by its self, but the power required to get that lift. The power coefficient is defined as:

$$C_P = \frac{P}{\frac{1}{2}\rho(\omega R)^3 S}. \quad (4.3)$$

With this new definition it can be seen in Figure 4-15b that when the LEV becomes unstable performance decreases. With higher Reynolds numbers the flow indeed generates a stronger LEV with more circulation and therefore more lift, as claimed before in the literature [23]. However, this is not the final truth. Power requirements due to drag are also crucial. In the literature review it was observed that a lot emphasis was placed on 2D LEV dynamics. However, this overlooked transition of the LEV, which causes higher energy requirements during flapping. This is presumably crucial in the actual aerodynamics of dragonflies.

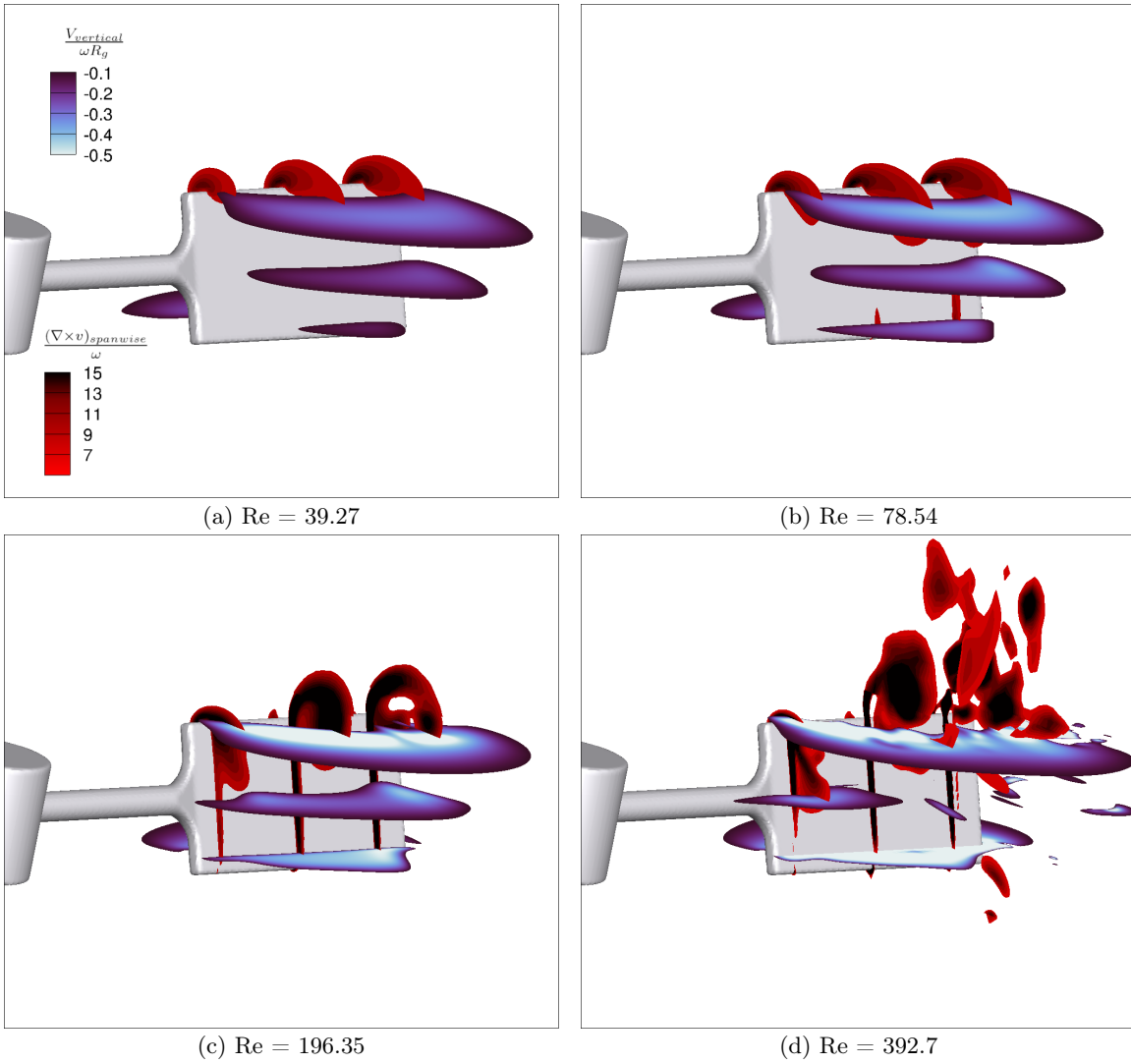


Figure 4-14: $\psi_0 = 20^\circ$. Black and red: slices at different spanwise distances, colored by spanwise vorticity. White and purple: velocity slices parallel to the flapping plane colored by vertical velocity. Instantaneously accelerated flat plate, $\alpha = 70^\circ$.

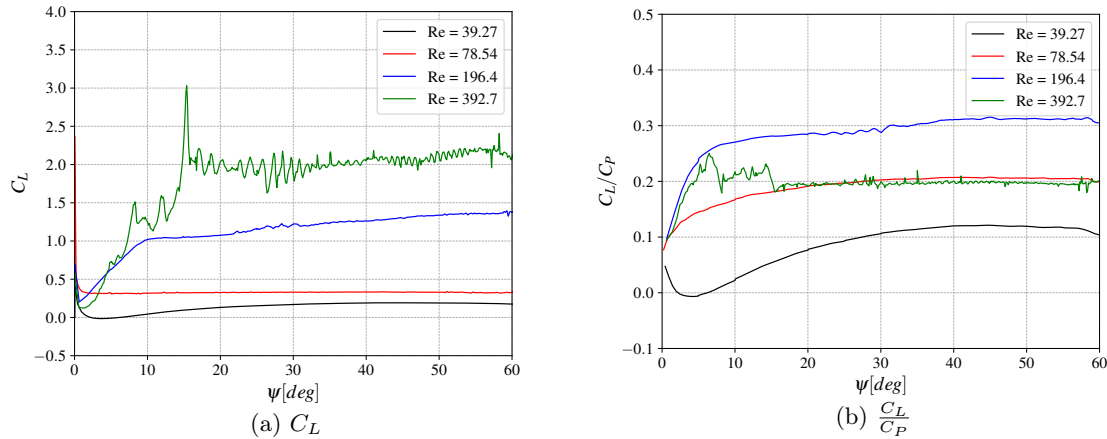
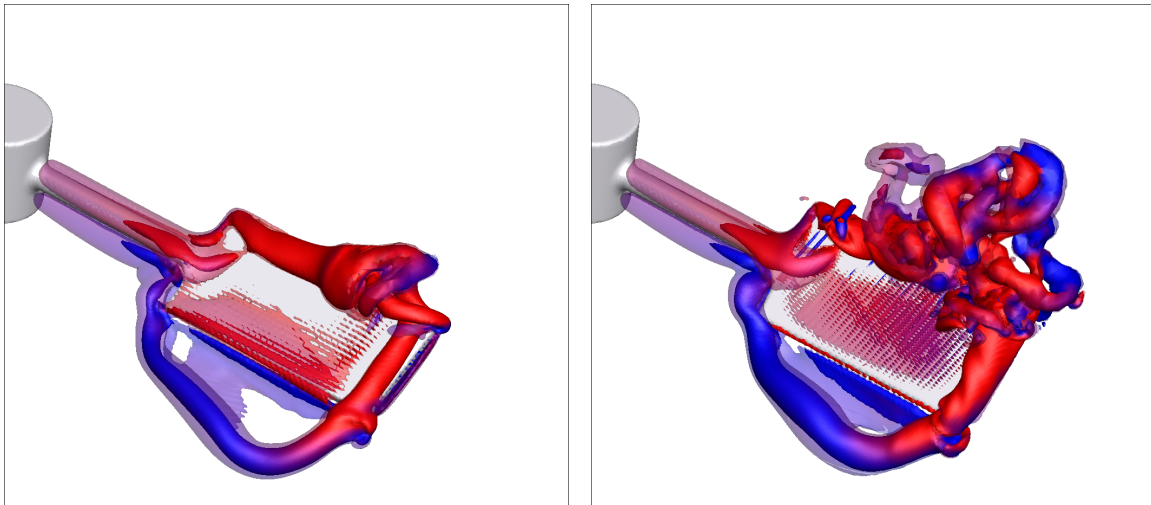


Figure 4-15: Comparison of lift and power coefficient dependence with Reynolds number. $AoA = 70^\circ$, instantaneously accelerated flat plate.

4.3 Angle of attack effect

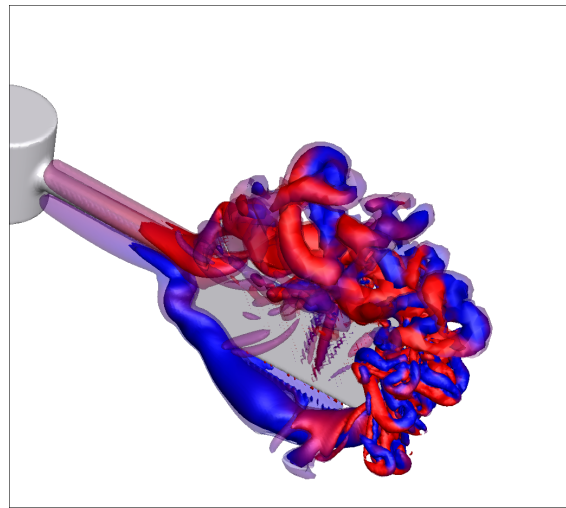
As explained in the literature review when reviewing dragonfly kinematics (see section 2.1), dragonflies in hovering typically have an angle of attack of 70° during the downstroke, the part of the flapping cycle where most of the vertical force is generated. For this reason in previous sections it was placed a lot of emphasis on this angle of attack. However, now a more in depth inspection of the angle of attack dependence is going to be performed.

To comprehend the LEV dependence on the angle of attack several Q-criterion isocontours colored by spanwise vorticity are shown for two flapping angles $\psi = 20^\circ$ Figure 4-16 and $\psi = 40^\circ$ Figure 4-17. The first thing that can be noticed is that the LEV coherent structure is more stable at lower angles of attack. Also note how the TEV is shed much faster for $AoA = 25^\circ$ while remains attached much longer to the higher angles of attack. The reason for this is that at high angles of attack the lack of momentum in the wake is more extended, and therefore the TEV cannot be so easily advected. The fact that the TEV is not shed has probably a negative effect on the stability of the LEV, as the flow it induces tends to push the LEV upwards and away from the leading edge.



(a) $AoA = 25^\circ$

(b) $AoA = 45^\circ$



(c) $AoA = 70^\circ$

Figure 4-16: $\psi_0 = 20^\circ$. Q-criterion isocontours colored by spanwise vorticity for different AoA. Instantaneously accelerated flat plate, $Re = 392.7$.

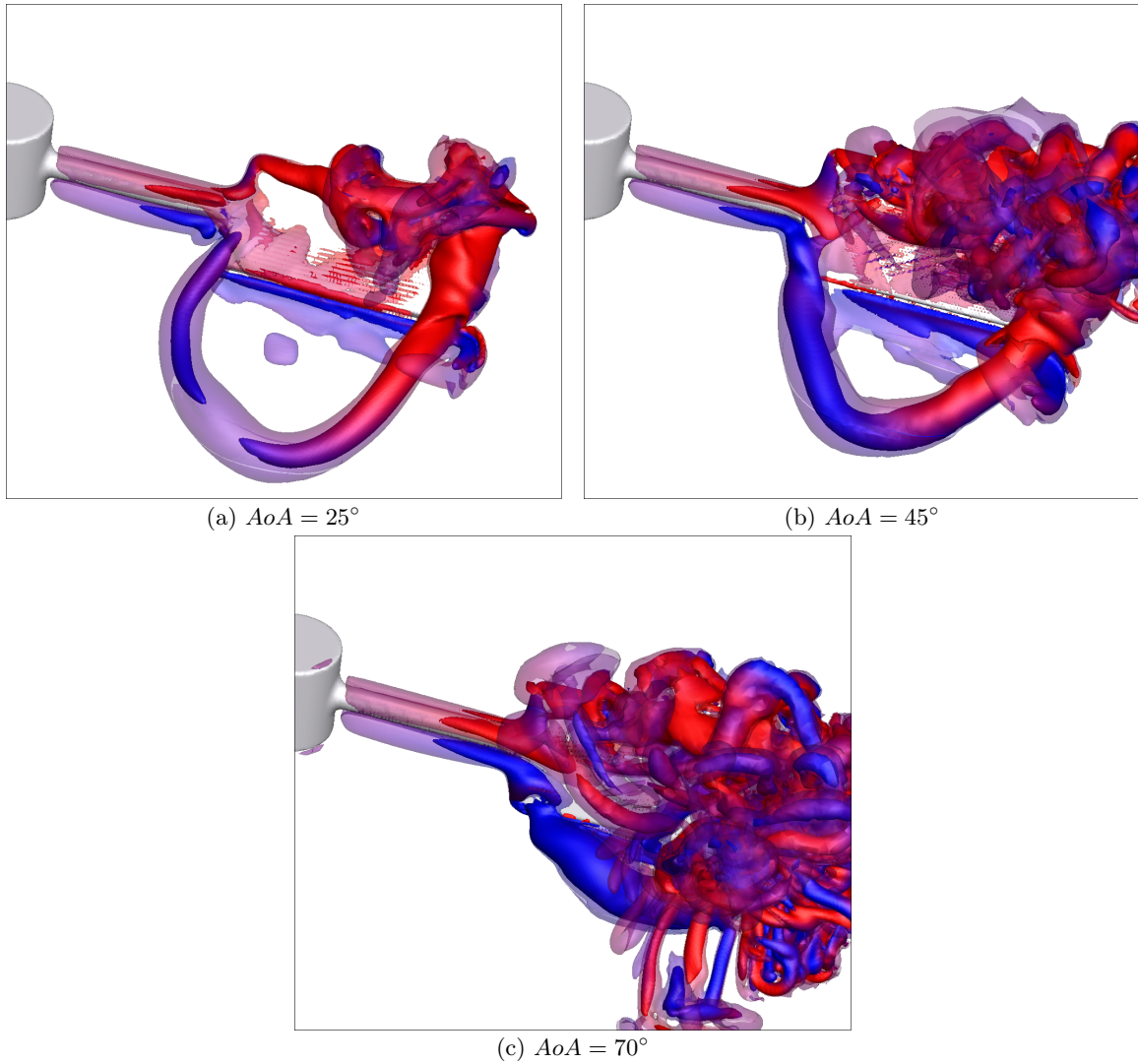


Figure 4-17: $\psi_0 = 40^\circ$. Q-criterion isocontours colored by spanwise vorticity for different AoA. Instantaneously accelerated flat plate, $Re = 392.7$.

Looking closer at the initial detachment of the LEV in Figure 4-16a, it can be seen that close the tip there seems to be a lift-up mechanism that pushes the LEV away from the flat plate, at approximately 3/4 of the span. To inspect why this is happening in more detail the plate is visualized from the wake downstream in Figure 4-18. A slice of the spanwise velocity is displayed with the streamlines projected on top. See how there are two jets (blue coming from the root vortex and red coming from the tip vortex) of opposite sign spanwise velocity colliding at around 3/4 of the span, just where the lift up mechanisms of the LEV was observed. As the flow is incompressible and is bounded by the flat plate, it has to be ejected away from it. This explains the lift-up mechanism of the LEV and shedding at 3/4 of the span. Remark that this lift-up mechanism was also seen in the experiment, see subsection 4.1.2.

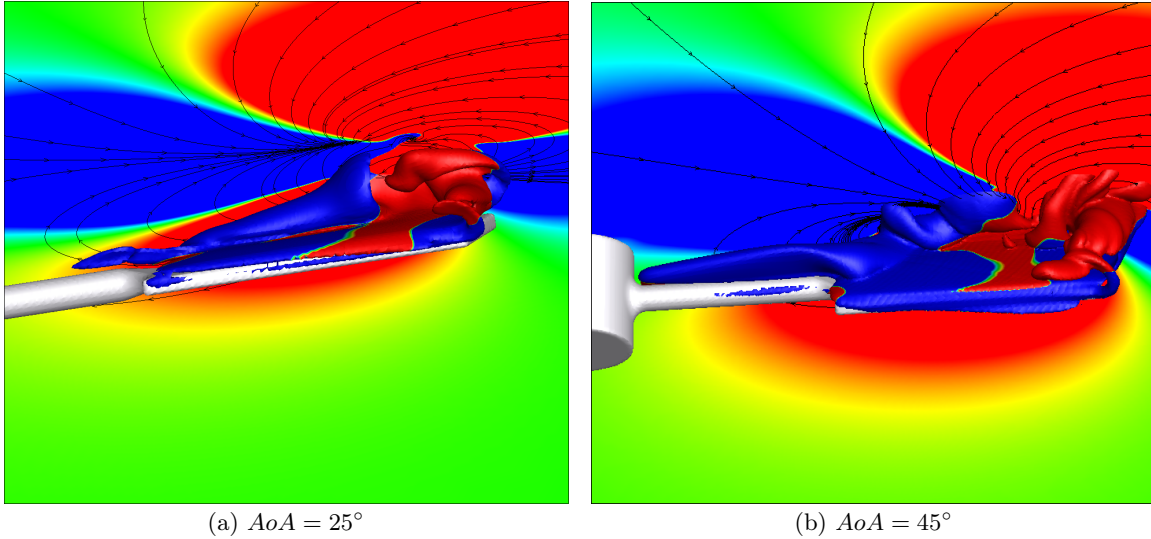


Figure 4-18: $Re = 392.7$. Flapping plate viewed from downstream. Slice colored by spanwise velocity component with projected streamlines. Blue (from root to tip) and red (from tip to root). Q-criterion that denotes the position of the LEV also colored with the same spanwise velocity color code.

To visualize the lift-up mechanism close to the tip, slices of the spanwise vorticity are shown in Figure 4-19. It can be clearly seen that indeed, at the point where both jets collided vorticity is shed upwards and away from the plate. The natural question to ask would be why this is stronger for higher angles of attack. The reason is that for higher angles of attack the tip and root vortex are more intense and the collision of opposite jets is consequently stronger. Additionally, it was seen that for higher angles of attack the TEV is not shed, and therefore it is also injecting another jet of mass from the lower part of the flat plate that will collide with the two other jets. All these components destabilize the LEV and cause its shedding.

Once the overall flow structure has been discussed, more focused is going to be placed into the actual quantities of interest such as lift and drag. First, going back to Figure 4-19a, observe how the vertical downwash is less intense for $AoA = 25^\circ$, increases its intensity for $AoA = 45^\circ$ and finally due to the large detachment of the LEV, at $AoA = 70^\circ$ it lowers a bit its intensity. This is reflected in the lift coefficient in Figure 4-20a. Once again the same three elements correlate: lift, LEV intensity and downwash. Note also in the lift coefficient the more abrupt oscillations at $AoA = 70^\circ$ due to the more unstable LEV.

Conversely, the drag coefficient in Figure 4-19b keeps increasing for larger angles of attack, as expected due to the higher momentum deficit in a larger wake. If the goal of a dragonfly is to have a high acceleration and do sudden maneuvers, then even though the lift is slightly smaller for $AoA = 70^\circ$ total force production $\sqrt{C_L^2 + C_D^2}$ would be higher. Also it should be considered that dragonflies can vary their stroke plane to orient the resultant force $\sqrt{C_L^2 + C_D^2}$ in the desired direction, see Figure 2-35b and subsection 2.2.4 for a more detailed explanation of how dragonflies

can redirect the resultant force. In Figure 4-19c the optimal stroke plane γ is calculated for each angle of attack to redirect the result force in the vertical direction, that is for pure hovering. For reference, as it was explained in section 2.1, the typical stroke plane for hovering in dragonflies is $\gamma = 60^\circ$. Note that with $AoA = 70^\circ$ which is also the observed angle of attack during dragonfly downstroke, they would be close to fully aligning the resultant force with the vertical direction. Also note that force results correspond to a flat plate, which is not exactly an actual dragonfly wing geometry. In section 4.5 a much closer vertical alignment is observed for $AoA = 70^\circ$ with an actual corrugated dragonfly wing.

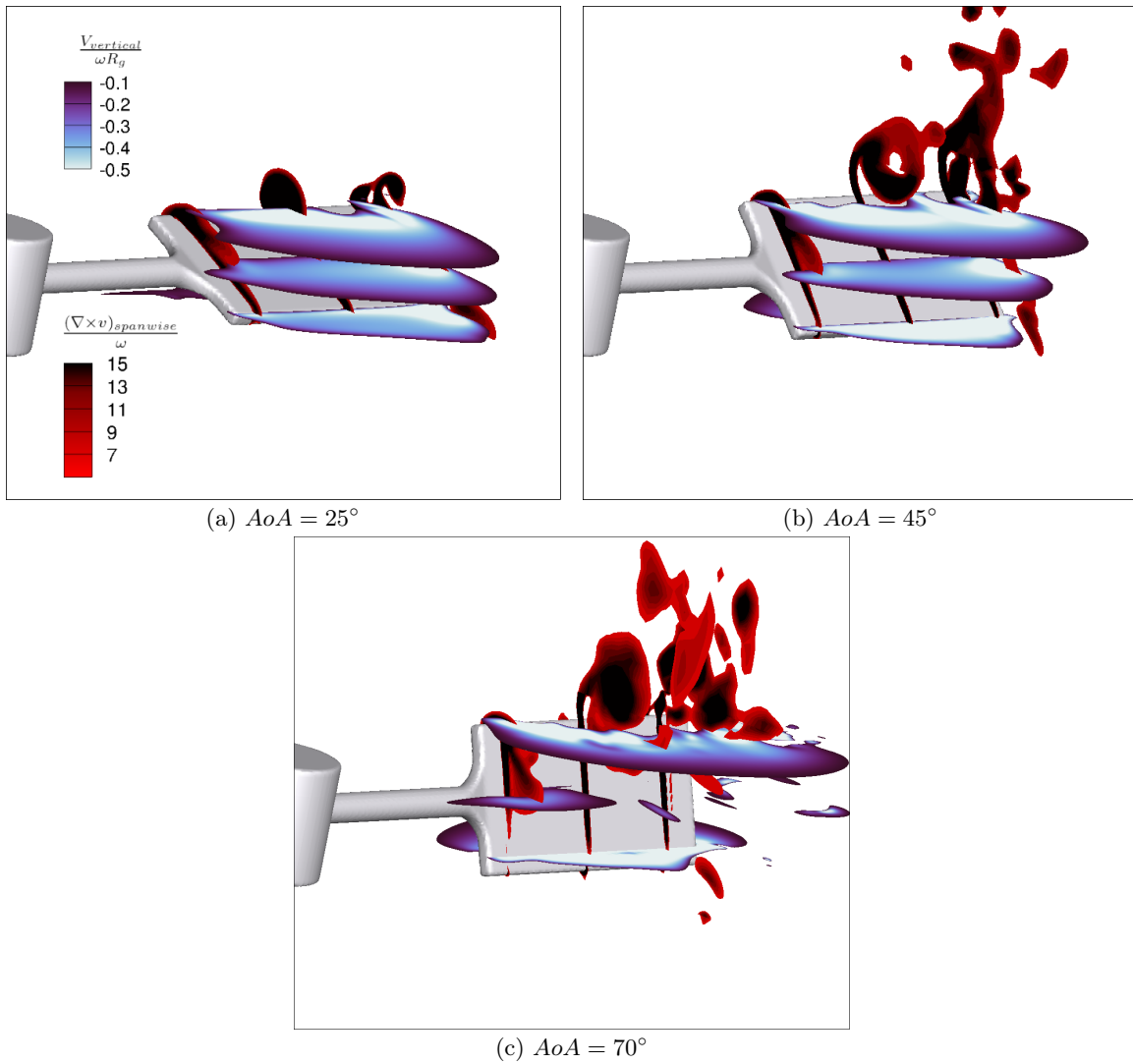


Figure 4-19: $\psi_0 = 20^\circ$. $Re = 392.7$. Violet and red: slices at different spanwise distances, colored by spanwise vorticity. White and blue: slices parallel to the flapping plane colored by vertical velocity. Instantaneously accelerated flat plate, $\alpha = 70^\circ$.

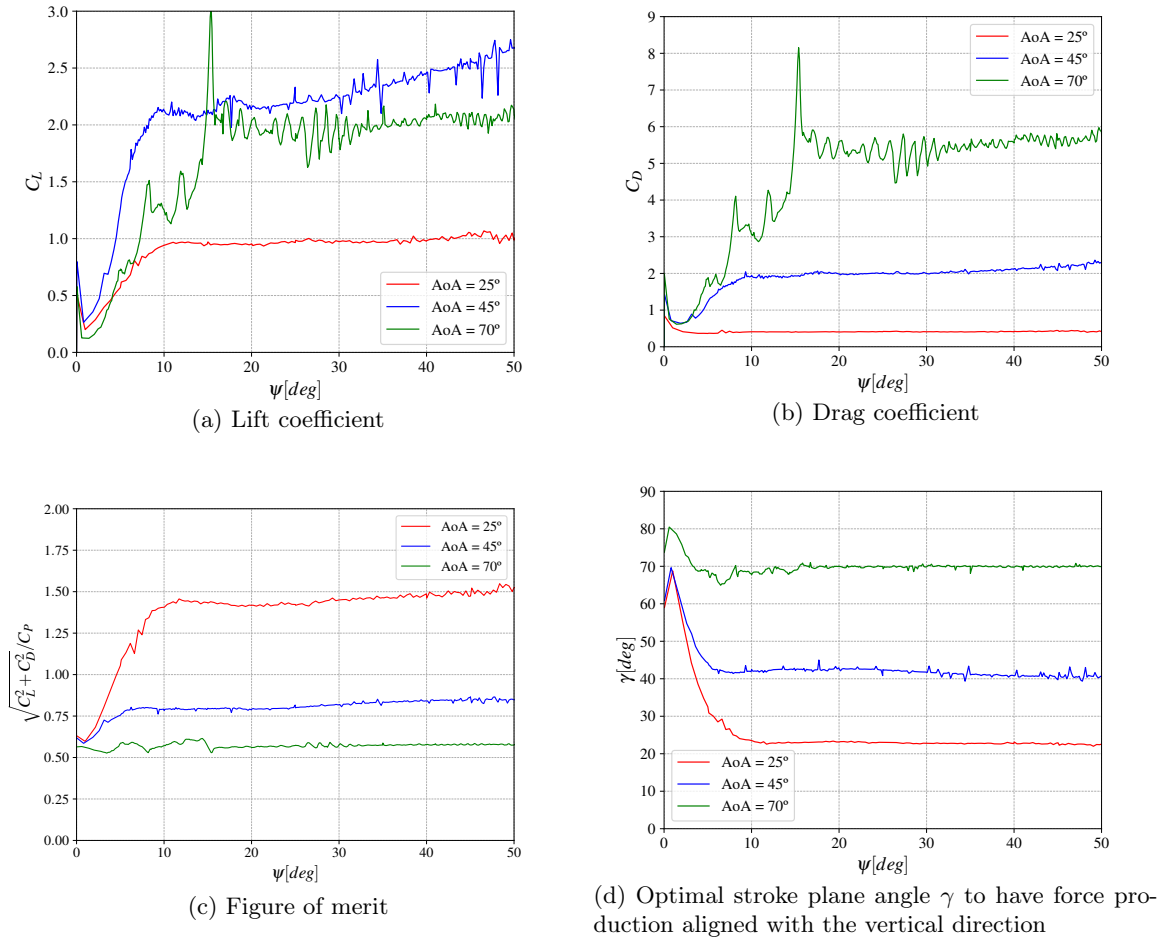


Figure 4-20: Assessment of flat plate at different angles of attack. Instantaneously accelerated flat plate, $Re = 392.7$.

So far it was concluded that $AoA = 70^\circ$ maximizes the amount of force production out of the alternatives inspected. Nevertheless, as it was mentioned before, it is also important to look at the amount of energy invested in this process. This is done in Figure 4-20c. Now, another perspective emerges. $AoA = 70^\circ$ might be optimal for large force production, but is not optimal from the point of view of energy consumption. This agrees with observations done in nature, for example for dragonfly *Anax Parthenope* hovering is estimated to be a quite energy consuming flying mode [9], see Figure 2-9. In fact, because of the high energy consumption, dragonflies tend to avoid this flying mode as much as possible, and for this reason hovering kinematics were one of the least documented flying modes in the literature review subsection 2.1.1. Another relevant question is whether it is really necessary such a high amount of force production for hovering. Steady lift generation mechanisms only achieved lift coefficient of around 1 see Figure 2-18. However, *Wakeling et al.* [122] estimated that a much higher lift coefficient was required for actual hovering, close to 5. Then the community reasoned that unsteady lift mechanisms were necessary to explain this phenomenon. However, even

with unsteady aerodynamics they were not close to the expected value. The reason for this is that they were looking only at the lift, but they did not consider the drag and the ability of dragonflies to use it as vertical force by modifying the stroke plane. With the current analysis it can be clearly seen that with $AoA = 70^\circ$ dragonflies mostly rely on drag as a mechanism to sustain hovering.

4.4 Start up effect

All the previous numerical results were obtained with an infinite acceleration at $t = 0$ to reach the uniform angular flapping velocity. However, in the experiment this was not the case, as an infinite acceleration is not possible. Given the response time of the servomotor used, $t = 0.02s$ (see subsection 3.2.1), a realistic acceleration response has been defined with:

$$\psi(t, \omega, k) = \frac{\omega t^2}{1+t} + \frac{e^{\omega t/k} - 1}{e^{\omega t/k} + 1} \left(\omega t - \frac{\omega t^2}{1+t} \right), \quad (4.4)$$

where $\omega = \dot{\psi}$ is the flapping speed, t is the dimensional time in seconds and $k = 0.004 [s^{-1}]$ is tuned to get the acceleration in the response time of the servomotor. The trajectories of the immediately accelerated and realistic profile are shown in Figure 4-21.

Three slices used for the PIV comparison are shown in Figure 4-22, Figure 4-23 and Figure 4-24. It can be seen that there are some differences due to the fact that the flow transitioned and is chaotic. For this reason it could not be expected an identical correlation between PIV and simulation. However, overall the general flow profile is pretty similar. The Q-criterion isocontours in Figure 4-25 show the same conclusions: not identical flow features due to the chaotic regime but overall similar flow structures. Moreover, when looking at the lift coefficient in Figure 4-26 a quite good agreement is observed. The main difference that can be observed, is that there is a negative lift coefficient at the beginning in the modified trajectory. That is due to the overshoot in the flapping speed in Figure 4-21b, that leads to a negative acceleration after the initial start-up.

Based on this analysis it can be concluded that the start-up effect that presumably happened in the experiment does not affect significantly the flow features, and therefore all analysis done with an immediate accelerated wing is also valid.

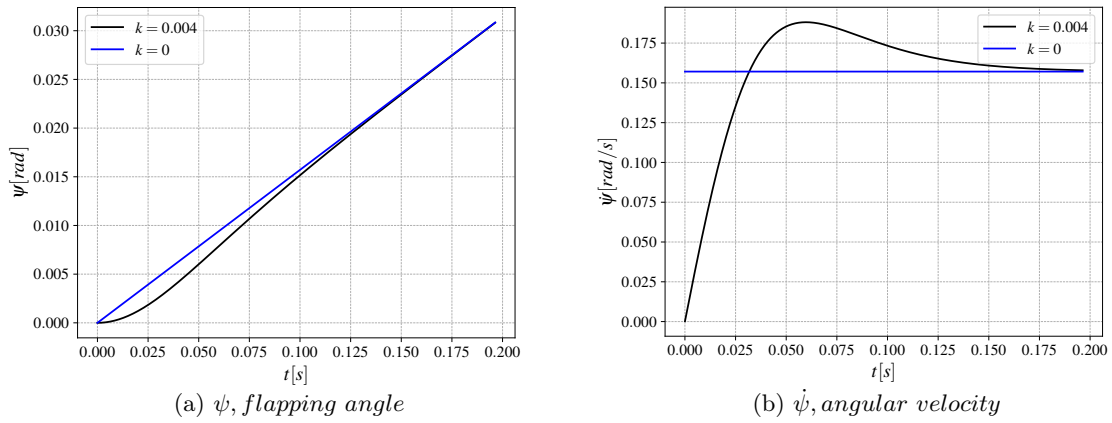


Figure 4-21: Evolution of the flapping angle and angular speed with time for the different start ups.

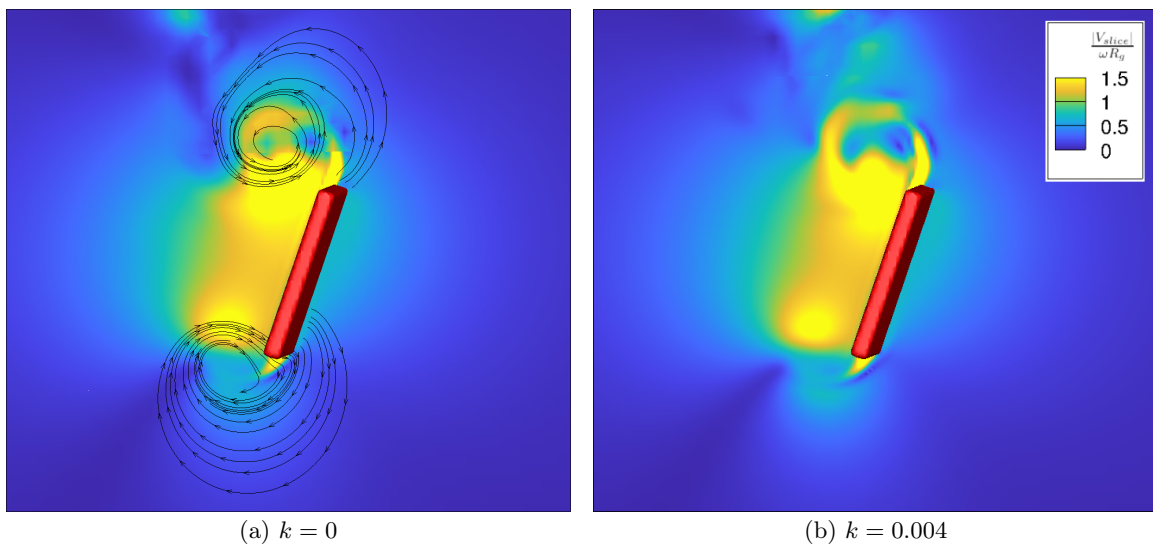


Figure 4-22: $\psi_0 = 20^\circ$. Streamlines colored by velocity magnitude projected onto the slice. $0.75b$. $\alpha = 70^\circ$.

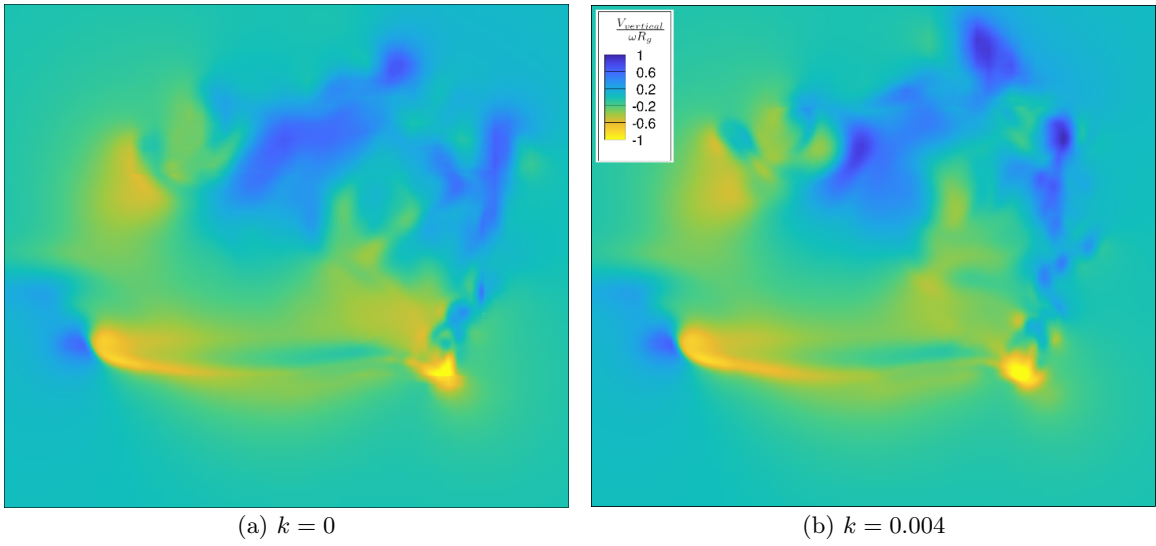


Figure 4-23: $\psi_0 = 40^\circ$. Wake results for $Re = 392.7$. $\alpha = 70^\circ$.

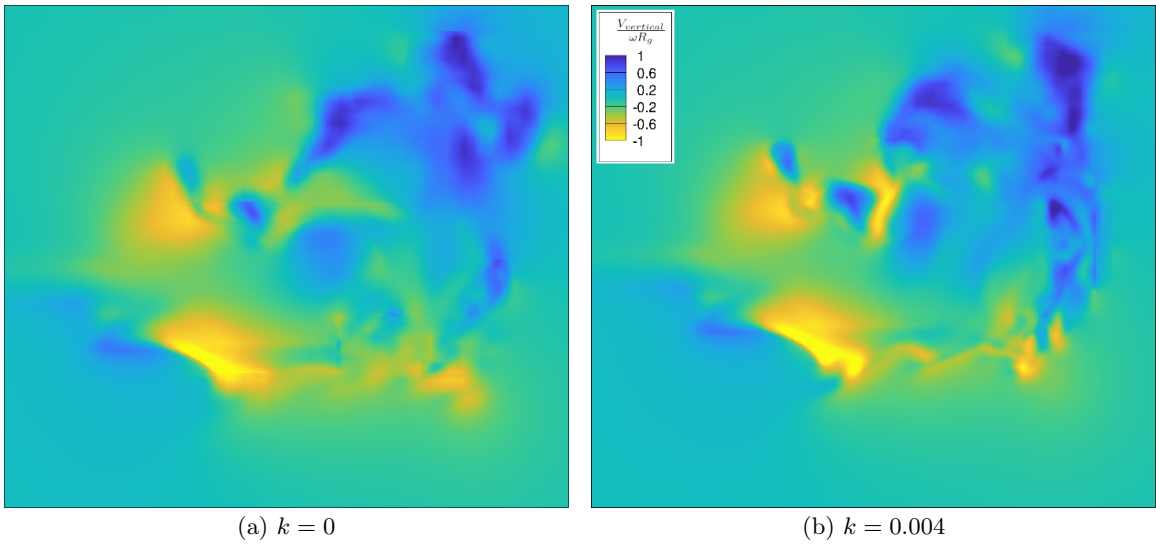


Figure 4-24: $\psi_0 = 60^\circ$. Wake results for $Re = 392.7$. $\alpha = 70^\circ$.

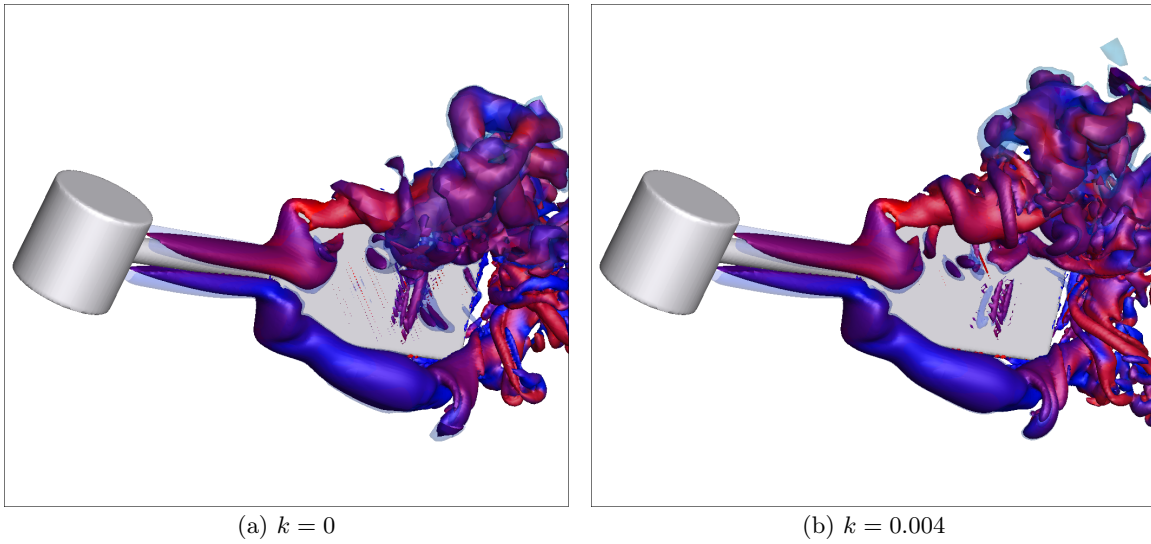


Figure 4-25: $\psi_0 = 20^\circ$. Q-criterion isocontours colored by spanwise vorticity for different AoA. Instantaneously accelerated flat plate, $Re = 392.7$.

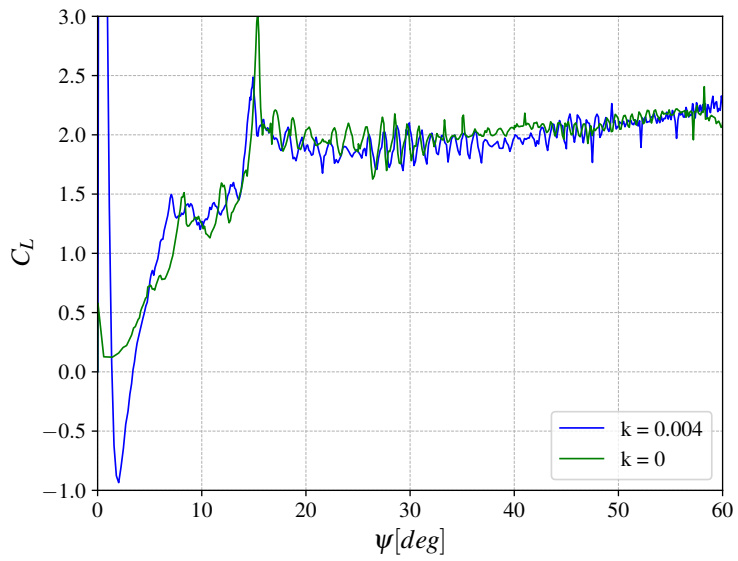


Figure 4-26: Comparison of the lift coefficient for the instantaneously accelerated flat plate $k = 0$ and the flat plate accelerating with a transient $k = 0.004$. $Re = 392.7$.

4.5 Corrugation and actual dragonfly wing analysis

Previously a detailed experimental and numerical study of a flat plate was conducted. Important conclusions were drawn regarding Reynolds numbers and angle of attack effects. However, the wing geometry was not representative of an actual dragonfly wing. In this study a real dragonfly *Neurobasis Daviesi* hindwing is going to be inspected. This geometry was generated with a detailed 3D scan with Micro CT of the actual dragonfly wing in [28]. The reconstructed geometry of the STL with cutcell intersections of the mesh used in the simulations is shown in Figure 4-27a. This gives an idea of the mesh resolution and the details of the wing geometry that will be perceived by the flow. Additionally, to inspect the effects of corrugation a smooth version of the corrugated wing is also going to be studied, see Figure 4-27b.

Regarding the flapping trajectory, the angle of attack of the wing is set to $AoA = 70^\circ$, which once again is the observed angle of attack during dragonfly downstroke. The angle of attack is defined with a linear regression of the wing geometry, that basically fits the least square error plane going across the wing points. Once this plane is characterized, the angle of attack can be defined as the angle between the fitted plane and the flapping plane trajectory. The Reynolds number is defined as:

$$Re = \frac{\omega R \bar{c}}{\nu} \quad (4.5)$$

$$\bar{c} = \frac{S_W}{2R}, \quad (4.6)$$

where ω is the flapping angular velocity, R the distance of the axis of rotation to the wing tip and \bar{c} the mean chord defined based on the wet surface S_W of the STL. Based on this definition $Re = 91.7$. This stands in the lower end of dragonfly species Reynolds numbers [2]. This low Reynolds number was selected for two reasons:

1. Ability to resolve all the flow scales (DNS) with a reasonable computational cost.
2. Stability of the LEV. It was seen before with a flat plate that at $Re = 196.35$ the LEV already started to oscillate and became unstable. In this case a fully stable and coherent LEV structure is desired to inspect it in detail. Lowering more the Reynolds number would also give a stable LEV, but its circulation intensity and force production would be lower, see Figure 4-15.

Once the simulation set up has been described, the results are going to be analyzed. The flow field is going to be inspected via streamlines after $\psi = 40^\circ$ of flapping, see Figure 4-28. First, observe how most of the suction that is later responsible for lift and force production occurs in the corrugated channels of the wing. This will be inspected later in more detail. Second, two types of streamlines are shown. The black streamlines denote the flow in the vortex core. Note how the vortex core is

advected from the root to $3/4$ of the span in a spiral way. However, the vortex core from the tip is also advected in the opposite direction towards $3/4$ of the span. These are exactly the opposite jets that met at $3/4$ of the span which were also detected with the flat plate, see Figure 4-18. Due to mass conservation in an incompressible flow, and the presence of the wing, this generated the previously called lift-up mechanism. This is observed in the green streamlines, which are generated upstream from the flat plate. Note how exactly at around $3/4$ of the span, the flow coming from upstream is not able to do a small radius circle, as it happened close to the root. The upstream flow is forced at $3/4$ of the span to be lifted away from the wing to preserve mass because of the two opposite jets at the vortex core, the so called lift-up mechanism. Most of the authors in the literature realize of the jet at the vortex core which advects flow from the root to the tip, due to the so called Coriolis spanwise blowing, but up to the author's knowledge no one has realized before of the importance of the so called here lift-up mechanism when the Coriolis spanwise blowing meets the opposite jet generated by the tip vortex. This is crucial because it changes completely the morphology of the LEV, and gives a clear mechanism to try to avoid its lift-up: avoid somehow the collision of the two opposing jets. Also observe that when the lift-up mechanism kicks in, the suction disappears, which basically makes the last $1/4$ of the wing useless in terms of lift and force production.

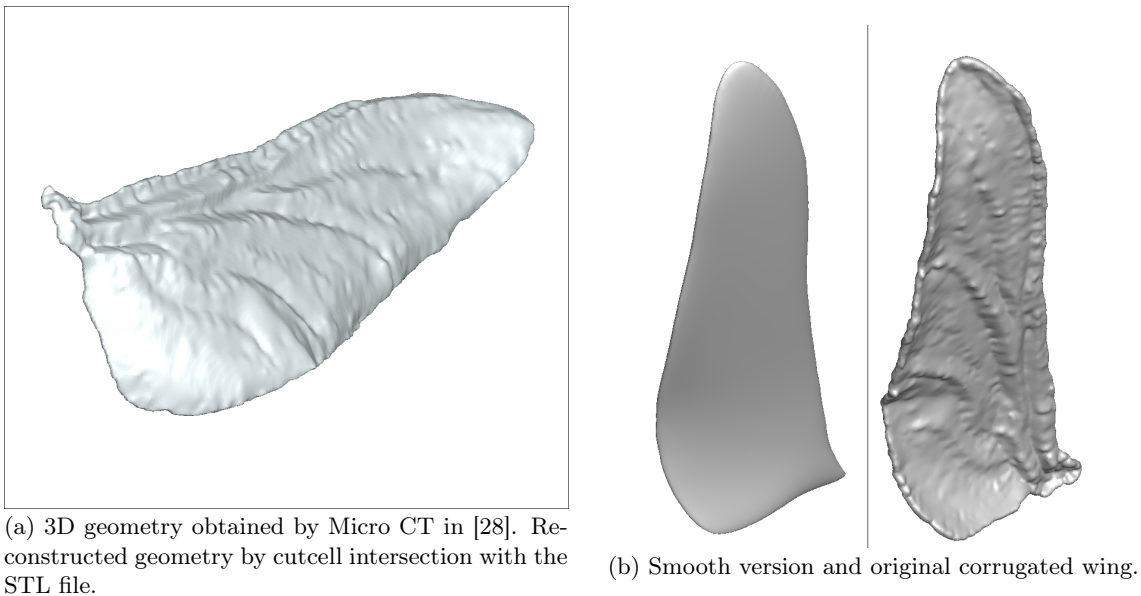


Figure 4-27: Dragonfly species *Neurobasis Daviesi* hindwing.

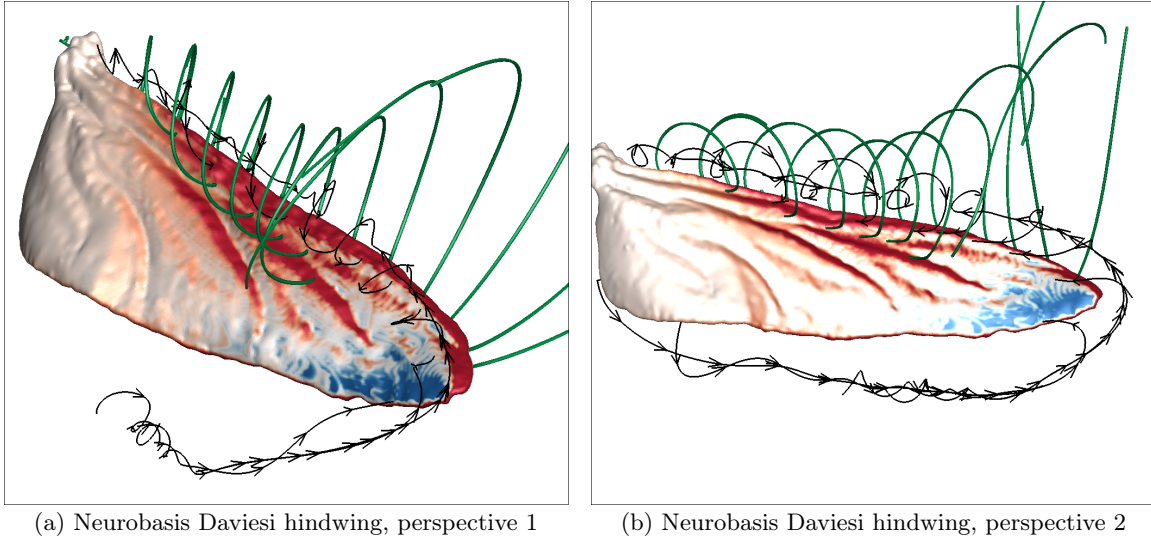


Figure 4-28: $\psi_0 = 40^\circ$, $\alpha = 70^\circ$ and $Re = 91.7$. Green streamlines start upstream from the wing and are advected downstream. Black streamlines are generated along the the vortex core. Wing surface colored by pressure (suction red, pressure blue).

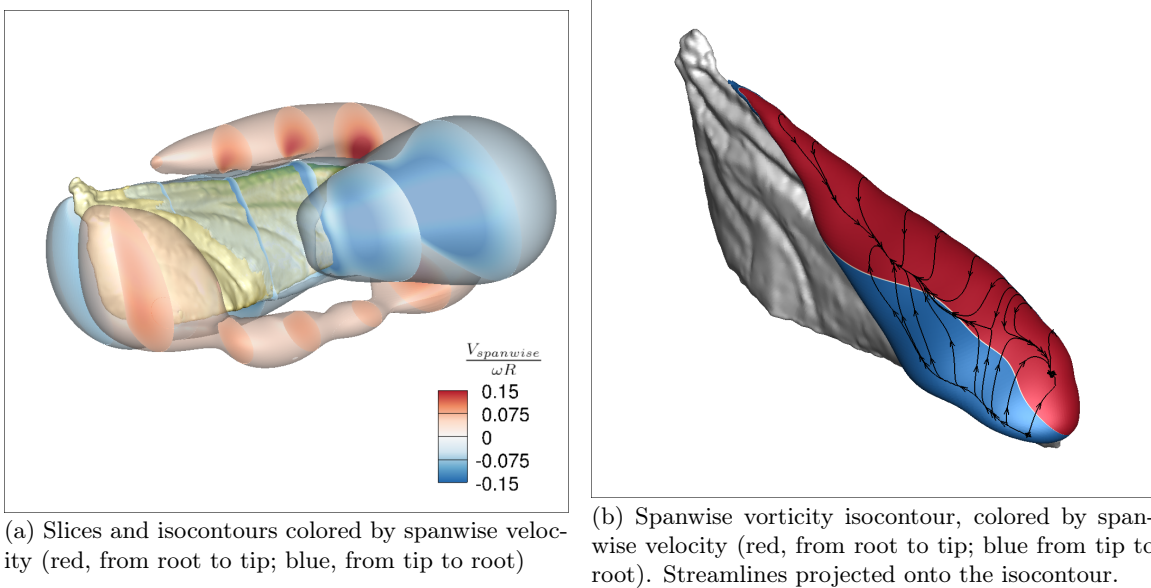


Figure 4-29: $\psi = 20^\circ$, $\alpha = 70^\circ$ and $Re = 91.7$. Corrugated wing.

To better appreciate the spanwise flow structure, isocontours of spanwise velocity magnitude are shown at Figure 4-29a. The LEV vortex core region has spanwise blowing from the root to the tip, specially close to the wing mid span and root. However, note that a huge jet of opposite spanwise velocity is generated at tip, going from the tip to the root. They collide at the position of the LEV at around $3/4$ of the span as explained before. This can be better visualized in Figure 4-29b. See how at the vortex core position the projection of the streamlines collide in two opposite directions,

creating the so called lift-up effect.

Next, the effects of corrugation are going to be inspected. The wings colored by pressure are shown in Figure 4-30. Vorticity contours that define the position of the leading edge vortex look quite similar. However, the pressure distribution on the wing surface is significantly different. In the corrugated wings intense suction is distributed over the corrugated channels of the wing, while in the smooth version, suction is distributed uniformly. Looking at Q-criterion isocontours in Figure 4-31 it can be seen that the corrugated channels indeed play an important role. They transport momentum and vorticity in the spanwise direction, and additionally as seen before create a concentrated suction spot.

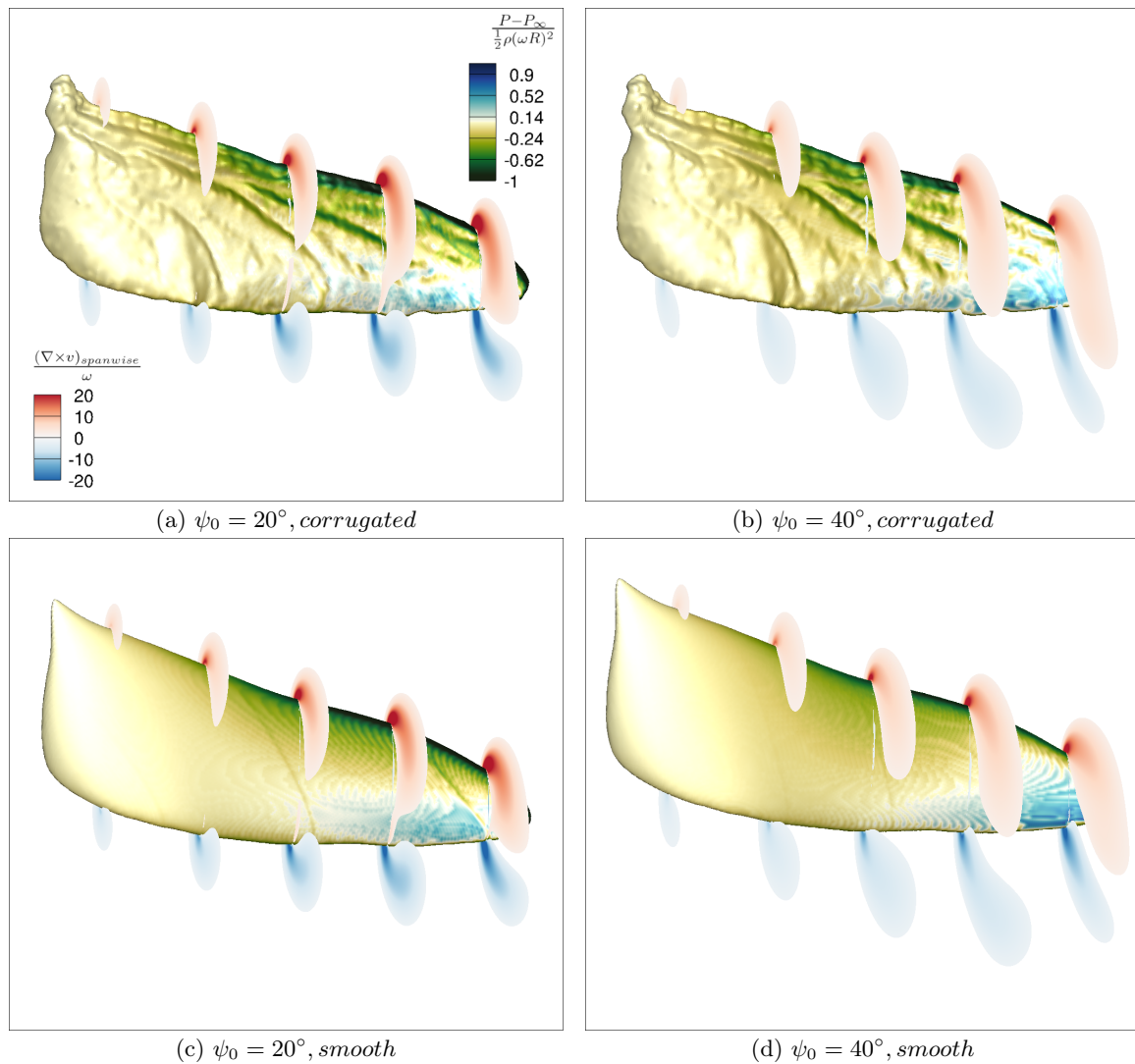
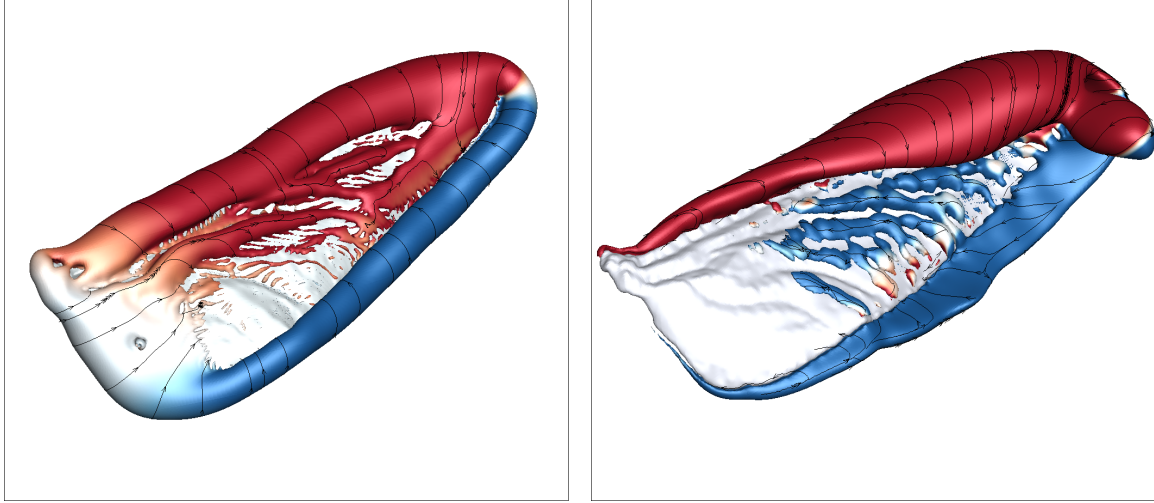
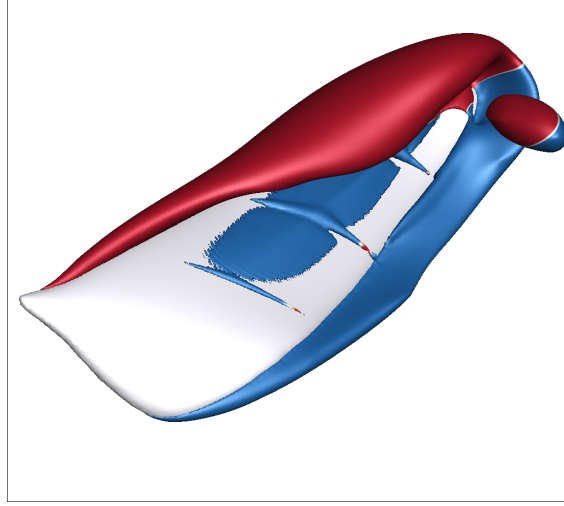


Figure 4-30: $\psi_0 = 20^\circ$, $\alpha = 70^\circ$. Slices colored by spanwise vorticity for two different flapping angles. $Re = 91.7$. Wing surface colored by pressure (suction green, pressure blue).



(a) $\psi_0 = 2.5^\circ$, Q - criterion = 0.3, corrugated.

(b) $\psi_0 = 40^\circ$, Q - criterion = 1, corrugated.



(c) $\psi_0 = 40^\circ$, Q - criterion = 1, smooth.

Figure 4-31: $\alpha = 70^\circ$ and $Re = 91.7$. Q -criterion isocontours colored by spanwise vorticity. Streamlines projected onto the isocontour.

To quantify the effects of these variations of the flow field the following quantities are defined:

$$C_L = \frac{L}{\frac{1}{2}\rho(\omega R)^2 \frac{S_W}{2}} \quad (4.7)$$

$$C_D = \frac{D}{\frac{1}{2}\rho(\omega R)^2 \frac{S_W}{2}} \quad (4.8)$$

$$C_P = \frac{P}{\frac{1}{2}\rho(\omega R)^3 \frac{S_W}{2}}, \quad (4.9)$$

where L is the lift, D the drag, P the power, ρ the density, ω the rotation speed, S_W the wet surface

of the wing and R the distance between the rotation axis and the wing tip.

The effect of the corrugation can be now quantified, see Figure 4-32. The main difference is that the lift coefficient is higher in the corrugated wing, Figure 4-32a. On the other hand, the drag coefficient stays almost identical Figure 4-32b. This allows to have higher efficiency in terms of total force generated for a given power, Figure 4-32c. The reason for this, is that the gain in lift, does not contribute to the power budget, as the lift is orthogonal to the flapping plane. This is a very relevant finding: corrugation enhances flying efficiency in hovering for the Reynolds number inspected. Finally, as explained in previous sections dragonflies can point the resulting force upwards. For this the optimal stroke plane at each time is shown Figure 4-32d. Observed, how now with an actual dragonfly wing (see results before in Figure 4-20d for comparison with the flat plate), this value is much closer to the stroke plane angle observed in nature of $\gamma = 60^\circ$, specially for the corrugated version.

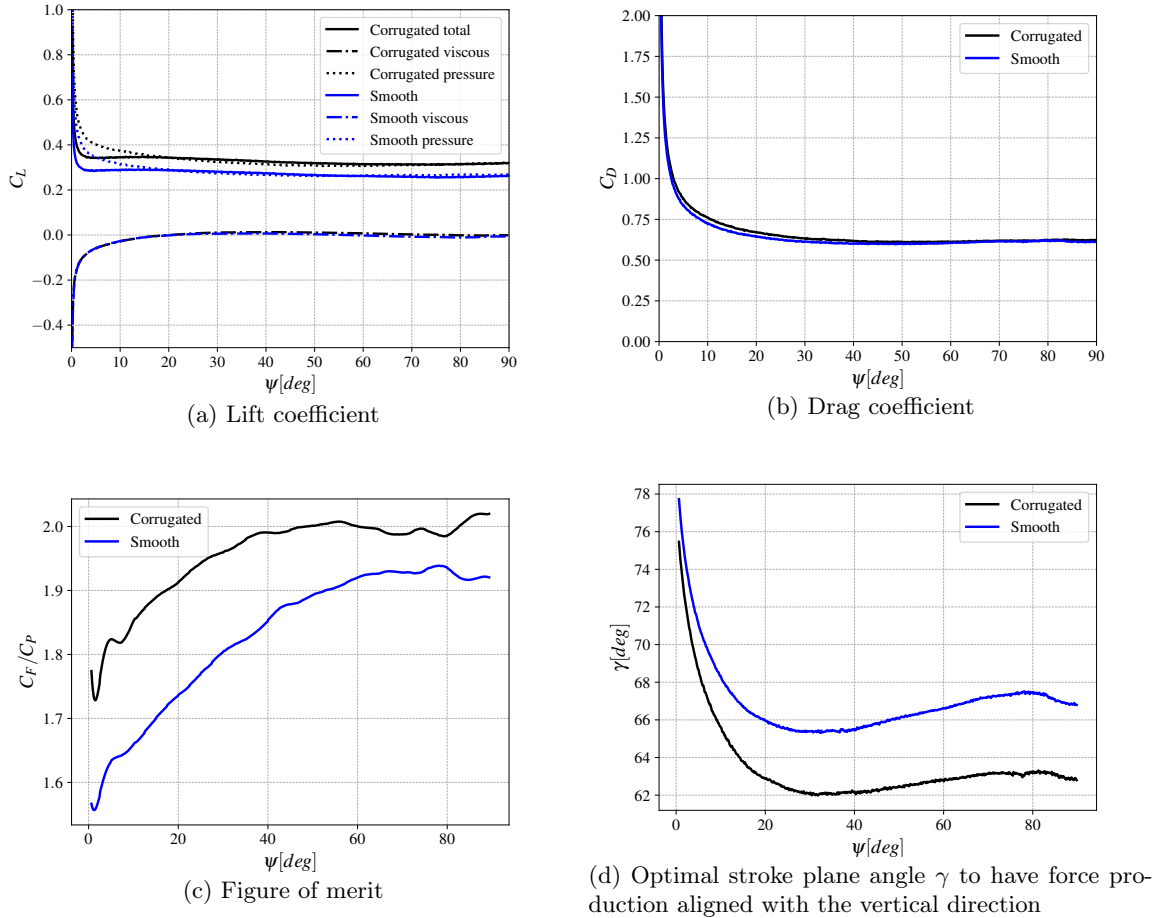


Figure 4-32: $\alpha = 70^\circ$ and $Re = 91.7$. Comparison of corrugated and smooth wing.

In Figure 4-33 the shear stress magnitude is shown for two spanwise slices in the corrugated

and smooth wings. See how there are small differences in the shear stress profile specially close to the wing boundary. However, in Figure 4-32a the lift was decomposed into its viscous and pressure components. See how due to the Reynolds number the pressure component dominates. Consequently, the shear stress magnitude differences are not responsible for the lift coefficient disparities that were observed. Therefore, as shown in Figure 4-32a the pressure component should be the one responsible for the change.

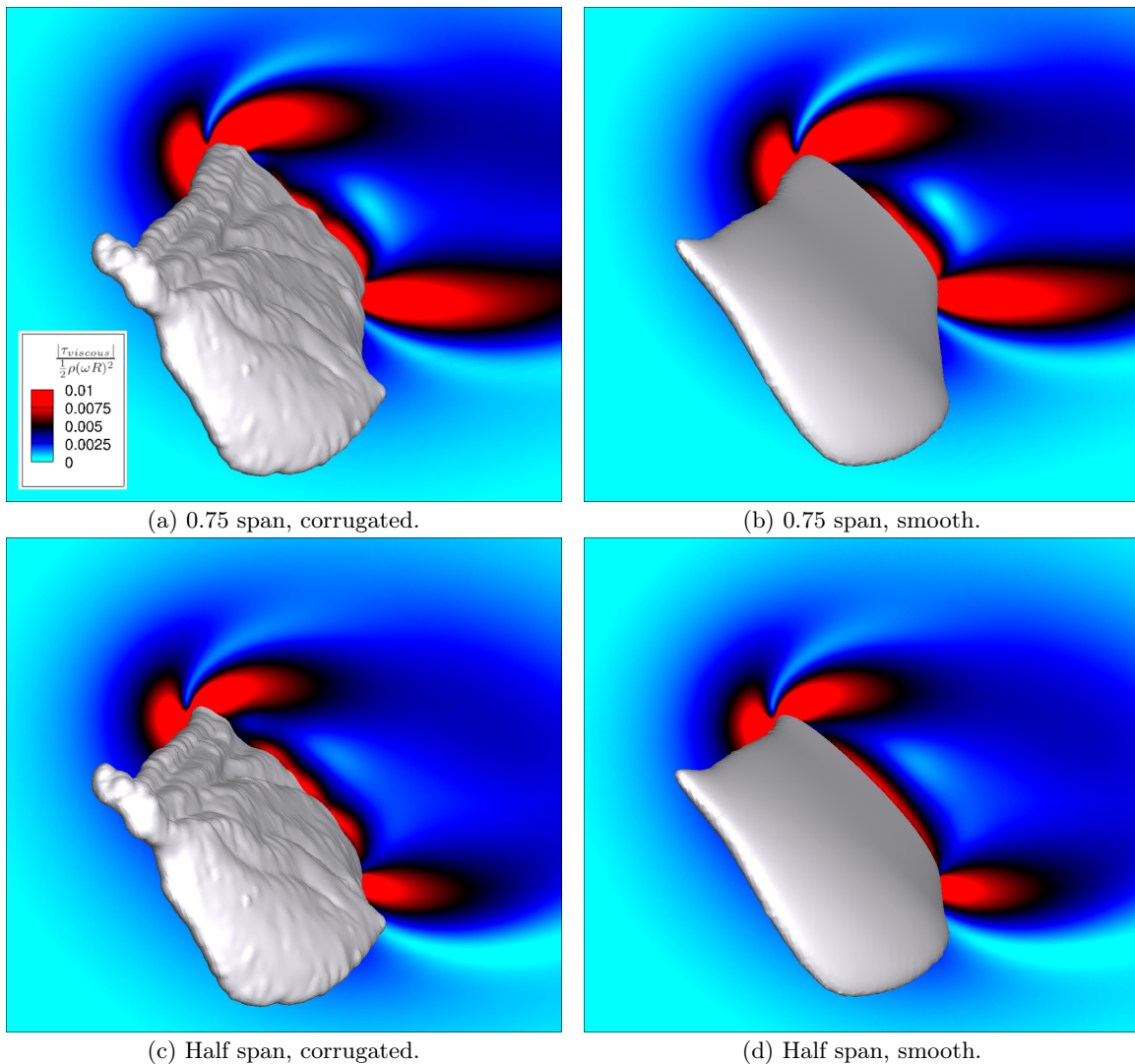


Figure 4-33: Shear stress magnitude (red high, blue low). $\alpha = 70^\circ$, $\psi = 40^\circ$ and $Re = 91.7$. Comparison of corrugated and smooth wing.

In Figure 4-34 a pressure slice is shown at half the span. Looking closely at the leading edge, it can be seen that a second high suction spot is generated only in the corrugated version. This occurs exactly in the corrugation channels, as it was clearly visualized in Figure 4-28 and Figure 4-30. The key is that the normal vector to the wing surface, exactly where the suction spots in the corrugation

channels are, is almost vertical. Therefore pressure suction generates solely lift and not drag in the corrugation channel as seen in Figure 4-32. Therefore, the increase in force production does not contribute to power requirements (lift orthogonal to flapping plane), and force production is more energetically efficient in the corrugated wing.

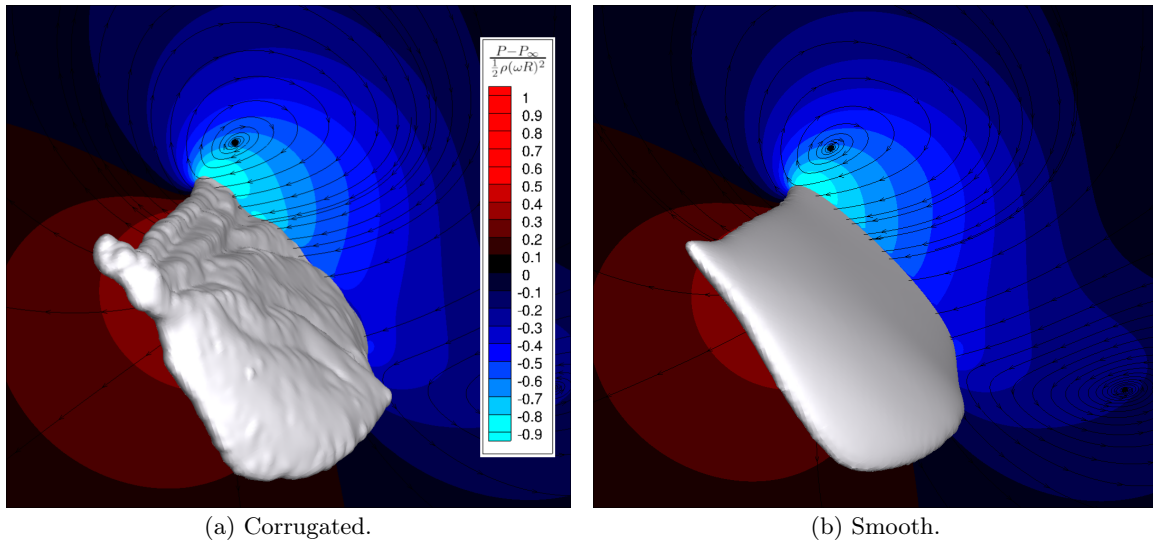


Figure 4-34: Pressure field contours (blue suction, red pressure). $\alpha = 70^\circ$, $\psi = 40^\circ$ and $Re = 91.7$. Comparison of corrugated and smooth wing. Slice at half span.

Chapter 5

Numerical analysis of wing-wing interaction effects

5.1 Numerical set up

5.1.1 Hovering

The kinematics are defined according to the 3-1-3 Euler intrinsic rotation defined in Figure 2-2, with the same axis convention as in the plot:

$$\gamma_F = \pi/3 \quad (5.1)$$

$$\gamma_H = \pi/3 \quad (5.2)$$

$$\psi_F = -\frac{7\pi}{36} \sin(2\pi ft) \quad (5.3)$$

$$\psi_H = -\frac{7\pi}{36} \sin(2\pi ft + \psi_0) \quad (5.4)$$

$$\theta_F = \frac{7\pi}{18} - \frac{5\pi}{9} \sin(2\pi ft) \quad (5.5)$$

$$\theta_H = \frac{7\pi}{18} - \frac{5\pi}{9} \sin(2\pi ft + \psi_0). \quad (5.6)$$

The subindex H and F refer to the hindwing and forewing respectively. γ is the stroke plane angle (first 3-axis rotation in 3-1-3 sequence), ψ the flapping angle (second 1-axis rotation in 3-1-3 sequence) and θ the feathering angle (third 3-axis rotation in 3-1-3 sequence). In Figure 2-2 the exact definition of each angle is given in more detail. The Cartesian axis used in the simulation and to analyze the results are shown in Figure 5-1 and the center of the Cartesian system is placed at the beginning of the dragonfly head, in the symmetry plane. This will be useful because the application

point of the resultant force will be defined based on the x coordinate starting from the head. The center of rotation from the hindwings non-dimensionalized with the body length (from head to tail) is $x_H/L = 2$ and $x_F/L = 1$ for the forewings.

The stroke plane has been defined according to the work done by Norberg [74]. The flapping trajectory uses a slightly larger amplitude than the one found by Norberg, to find a compromise with the large flapping amplitudes reported by Ruppell [96]. Finally, the feathering angle has been matched to the range of mid downstroke and mid upstroke angles of attack reported by Ruppell [96] during hovering. The phase between hindwings and forewings is going to be varied to inspect its effect.

The Reynolds number defined based on the tip velocity is defined as:

$$Re = \frac{2\pi \frac{7\pi}{36} R_H \bar{c}}{\nu} \quad (5.7)$$

$$\bar{c} = \frac{S_W^H}{2R_H}, \quad (5.8)$$

where S_W^H is the wet surface of the hindwing, R_H the distance from the rotation axis to the hindwing tip. In particular, for all the following simulations $Re = 85.25$. This is in the low end of Reynolds numbers for dragonflies, and would be the flow regime of a dragonfly like *Nannophya pygmaea*. Once again this range is selected to avoid transition. Remark that once the flapping non dimensional trajectory is given, there is no Strouhal number dependence with size or frequency scaling f , as explained in section 4.1.

Finally, wings and body geometry are taken from [137].

5.1.2 Forward-flight

In this flapping mode a slight change is going to be done in the initial pitch angle of the hindwing:

$$\gamma_F = \pi/3 \quad (5.9)$$

$$\gamma_H = \pi/3 \quad (5.10)$$

$$\psi_F = -\frac{7\pi}{36} \sin(2\pi ft) \quad (5.11)$$

$$\psi_H = -\frac{7\pi}{36} \sin(2\pi ft + \psi_0) \quad (5.12)$$

$$\theta_F = \frac{7\pi}{18} - \frac{5\pi}{9} \sin(2\pi ft) \quad (5.13)$$

$$\theta_H = \frac{11\pi}{18} - \frac{5\pi}{9} \sin(2\pi ft + \psi_0). \quad (5.14)$$

The phase angle is set to $\psi_0 = \pi$, counter-stroking. All the rest Reynolds number and geometric definition still apply. This apparent insignificant change will completely change the resultant forces

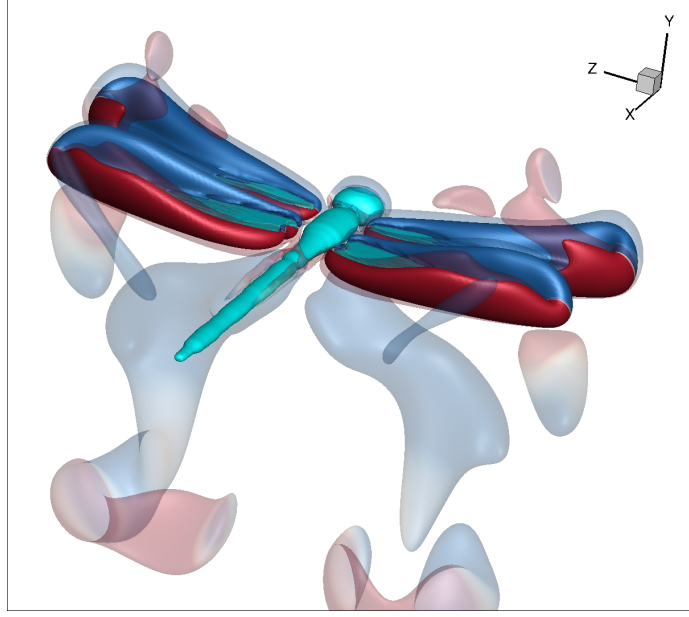


Figure 5-1: Q-criterion isocontours colored by z -vorticity component. Hovering $\psi_0 = 0^\circ$. End of fourth flapping cycle: $4.00 t/T$.

and flow fields. The aim of this is to show the versatility of dragonfly of adjusting their force production with the feathering angle. This is probably a much faster way of suddenly varying force production, as modifying the stroke plane would take much more time, and according to Ruppell [96] did not observe a significant variation of this parameter in the studied dragonflies.

5.2 Comparison between different flapping strokes

In Figure 5-2 a selection of two snapshots for each stroke is shown. All plots visualizing in detail the flapping strokes and the flow are included in Appendix B. Additionally, the detailed contribution of each body component across the four flapping cycles is shown in Appendix C. Here for brevity only numerical quantities of the flapping cycles will be analyzed, and when required the reader will be referred to Appendix B or Appendix C for a better understanding of the flow dynamics.

To analyze the flapping strokes the following non dimensional coefficients are defined:

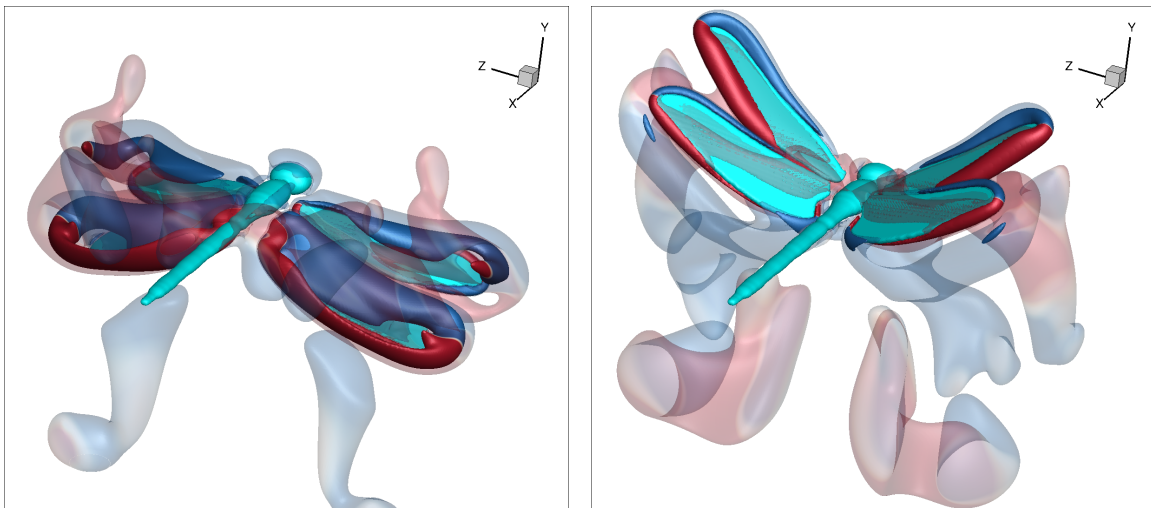
$$C_L = \frac{F_y}{\frac{1}{2}\rho(2\pi f R_F)^2 S_T} \quad (5.15)$$

$$C_D = \frac{F_x}{\frac{1}{2}\rho(2\pi f R_F)^2 S_T} \quad (5.16)$$

$$C_P = \frac{P}{\frac{1}{2}\rho(2\pi f R_F)^3 S_T} \quad (5.17)$$

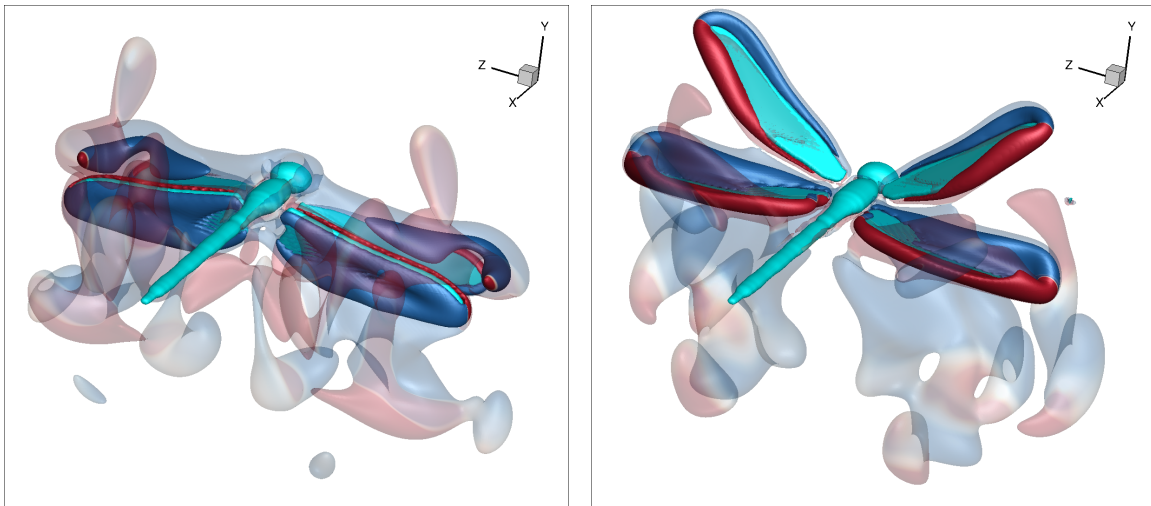
$$S_T = S_W^H + S_W^F, \quad (5.18)$$

where the total surface of the four wings S_T is computed with the wet surface of one hindwing and one forewing. R_F is the distance from the gyration axis to the forewing tip. The lift coefficient C_L is defined to show the non-dimensional vertical force, $y - axis$ in Figure 5-1. The drag refers to the force pointing in the $x - axis$ direction.



(a) 3.20 t/T, hovering $\psi_0 = 0^\circ$

(b) 3.80 t/T, hovering $\psi_0 = 0^\circ$



(c) 3.20 t/T, hovering $\psi_0 = 90^\circ$

(d) 3.80 t/T, hovering $\psi_0 = 90^\circ$

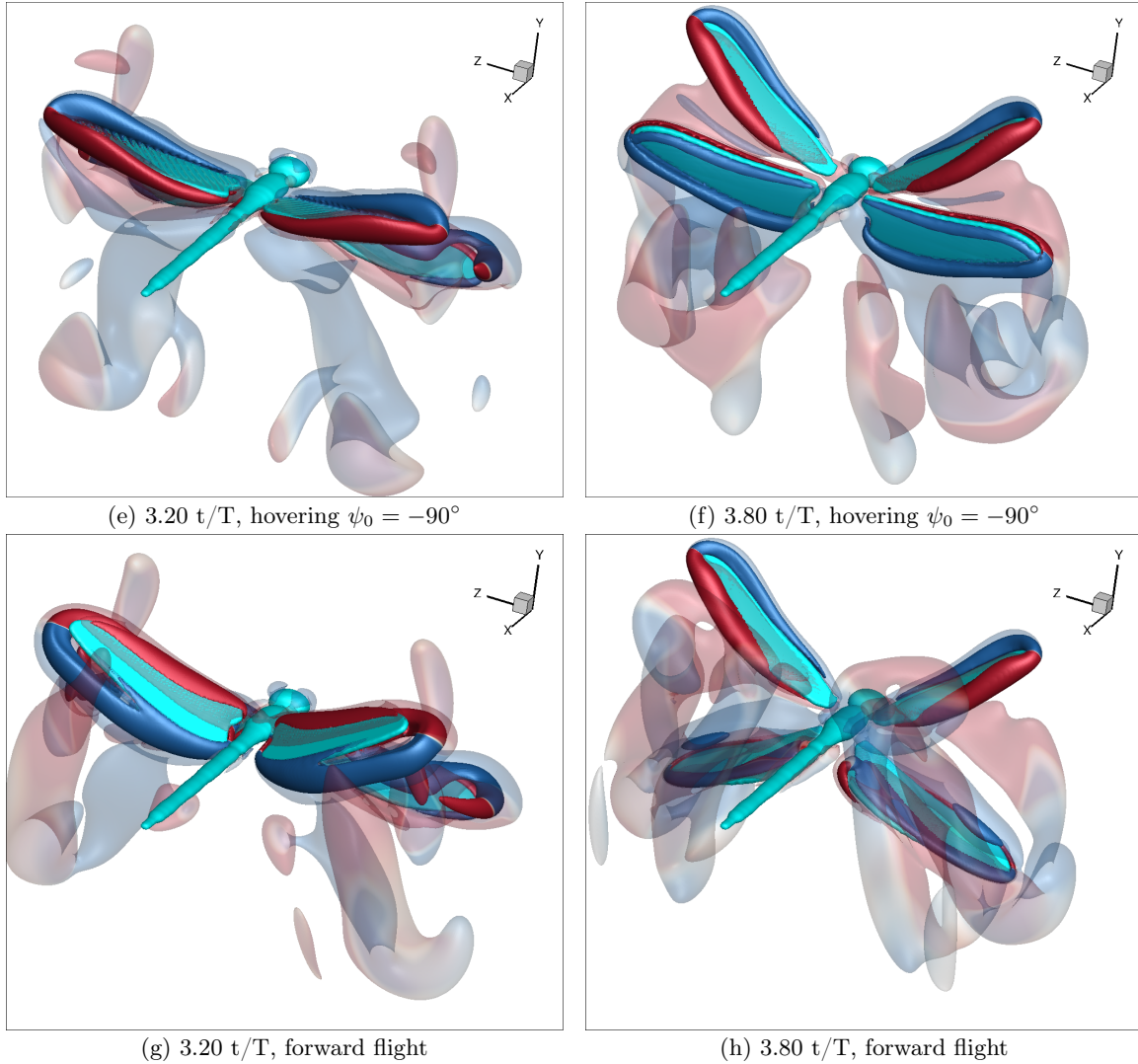


Figure 5-2: Q-criterion, colored by z-vorticity component.

To compare the different flapping strokes the mean quantities in Table 5.1 are shown. Also comment on the fact that the mean quantities are computed based on the fourth flapping cycle. As seen in Figure C-1, Figure C-2, Figure C-3 and Figure C-4 the quantities are well converged for the fourth flapping cycle, so this values can be considered as the steady state flapping values of the dragonfly. First, in Table 5.1 observe how phased-stroking $\psi_0 = 0^\circ$ is the stroke with higher lift production. This agrees with the observations from [115] and [124]: dragonflies typically use phased stroking for rapid acceleration maneuvers. Not only is the stroke with higher force production on average, but also has a huge acceleration production at the beginning of the stroke, see the lift comparison of all lift strokes in Figure 5-4. This explains the position of dragonfly wings at rest. They put their wings as shown in Figure 5-3 (exactly the kinematic position of $t/T = 3$ in Figure 5-4 and $\psi_0 = 0^\circ$), and start to flap in phase with both wings. This gives them a maximum acceleration

in the initial moments of their fly, which will be crucial to rapidly approach their prey from rest. However, this huge acceleration comes at a cost: power requirements. As shown in Table 5.1 this stroke is the most expensive in terms of power requirements on average. For this reason, unless desired in extreme maneuvers dragonflies have been observed to modify the phase for a more energy efficient flapping [74] [96]. Additionally, it should be remarked that modifying the phase between wings can also result in a much more stable hovering. Looking at the lift root mean square, it can be seen that for example with $\psi = -90^\circ$ the vertical oscillations of the dragonfly during hovering would decrease significantly. This more uniform lift generation for $\psi_0 = -90^\circ$ can be clearly appreciated in Figure 5-4.

Another important concept is the drag coefficient. In all defined strokes it can be seen that the vertical force dominates, but there is still non-zero contribution on average in the forward direction. That means, these strokes would not be pure hovering strokes, dragonflies would be moving slightly forwards. A bit more tuning would be required to modify the kinematics to maintain pure hovering. Additionally, it is interesting to observe that the modification done to the hindwing pitch angle, has completely changed the so called forward stroke. Now the lift coefficient has been decreased significantly, and the negative drag increased in magnitude more than two times. In Figure C-2d it can be clearly seen that indeed the new increase of drag magnitude is due to the modified hindwing, while the forewing is still responsible for providing a minimum lift amount to maintain flight level. This means with this tiny adjustment the dragonfly would stop a potential upwards maneuver to move forwards really fast. This was achieved with a relatively small variation of the pitch angle, and exemplifies the versatility that offers the adjustment of the feathering angle with four wings.



Figure 5-3: Norfolk-hawker dragonfly at rest [1].

Next, the pitching moment will be inspected, which is going to be expressed through the x_F position of the equivalent points where the resultant force should be applied to provide that pitching

moment. The value x_F is non-dimensionalized in terms of the dragonfly body length (from head to tail) L . In Figure 5-7 this mentioned value is represented for all strokes. It can be seen that it varies across the flapping strokes, but on average in Table 5.1, its value is relatively small. For hovering, it is almost the same in all cases, and the application force point would be just in the dragonfly abdomen, quite close to where they usually have their center of mass [18]. That means that in the hovering strokes the dragonfly as expected would have a very small pitching moment. However, for the forward stroke, the point of force application shifts to a point in front of the head, away from the mass center, which would create a positive pitching moment, following the sign convention used in Figure 2-1. Consequently, in the forward flapping, the dragonfly would move forwards and would also increase the pitch angle.

Coefficient	<i>hover</i> $\psi_0 = 90^\circ$	<i>hover</i> $\psi_0 = -90^\circ$	<i>hover</i> $\psi_0 = 0^\circ$	<i>forward</i>
$\overline{C_L}$	0.2007	0.2158	0.2270	0.0576
$\overline{C_L}$, % 2 forewings	33.41	31.19	34.31	0.1531
$\overline{C_L}$, % 2 hindwings	67.45	69.78	66.87	129.3
$\overline{C_L}$, % body	-0.8710	-0.9746	-1.181	-33.77
$rms(C_L)$	0.5140	0.3931	0.6473	0.1531
$\overline{C_D}$	-0.0810	-0.0809	-0.0846	-0.1567
$\overline{C_D}$, % 2 forewings	25.03	32.49	57.04	10.49
$\overline{C_D}$, % 2 hindwings	75.34	68.25	44.60	89.64
$\overline{C_D}$, % body	- 0.3712	-0.7480	-1.646	-0.1318
$rms(C_D)$	0.3124	0.1993	0.3055	0.2974
$\overline{C_P}$	0.2261	0.2122	0.2427	0.2120
$\overline{C_P}$, % 2 forewings	42.46	45.73	43.90	46.20
$\overline{C_P}$, % 2 hindwings	57.54	54.27	56.10	53.80
$\overline{C_P}$, % body	0.000	0.000	0.000	0.000
$rms(C_P)$	0.2750	0.2557	0.3066	0.2773
$\frac{x_F}{L}$	0.0399	0.0430	0.0427	-0.0321

Table 5.1: Statistics of each dragonfly body component and stroke type in the 4th flapping cycle.

Next, the individual effects of the hindwings on the forewings Figure 5-8 and of the forewings on the hindwings Figure 5-9 are going to be inspected for the different strokes. In particular, the goal is going to be to understand what types of flow interactions are desired between hindwings and forewings. First, looking at Table 5.1 it can be seen that even though introducing phase difference between hindwings and forewings is beneficial, for $\psi_0 = -90^\circ$ more lift is achieved at a lower power requirement, compared to $\psi_0 = 90^\circ$. To understand why this happened, the reader should look at the vertical velocity slices from Figure B-9c and Figure B-9d, the most efficient phasing stroke

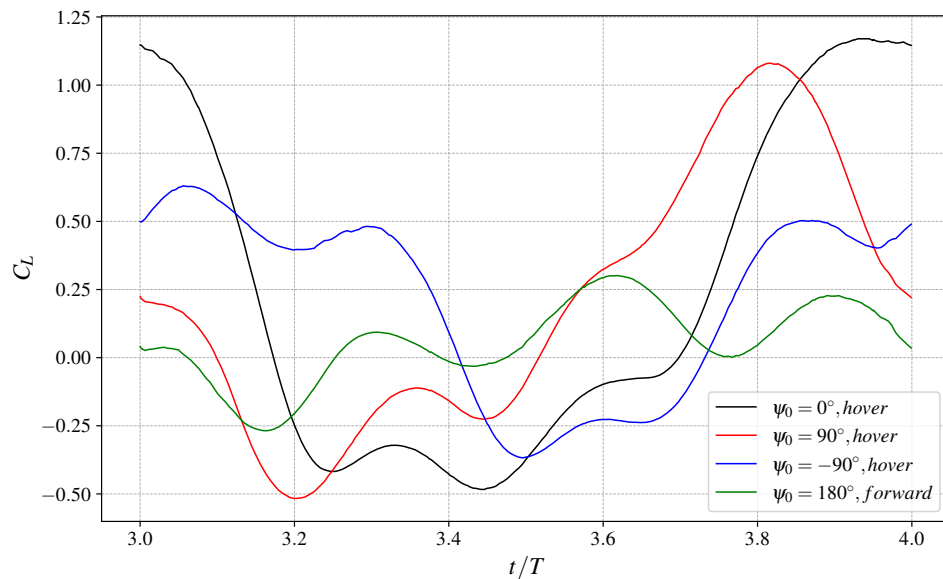


Figure 5-4: Lift coefficients of all strokes. 4th flapping cycle.

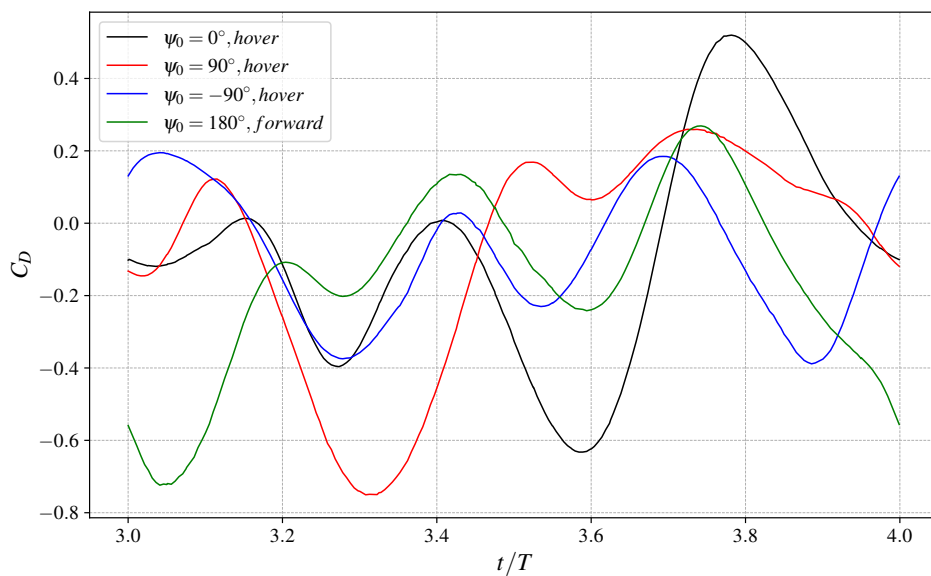


Figure 5-5: Drag coefficients of all strokes. 4th flapping cycle.

$\psi_0 = -90^\circ$. It can be seen that in this optimal phasing the hindwing is following the wake of the forewing during the upstroke. Upstroke should be considered as something in general negative for hovering that dragonflies want to minimize. The reason is basically that they are consuming energy by moving the wings upwards, but they are not able to convert this energy into useful lift. However,

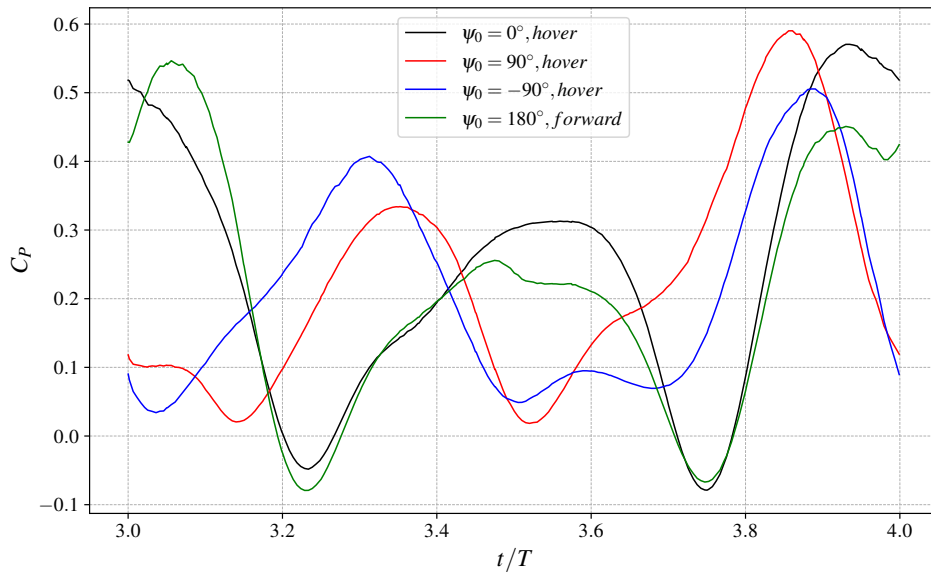


Figure 5-6: Power coefficients of all strokes. 4th flapping cycle.

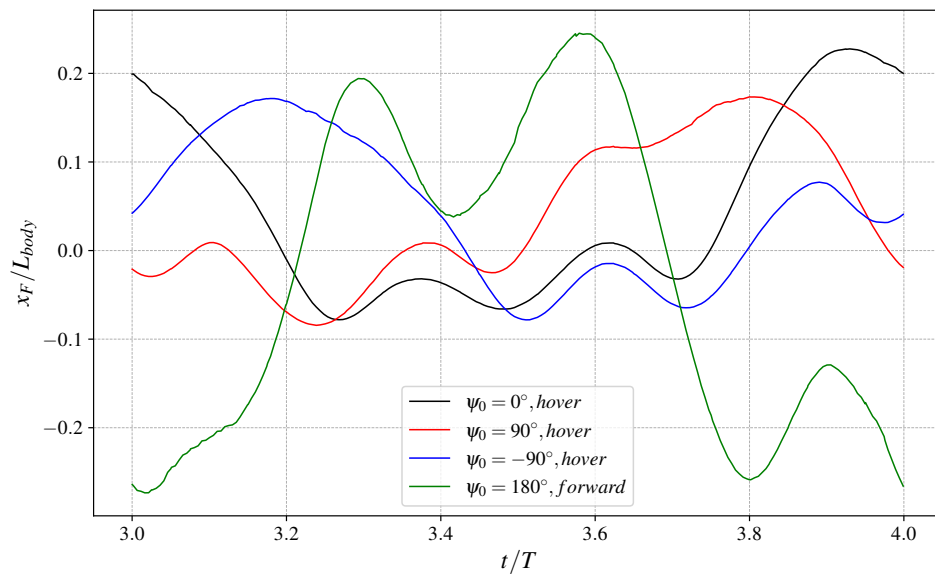


Figure 5-7: x-coordinate of the point of resultant force application, non-dimensionalized with the length of the dragonfly wing body. 4th flapping cycle.

they need to have an upstroke in order to later have a downstroke. Therefore, if both wings require an upstroke, then it is optimal if just one of them leads (the forewing in Figure B-9c and Figure B-9d) a gets all the power consumption, while the other one just follows the wake and makes use of the energy waste done by its wing pair (the hindwing in Figure B-9c and Figure B-9d). Observe,

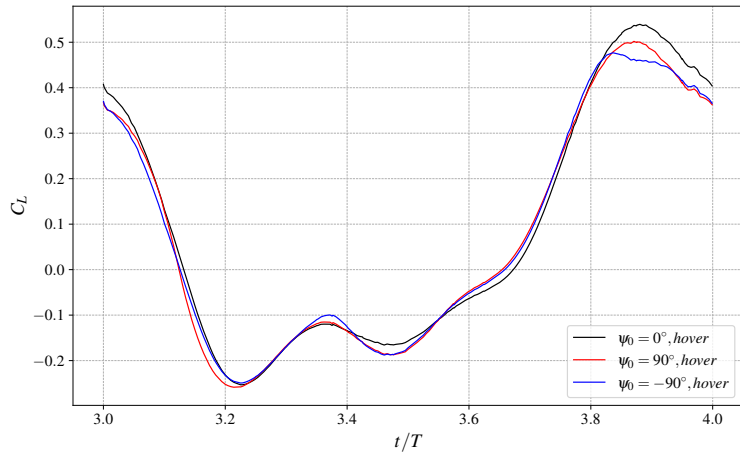
how this is translated into power savings for the hindwing during the upstroke phase, $t/T = 3.4$ to $t/T = 3.7$ for $\psi_0 = -90^\circ$ in Figure 5-9c. On the other, hand the forewing Figure 5-8c still has similar power consumptions than the one with $\psi_0 = 90^\circ$ because it had to lead. However, overall the stroke is more efficient.

Finally, comment on another important issue related to energy harvesting during the upstroke. In Figure B-9c and Figure B-9d it was seen that the hindwing followed the wake of the forewing during the upstroke. This added the upwash of the two upstrokes, creating a bigger upwash effect, see Figure B-9d. However, in Figure B-9e the hindwing pronates and recovers part of this upwash pushing it once again downwards. That is, the hindwing is converting the energy wasted during the synchronized upstrokes of both wings that did not contribute to lift, and is pushing it downwards, generating therefore a lift gain that can be observed in Figure 5-9a for $\psi_0 = -90^\circ$, between the pronation and start of the downstroke $t/T = 3.8$ and $t/T = 4$. Also note that this increase in lift does increase power consumption Figure 5-9c, but in a smaller way compared to the lift gain.

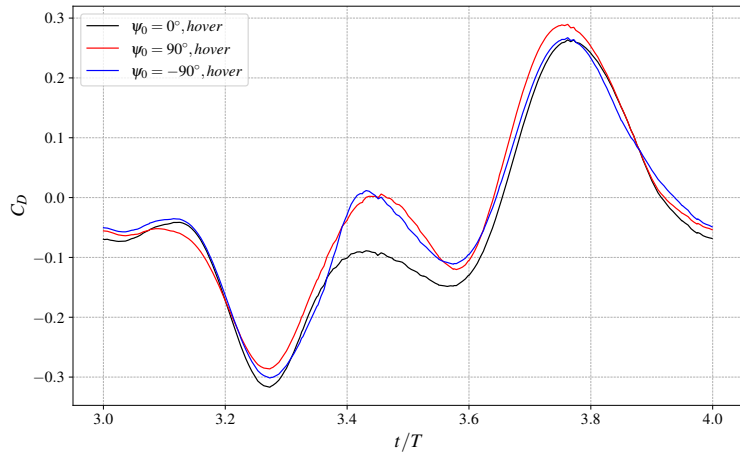
Therefore, two important lesson can be learnt from wing interaction effects:

1. Wake capturing during the upstroke can prevent one of the two wings of also wasting a lot of useless energy (in terms of no lift production), decreasing this way the follower-wing power consumption during the upstroke.
2. During the upstroke it is inevitable to generate an upwash jet, which provides negative lift. This is of course negative. If pronation and the start of the downstroke is tuned appropriately, this upwash can be reconverted into downwash, generating extra lift at smaller additional power requirement.

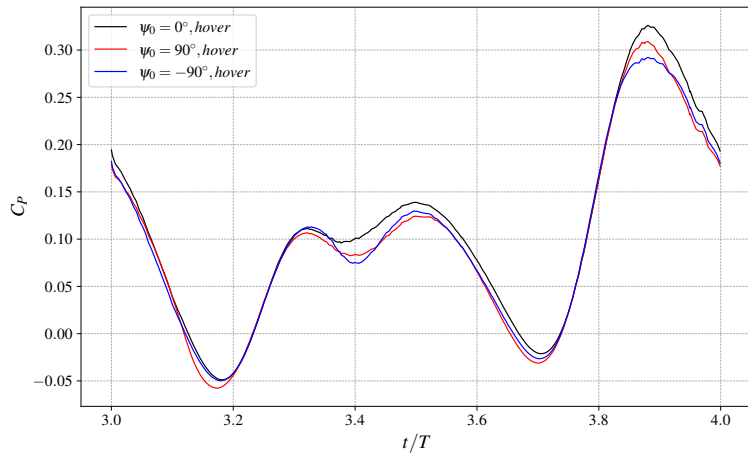
Moreover, it was seen that phasing can produce a more stable hovering, and that as seen in nature, phased stroking produces the maximum force, but at a higher power cost.



(a) Lift coefficient

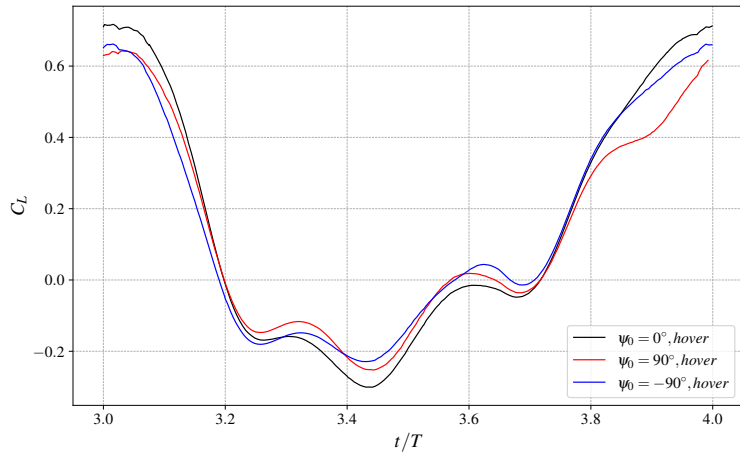


(b) Drag coefficient

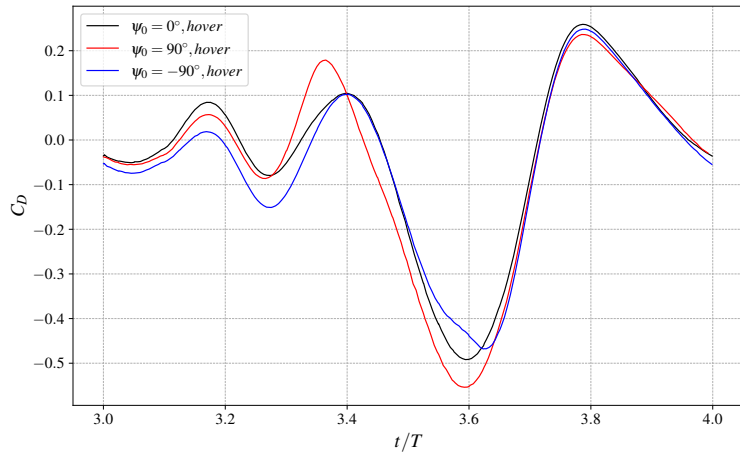


(c) Power coefficient

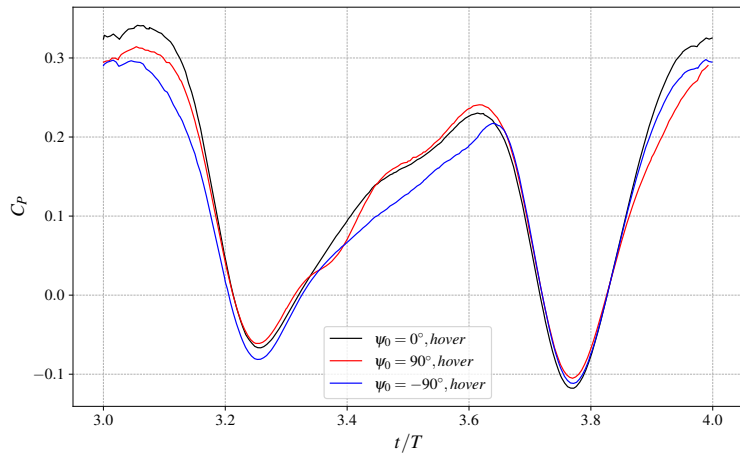
Figure 5-8: 2 forewings results. Hindwing effects on the forewings.



(a) Lift coefficient



(b) Drag coefficient



(c) Power coefficient

Figure 5-9: 2 hindwings results. Forewings effects on the hindwings.

5.3 Self-induced-dipole vorticity removal

When dragonflies flap continuously in a similar place in space, vorticity accumulation can create a chaotic flow that makes flying less energy efficient [109], see for example Figure 2-44. This is specially true for higher Reynolds numbers, where diffusion and dissipation mechanisms are almost negligible to get rid of the created vorticity generated by the wings.

To avoid this, Wang [129] hypothesized a dipole self induction as a mechanism of vortex shedding. In the literature review, Figure 2-45 the mentioned mechanism is shown. This was done in 2 dimensions and with a simple flat plate, so it was still to be proved that this could be extended for a real insect flapping.

Interestingly, this mechanism has been observed in the 3D dragonfly flapping in hovering. For example, look at Figure B-1 to see the downwards ejection of vortex structures. Nevertheless, Wang's mechanism cannot be easily identified in these plots. For this reason, only vorticity slices are shown in Figure 5-10. Looking now at the vorticity slices, Wang's dipole-self-induction mechanism is evident. Each vortex in the dipole induces a velocity component to the other vortex downwards and away from the dragonfly. Also, in case the reader did not noticed, the temporal sequence of the plots is shifted to show an entire cycle of the self-induced-dipole mechanism, that is Figure 5-10a starts with $3.60t/T$ and ends with $3.40t/T$. However, the evolution of vorticity looks like time just goes forwards. The reason for this is the periodicity of the cycle that reflects that in the fourth cycle statistics are well converged.

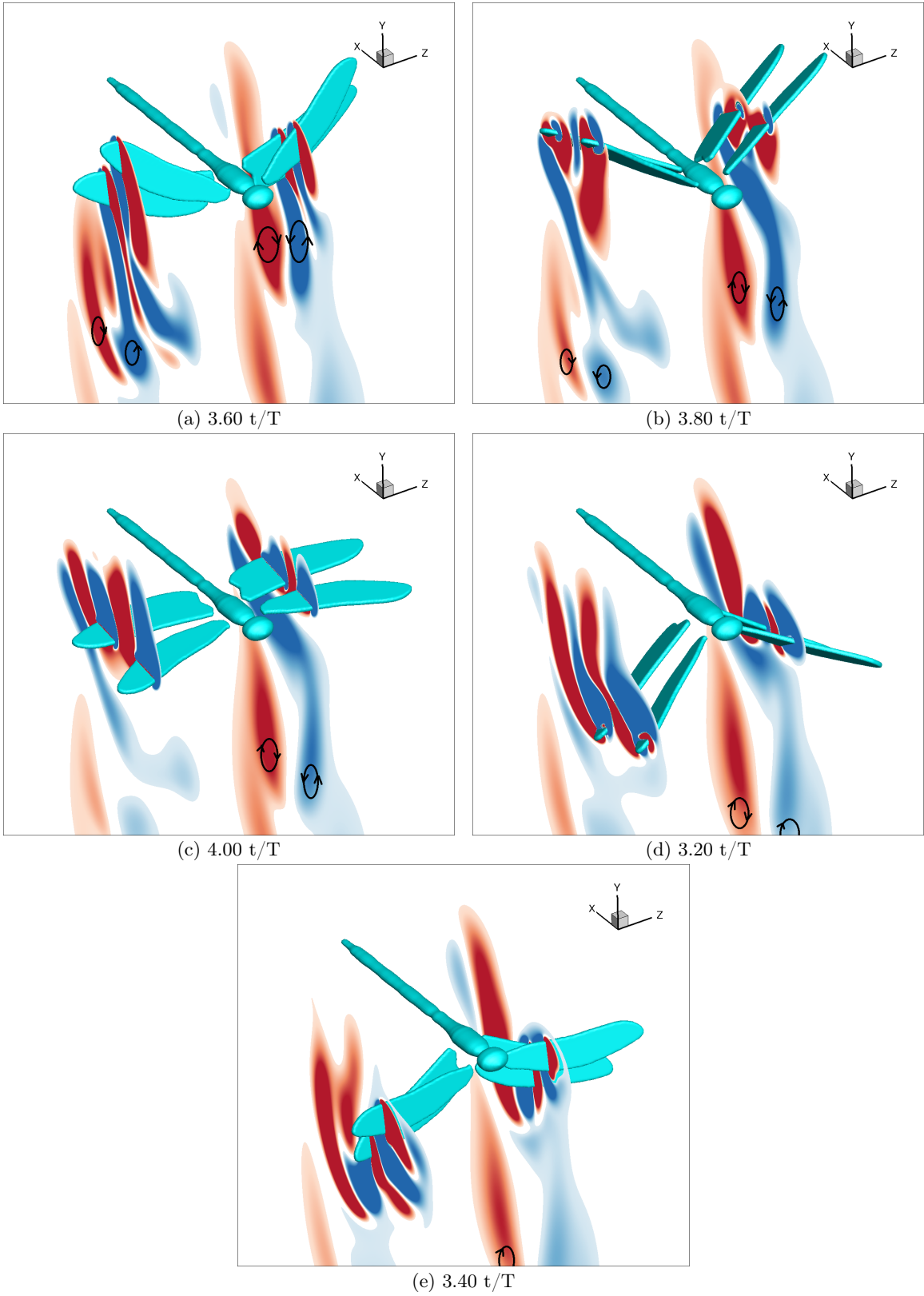


Figure 5-10: Self induction dipole mechanism in a dragonfly with $\psi_0 = 0^\circ$, phased-stroking. Slices with z-vorticity.

Chapter 6

Conclusions

In the present document dragonfly aerodynamics have been inspected both numerically and experimentally. The goal of the thesis has been to identify aerodynamic mechanisms that allow dragonflies to have such an excellent flying performance. In the future some of these findings could be useful to improve aerodynamic efficiency for low Reynolds number vehicles, such as Micro Air Vehicles.

First, the computational methodology was developed to answer the challenges posed in the literature review chapter 2. A multibody solver was developed in Fortran to solve N-body three-dimensional body problems with any given constraints between each body, Appendix A. For this, Euler parameters were used to avoid the singularities of the Euler angles. A matrix was created with the dynamics of each body and its constraints, and afterwards it was inverted with LU decomposition to obtain the Euler parameter accelerations of each body. The system was integrated in time with an implicit Newmark algorithm. Additionally, a novel correction was added to analytically impose constraints after time integration and avoid constraints-drifts for large time integrations. The solver was extensively validated through numerous test cases (subsection 3.1.1), first in an uncoupled way, and second coupled to the fluid solver INCA. Thanks to the usage of high performance computing the computational methodology provided a useful insight into most of the physical concepts that were set as relevant in the literature review. The main limitation of numerical simulations was the impossibility of exploring the higher Reynolds number regime of bigger dragonflies. After transition the flow structures became extremely small and required a very high amount of computational resources to be resolved with DNS. It would be interesting to study in the future the structure of the leading edge vortex in fully turbulent regimes, as this could provide insights into useful mechanisms for larger size vehicles.

Second, the experimental methodology was designed to represent meaningful physics that complement and improve the conclusions derived from numerical simulations. An experiment was designed during a stay at California Institute of Technology (section 3.2): a servo-motor connected to a flap-

ping flat plate immersed in a water tank with PIV measurements. This allowed to obtain velocity vector fields projected in the laser plane. This was later used to compare and further assess the developed multibody-fluid solver. A reasonable agreement was found in the results. The leading edge and trailing edge vortices were identified, and the velocity magnitude at the wake and at slices perpendicular to the flat plate agreed well between the experiment and simulation. However, due to the transition of the leading edge vortex, this led to a chaotic flow and exact correlation could not be achieved. Nevertheless, both experiment and simulation detected the same flow instabilities and resembled the flow structure accurately in the regions where the flow was more stable: close to the flat plate root and in the early flapping stages. The main limitation of the experiment was the inability to measure forces in the low Reynolds numbers where it was feasible to do direct numerical simulation. The wings had to flap very fast in the experiment in order to measure force signals that were not obscured by sensors noise. In the future it would be interesting to improve the experimental set up by changing water by a more viscous flow such as mineral oil. This way it would still be possible to flap faster and measure forces while maintaining a lower Reynolds number that is more meaningful for dragonfly aerodynamics. On the other hand, planar PIV also had a clear limitation as it is only allowed to access two dimensions of the flow. This was mitigated by conducting experiments at several slices to inspect the 3D structure of the leading edge vortex. It would be interesting to use for example stereoscopic PIV to get a better idea of the whole flow field and compare it with the numerical simulations.

One of the more relevant findings regarding **Leading Edge Vortex** stability was the existence of the spanwise advection mechanism at the wake, commonly justified in the literature by the Coriolis spanwise blowing. However, the novelty of the spanwise blowing in this case, is that it was redirected to the trailing edge. This justifies the lack of spanwise blowing at the vortex core that surprised the authors of a well-known paper published in Nature [13]. This phenomenon occurred due to the presence of the tip-vortex that generated a strong opposite jet that collided with the spanwise blowing, and redirected it downwards. In later numerical simulations this was further explored with detailed visualizations of the flow, section 4.3. It could be clearly seen the two opposing jets colliding at around 3/4 of the span, one caused by the Coriolis spanwise blowing and root vortex, and the other caused by the tip vortex. This generated a "lift-up" mechanism that occurred both in the inspected flat plate, and in an actual corrugated dragonfly wing geometry (section 4.5). The result of this "lift-up" mechanism was the sudden growth of the leading edge vortex.

Additionally, with numerical simulations special emphasis was placed on exploring detailed flow dynamics and different flow regimes that could not be achieved with the experiment and affected **Leading Edge Vortex** stability. Reynolds number was varied (section 4.2) and it was seen that around Reynolds 300, the tip vortex transitioned via a Kelvin-Helmholtz type instability. This chaotic regime was the one in which the experiment was done, and for this reason exact correlation

could not be expected. The instability at the tip destabilized all the leading edge vortex structure. Moreover, low Reynolds numbers mechanisms of vorticity removal via diffusion; and high Reynolds numbers mechanisms via vortex shedding due to the Kelvin-Helmholtz instability were identified. These mechanisms were able to control the growth of the leading edge vortex, and therefore avoided its sudden detachment and deep dynamics stall. The investigation of Reynolds number dependence of the **Leading Edge Vortex** stability was quite insightful to determine typical transition parameters, as the **Leading Edge Vortex** changes dramatically after transition. Previous literature has overlooked this issue because most simulations have been done in 2D where no vortex stretching exists and transition mechanisms could not be inspected.

Moreover, the effects of the **Leading Edge Vortex** in relevant quantities such as force production and energy requirements were analyzed for a flat plate at different Reynolds numbers section 4.2. First, it was shown that total force production increased with circulation growth of the leading edge vortex, as expected due to the Kutta–Joukowski theorem. Moreover, circulation grew with the Reynolds number (and lift consequently), because vorticity diffusion decreased with Reynolds number, and therefore low Reynolds number mechanisms were not able to remove vorticity fast enough to control vortex growth. Nevertheless, when transition kicked in vortex shedding was the mechanism responsible for decreasing circulation and therefore controlling lift growth for higher Reynolds number. However, in the range of Reynolds number inspected, force production always increased with Reynolds number. This might seem to indicate that natural fliers should then tend to fly at higher Reynolds number. On the contrary, this is not so clear, because even though total force production increased, when the leading edge vortex became unstable the ratio of total force production to power requirements decreased. This quantity is of more interest to animals as energy expenditure is limited and they desire to accomplish the maximum possible force with the minimum possible energy consumption. In summary, findings seem to indicate that for the studied flat plate, flying at the highest possible Reynolds numbers before transition is the most energy efficient alternative.

Next, angle of attack effect on the **Leading Edge Vortex** was studied. It was seen that hovering is energetically expensive due to the high lift coefficient that is required. This agreed well with the observation made in the literature review: dragonflies tend to avoid hovering for more energetically efficient regimes. Furthermore, only lift coefficient is typically considered in the force budget, however, in dragonflies flapping it was illustrated that most of the force production is achieved via drag. It was shown that dragonflies are able to use **Drag as Vertical Force** thanks to adjustments in the stroke plane. In fact, it was proven that for the studied flat plate and actual corrugated dragonfly wings, they are able to orient the total force production almost completely vertically, given the dragonfly kinematics that have been observed in nature. This was one of the main unknowns of the first authors that tried to unveil dragonfly aerodynamics, as without drag contribution it is not possible to justify the force coefficients that are observed in nature.

Furthermore, **Corrugation** effects were inspected section 4.5. So far it was well known in the literature that corrugation effects had a positive effect in providing the right stiffness to the dragonfly wings, while maintaining a light structure. However, up to the author's knowledge, there have not been actual aerodynamic benefits found with an actual corrugated wing in dynamic flapping. Nevertheless, it was found that for Reynolds numbers in the low end of dragonfly species, corrugation channels advect spanwise flow and vorticity and create an additional suction, that was not found in the equivalent smooth wing. Due to the corrugation channels geometry, this suction was oriented solely in the vertical direction, and therefore only contributed to lift. As lift is orthogonal to the flapping trajectory, this did not increase power requirements. Consequently, it was found that for an actual dragonfly wing corrugation increases lift at no energy cost, and therefore improves flapping efficiency. Nevertheless, this was only identified for one Reynolds number, which is in the low range of dragonflies Reynolds numbers. Further studies should be done to see if this can be extended for higher Reynolds numbers and other insect wing. If different species wings show this benefit, a general pattern of corrugation could be extracted that might be extensible to many different type of vehicles.

Finally, all the *building blocks* that were identified in the literature review were placed together into the final numerical study of a whole dragonfly section 4.1. Several strokes were inspected to unveil the intricacies of wings interaction and **Wake Capture**. Remark that the study was also done for relatively low Reynolds numbers to assure stability of the leading edge vortex and guarantee DNS resolution at a reasonable cost. It was found that phased stroking is justifiably the observed acceleration stroke used by dragonflies: it provides the maximum force production. However, it also demands more power requirements, so for this reason dragonflies introduce phase between their forewings and hindwings, to achieve more energy efficient flapping. Additionally, phase was found to accomplish a more stable hovering, as it provided a more uniform lift distribution across the flapping cycle. On the other hand, feathering angle was discovered to be a powerful strategy to suddenly change force production and its orientation. Furthermore, two **Wake Capture** strategies to introduce phasing between wings in an efficient way were identified: energy harvesting of the follower-wing from the leading-wing wake during the upstroke, and upwash conversion into downwash during the pronation and start of the downstroke. To conclude, the dipole-self-induction mechanism that was characterized in 2 dimensions by Wang [129] was found to apply for an actual dragonfly hovering stroke. This was the first time this hypothesis was tested with an actual 3D dragonfly with realistic kinematics. Thanks to this mechanism dragonflies are able to remove vorticity in high Reynolds numbers regimes, and therefore still maintain an efficient stroke in a relatively clean flow.

Appendix A

Multibody solver

The multibody solver used to solve the solid dynamics and couplings between all the parts of the dragonfly (4 wings and 1 body) is presented in this chapter. This solver has been implemented in Fortran and coupled to TU Delft research code INCA. The solver has been developed for a generic problem of N bodies, with different constraints between them. Forces at every timestep on every solid can be applied externally. In particular, for the dragonfly problem, external forces on each body element are determined by INCA fluid solver.

The structure of the chapter is the following: first, the mathematical formulation of the dynamic problem is formulated in section A.1; second, verification cases of the multibody solver are discussed in section A.2. All verification cases in this chapter are of the multibody solver without being coupled to INCA fluid solver. Fluid coupling will be discussed in next chapter, chapter 3.

A.1 Theoretical formulation

A.1.1 Kinematic equations

All the equations of motion are going to be formulated considering a Cartesian inertial system \mathbf{X}_0 of reference at $\mathbf{r}^0 = \mathbf{0}$. Additionally, a number of solid bodies N is going to be defined, so that the position of the center of mass of each rigid body in the Cartesian inertial system of reference \mathbf{X}_0 is \mathbf{r}_0^i , $i = 1, \dots, N$. Finally, N systems of reference attached to each body are defined: \mathbf{X}_j , $j = 1, \dots, N$. Based on these newly defined body systems of reference, \mathbf{X}_j , the position of each body can be expressed in several systems of coordinates: \mathbf{r}_j^i , $i = 1, \dots, N$; $j = 0, 1, \dots, N$. A sketch of this notation can be observed in Figure A-1.

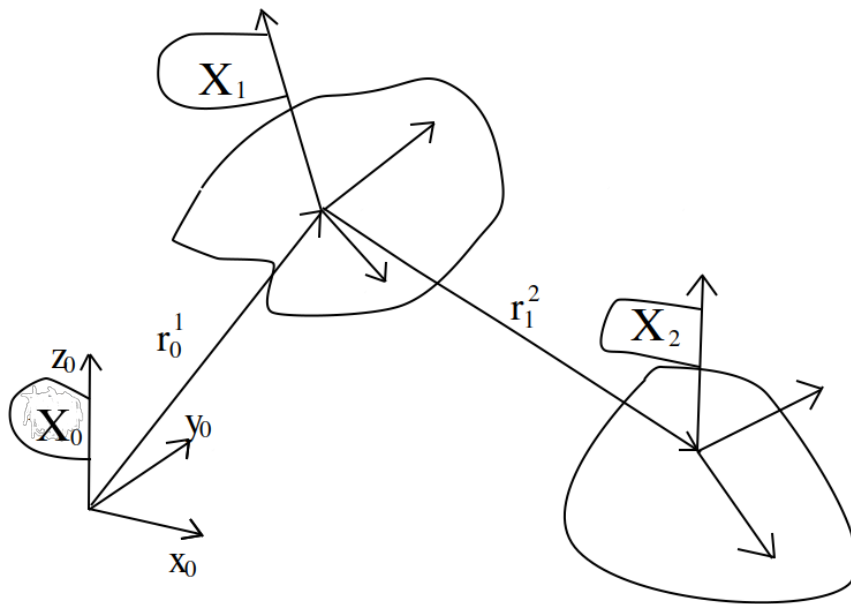


Figure A-1: Sketch of the notation used in the different reference systems and position of each body.

Next, the orientation of each reference system \mathbf{X}_j has to be defined with respect to the inertial reference system \mathbf{X}_0 . For this, the Euler Angles are used. In particular, the 3-1-3 Euler rotation is chosen, see Figure A-2. The first rotation is done around the z axis, precession ψ ; the second around the x axis, nutation θ ; and finally a third rotation again around the z axis, intrinsic rotation ϕ .

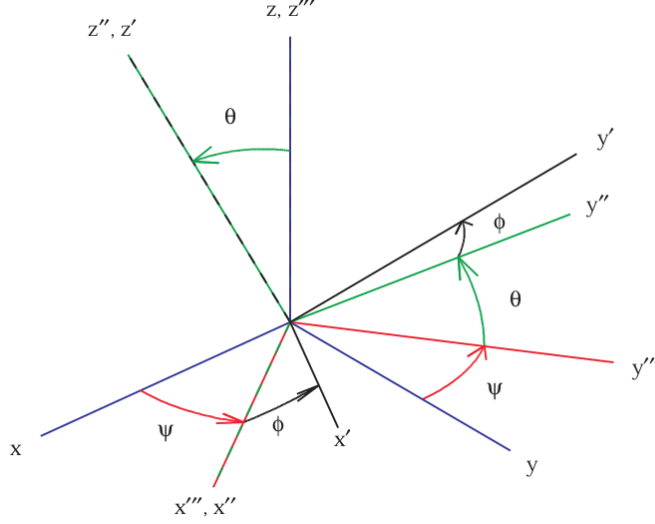


Figure A-2: (3-1-3) rotation sequence with Euler angles.

[37]

Based on this rotation system, a rotation matrix \mathbf{A}_k can be defined that relates the position of any body in different reference systems \mathbf{X}_j . In particular, we are interested in the relation between the inertial coordinates of two generic bodies i and k ($i \neq k$) and their coordinates in body coordinates. This is going to be useful when applying constraints between bodies i and k :

$$\mathbf{r}_0^i = \mathbf{r}_0^k + \mathbf{A}_k \mathbf{r}_k^i, \quad (\text{A.1})$$

where \mathbf{A}_k would be the rotation matrix between systems of reference \mathbf{X}_k and \mathbf{X}_0 . This rotation can be expressed in terms of the 3-1-3 Euler sequence as follows [37]:

$$\mathbf{A}_k = \begin{bmatrix} \cos(\phi)\cos(\psi) - \sin(\phi)\cos(\theta)\sin(\psi) & \cos(\phi)\sin(\psi) + \sin(\phi)\cos(\theta)\cos(\psi) & \sin(\phi)\sin(\theta) \\ -\sin(\phi)\cos(\psi) - \cos(\phi)\cos(\theta)\sin(\psi) & -\sin(\phi)\sin(\psi) + \cos(\phi)\cos(\theta)\cos(\psi) & \cos(\phi)\sin(\theta) \\ \sin(\theta)\sin(\psi) & -\sin(\theta)\cos(\psi) & \cos(\theta) \end{bmatrix}. \quad (\text{A.2})$$

However, there is a problem with the Euler angles, they have singularities that lead to numerical instabilities in numerical solvers [108]. To solve this, Euler parameters were devised, $\boldsymbol{\theta} = [\theta_0, \theta_1, \theta_2, \theta_3]^T$, which are an extension of the Euler angles. They can be related to the 3-1-3 sequence of Euler angles as follows:

$$\theta_0 = \cos(\theta/2)\cos\left(\frac{\psi + \phi}{2}\right) \quad (\text{A.3})$$

$$\theta_1 = \sin(\theta/2)\cos\left(\frac{\psi - \phi}{2}\right) \quad (\text{A.4})$$

$$\theta_2 = \sin(\theta/2)\sin\left(\frac{\psi - \phi}{2}\right) \quad (\text{A.5})$$

$$\theta_3 = \cos(\theta/2)\sin\left(\frac{\psi + \phi}{2}\right). \quad (\text{A.6})$$

Note that with the Euler parameters there is one more degree of freedom. Of course, a solid body only has three rotation degrees of freedom, so to maintain this the following relationship of the Euler parameters must be preserved:

$$\sum_{k=0}^3 (\theta_k)^2 = \boldsymbol{\theta}^T \boldsymbol{\theta} = 1. \quad (\text{A.7})$$

The rotation matrix \mathbf{A}_k can be expressed using these new Euler parameters [108]:

$$\mathbf{A}_k = \begin{bmatrix} 1 - 2(\theta_2)^2 - 2(\theta_3)^2 & 2(\theta_1\theta_2 - \theta_0\theta_3) & 2(\theta_1\theta_3 + \theta_0\theta_2) \\ 2(\theta_1\theta_2 + \theta_0\theta_3) & 1 - 2(\theta_1)^2 - 2(\theta_3)^2 & 2(\theta_2\theta_3 - \theta_0\theta_1) \\ 2(\theta_1\theta_3 - \theta_0\theta_2) & 2(\theta_2\theta_3 + \theta_0\theta_1) & 1 - 2(\theta_1)^2 - 2(\theta_2)^2 \end{bmatrix}. \quad (\text{A.8})$$

Velocity can be obtained by deriving Equation A.1 with respect to time:

$$\dot{\mathbf{r}}_0^i = \dot{\mathbf{r}}_0^k + \mathbf{A}_k \dot{\mathbf{r}}_k^i + \dot{\mathbf{A}}_k \mathbf{r}_k^i. \quad (\text{A.9})$$

$\dot{\mathbf{r}}_k^i$ will be set to zero in many cases of interest, for example, when there is a fix constraint between two rigid bodies i and k . The matrix $\dot{\mathbf{A}}_k$ can be rewritten as [108]:

$$\dot{\mathbf{A}}_k \mathbf{r}_k^i = -\mathbf{A}_k \tilde{\mathbf{r}}_k^i \bar{\mathbf{G}}_k \dot{\boldsymbol{\theta}}_k \quad (\text{A.10})$$

$$\tilde{\mathbf{r}}_k^i = \begin{bmatrix} 0 & -(r_k^i)_3 & (r_k^i)_2 \\ (r_k^i)_3 & 0 & -(r_k^i)_1 \\ -(r_k^i)_2 & (r_k^i)_1 & 0 \end{bmatrix} \quad (\text{A.11})$$

$$\bar{\mathbf{G}}_k^i = 2 \begin{bmatrix} -\theta_1 & \theta_0 & \theta_3 & -\theta_2 \\ -\theta_2 & -\theta_3 & \theta_0 & \theta_1 \\ -\theta_3 & \theta_2 & -\theta_1 & \theta_0 \end{bmatrix}. \quad (\text{A.12})$$

This way of expressing $\dot{\mathbf{A}}_k$ is more convenient because now all derivatives of Euler parameters are included in the term $\dot{\boldsymbol{\theta}}_k$, and can be obtained directly from solving a linear system of equations given a certain constraint between two bodies i and k . Also note that $(r_k^i)_3$ refers to the third component of the vector \mathbf{r}_k^i . Additionally, $\tilde{\mathbf{r}}_k^i$ will remain constant if bodies i and k have a constraint (fixed distance) between each other, and this also another reason why this notation is so convenient. This will be explained in more detail afterwards, in subsection A.1.4. With this, Equation A.9 can be rewritten as:

$$\dot{\mathbf{r}}_0^i = \dot{\mathbf{r}}_0^k + \mathbf{A}_k \dot{\mathbf{r}}_k^i - \mathbf{A}_k \tilde{\mathbf{r}}_k^i \bar{\mathbf{G}}_k \dot{\boldsymbol{\theta}}_k, \quad (\text{A.13})$$

where the term $\dot{\mathbf{r}}_0^k$ refers to the displacement of the centre of mass of body k with respect to the inertial system X_0 , and $-\mathbf{A}_k \tilde{\mathbf{r}}_k^i \bar{\mathbf{G}}_k \dot{\boldsymbol{\theta}}_k$ to the relative rotation motion within the reference system of body k . It also useful to realize that the term $\bar{\mathbf{G}}_k \dot{\boldsymbol{\theta}}_k$ refers to the angular velocity vector in body coordinates: $\bar{\mathbf{G}}_k \dot{\boldsymbol{\theta}}_k = \bar{\boldsymbol{\omega}}_k$.

Finally, the accelerations are going to be found deriving Equation A.14 once again with respect to time:

$$\ddot{\mathbf{r}}_0^i = \ddot{\mathbf{r}}_0^k + \frac{\partial}{\partial t} (\mathbf{A}_k \dot{\mathbf{r}}_k^i) - \mathbf{A}_k \frac{\partial}{\partial t} (\tilde{\mathbf{r}}_k^i \bar{\mathbf{G}}_k) \dot{\boldsymbol{\theta}}_k - \dot{\mathbf{A}}_k \tilde{\mathbf{r}}_k^i \bar{\mathbf{G}}_k \dot{\boldsymbol{\theta}}_k - \mathbf{A}_k \tilde{\mathbf{r}}_k^i \bar{\mathbf{G}}_k \ddot{\boldsymbol{\theta}}_k. \quad (\text{A.14})$$

Once again it is interesting to mention that in case of a rigid constraint between bodies i and k , the terms $\frac{\partial}{\partial t} (\mathbf{A}_k \dot{\mathbf{r}}_k^i) - \mathbf{A}_k \frac{\partial}{\partial t} (\tilde{\mathbf{r}}_k^i \bar{\mathbf{G}}_k) \dot{\boldsymbol{\theta}}_k$ are equal to zero.

A.1.2 Kinetic energy and generalized forces

The kinetic energy of body k in the inertial reference T_0^k is defined as:

$$T_0^k = \frac{1}{2} \int_{V^k} \rho^i \dot{\mathbf{r}}_0^i \dot{\mathbf{r}}_0^i dV^k \quad (\text{A.15})$$

which is a weighted integral over all the point i in the body k . The volume of body k is V^k , and the density at a generic point i within this body k is ρ^i . Substituting Equation A.14 into Equation A.15 it is obtained the following:

$$T_0^k = \frac{1}{2} \int_{V^k} \rho^i \begin{bmatrix} \dot{\mathbf{r}}_0^k{}^T \\ \dot{\boldsymbol{\theta}}_k^T \end{bmatrix} \begin{bmatrix} \mathbf{I} \\ -\bar{\mathbf{G}}_k^T \tilde{\mathbf{r}}_k^i{}^T \mathbf{A}_k^T \end{bmatrix} \begin{bmatrix} \mathbf{I} & -\mathbf{A}_k \tilde{\mathbf{r}}_k^i \bar{\mathbf{G}}_k \end{bmatrix} \begin{bmatrix} \dot{\mathbf{r}}_0^k \\ \dot{\boldsymbol{\theta}}_k \end{bmatrix} dV^k, \quad (\text{A.16})$$

where the term $\mathbf{A}_k \dot{\mathbf{r}}_k^i$ was set to zero, because in a rigid body the distance between points i and k in the body frame \mathbf{X}_k is constant. If the inner matrix multiplication is done, it yields:

$$T_0^k = \frac{1}{2} \int_{V^k} \rho^i \begin{bmatrix} \dot{\mathbf{r}}_0^k{}^T \\ \dot{\boldsymbol{\theta}}_k^T \end{bmatrix} \begin{bmatrix} \mathbf{I} & -\mathbf{A}_k \tilde{\mathbf{r}}_k^i \bar{\mathbf{G}}_k \\ SYM & \bar{\mathbf{G}}_k^T \tilde{\mathbf{r}}_k^i{}^T \tilde{\mathbf{r}}_k^i \bar{\mathbf{G}}_k \end{bmatrix} \begin{bmatrix} \dot{\mathbf{r}}_0^k \\ \dot{\boldsymbol{\theta}}_k \end{bmatrix} dV^k. \quad (\text{A.17})$$

The previous expression can be written in a more compact notation using $\dot{\mathbf{q}}_0^k = \begin{bmatrix} \dot{\mathbf{r}}_0^k \\ \dot{\boldsymbol{\theta}}_k \end{bmatrix}$ and

$$\mathbf{M}^k = \int_{V^k} \rho^i \begin{bmatrix} \mathbf{I} & -\mathbf{A}_k \tilde{\mathbf{r}}_k^i \bar{\mathbf{G}}_k \\ SYM & \bar{\mathbf{G}}_k^T \tilde{\mathbf{r}}_k^i{}^T \tilde{\mathbf{r}}_k^i \bar{\mathbf{G}}_k \end{bmatrix} dV^k:$$

$$T_0^k = \frac{1}{2} (\dot{\mathbf{q}}_0^k)^T \mathbf{M}^k \dot{\mathbf{q}}_0^k, \quad (\text{A.18})$$

where $\dot{\mathbf{q}}_0^k$ are the generalized coordinates of reference frame \mathbf{X}_k , which is fixed to body k ; and \mathbf{M}^k is the inertia matrix of body k in body reference frame \mathbf{X}_k .

Now each term of the inertia matrix \mathbf{M}^k is going to be studied in more detail:

$$\mathbf{M}^k = \int_{V^k} \rho^i \begin{bmatrix} \mathbf{I} & -\mathbf{A}_k \tilde{\mathbf{r}}_k^i \bar{\mathbf{G}}_k \\ SYM & \bar{\mathbf{G}}_k^T \tilde{\mathbf{r}}_k^i T \tilde{\mathbf{r}}_k^i \bar{\mathbf{G}}_k \end{bmatrix} dV^k \quad (\text{A.19})$$

$$\mathbf{m}_{rr}^k = \int_{V^k} \rho^i \mathbf{I} dV^k \quad (\text{A.20})$$

$$\mathbf{m}_{r\theta}^k = - \int_{V^k} \rho^i \mathbf{A}_k \tilde{\mathbf{r}}_k^i \bar{\mathbf{G}}_k dV^k \quad (\text{A.21})$$

$$\mathbf{m}_{\theta\theta}^k = \int_{V^k} \rho^i \bar{\mathbf{G}}_k^T \tilde{\mathbf{r}}_k^i T \tilde{\mathbf{r}}_k^i \bar{\mathbf{G}}_k dV^k \quad (\text{A.22})$$

The term $\mathbf{m}_{r\theta}^k$ of the inertia matrix \mathbf{M}^k can be further simplified [108] if a rigid body is considered with the body reference system: $\mathbf{m}_{r\theta}^k = 0$. Consequently, the inertia matrix can be computed more easily. The kinetic energy can be written with this simplification as:

$$T_0^k = \frac{1}{2} (\dot{\mathbf{q}}_0^k)^T \mathbf{m}_{rr}^k \dot{\mathbf{q}}_0^k + \frac{1}{2} (\dot{\mathbf{q}}_{\theta_0}^k)^T \mathbf{m}_{\theta\theta}^k \dot{\mathbf{q}}_{\theta_0}^k \quad (\text{A.23})$$

Then, the generalized forces have to be defined \mathbf{Q}_0^k . The virtual work of externally applied forces is:

$$\delta \mathbf{W}_0^k = (\mathbf{Q}_0^k)^T \delta \mathbf{q}_0^k = \begin{bmatrix} \mathbf{Q}_{r0}^k & \mathbf{Q}_{\theta 0}^k \end{bmatrix}^T \begin{bmatrix} \delta \mathbf{r}_0^k \\ \delta \boldsymbol{\theta}_k \end{bmatrix} \quad (\text{A.24})$$

$(\mathbf{Q}_r)_0^k$ are exactly the forces in inertial coordinates, because the Cartesian coordinates were not

modified: $(\mathbf{Q}_r)_0^k = \begin{bmatrix} F_x \\ F_y \\ F_z \end{bmatrix}$.

However, the generalized forces for the Euler parameters are different than the x,y,z moments typically used. Since working with x,y,z moments is more intuitive, these can be converted to $(\mathbf{Q}_\theta)_0^k$ equating the virtual work in both coordinate systems:

$$M_x \delta \alpha_x + M_y \delta \alpha_y + M_z \delta \alpha_z = Q_{\theta_0} \delta \theta_0 + Q_{\theta_1} \delta \theta_1 + Q_{\theta_2} \delta \theta_2 + Q_{\theta_3} \delta \theta_3, \quad (\text{A.25})$$

where $[M_x, M_y, M_z]$ and $[\delta \alpha_x, \delta \alpha_y, \delta \alpha_z]$ are respectively the moments and differential angle dis-

placements around the three Cartesian inertial axis; and $[Q_{\theta_0}, Q_{\theta_1}, Q_{\theta_2}, Q_{\theta_3}]$ and $[\delta\theta_0, \delta\theta_1, \delta\theta_2, \delta\theta_3]$ the generalized forces and differential Euler parameters displacements. Based on this equation, the following relationships can be obtained for one differential displacement of the Euler parameters:

$$Q_{\theta_0} = M_x \frac{\partial \alpha_x}{\partial \theta_0} + M_y \frac{\partial \alpha_y}{\partial \theta_0} + M_z \frac{\partial \alpha_z}{\partial \theta_0} \quad (\text{A.26})$$

$$Q_{\theta_1} = M_x \frac{\partial \alpha_x}{\partial \theta_1} + M_y \frac{\partial \alpha_y}{\partial \theta_1} + M_z \frac{\partial \alpha_z}{\partial \theta_1} \quad (\text{A.27})$$

$$Q_{\theta_2} = M_x \frac{\partial \alpha_x}{\partial \theta_2} + M_y \frac{\partial \alpha_y}{\partial \theta_2} + M_z \frac{\partial \alpha_z}{\partial \theta_2} \quad (\text{A.28})$$

$$Q_{\theta_3} = M_x \frac{\partial \alpha_x}{\partial \theta_3} + M_y \frac{\partial \alpha_y}{\partial \theta_3} + M_z \frac{\partial \alpha_z}{\partial \theta_3}. \quad (\text{A.29})$$

After operating this results in [37]:

$$(\mathbf{Q}_\theta)_0^k = \frac{1}{2} \begin{bmatrix} -\theta_1 & -\theta_2 & -\theta_3 \\ \theta_0 & \theta_3 & -\theta_2 \\ -\theta_3 & \theta_0 & \theta_1 \\ \theta_2 & -\theta_1 & \theta_0 \end{bmatrix} \begin{bmatrix} M_x \\ M_y \\ M_z \end{bmatrix}. \quad (\text{A.30})$$

A.1.3 Solid dynamic equations

In previous section, subsection A.1.3, the kinetic energy of each body k of the system in inertial coordinates was determined, T_0^k . Now, the Lagrange equation is going to be used to determine the solid dynamic equations of each body of the system. Note that here no constraints are defined, each body evolves freely under the action of a user defined generalized force.

$$\frac{d}{dt} \left(\frac{\partial T_0^k}{\partial \dot{\mathbf{q}}_0^k} \right) - \frac{\partial T_0^k}{\partial \mathbf{q}_0^k} = (\mathbf{Q}_0^k)^T. \quad (\text{A.31})$$

The derivatives give the following expressions [108]:

$$\frac{d}{dt} \left(\frac{\partial T_0^k}{\partial \dot{\mathbf{r}}_0^k} \right) = (\dot{r}_0^k)^T \mathbf{m}_{rr}^k \quad (\text{A.32})$$

$$\frac{d}{dt} \left(\frac{\partial T_0^k}{\partial \dot{\boldsymbol{\theta}}_k} \right) = \ddot{\boldsymbol{\theta}}_k^T \mathbf{m}_{\theta\theta}^k + \dot{\boldsymbol{\theta}}_k^T \bar{\mathbf{G}}_k^T \mathbf{m}_{\theta\theta}^k \dot{\bar{\mathbf{G}}}_k \quad (\text{A.33})$$

$$\frac{\partial T_0^k}{\partial \boldsymbol{\theta}_k} = \mathbf{0}^T \quad (\text{A.34})$$

$$\frac{\partial T_0^k}{\partial \mathbf{r}_0^k} = -\dot{\boldsymbol{\theta}}_k^T \bar{\mathbf{G}}_k^T \mathbf{m}_{\theta\theta}^k \dot{\bar{\mathbf{G}}}_k. \quad (\text{A.35})$$

Applying Lagrange identity, the following system of equations for body k is obtained:

$$\begin{bmatrix} \mathbf{m}_{rr}^k & 0 \\ 0 & \mathbf{m}_{\theta\theta}^k \end{bmatrix} \begin{bmatrix} \ddot{\mathbf{r}}_0^k \\ \ddot{\boldsymbol{\theta}}_k \end{bmatrix} = \begin{bmatrix} (\mathbf{Q}_r)_0^k \\ (\mathbf{Q}_\theta)_0^k - 2\dot{\bar{\mathbf{G}}}_k^T \mathbf{m}_{\theta\theta}^k \bar{\mathbf{G}}_k \dot{\boldsymbol{\theta}}_k \end{bmatrix}. \quad (\text{A.36})$$

However, with this the system of equations is still incomplete. An additional equation that imposes the requirement $\boldsymbol{\theta}_k^T \boldsymbol{\theta}_k = \mathbf{1}$ is needed. This is so as to preserve the correct definition of the Euler parameters. In particular if we derive this expression with respect to time two times we have:

$$\boldsymbol{\theta}^T \boldsymbol{\theta} = \mathbf{1} \quad (\text{A.37})$$

$$\dot{\boldsymbol{\theta}}^T \boldsymbol{\theta} = \mathbf{0} \quad (\text{A.38})$$

$$\ddot{\boldsymbol{\theta}}^T \boldsymbol{\theta} = -\dot{\boldsymbol{\theta}}^T \dot{\boldsymbol{\theta}}. \quad (\text{A.39})$$

Then, the constraint of the Euler parameters is imposed in the acceleration form:

$$\begin{bmatrix} \mathbf{m}_{rr}^k & 0 & 0 \\ 0 & \mathbf{m}_{\theta\theta}^k & \boldsymbol{\theta}_k \\ 0 & \boldsymbol{\theta}_k^T & 0 \end{bmatrix} \begin{bmatrix} \ddot{\mathbf{r}}_0^k \\ \ddot{\boldsymbol{\theta}}_k \\ \lambda_\theta \end{bmatrix} = \begin{bmatrix} (\mathbf{Q}_r)_0^k \\ (\mathbf{Q}_\theta)_0^k - 2\dot{\bar{\mathbf{G}}}_k^T \mathbf{m}_{\theta\theta}^k \bar{\mathbf{G}}_k \dot{\boldsymbol{\theta}}_k \\ -\dot{\boldsymbol{\theta}}_k^T \dot{\boldsymbol{\theta}}_k \end{bmatrix} \quad (\text{A.40})$$

, note how the Lagrange multiplier λ_θ was introduced as a forcing term to impose the mentioned

equation. Also remark that the mass matrix, denoted as $\mathbf{M} = \begin{bmatrix} \mathbf{m}_{rr}^k & 0 & 0 \\ 0 & \mathbf{m}_{\theta\theta}^k & \boldsymbol{\theta}_k \\ 0 & \boldsymbol{\theta}_k^T & 0 \end{bmatrix}$ is a symmetric matrix. This guarantees the existence of a unique solution if the body k has non-zero mass and inertia [108].

A.1.4 Constraints

Some of the most common holonomic constraints are going to be defined in the present multibody solver. More user defined constraints can be added to the system in a similar fashion: adding the desired constraint equation and a Lagrange multiplier to force the system to follow the constraint.

First, the holonomic rotation constraints are going to be defined. A generic slave body k is going to have fixed some of its angles to a master body i . Therefore, the slave body k , \mathbf{X}_k , is going to follow a chosen number of angles (0, 1, 2 or 3) of the master body \mathbf{X}_i . The possible fixed angles are $\alpha_0^x, \alpha_0^y, \alpha_0^z$, rotations around the axis of the inertial reference system \mathbf{X}_0 . For example, a body k is forced to follow α_0^x and α_0^z of a master body i . However, in this case α_0^y or the translation degrees of freedom are not constrained. As the system of equations of a generic body k solves the accelerations, Equation A.40, the holonomic constrains are going to be imposed based on the accelerations:

$$\mathbf{G}_k^* \ddot{\boldsymbol{\theta}}_k = \mathbf{G}_i^* \ddot{\boldsymbol{\theta}}_i, \quad (\text{A.41})$$

where the matrix \mathbf{G}^* is defined as:

$$\mathbf{G} = 2 \begin{bmatrix} -\theta_1 & \theta_0 & -\theta_3 & \theta_2 \\ -\theta_2 & \theta_3 & \theta_0 & -\theta_1 \\ -\theta_3 & -\theta_2 & \theta_1 & \theta_0 \end{bmatrix} \quad (\text{A.42})$$

$$\mathbf{G}^* = \text{rows_constrained}(\mathbf{G}). \quad (\text{A.43})$$

The function *rows_constrained* truncates the input matrix and constructs a matrix removing the rows that are not constrained. For example, in the previous example where α_0^x and α_0^z were

constrained,

$$\mathbf{G}^* = \text{rows_constrained}(\mathbf{G}) = 2 \begin{bmatrix} -\theta_1 & \theta_0 & -\theta_3 & \theta_2 \\ -\theta_3 & -\theta_2 & \theta_1 & \theta_0 \end{bmatrix}. \quad (\text{A.44})$$

Also note the usefulness of defining a generic master body i , if this body is the inertial reference system \mathbf{X}_0 , then the constrained body k would have zero α_0^x and α_0^z rotation.

Second, the holonomic constraints for translation degrees of freedom are going to be defined. In this a generic point in the reference frame of the slave body \mathbf{r}_k^P is fixed to a point in the reference frame of the master body \mathbf{r}_i^P . This mathematically can be expressed using the kinematic equations, Equation A.1:

$$\mathbf{r}_0^i + \mathbf{A}_i \mathbf{r}_i^P = \mathbf{r}_0^k + \mathbf{A}_k \mathbf{r}_k^P, \quad (\text{A.45})$$

where the distances \mathbf{r}_k^P and \mathbf{r}_i^P are constant as they are a point belonging to a rigid body in the solid reference frame. Once again, the constraints have to be translated to accelerations. For this the kinematic relationship in Equation A.14 is used, but the terms with $\frac{\partial}{\partial t}$ are set to zero, due to the rigid constraint:

$$\ddot{\mathbf{r}}_0^k - \dot{\mathbf{A}}_k \tilde{\mathbf{r}}_k^P \bar{\mathbf{G}}_k \dot{\boldsymbol{\theta}}_k - \mathbf{A}_k \tilde{\mathbf{r}}_k^P \bar{\mathbf{G}}_k \ddot{\boldsymbol{\theta}}_k = \ddot{\mathbf{r}}_0^i - \dot{\mathbf{A}}_i \tilde{\mathbf{r}}_i^P \bar{\mathbf{G}}_i \dot{\boldsymbol{\theta}}_i - \mathbf{A}_i \tilde{\mathbf{r}}_i^P \bar{\mathbf{G}}_i \ddot{\boldsymbol{\theta}}_i. \quad (\text{A.46})$$

In this model, the three translation degrees of freedom are constrained. However, in order to set a more general scenario, the same procedure as with the rotation constraints is going to be followed. Only a number between 0 and 3, both included, are going to be constrained within the inertial reference frame axes \mathbf{X}_0 . For example, only x_0 and z_0 are constrained, so only rows 1 and 3 are imposed. Finally it results:

$$(\ddot{\mathbf{r}}_0^k)^* - (\dot{\mathbf{A}}_k)^* \tilde{\mathbf{r}}_k^P \bar{\mathbf{G}}_k \dot{\boldsymbol{\theta}}_k - (\mathbf{A}_k)^* \tilde{\mathbf{r}}_k^P \bar{\mathbf{G}}_k \ddot{\boldsymbol{\theta}}_k = (\ddot{\mathbf{r}}_0^i)^* - (\dot{\mathbf{A}}_i)^* \tilde{\mathbf{r}}_i^P \bar{\mathbf{G}}_i \dot{\boldsymbol{\theta}}_i - (\mathbf{A}_i)^* \tilde{\mathbf{r}}_i^P \bar{\mathbf{G}}_i \ddot{\boldsymbol{\theta}}_i \quad (\text{A.47})$$

$$(\ddot{\mathbf{r}}_0^k)^* = \text{rows_constrained}(\ddot{\mathbf{r}}_0^k) \quad (\text{A.48})$$

$$(\mathbf{A}_k)^* = \text{rows_constrained}(\mathbf{A}_k) \quad (\text{A.49})$$

$$(\dot{\mathbf{A}}_k)^* = \text{rows_constrained}(\dot{\mathbf{A}}_k), \quad (\text{A.50})$$

with this, the kinematic equations of the constraints have been imposed. However, in the dynamic

equations, Lagrange multipliers have to be included as a forcing term to impose these boundary conditions. Assume once again a slave k and a master body i . The slave body dynamic equations would be [108]:

$$\mathbf{m}_{rr}^k \ddot{\mathbf{r}}_0^k + (\boldsymbol{\lambda}_r^k)^* = (\mathbf{Q}_r)_0^k \quad (\text{A.51})$$

$$\mathbf{m}_{\theta\theta}^k \ddot{\boldsymbol{\theta}}_k + (\mathbf{G}_k^*)^T (\boldsymbol{\lambda}_\theta^k)^* - (\mathbf{A}_k^* \tilde{\mathbf{r}}_k^P \bar{\mathbf{G}}_k)^T (\boldsymbol{\lambda}_r^k)^* = (\mathbf{Q}_\theta)_0^k - 2\dot{\bar{\mathbf{G}}}_k^T \mathbf{m}_{\theta\theta}^k \bar{\mathbf{G}}_k \dot{\boldsymbol{\theta}}_k, \quad (\text{A.52})$$

where the Lagrange multipliers $(\boldsymbol{\lambda}_r^k)^* = \text{rows_constrained}(\boldsymbol{\lambda}_r^k)$ and $(\boldsymbol{\lambda}_\theta^k)^* = \text{rows_constrained}(\boldsymbol{\lambda}_\theta^k)$ are defined to force the dynamic evolution of the slave body k following the kinematic constraints. Note that once again the Lagrange multipliers are also reduced based on the number of actual constraints that were selected for the displacements r and rotations θ . The Lagrange multiplier $(\boldsymbol{\lambda}_r^k)^*$ physically represents the force applied by the slave body k to the master body i , and projected into the inertial reference system \mathbf{X}_0 . On the other hand, $(\boldsymbol{\lambda}_\theta^k)^*$ is the momentum in the inertial reference system. The term $-(\mathbf{A}_k^* \tilde{\mathbf{r}}_k^P \bar{\mathbf{G}}_k)^T (\boldsymbol{\lambda}_r^k)^*$ reflects the fact that if the force applied at the constraint point is not in the centre of mass, $\tilde{\mathbf{r}}_k^P \neq \mathbf{0}$, it is going to give momentum to the body k .

The tricky part comes when defining the master body i equations:

$$\mathbf{m}_{rr}^i \ddot{\mathbf{r}}_0^i - (\boldsymbol{\lambda}_r^k)^* = (\mathbf{Q}_r)_0^i \quad (\text{A.53})$$

$$\mathbf{m}_{\theta\theta}^i \ddot{\boldsymbol{\theta}}_i - (\mathbf{G}_i^*)^T (\boldsymbol{\lambda}_\theta^k)^* + (\mathbf{A}_i^* \tilde{\mathbf{r}}_i^P \bar{\mathbf{G}}_i)^T (\boldsymbol{\lambda}_r^k)^* = (\mathbf{Q}_\theta)_0^i - 2\dot{\bar{\mathbf{G}}}_i^T \mathbf{m}_{\theta\theta}^i \bar{\mathbf{G}}_i \dot{\boldsymbol{\theta}}_i. \quad (\text{A.54})$$

It can be seen that there are new terms that did not appear in the slave equations. These terms stem from the third Newton Law: the law of action and reaction. The force supplied to the slave body k to follow its constraints has a reaction of the opposite sign on the master body. Note how the matrices $-(\mathbf{G}_i^*)^T$, $(\mathbf{A}_i^* \tilde{\mathbf{r}}_i^P \bar{\mathbf{G}}_i)^T$ also changed to index i because now forces and moments of the constraints in system \mathbf{X}_0 , $(\boldsymbol{\lambda}_r^k)^*$, $(\boldsymbol{\lambda}_\theta^k)^*$, have to be converted to the reference system of the master body i .

Finally, the system of equations of a generic slave body k and a master body i that are constrained between each other can be expressed as:

$$\begin{bmatrix}
\mathbf{m}_{rr}^i & 0 & 0 & 0 & 0 & 0 & -(\mathbf{I}^*)^T & 0 \\
0 & \mathbf{m}_{\theta\theta}^i & \boldsymbol{\theta}_i & 0 & 0 & 0 & (\mathbf{A}_i^* \tilde{\mathbf{r}}_i^P \bar{\mathbf{G}}_i)^T & -(\mathbf{G}_i^*)^T \\
0 & \boldsymbol{\theta}_i^T & 0 & 0 & 0 & 0 & 0 & 0 \\
0 & 0 & 0 & \mathbf{m}_{rr}^k & 0 & 0 & (\mathbf{I}^*)^T & 0 \\
0 & 0 & 0 & 0 & \mathbf{m}_{\theta\theta}^k & \boldsymbol{\theta}_k & -(\mathbf{A}_k^* \tilde{\mathbf{r}}_k^P \bar{\mathbf{G}}_k)^T & (\mathbf{G}_k^*)^T \\
0 & 0 & 0 & 0 & \boldsymbol{\theta}_k^T & 0 & 0 & 0 \\
-\mathbf{I}^* & \mathbf{A}_i^* \tilde{\mathbf{r}}_i^P \bar{\mathbf{G}}_i^T & 0 & \mathbf{I}^* & -\mathbf{A}_k^* \tilde{\mathbf{r}}_k^P \bar{\mathbf{G}}_k & 0 & 0 & 0 \\
0 & -\mathbf{G}_i^* & 0 & 0 & \mathbf{G}_k^* & 0 & 0 & 0
\end{bmatrix}
\begin{bmatrix}
\ddot{\mathbf{r}}_0^i \\
\ddot{\boldsymbol{\theta}}_i \\
\lambda_{\theta i} \\
\ddot{\mathbf{r}}_0^k \\
\ddot{\boldsymbol{\theta}}_k \\
\lambda_{\theta k} \\
(\boldsymbol{\lambda}_r^k)^* \\
(\boldsymbol{\lambda}_\theta^k)^*
\end{bmatrix}
=
\begin{bmatrix}
(\mathbf{Q}_r)_0^k \\
(\mathbf{Q}_\theta)_0^k - 2\dot{\mathbf{G}}_k^T \mathbf{m}_{\theta\theta}^k \bar{\mathbf{G}}_k \dot{\boldsymbol{\theta}}_k \\
-\dot{\boldsymbol{\theta}}_k^T \dot{\boldsymbol{\theta}}_k \\
(\mathbf{Q}_r)_0^k \\
(\mathbf{Q}_\theta)_0^k - 2\dot{\mathbf{G}}_k^T \mathbf{m}_{\theta\theta}^k \bar{\mathbf{G}}_k \dot{\boldsymbol{\theta}}_k \\
-\dot{\boldsymbol{\theta}}_k^T \dot{\boldsymbol{\theta}}_k \\
(\dot{\mathbf{A}}_k)^* \tilde{\mathbf{r}}_k^P \bar{\mathbf{G}}_k \dot{\boldsymbol{\theta}}_k - (\dot{\mathbf{A}}_i)^* \tilde{\mathbf{r}}_i^P \bar{\mathbf{G}}_i \dot{\boldsymbol{\theta}}_i \\
0
\end{bmatrix}. \tag{A.55}$$

Once again the resulting system is symmetric. Now, apart from non-zero mass and inertia moments, non-linearly-dependent constraints are also required to guarantee the existence and uniqueness of the solution (non-singular matrix). For whatever multibody problem that has to be defined, this block matrix slave-master has to be set for the number of bodies that is desired. This gives the possibility to implement the solver in a general way, for a N body problem with user defined constraints.

A.1.5 Constraints controller

During simulations, it is sometimes interesting to move the relative position between master-slave bodies. For example, take as an example an airfoil with a flap, Figure A-3. The inertial frame is the reference frame \mathbf{X}_0 , the airfoil is attached to reference frame \mathbf{X}_1 and the flap is attached to reference frame \mathbf{X}_2 . Initially the airfoil has all its degrees of freedom fixed to the inertial reference frame \mathbf{X}_0 , and the flap has all its degrees of freedom fixed to the airfoil \mathbf{X}_1 . However, after sometime of simulation of steady flight in a fluid solver a maneuver of landing wants to be simulated. Therefore the angle of attack of the airfoil has to be increased, therefore the relative pitching angle between systems \mathbf{X}_0 and \mathbf{X}_1 has to be modified. Also the flap has to be deflected during the landing, so the relative pitching angle and position \mathbf{X}_1 and \mathbf{X}_2 is modified. This can be done with a constraints controller.

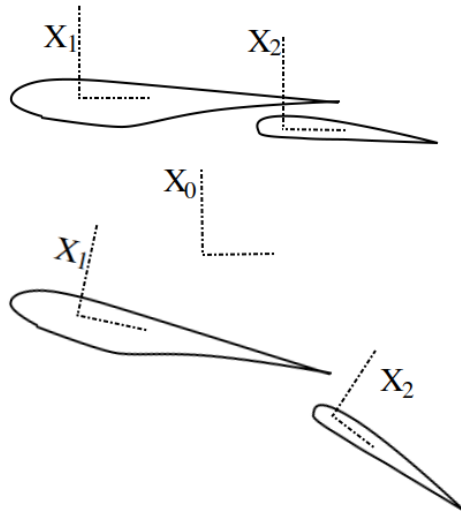


Figure A-3: System of an airfoil and a flap. Modified configuration for landing.

To impose the relative displacement between two constrained bodies an relative prescribed acceleration is going to be prescribed between the master and the slave:

$$\mathbf{G}_k^* \ddot{\theta}_k = \mathbf{G}_i^* \ddot{\theta}_i + (\alpha_{pres}^{i-k})^* \quad (\text{A.56})$$

$$(\ddot{\mathbf{r}}_0^{\mathbf{k}})^* - (\dot{\mathbf{A}}_k)^* \tilde{\mathbf{r}}_k^P \bar{\mathbf{G}}_k \dot{\boldsymbol{\theta}}_k - (\mathbf{A}_k)^* \tilde{\mathbf{r}}_k^P \bar{\mathbf{G}}_k \ddot{\boldsymbol{\theta}}_k = (\ddot{\mathbf{r}}_0^{\mathbf{i}})^* - (\dot{\mathbf{A}}_i)^* \tilde{\mathbf{r}}_i^P \bar{\mathbf{G}}_i \dot{\boldsymbol{\theta}}_i - (\mathbf{A}_i)^* \tilde{\mathbf{r}}_i^P \bar{\mathbf{G}}_i \ddot{\boldsymbol{\theta}}_i + (\ddot{\mathbf{r}}_{pres}^{i-k})^*. \quad (\text{A.57})$$

Note how the prescribed angular and translation accelerations have also been reduced to account only for the actual constrained dimensions:

$$(\ddot{\mathbf{r}}_{pres}^{i-k})^* = \text{rows_constrained}(\ddot{\mathbf{r}}_{pres}^{i-k}) \quad (\text{A.58})$$

$$(\boldsymbol{\alpha}_{pres}^{i-k})^* = \text{rows_constrained}(\boldsymbol{\alpha}_{pres}^{i-k}). \quad (\text{A.59})$$

The dynamic equations accounting for forces and momentum do not have to be modified. The Lagrange multipliers will automatically adjust themselves to achieve the relative acceleration between the two reference systems. This is really useful, for example in the airfoil-flap configuration, the Lagrange multipliers will tell the needed forces and moments in the inertial frame to achieve the desired manoeuvres. With these the internal actuators between the wing and flap can be designed, for example.

A.1.6 Solver of the systems of equations

The numerical solver of the system of equation was chosen considering that the multibody system is not going to have too many bodies. That is, more or less no more than 10 bodies, and matrices smaller than 100×100 . In this scenario, a direct numerical method is appropriate. In particular, LU decomposition with partial pivoting was chosen. The partial pivoting was selected because in the present formulation there are zeros in the diagonal that can make the numerical method diverge during the pivoting. The advantage of this numerical method is that it finds the exact solution (except for truncation errors) if the matrix of the system is non-singular [121]. This is true as it was explained before when the mass and inertia of each body are non-zero, and when non-redundant constraints have been provided. Therefore, a well defined multibody system should always be solved in a correct way by the chosen method.

The system to be solved is defined as: $\mathbf{Ax} = \mathbf{b}$. The LU decomposition is defined in the following way: $\mathbf{PA} = \mathbf{LU}$. The numerical algorithm consists of two steps:

1. LU factorization with partial pivoting.
2. Solve the system:

$$\mathbf{Ly} = \mathbf{Pb}$$

$$\mathbf{Ux} = \mathbf{y}.$$

The computational cost is governed by the LU decomposition step, and scales with N^3 , given a matrix of dimensions $N \times N$. This scaling is quite strong and there are other numerical methods that have a much better scaling with matrix size, iterative methods or conjugate gradient for example [121]. That is the reason why the direct solver strategy was chosen given the condition that the number of bodies to be solved was not high. In case many more bodies are included in the system other solving strategies have to be used.

A.1.7 Time integration

A Newmark integration family has been chosen as an integrator for the solid dynamic equations.

$$\dot{\mathbf{q}}_{t+\Delta t} = \dot{\mathbf{q}}_t + \Delta t [(1 - \gamma)\ddot{\mathbf{q}}_t + \ddot{\mathbf{q}}_{t+\Delta t}] \quad (\text{A.60})$$

$$\mathbf{q}_{t+\Delta t} = \mathbf{q}_t + \Delta t \dot{\mathbf{q}}_t + (\Delta t)^2 \left[\left(\frac{1}{2} - \beta\right)\ddot{\mathbf{q}}_t + \beta\ddot{\mathbf{q}}_{t+\Delta t} \right]. \quad (\text{A.61})$$

The main reason for choosing this solver is that it offers a range of first, second and third order implicit schemes, just by modifying the parameters of the model γ and β . Moreover, the scheme is unconditionally stable for [113]:

$$\frac{1}{2} \leq \gamma \leq 2\beta. \quad (\text{A.62})$$

In Table A.1 a summary of some of the most popular Newmark schemes are shown:

Description	γ	β	Order	Stability	Type
Trapezoidal rule	$\frac{1}{2}$	$\frac{1}{4}$	2	Unconditional	Implicit
Linear acceleration	$\frac{1}{2}$	$\frac{1}{6}$	2	Conditional	Implicit
Fox-Goodwin	$\frac{1}{2}$	$\frac{1}{12}$	3	Conditional	Implicit

Table A.1: Family of Newmark integration schemes.

[113]

During the present document, the Trapezoidal rule is going to be used, due to its unconditional stability and second order convergence.

The Newmark methods are implicit because they require the acceleration at $t + \Delta t$. This means that a iterative process has to be followed to solve the equations. The used algorithm for one implicit time step is depicted below:

```

q_res = 1
dq_res = 1
i = 1
while (q_res ≥ ε).AND.(dq_res ≥ ε) do
  A = f1(q_i, q̇_i)
  b = f2(q_i, q̇_i)
  Aq̈_{i+1} = b
  q̇_{i+1} = q̇_t + Δt [(1 - γ)q̈_t + q̈_{i+1}]
  q_{i+1} = q_t + Δt q̇_t + (Δt)2 [(1/2 - β)q̈_t + βq̈_{i+1}]
  q_{i+1} = αq_{i+1} + (1 - α)q_i
  dq_{i+1} = αdq_{i+1} + (1 - α)dq_i
  q_res = √||q_{i+1} - q_i||
  dq_res = √||dq_{i+1} - dq_i||
  i = i + 1
end while

q_{t+Δt} = q_{i+1}
dq_{t+Δt} = dq_{i+1}

```

An additional relaxation step was added in the previous algorithm. This can help with the convergence of the Newmark integration. Even though the numerical scheme is implicit, the iterative steps to achieve the implicit convergence are explicit and can diverge. That is the reason why the relaxation factor α is included. Normally, during the present simulations the time step is small enough (due to presence of the fluid scales) that almost no relaxation is needed, and the residuals converge to machine precision within 4-5 sub iterations.

A.1.8 Additional corrections

Euler parameters norm

Euler parameters add an additional degree of freedom and to solve this, the norm of the Euler parameters should be equal to 1, see Equation A.37. As the multibody solver solved for the accelerations, the constraint was imposed in its acceleration form, Equation A.39. However, the integration of acceleration is not exact. It has discretization error due to the finite time step. This means that the norm of the Euler parameters starts to have a drift, and does not fulfil its definition.

To solve this issue the following iterative correction was imposed for every body k :

$$\boldsymbol{\theta}_k = \frac{\boldsymbol{\theta}_k}{\sqrt{\boldsymbol{\theta}_k^T \boldsymbol{\theta}_k}}. \quad (\text{A.63})$$

Therefore, the iterative algorithm of the Newmark integration is modified in the following way:

```

q_res = 1
dq_res = 1
i = 1
while (q_res ≥ ε).AND.(dq_res ≥ ε) do
  A = f1(q_i, q̇_i)
  b = f2(q_i, q̇_i)
  Aq̈_{i+1} = b
  q̇_{i+1} = q̇_t + Δt [(1 - γ)q̈_t + q̈_{i+1}]
  q_{i+1} = q_t + Δt q̇_t + (Δt)^2 [(1/2 - β)q̈_t + βq̈_{i+1}]
  q_{i+1} = αq_{i+1} + (1 - α)q_i
  dq_{i+1} = αdq_{i+1} + (1 - α)dq_i
  θ = θ / √(θ^T θ)
  q_res = √(||q_{i+1} - q_i||)
  dq_res = √(||dq_{i+1} - dq_i||)
  i = i + 1
end while

q_{t+Δt} = q_{i+1}
dq_{t+Δt} = dq_{i+1}

```

Note how the correction is done just before calculating the residuals. This means that the method will not converge until the Euler parameters norm is corrected to be equal to one, up to machine precision error.

Position correction of constraints

Another problem observed during the simulations was that, due to the discretization error of the Newmark integration, the constraints were not fulfilled for large integration times. The reason for this is that the constraints are imposed in the acceleration terms, Equation A.47. Therefore, accelerations fulfilled the constraints, but the numerical integration leads to the accumulation of discretization error in the actual position of the constraints. To solve this, a correction was included that forces the bodies to follow the actual constraints position. The reduced position of each slave body k , $(\mathbf{r}_0^k)^*$, is corrected as:

$$(\mathbf{r}_0^k)^* = (\mathbf{r}_0^i)^* + (\mathbf{A}_i)^* \mathbf{r}_i^P - (\mathbf{A}_k)^* \mathbf{r}_k^P. \quad (\text{A.64})$$

For the correction of the Euler angles constraints applies:

$$\mathbf{G}_k^* \ddot{\boldsymbol{\theta}}_k = \mathbf{G}_i^* \ddot{\boldsymbol{\theta}}_i. \quad (\text{A.65})$$

Note that the position and Euler parameters constraints corrections of the master body i always have to be updated before of the constrained slave body k . An analogy could be made with a tree, which will be called the "tree system", where the slaves depend on each upper element of the branch. For example, in Figure A-4, to include the correction for body 3, the corrections for bodies 2 and 0 are required. Therefore, each level of the "tree system" has to be corrected before going to the next one.

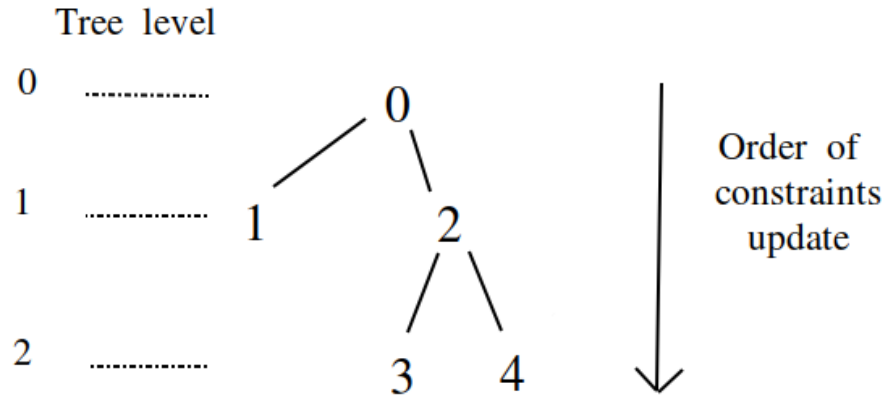


Figure A-4: Dependencies of constraints within the "tree system".

Finally, the algorithm for one implicit time step is:

```

q_res = 1
dq_res = 1
i = 1
while (q_res ≥ ε).AND.(dq_res ≥ ε) do
  A = f1(qi, q̇i)
  b = f2(qi, q̇i)
  Aq̈i+1 = b
  q̇i+1 = q̇t + Δt [(1 - γ)q̈t + q̈i+1]
  qi+1 = qt + Δtq̇t + (Δt)2 [(1/2 - β)q̈t + βq̈i+1]
  qi+1 = αqi+1 + (1 - α)qi
  dqi+1 = αdqi+1 + (1 - α)dqi
  θ =  $\frac{\boldsymbol{\theta}}{\sqrt{\boldsymbol{\theta}^T \boldsymbol{\theta}}}$ 
  treelevel = 0

```

```

for (tree_level = 0, final_tree_level) do
    call Position_Correction( $\mathbf{q}_{i+1}$ )
    tree_level = tree_level + 1
end for
 $\mathbf{q\_res} = \sqrt{\|\mathbf{q}_{i+1} - \mathbf{q}_i\|}$ 
 $\mathbf{dq\_res} = \sqrt{\|\mathbf{dq}_{i+1} - \mathbf{dq}_i\|}$ 
i = i + 1
end while
 $\mathbf{q}_{t+\Delta t} = \mathbf{q}_{i+1}$ 
 $\mathbf{dq}_{t+\Delta t} = \mathbf{dq}_{i+1}$ 

```

It should be remarked that once again the correction is done just before calculating the residuals. Consequently, the algorithm will not converge until the accelerations are adjusted to fulfill the actual constraints position.

A.2 Verification cases

The multibody solver is now going to be tested with different verification cases. First, a Simple Pendulum is proposed to assess one single constraint, subsection A.2.1. Second, the preservation of inertia moments and the Euler parameters are verified with a Pivoting Body, subsection A.2.2. Third, a Spherical Body is selected because it has analytical solution, and shows that the algorithm is working correctly in a 3D problem, subsection A.2.3. Finally, several bodies are tested with a Double Pendulum, subsection A.2.4. All the simulations are given using a *.txt* file as an input, see ??

A.2.1 Simple Pendulum

The simple pendulum is going to be characterized by the length of the pendulum l , its mass m , x moment of inertia I_x (around its centre of mass), the gravity g , and the nutation angle θ that defines its position, see Figure A-5. The pendulum has attached the reference system X_1 . It oscillates in the $y - z$ plane and it is fixed at $\vec{x} = [0, 0, 0]$ to the inertial reference system X_0 . The pendulum is placed initially at θ_0 with zero velocity. The dynamic equations of the pendulum are [89]:

$$(m l^2 + I_x) \ddot{\theta} + m g l \sin(\theta) = 0. \quad (\text{A.66})$$

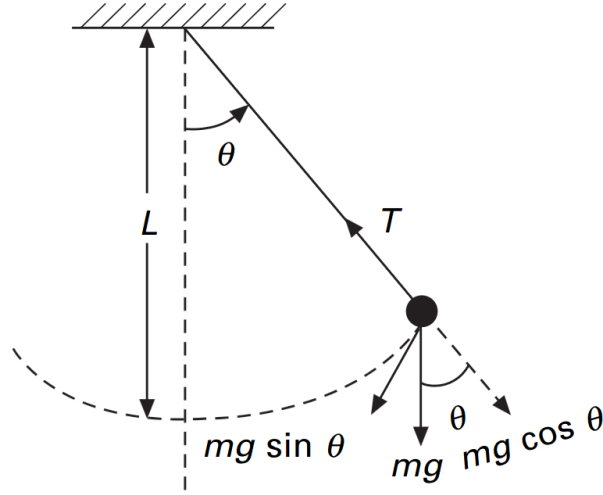


Figure A-5: Variables that define the simple pendulum verification case.

[89]

Note how in Equation A.66 the pendulum has a non-zero inertia moment around its x axis. This differential equation does not have an analytical solution. Therefore, in order to assess the validity of the numerical solution it will be linearized assuming small angles θ :

$$\left(1 + \frac{I_x}{m l^2}\right) \ddot{\theta} + \frac{g}{l} \sin(\theta) = \left(1 + \frac{I_x}{m l^2}\right) \ddot{\theta} + \frac{g}{l} (\theta + O(\theta^3)) = 0. \quad (\text{A.67})$$

Now an analytical solution exists:

$$\theta = \theta_0 \cos(\omega t) + O(\theta_0^3) \quad (\text{A.68})$$

$$\omega = \sqrt{\frac{g}{l \left(1 + \frac{I_x}{m l^2}\right)}}. \quad (\text{A.69})$$

First, a small angle is going to be chosen $\theta_0 = 0.001$, so that the error done during linearization is smaller than the integration error. Then the dimensionless variables are defined: $g = 2$, $l = 1$, $m = 1$, I_x and $\omega = 1$. The comparison of the analytical expression and the obtained numerical solution is shown in Figure A-6. The integration was done between $t = 0$ and $t = 50$, and with $N = 500$ time steps. It can be seen how the agreement is quite good.

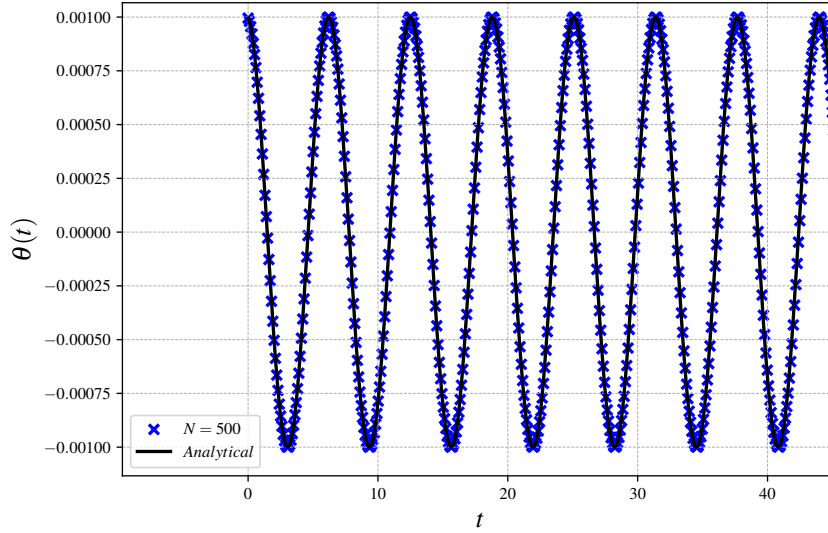


Figure A-6: Simple pendulum. Comparison of analytical (black line) and numerical solution (blue x). $N = 500$, $t = 0$ to $t = 50$. $\omega = 1$ and $\theta_0 = 0.001$ [rad].

Furthermore, in Equation A.40 the error between the linearized analytical $\theta(t)$ and the numerical solution $\theta_{exact}(t)$ is shown. As expected the error increases linearly with time. Moreover, it can be seen that the error diminishes when the time step is reduced. In particular, it can be seen that the error convergence is approximately second order, for a half the time step, the error is reduced more or less four times. This will be inspected in more detail later.

Also, in this analysis is important to mention that the error done during the linearization process is way below the numerical error: $linearization_error = O(10^{-9})$ and $\theta - \theta_{exact} = O(10^{-5})$. Consequently, the analytical solution can be considered as exact for this degree of time step refinement.

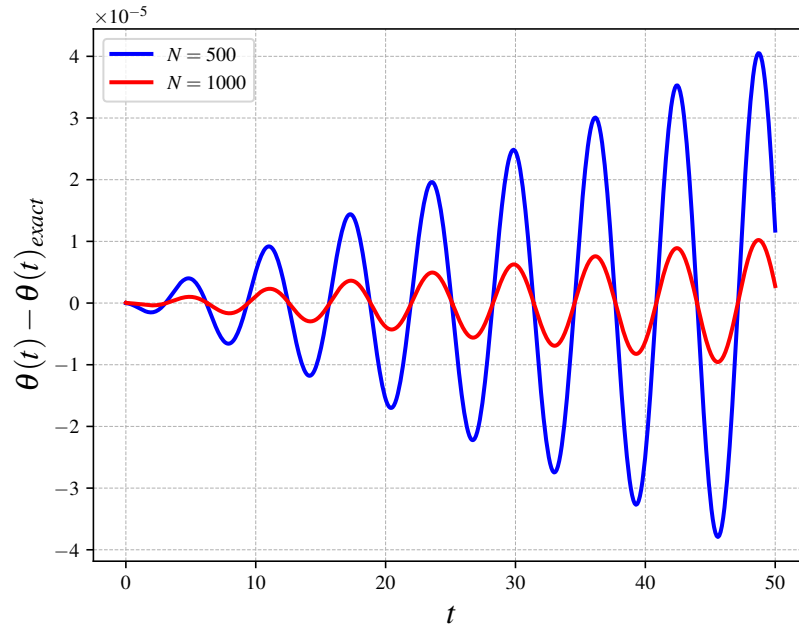


Figure A-7: Simple pendulum. Analysis of numerical error with time for $N = 500$ and $N = 1000$. $t = 0$ to 50 . $\omega = 1$ and $\theta_0 = 0.001$ [rad].

Next, the non-linear solution, for large values of θ_0 is going to be studied. The new parameters are going to be slightly modified for large angles: $g = 2$, $l = 1$, $m = 1$, I_x , $\omega = 1$ and $\theta_0 = \frac{\pi}{2}$. Once again, the pendulum will oscillate in the $y - z$ plane, and it will be fixed to $\vec{x} = [0, 0, 0]$. In Figure A-8a the trajectory in the $y - z$ plane is shown for $t = 0$ to $t = 5$. The nutation angle evolution with time is shown in Figure A-8b.

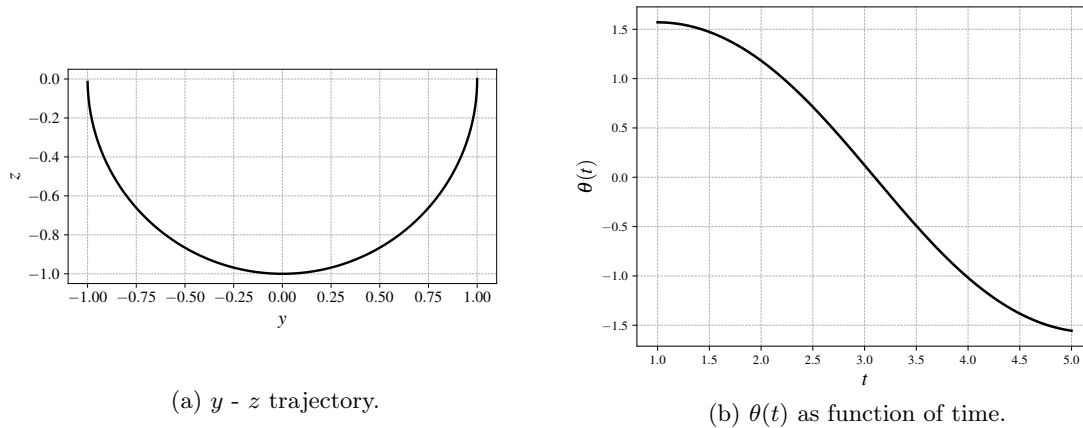


Figure A-8: Simple pendulum. $N = 500000$, $t = 0$ to 5 . $\omega = 1$ and $\theta_0 = \frac{\pi}{2}$ [rad].

In this case, the previous analytical solution is no longer valid. Therefore, to study the con-

vergence with the time step, a reference solution θ^{ref} is considered of $N = 500000$. This solution has a discretization error order of magnitudes lower than solutions with a smaller N , so it can be considered as exact for convergence analysis. More precisely, the discretization error is going to be defined as:

$$\epsilon^N = \sum_{i=1}^N |\theta_i^N - \theta_i^{ref}|/N \quad (\text{A.70})$$

The convergence of the discretization error with the number of time steps N is shown in Figure A-10. Observing the slope, it is seen clearly that the integration scheme has second order convergence. This agrees with the theoretical analysis of the Newmark scheme with $\gamma = 0.5$ and $\beta = 0.25$, as explained in Table A.1.

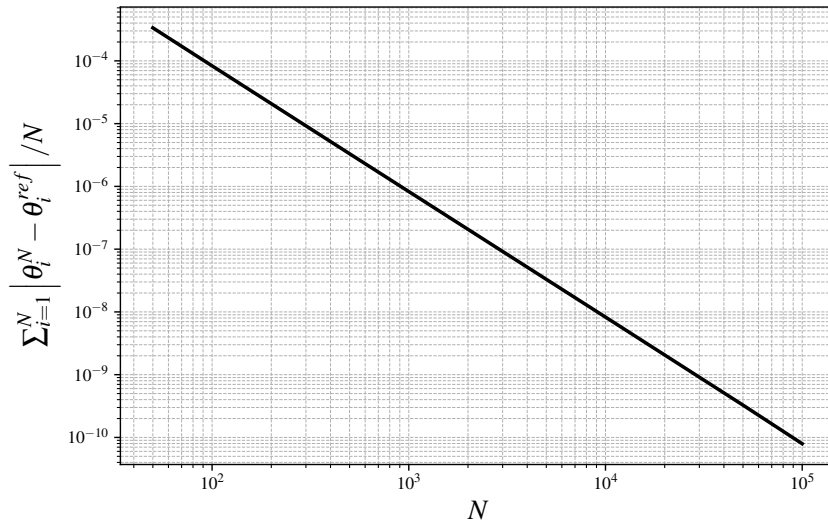


Figure A-9: Simple pendulum. Convergence of numerical error with the number of time steps N . $t = 0$ to 5. $\omega = 1$ and $\theta_0 = \frac{\pi}{2}$ [rad]. Newmark Trapezoidal time integration.

Next, the preservation of energy is studied. Total energy is computed from kinetic and potential energy:

$$E = \frac{1}{2} I_x \dot{\theta}^2 + \frac{1}{2} m (\dot{x}^2 + \dot{y}^2 + \dot{z}^2) - m g z = E^{ref} \quad (\text{A.71})$$

In the initial condition $\vec{x} = [0, 1, 0]$, $\dot{\vec{x}} = [0, 0, 0]$ and $\dot{\theta} = 0$, so it can be inferred that $E^{ref} = 0$. The preservation of the total energy is going to be computed using the following expression:

$$\epsilon_E^N = \sum_{i=1}^N |E_i^N - E_i^{ref}|/N. \quad (\text{A.72})$$

Energy preservation converges also as second order, see Figure A-10. This makes sense, as in Newmark integration with the Trapezoidal rule, the velocities also have second order convergence, [113].

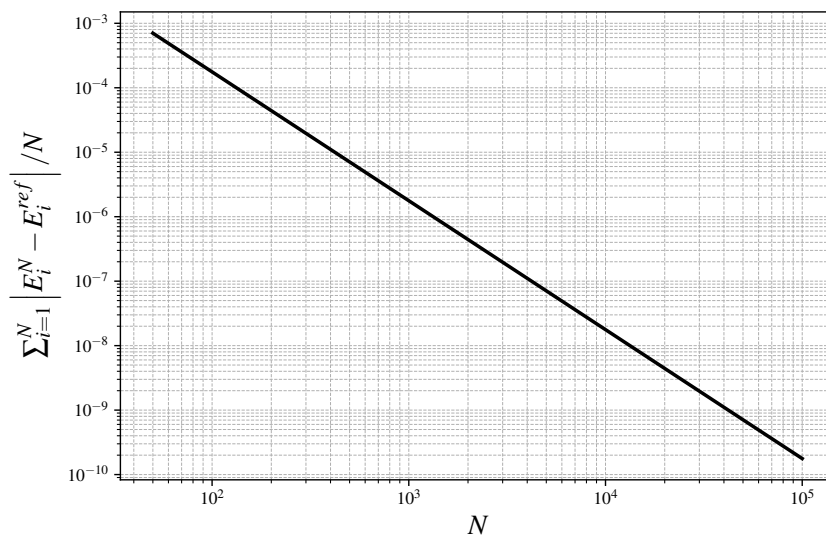


Figure A-10: Simple pendulum. Energy preservation with the number of time steps N . $t = 0$ to 5. $\omega = 1$ and $\theta_0 = \frac{\pi}{2}$ [rad]. Newmark Trapezoidal time integration.

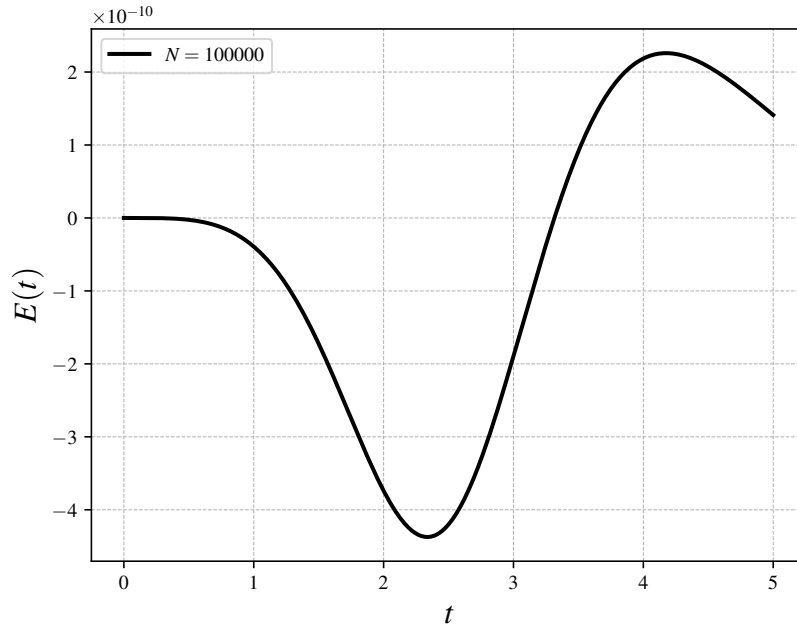


Figure A-11: Simple pendulum. Energy preservation with time. $N = 500000$ and $t = 0$ to 5 . $\omega = 1$ and $\theta_0 = \frac{\pi}{2}$ [rad]. Newmark Trapezoidal time integration.

It is also interesting to see energy preservation with time. This is observed in Figure A-11. Energy preservation oscillates with time during the swings of the pendulum. However, there is a linear dissipative trend with increasing time (the second oscillation has a lower positive peak). The reason for this is that the Trapezoidal Newmark integration is slightly dissipative [113]. On the one hand this guarantees the unconditional stability, but on the other hand, makes the system dissipative.

Finally, the effects of the implemented corrections is going to be assessed, see subsection A.1.8. First, the correction for the constraints is assessed. During the integration, constraints were imposed in accelerations and this derived in shifts of the constraints position for large time integration. The error of the constraints (in this case position constraints, but can also be angles, see subsection A.1.4) is going to be defined as:

$$\epsilon_C^N = \sum_{i=1}^N (|\vec{x}_i| - |\vec{l}|) / N. \quad (\text{A.73})$$

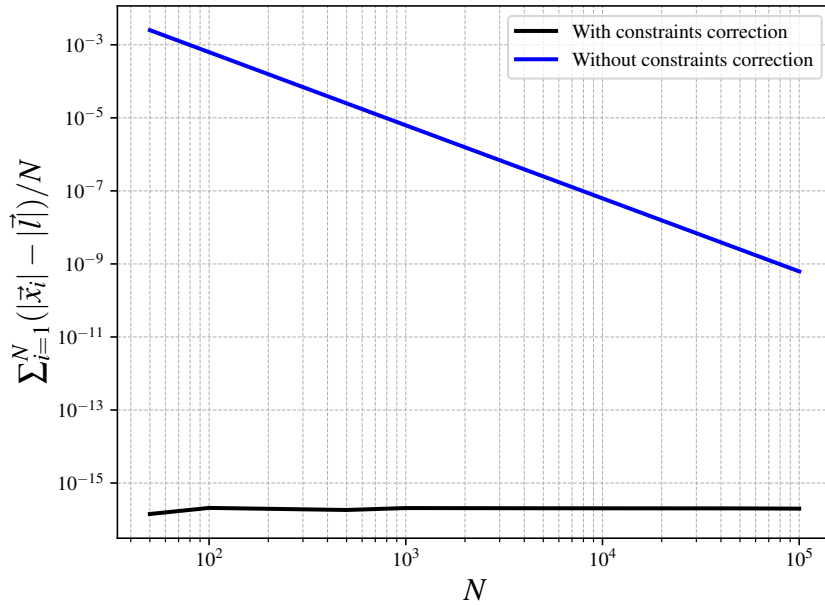


Figure A-12: Simple pendulum. Convergence of constraints error with time step N . $t = 0$ to 5. $\omega = 1$ and $\theta_0 = \frac{\pi}{2}$ [rad]. Newmark Trapezoidal time integration.

Figure A-12 shows how the corrections effectively remove this drift in the constraints position, achieving machine precision (double precision 10^{-16} residuals). Without the constraints correction the drift of the constraints has a second order convergence, the same as the body coordinates convergence shown in Figure A-9. The reason for this is that both constraints and body coordinates are integrated with a second order Newmark Trapezoidal scheme.

The norm of the Euler parameters should also be one. Nevertheless, this was also imposed in the acceleration terms, and for large time integration the norm suffered a drift away from one. To prove the validity of the correction the following error is defined:

$$\epsilon_{\theta}^N = \sum_{i=1}^N \left(|\vec{\theta}_i - 1| \right) / N. \quad (\text{A.74})$$

Once again the same behavior is observed. The correction reduces the error to machine precision, while a second order drift occurs without correction.

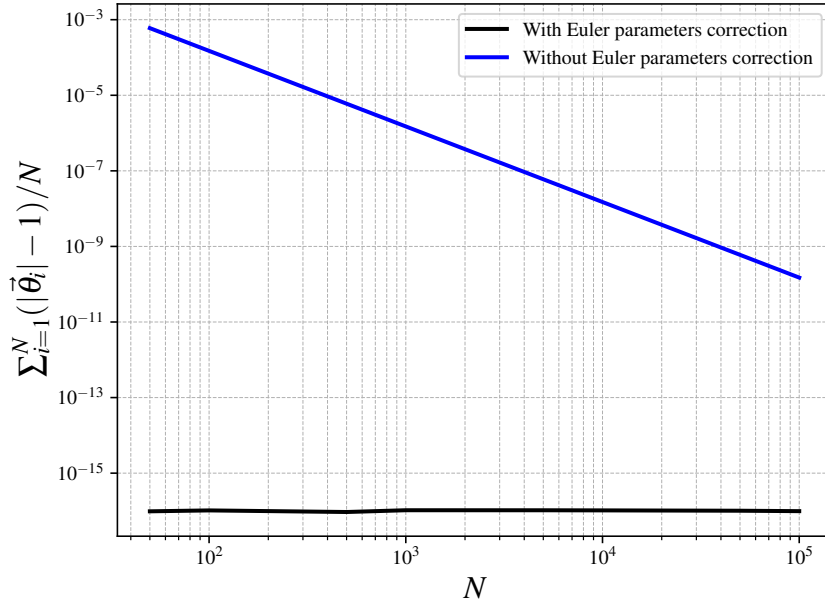


Figure A-13: Simple pendulum. Analysis of numerical error with time for $N = 500$ and $N = 1000$. $t = 0$ to 5 . $\omega = 1$ and $\theta_0 = \frac{\pi}{2}$ [rad]. Newmark Trapezoidal time integration.

Finally, it should be remarked that convergence studies in Figure A-9 and Figure A-10 were done with the corrections applied, and it was observed that the corrections did not influence body coordinates error convergence. However, it is interesting to keep the exact position of constraints during long time simulations, so as to preserve the geometry between different bodies, for example relative position between a flap and a wing. It is not desirable to reach a steady state where the flap has moved away from the wing several meters. Euler parameters norm criterion is also important and has to be maintained: to convert this parameters back Euler angles with physical meaning, and therefore process solution data, the mathematical definition with norm equal to one has to be fulfilled.

A.2.2 Euler-Poinsot solid

Poinsot solid is a rigid body that has its position fixed to a point in an inertial system X_0 . Therefore, its translations are constrained, but it has free rotation. Moreover, exterior forces do not give momentum with respect to the fixed point [104]. Intuitively, an example of a Poinsot solid would be a gyroscope.

In this case, the mass m of the Poinsot solid is not relevant, as translational degrees of freedom are fixed. What is important is the inertia tensor:

$$\dot{\theta} = 0 \quad (\text{A.76})$$

$$\dot{\psi} = \frac{D\mu}{A} \quad (\text{A.77})$$

$$\dot{\phi} = \frac{C\mu}{A} \cos(\theta_0) \left(\frac{A}{C} - 1 \right), \quad (\text{A.78})$$

where D and μ are integration constants related to the angular velocity of the Poincot solid. ψ , θ and ϕ are the three Euler angles with the 3-1-3 convention. In this case for simplicity, the following test case parameters are going to be defined: $A = 1$, $B = 1$, $C = 2$, $\mu = 1$ and $D = 1$. The initial conditions for the test case are: $\theta_0 = \frac{\pi}{3}$, $\phi_0 = 0$, $\psi_0 = 0$, $\dot{\theta}_0 = 0$, $\dot{\phi}_0 = -\frac{1}{4}$ and $\dot{\psi}_0 = 1$. With this particular conditions, the analytical solution is:

$$\theta(t) = \frac{\pi}{3} \quad (\text{A.79})$$

$$\psi(t) = t \quad (\text{A.80})$$

$$\phi(t) = -\frac{1}{4}t. \quad (\text{A.81})$$

The comparison between the analytical solution and the numerical results is done in Figure A-15. For $N = 50$, a quite good agreement is achieved as it can be observed. The discontinuities in the angle ψ are due to the definition of Fortran trigonometric functions.

The error of a generic Euler angle Eu_Ang with a discretization of N time steps is defined as:

$$\epsilon_{Eu}(t) = Eu_Ang^N(t) - Eu_Ang^{exact}(t). \quad (\text{A.82})$$

This error is plotted for the three Euler angles in Figure A-16. θ_{100} and θ_{50} are almost overlapped, because the error in θ is several orders of magnitude smaller. This is due to the null acceleration in θ , so there is no error propagation through the Newmark integration. ψ and ϕ show a linear increase of the error with time, and also a quadratic convergence with time discretization refinement. Therefore, for a large integration time, the time step size also has to be decreased if the numerical error has to be below a certain threshold.

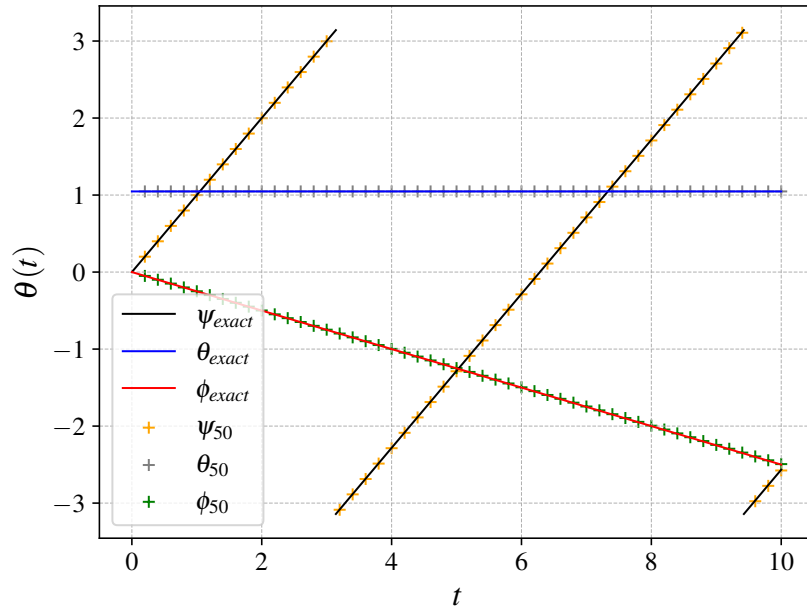


Figure A-15: Poinsot solid. Comparison of numerical and exact solution. $t = 0$ to 10. $N = 50$. Newmark Trapezoidal time integration.

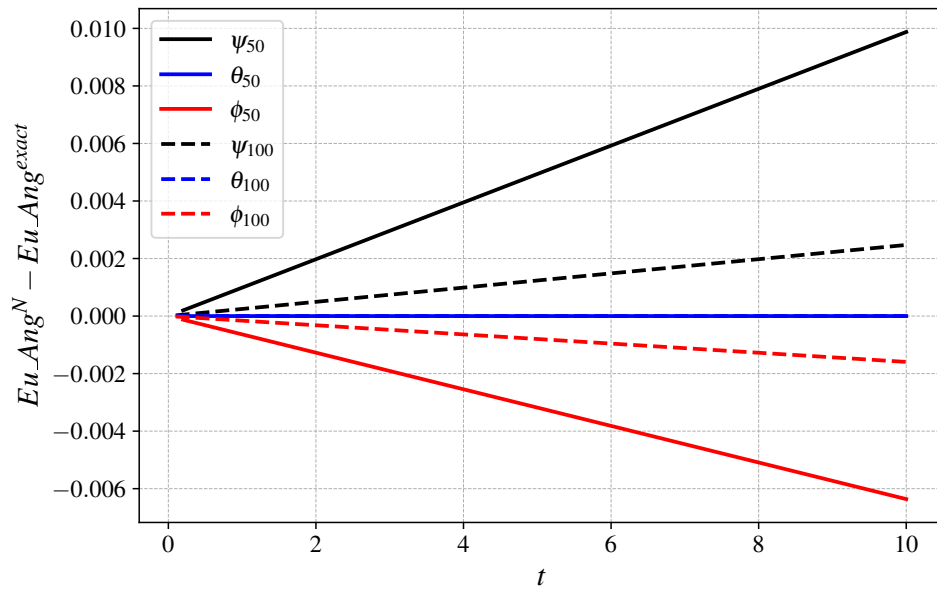


Figure A-16: Poinsot solid. Analysis of numerical error with time for $N = 50$ and $N = 100$. $t = 0$ to 10. Newmark Trapezoidal time integration.

Finally, the error convergence is inspected in more detail in Figure A-17. The error is averaged throughout all the time domain as follows:

$$\epsilon_{Eu}^N = \sum_{i=1}^N |Eu_Ang_i^N - Eu_Ang_i^{ref}|/N. \quad (\text{A.83})$$

Here it can be clearly seen that the error convergence is second order, as it was observed in previous cases. Once again, this proves the correct implementation of the Newmark algorithm, Table A.1. θ error does not converge because it is not integrated: acceleration is automatically set to zero due to the dynamic equations $\ddot{\theta} = 0$, and its non-zero value is probably due to the numerical precision provided during the initial conditions set up.

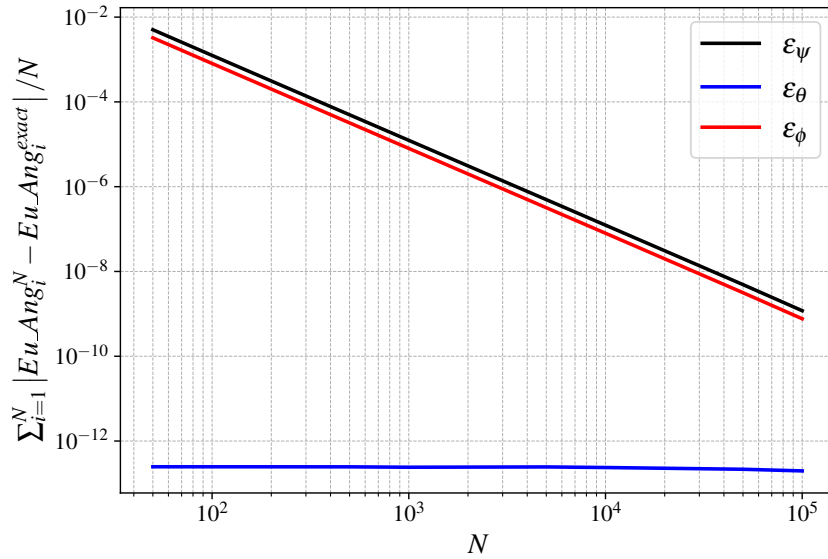


Figure A-17: Poinsot solid. Analysis of convergence of numerical error with time step size. $t = 0$ to 10. Newmark Trapezoidal time integration.

A.2.3 Spherical Pendulum

The Spherical Pendulum is a well known of problem of solid mechanics. It consists of a point mass (zero inertia tensor around its centre of mass) that is fixed at a distance l to an inertial system X_0 , see Figure A-18.

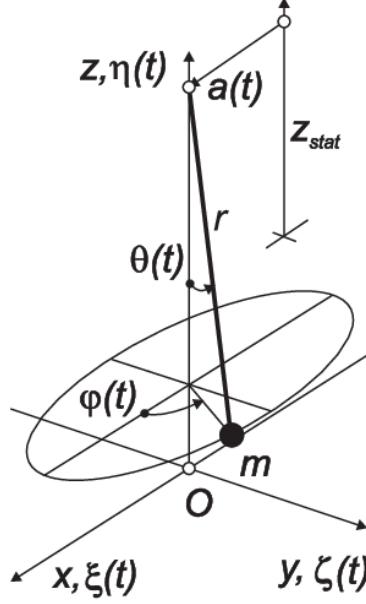


Figure A-18: Spherical pendulum. Analysis of convergence of numerical error with time step size. $t = 0$ to 10. Newmark Trapezoidal time integration.

The point mass m is going to be under the effect of a uniform gravitational field: $\vec{g} = [0, 0, -g]_{X_0}$. This configuration does not have an analytic solution for a generic set of initial conditions $\theta, \psi, \dot{\theta}$ and $\dot{\psi}$ [77]. However, for some specific initial conditions, a solution exists. In particular, for the following initial conditions, a perpetual circular motion in the $x - y$ plane is achieved, centrifugal force is balanced with gravity and cable tension:

$$\theta = \theta_0 \tag{A.84}$$

$$\dot{\psi} = -\sqrt{\frac{g}{l \cos(\theta_0)}} \tag{A.85}$$

$$\psi = \psi_0 \tag{A.86}$$

$$\dot{\theta} = 0. \tag{A.87}$$

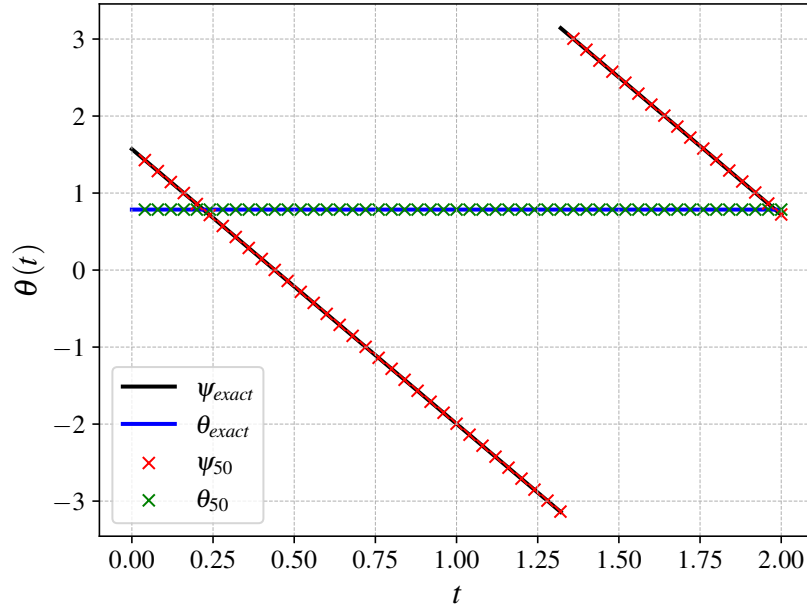


Figure A-19: Spherical pendulum. Comparison of ψ and θ between numerical solution with $N = 50$ and exact values. $t = 0$ to 2. Newmark Trapezoidal time integration.

Moreover, for this initial conditions the analytical solution of the centre of mass is a circumference in the $x - y$ plane:

$$x_{CM}(t) = l \sin(\theta_0) \cos\left(\psi_0 - \sqrt{\frac{g}{l \cos(\theta_0)}} t\right) \quad (\text{A.88})$$

$$y_{CM}(t) = l \sin(\theta_0) \sin\left(\psi_0 - \sqrt{\frac{g}{l \cos(\theta_0)}} t\right) \quad (\text{A.89})$$

$$z_{CM}(t) = -l \cos(\theta_0). \quad (\text{A.90})$$

During this test case, the following parameters are going to be used: $g = 9$, $l = 1$, $\psi_0 = -\frac{\pi}{2}$, $\theta_0 = \frac{\pi}{4}$. The movement is going to be characterized by ψ and θ , see Figure A-19. For $N = 50$ a quite good agreement between the numerical and analytical solution is obtained. θ remains constant and ψ keeps decreasing with a uniform speed. ψ experiences a jump between $-\pi$ and π due to the definition of the trigonometric functions in Fortran.

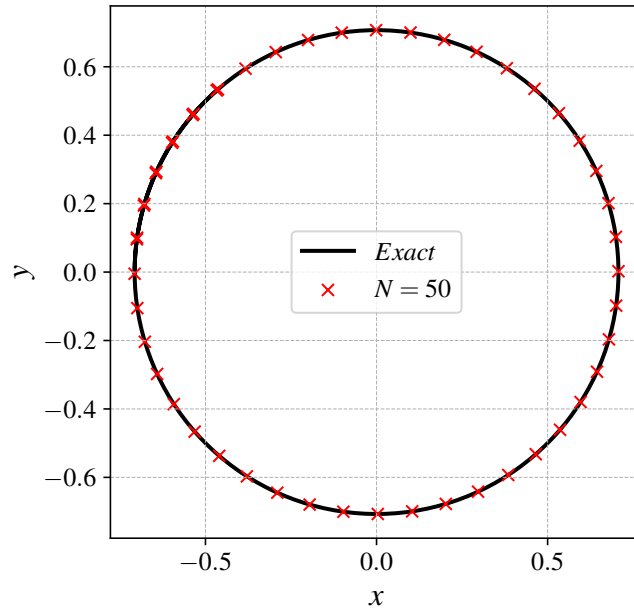


Figure A-20: Spherical pendulum. Comparison of x and y between numerical solution with $N = 50$ and exact values. Newmark Trapezoidal time integration.

Then, in Figure A-20 the trajectory in the $x - y$ plane of the centre of mass of the pendulum is shown. It can be seen how for these initial conditions the pendulum is oscillating in the $x - y$ plane, as it was expected. Once again, only for $N = 50$ a quite good agreement is achieved.

Euler Angle error, which was defined in Equation A.82, is plotted as a function of time for ψ and θ in Figure A-21. θ_{50} and θ_{100} cannot be distinguished because they are much smaller compared to ψ_{50} and ψ_{100} . The reason for this is that θ is a constant throughout integration and does not propagate the integration error of its acceleration, as it is zero (this also occurred in subsection A.2.2). Observing ψ the error increases linearly with time, and shows a quadratic convergence with the time step size. This coincides with the values expected from a Newmark Trapezoidal time integration, Table A.1. The second order convergence is further verified in Figure A-22. Here the convergence of the position of the pendulum is assessed, taking as an error the averaged norm of the deviation from the reference:

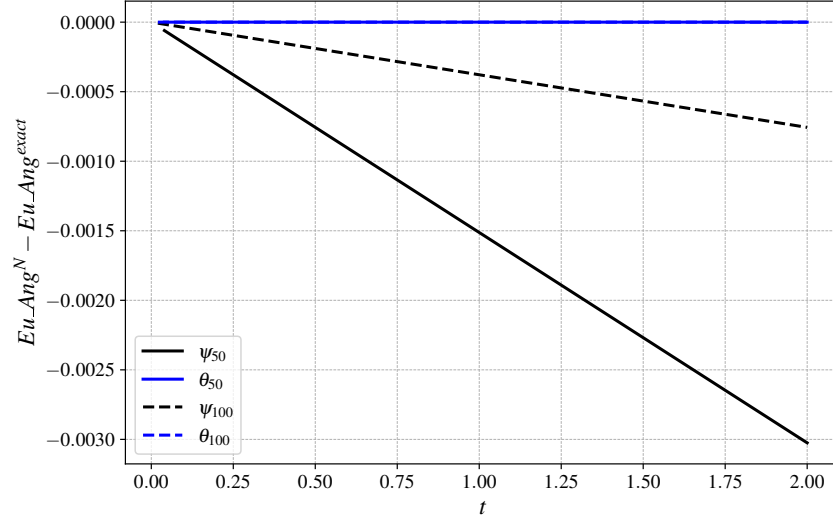


Figure A-21: Spherical pendulum. Euler Angles error evolution with time. Compared cases: $N = 50$ and $N = 100$. $t = 0$ to 2. Newmark Trapezoidal time integration.

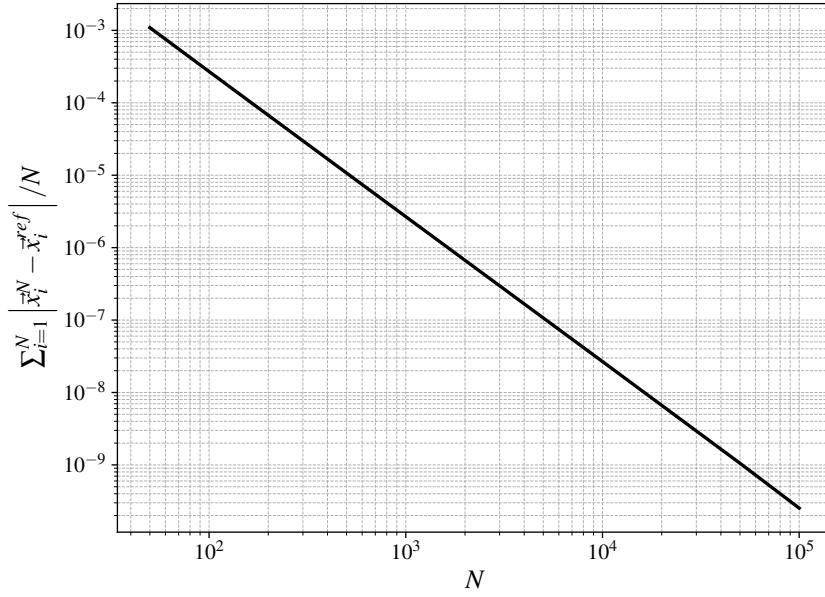


Figure A-22: Spherical pendulum. Analysis of convergence of numerical error in position with time step size. $t = 0$ to 2. Newmark Trapezoidal time integration.

$$\epsilon_x^N = \sum_{i=1}^N |\vec{x}_i^N - \vec{x}_i^{ref}| / N. \quad (\text{A.91})$$

Finally, in Figure A-23 and Figure A-24 energy preservation is studied. First, in Figure A-23 it is shown that the energy conservation also follows a second order convergence, as it was expected. Then, in Figure A-24 the evolution of energy conservation with time is presented for $N = 5000$. It can be seen how the method is slightly dissipative, as it was seen in subsection A.2.1. However, it is interesting to see that at the end of the oscillation period, the energy seems to recover once again its original value. The reason for this is that the error done during the Newmark integration depends on the sign of the higher order derivatives of the acceleration, so depending on the particular scenario, it may behave as dissipative or produce energy.

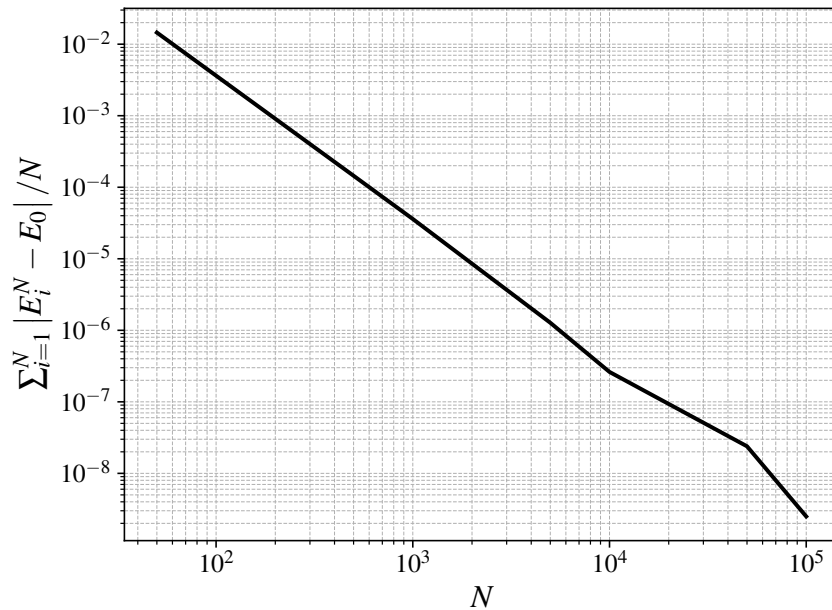


Figure A-23: Spherical pendulum. Convergence of energy preservation with time step size. $t = 0$ to 2. Newmark Trapezoidal time integration.

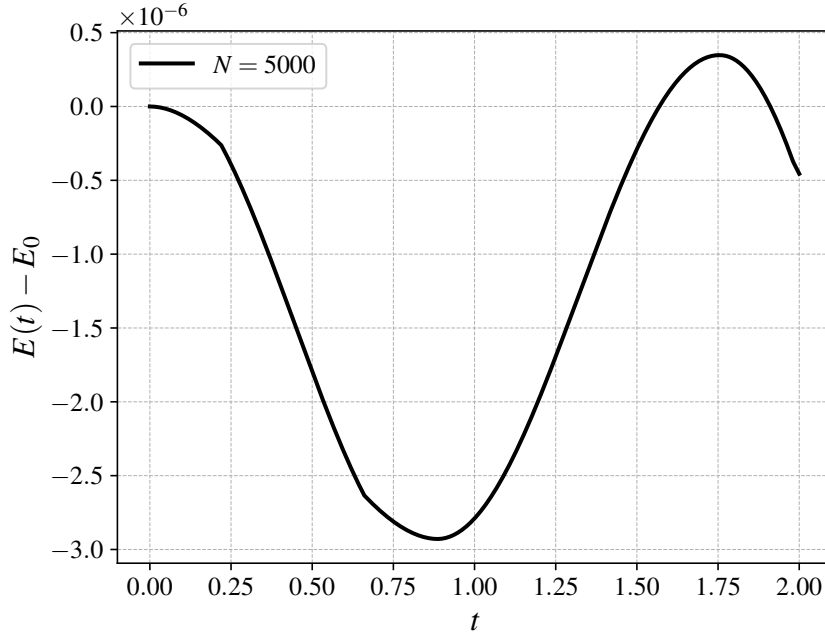


Figure A-24: Spherical pendulum. Energy preservation evolution with time. $N = 5000$. $t = 0$ to 2. Newmark Trapezoidal time integration.

A.2.4 Double Pendulum

A double pendulum is selected as the final test case to test the multibody solver. This system is known to have a chaotic behaviour: a tiny perturbation in the initial conditions gives a completely different solution for large time steps [110]. Moreover, two bodies are involved which make the system non trivial. Consequently, this is a convenient system to test all the capabilities of the multibody solver. In the present test case the movement is going to be studied only in the $y_0 - z_0$ plane, see Figure A-25. Note that it could be resolved in 3D, because the Multibody solver is developed to cover all the three dimensional degrees of freedom, however, for simplicity and to compare with benchmark solution only 2D initial conditions are provided. Therefore, the initial system is going to be defined by: $\theta_1 = 0$, $\theta_2 = \frac{\pi}{2}$, $\dot{\theta}_1 = 0$, $\dot{\theta}_2 = 0$, $l_1 = 1$, $l_2 = 1$, $m_1 = 1$, $m_2 = 1$, $I_1 = 1$ and $I_2 = 1$. m and I refer to the mass and moment of inertia around the x axis, the only rotation degree of freedom that is important in the 2D oscillation. Moreover, gravity constant is defined as $g = 9$, down in the negative z_0 direction.

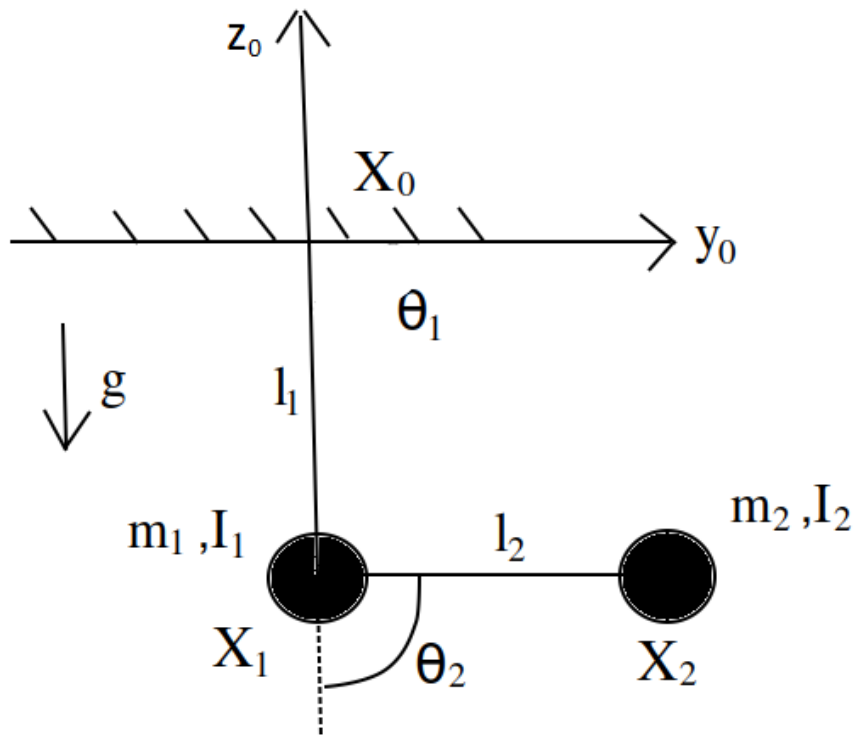


Figure A-25: Double pendulum. Sketch of the double pendulum system with parameters that define the problem.

This problem does not have an analytical solution. Therefore, to compare results numerical solutions from other authors are used [3]. The *Reference* is defined using this code, with the same initial conditions, an integration time between $t = 0$ and 5, $N = 500000$ time steps, and a 4th order *Runge – Kutta* integrator. Based, on the observed results, the discretization error of the *Reference* is much smaller than the cases with which it is compared, so it can be considered as an "exact" solution.

In Figure A-26 and Figure A-27 the *Reference* data is compared with the Multibody solver for $N = 50$. It can be seen how the movement is chaotic, both pendulums start swinging following complicated trajectories. Despite only having 50 time steps, a really good agreement is observed.

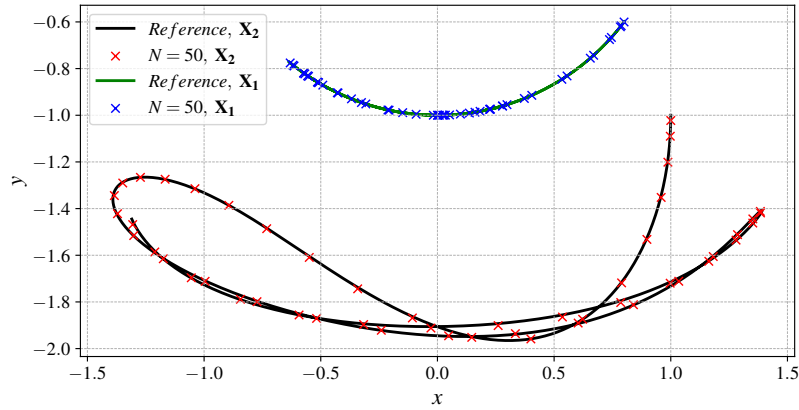


Figure A-26: Double pendulum. Comparison of the *Reference* $x - y$ coordinates with the numerical data obtained with the Multibody solver for $N = 50$. $t = 0$ to 5. Pendulum 1 X_1 , and pendulum 2 X_2 . Newmark Trapezoidal time integration.

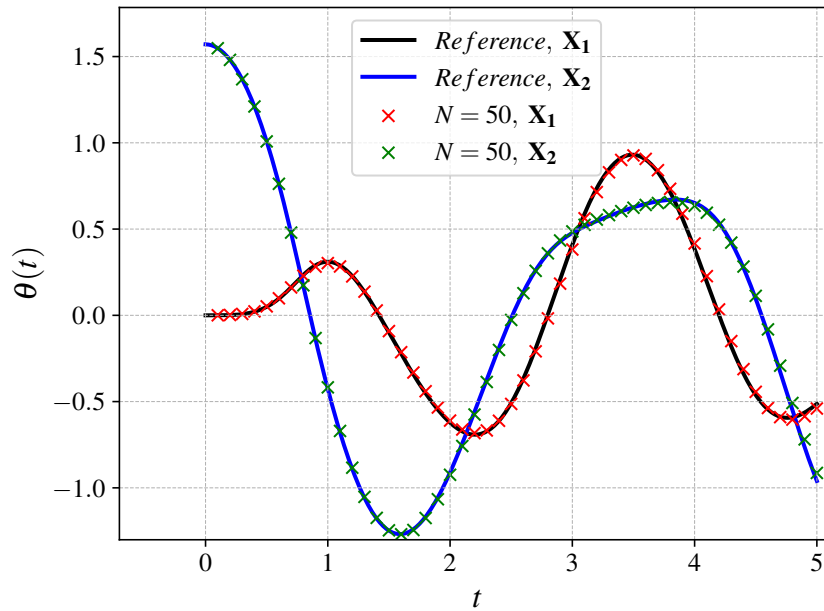


Figure A-27: Double pendulum. Evolution of θ with time. Comparison of the *Reference* and numerical data obtained with the Multibody solver for $N = 50$. $t = 0$ to 5. Pendulum 1 X_1 , and pendulum 2 X_2 . Newmark Trapezoidal time integration.

Then, the error in the position of the pendulums with time is analysed in Figure A-28. The error is defined for a generic coordinate as:

$$\epsilon_q = q^N - q^{ref}. \quad (\text{A.92})$$

Now the error evolution with time does not follow periodic or linear patterns as it was seen in the previous test cases. The reason for this is that now the higher order derivatives of the acceleration do not follow simple movements, so the residual during the time integration is also chaotic. However, a linear trend can be seen in the amplitude of the oscillations: they increase linearly with time. Moreover, between $N = 50$ and $N = 100$, a quadratic convergence is observed. It is curious to see that the refined solution follows the same error shape of the one with $N = 50$, but now with 4 times less amplitude. This is of course once again due to the higher order derivatives of the acceleration, which remain approximately the same throughout the path, but now Δt is much smaller, so the residual is scaled accordingly.

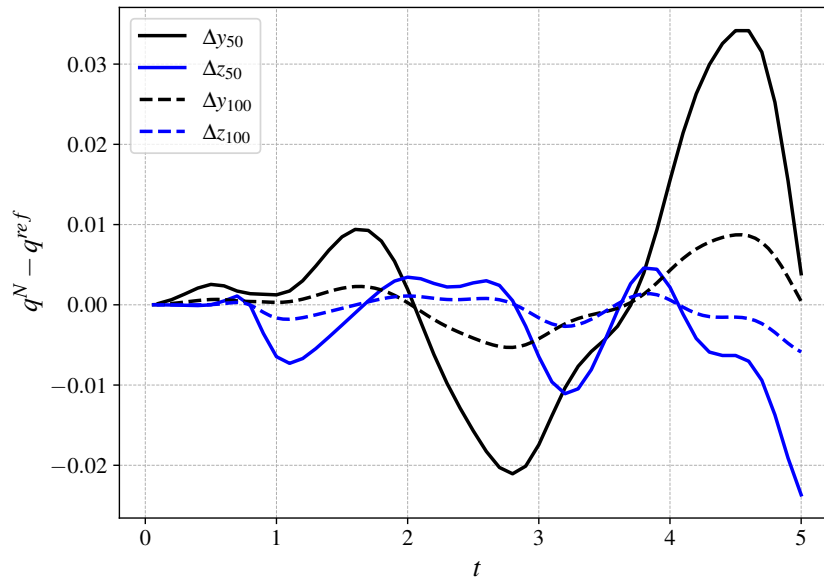


Figure A-28: Double pendulum. Analysis of Δz and Δy position error with respect to the *Reference*. $t = 0$ to 5. $N = 50$ and $N = 100$. Newmark Trapezoidal time integration.

Second order convergence for this chaotic case is verified in Figure A-29. Here the error is defined as in Equation A.91, an averaged of the position error within the time integration period. The results are plotted with a solid line for pendulum 1, X_1 , and with a cross for pendulum 2, X_2 . In both pendulums second order convergence is observed from the slope of the graph.

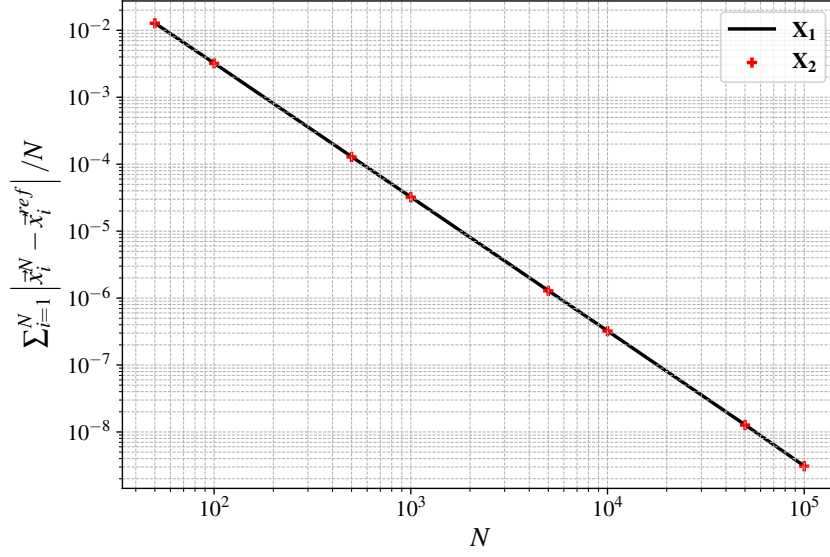


Figure A-29: Double pendulum. Analysis of convergence of numerical error with time step size. $t = 0$ to 5. Newmark Trapezoidal time integration.

Finally, energy conservation is studied in Figure A-30 and Figure A-31. Energy is defined as:

$$E = \frac{1}{2}m_1(\dot{y}_1^2 + \dot{z}_1^2) + \frac{1}{2}m_2(\dot{y}_2^2 + \dot{z}_2^2) + \frac{1}{2}I_2\dot{\theta}_2^2 + \frac{1}{2}I_2\dot{\theta}_1^2 + m_1gz_1 + m_2gz_2. \quad (\text{A.93})$$

Initially, the energy of the system is $E_0 = -18$. Energy preservation converges with smaller time steps, see Figure A-30, where a second order convergence is obtained. Energy conservation with time is shown in Figure A-31. Most of the time the energy budget is negative, which means that the integration is dissipative. Nevertheless, around $t = 5$ the system seems to recover energy due to integration error. Once again, second order convergence can be seen when the time step is refined.

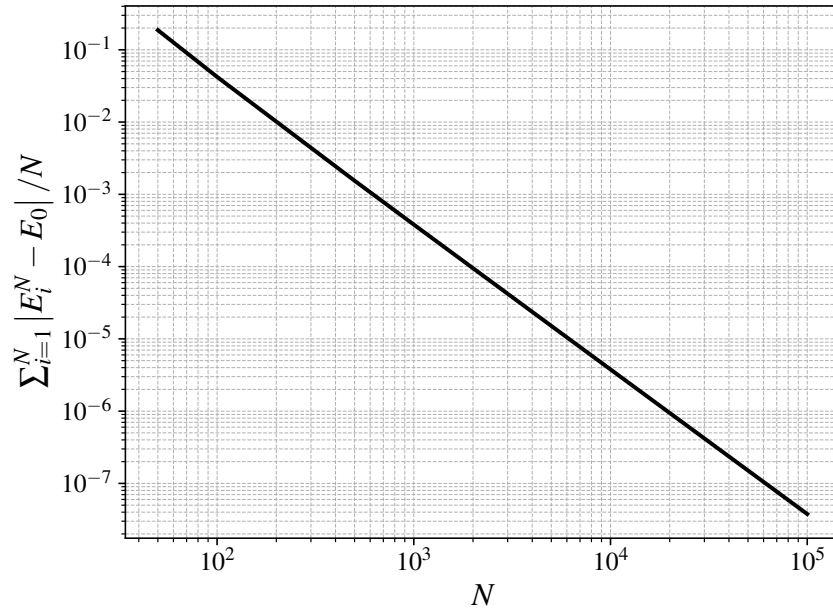


Figure A-30: Double pendulum. Energy preservation with smaller time steps. $t = 0$ to 5. Newmark Trapezoidal time integration.

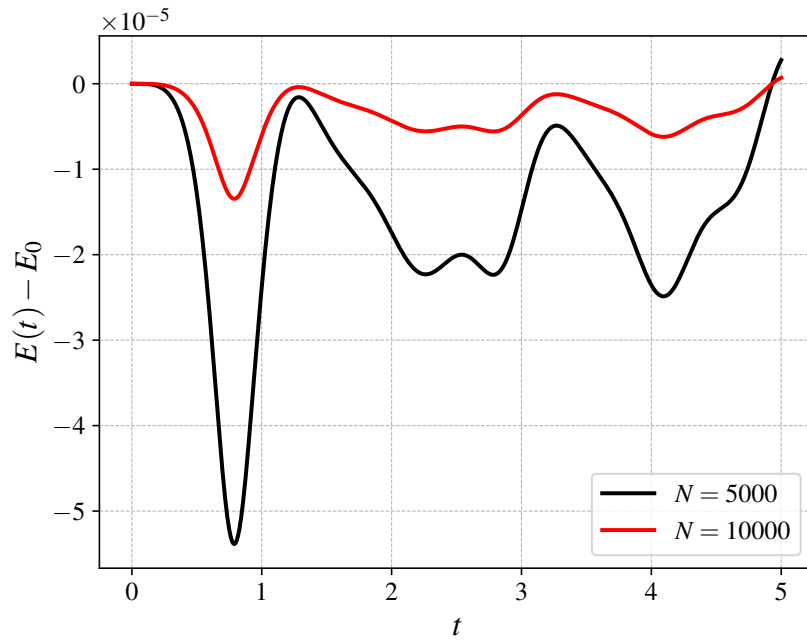


Figure A-31: Double pendulum. Energy conservation with time. $t = 0$ to 5. $N = 5000$ and $N = 10000$. Newmark Trapezoidal time integration.

Appendix B

Dragonfly strokes visualization

B.1 Hovering, phased-stroking $\psi_0 = 0^\circ$

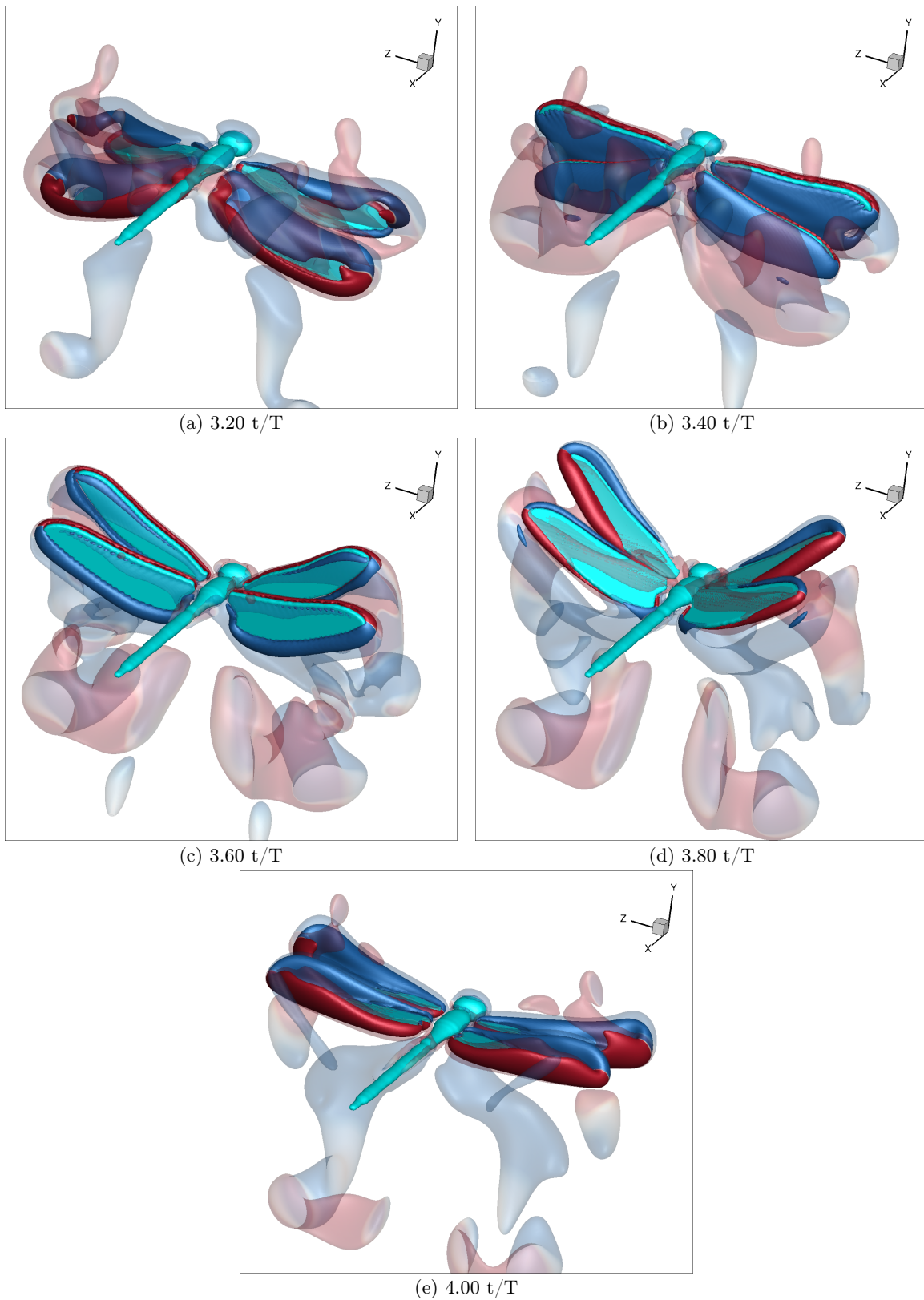


Figure B-1: Q-criterion, colored by z-vorticity component.

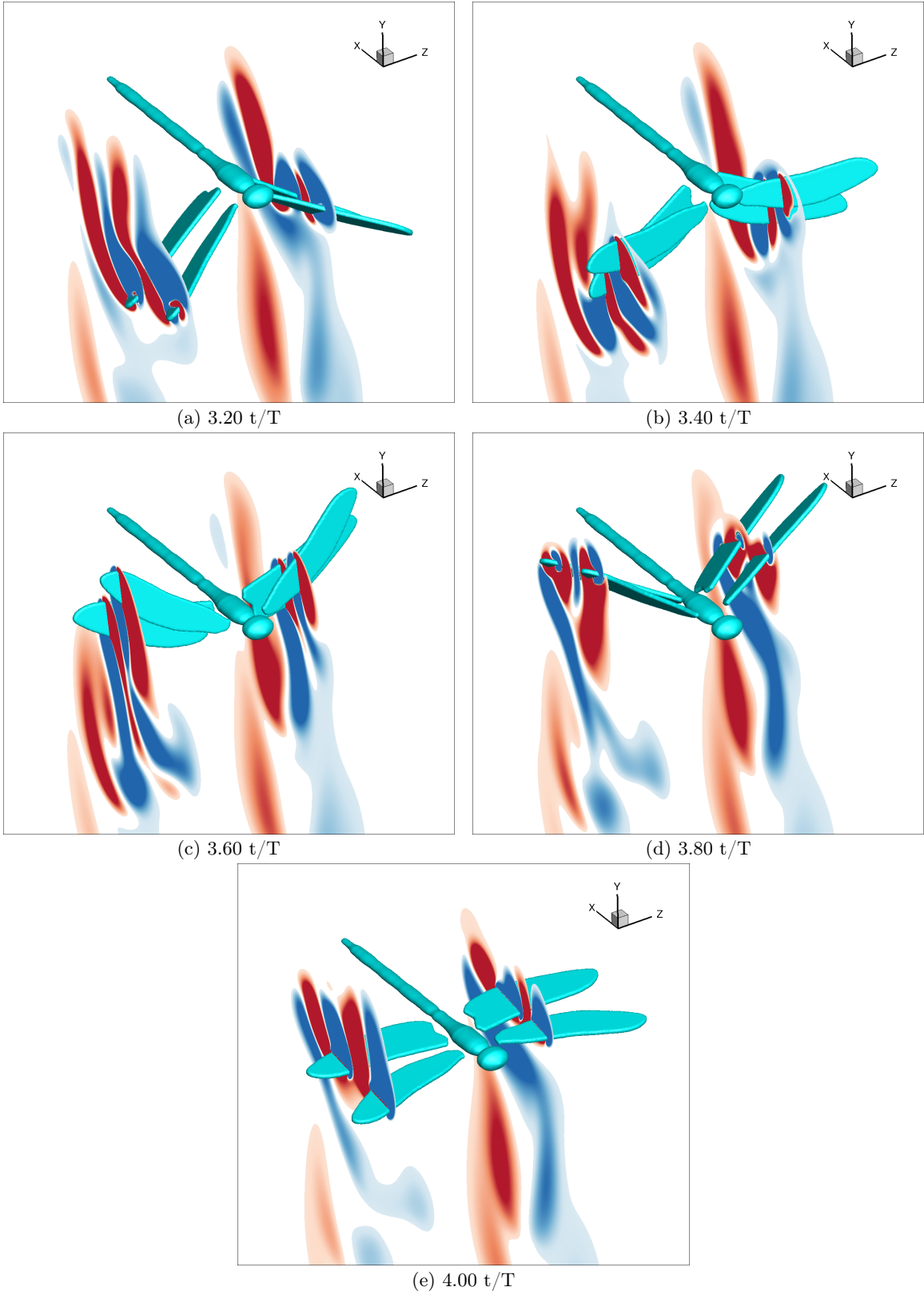


Figure B-2: Vorticity z-component slices.

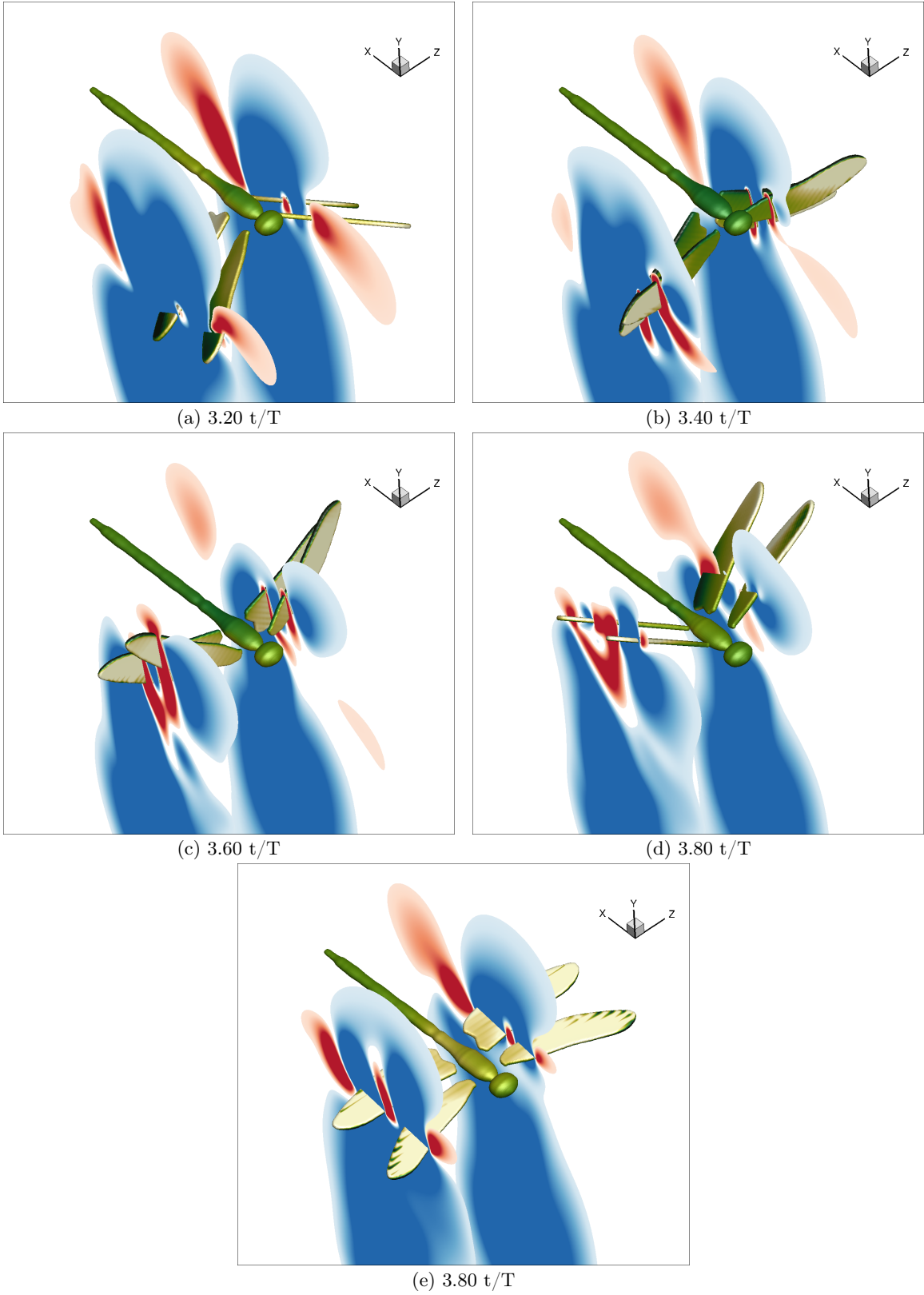


Figure B-3: Vertical y-velocity component slices.

B.2 Hovering, leading-hindwing $\psi_0 = 90^\circ$

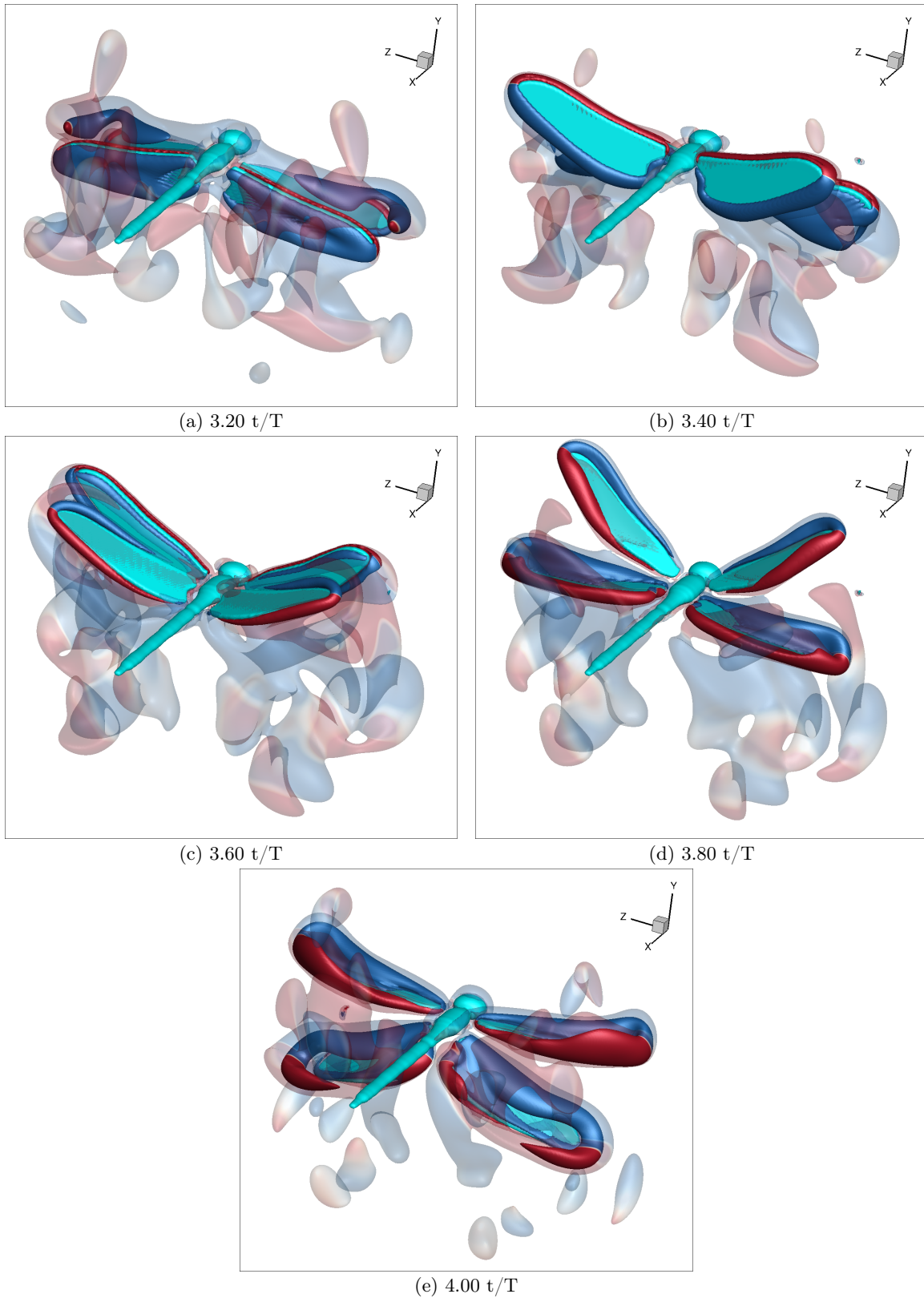


Figure B-4: Q-criterion, colored by z-vorticity component.

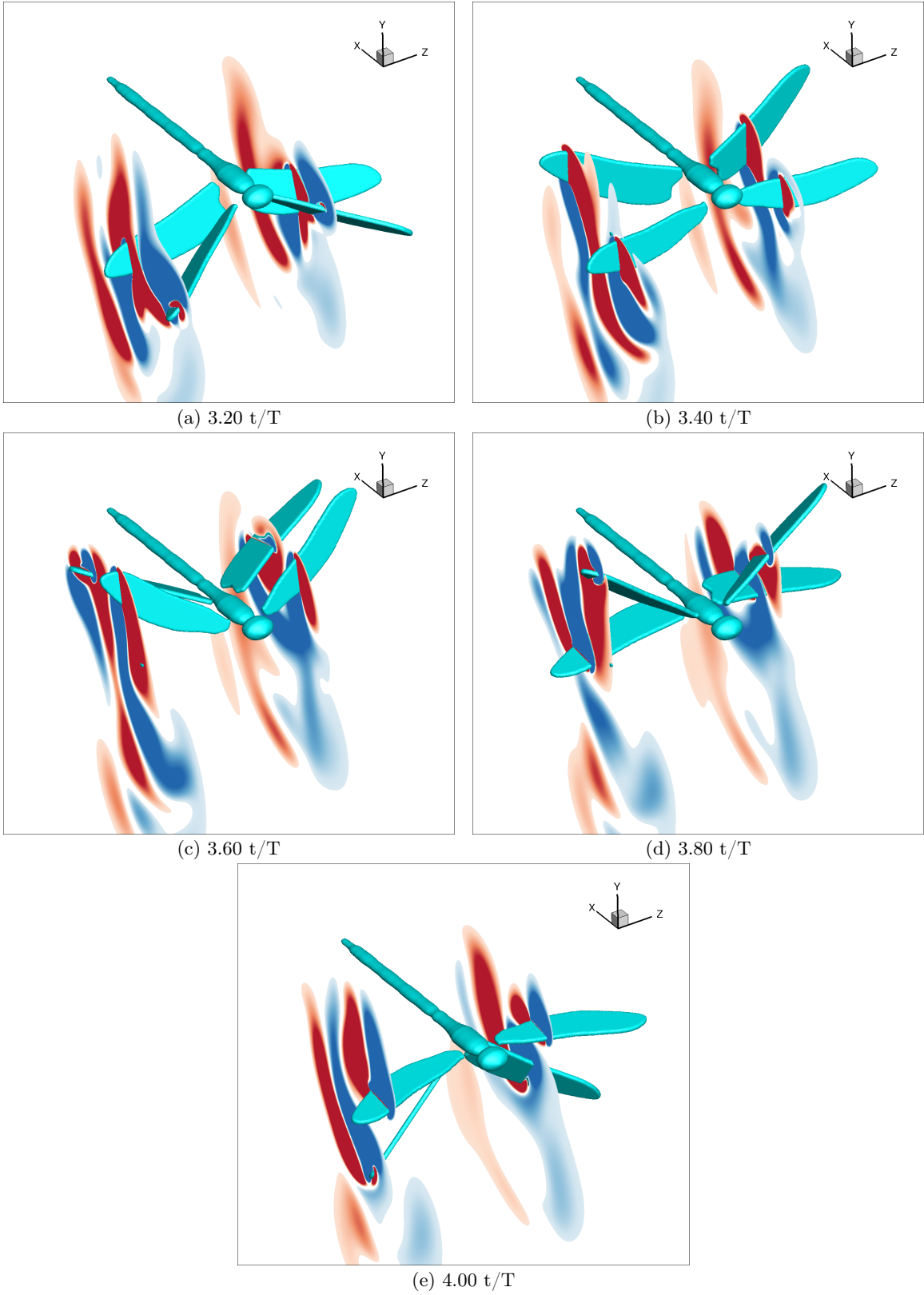


Figure B-5: Vorticity z-component slices.

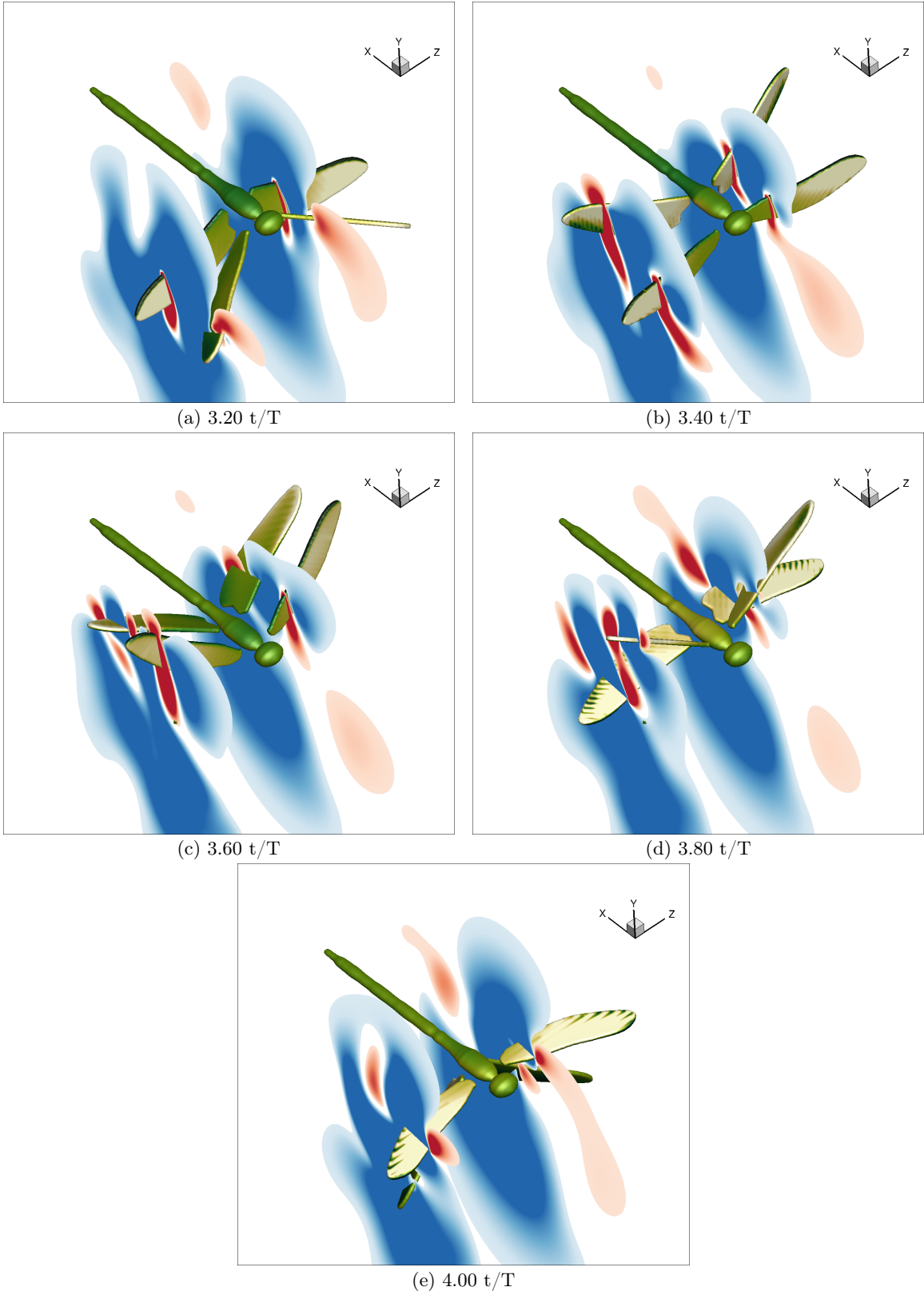


Figure B-6: Vertical y-velocity component slices.

B.3 Hovering, leading-forewing $\psi_0 = -90^\circ$

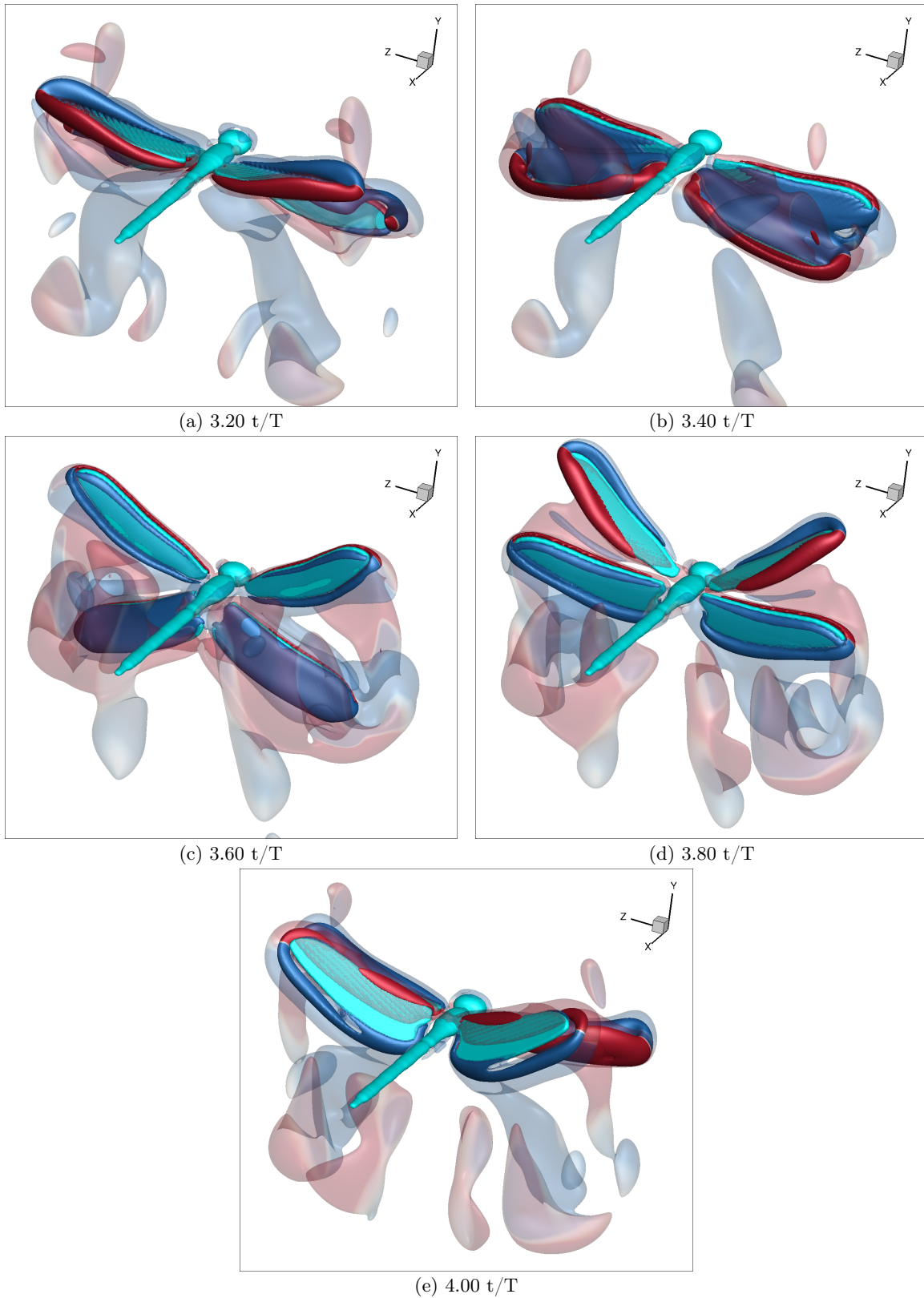


Figure B-7: Q-criterion, colored by z-vorticity component.

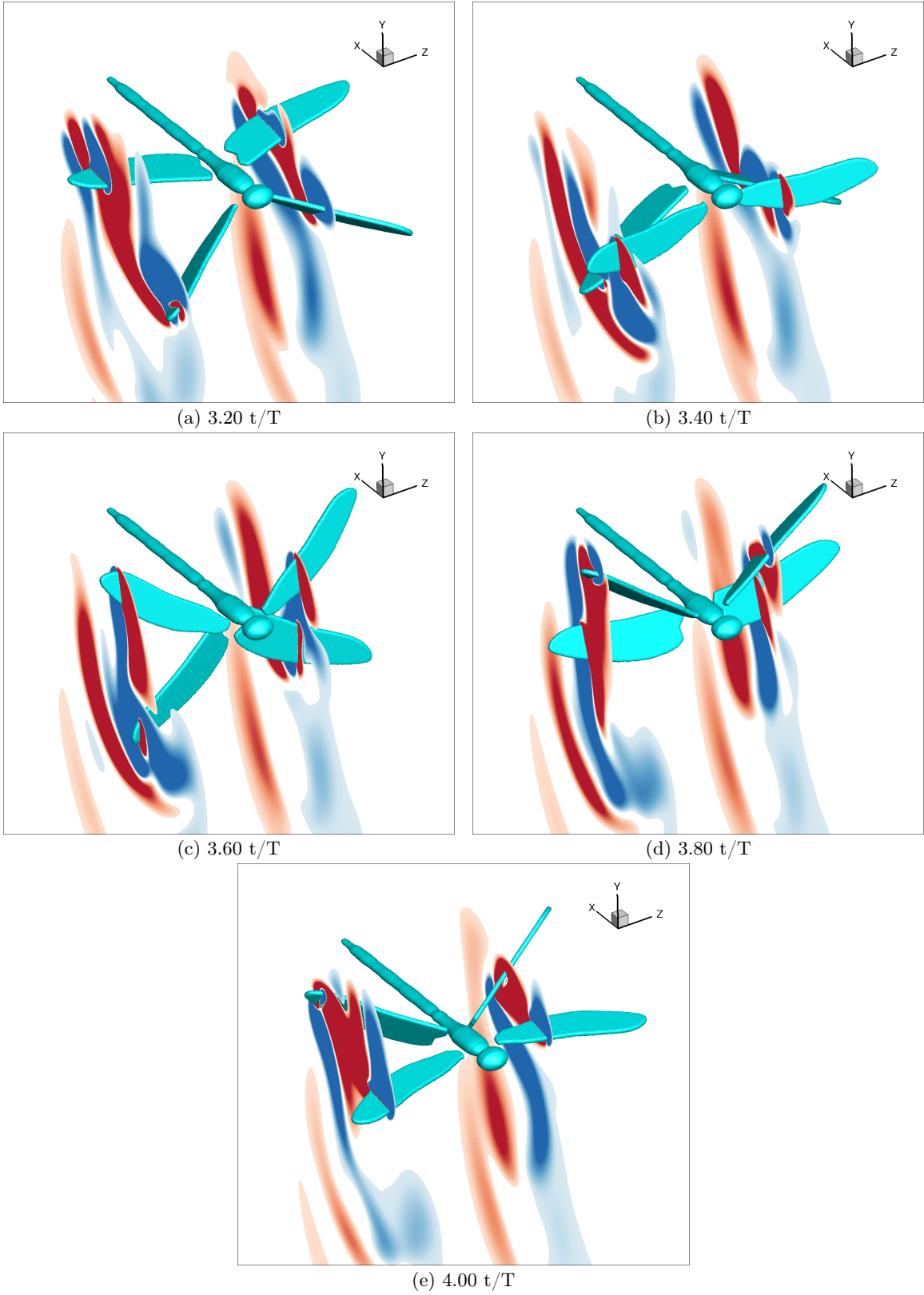


Figure B-8: Vorticity z-component slices.

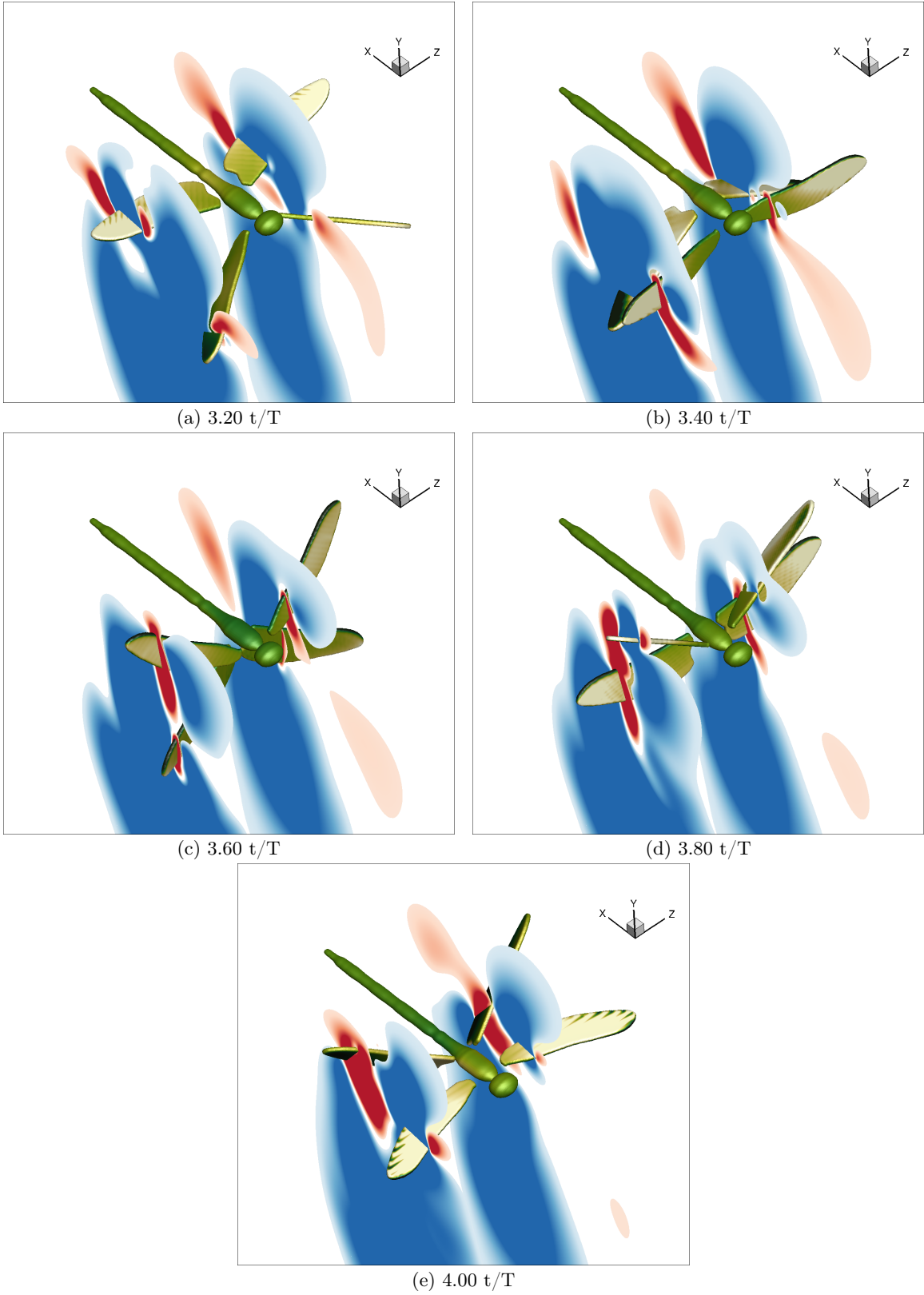


Figure B-9: Vertical y-velocity component slices.

B.4 Forward flight, counter-stroking $\psi_0 = 180^\circ$

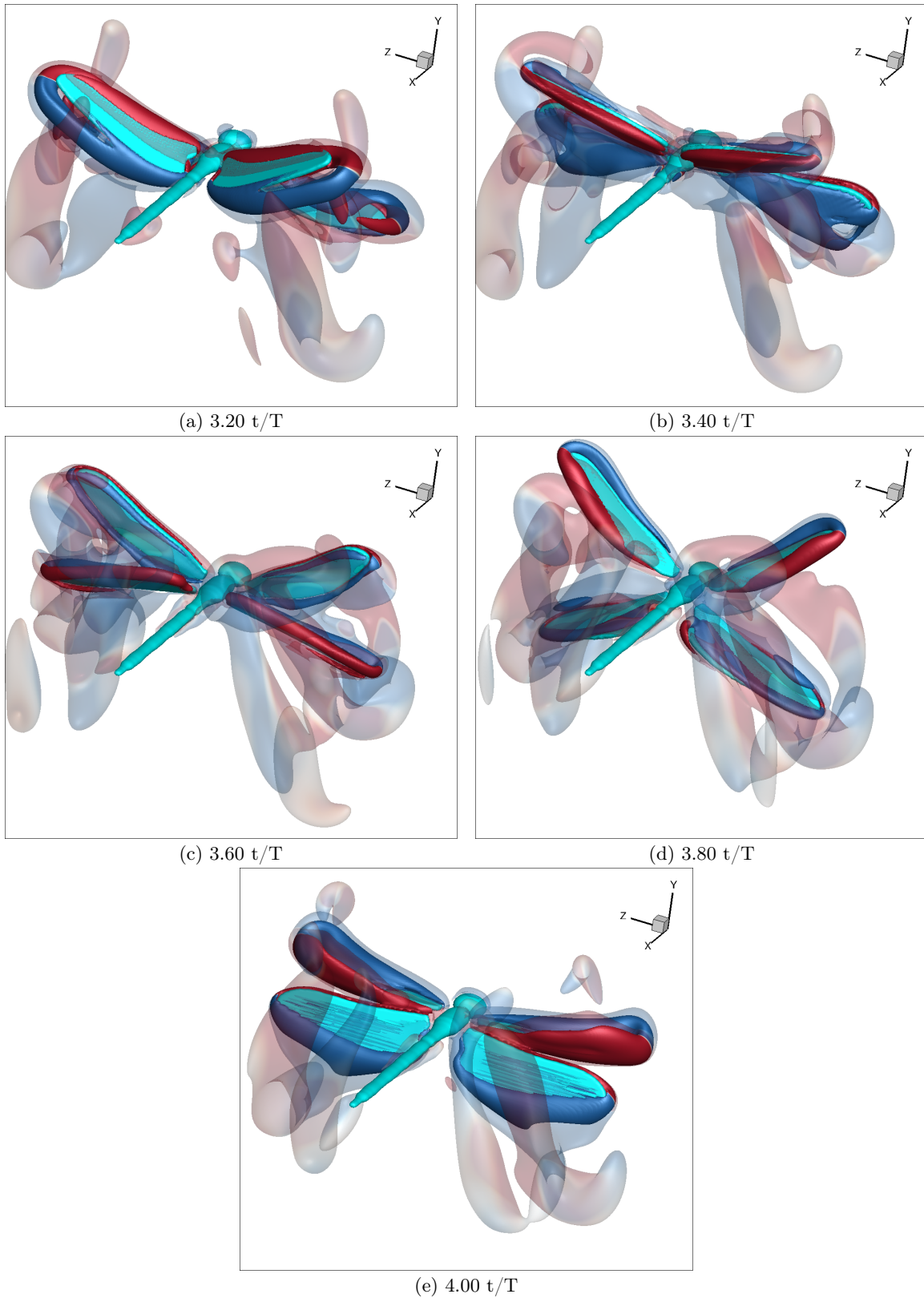


Figure B-10: Q-criterion, colored by z-vorticity component.

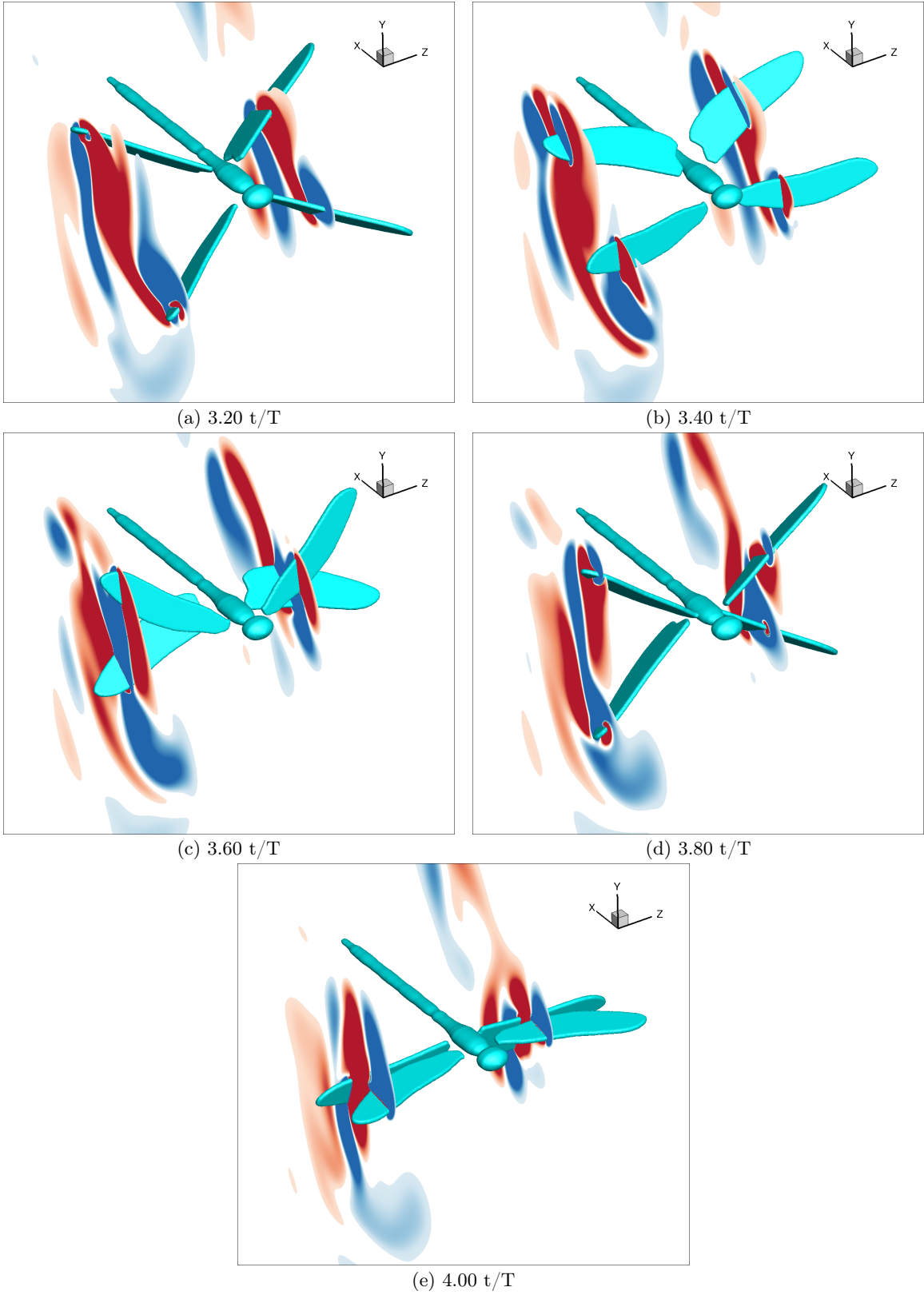


Figure B-11: Vorticity z-component slices.

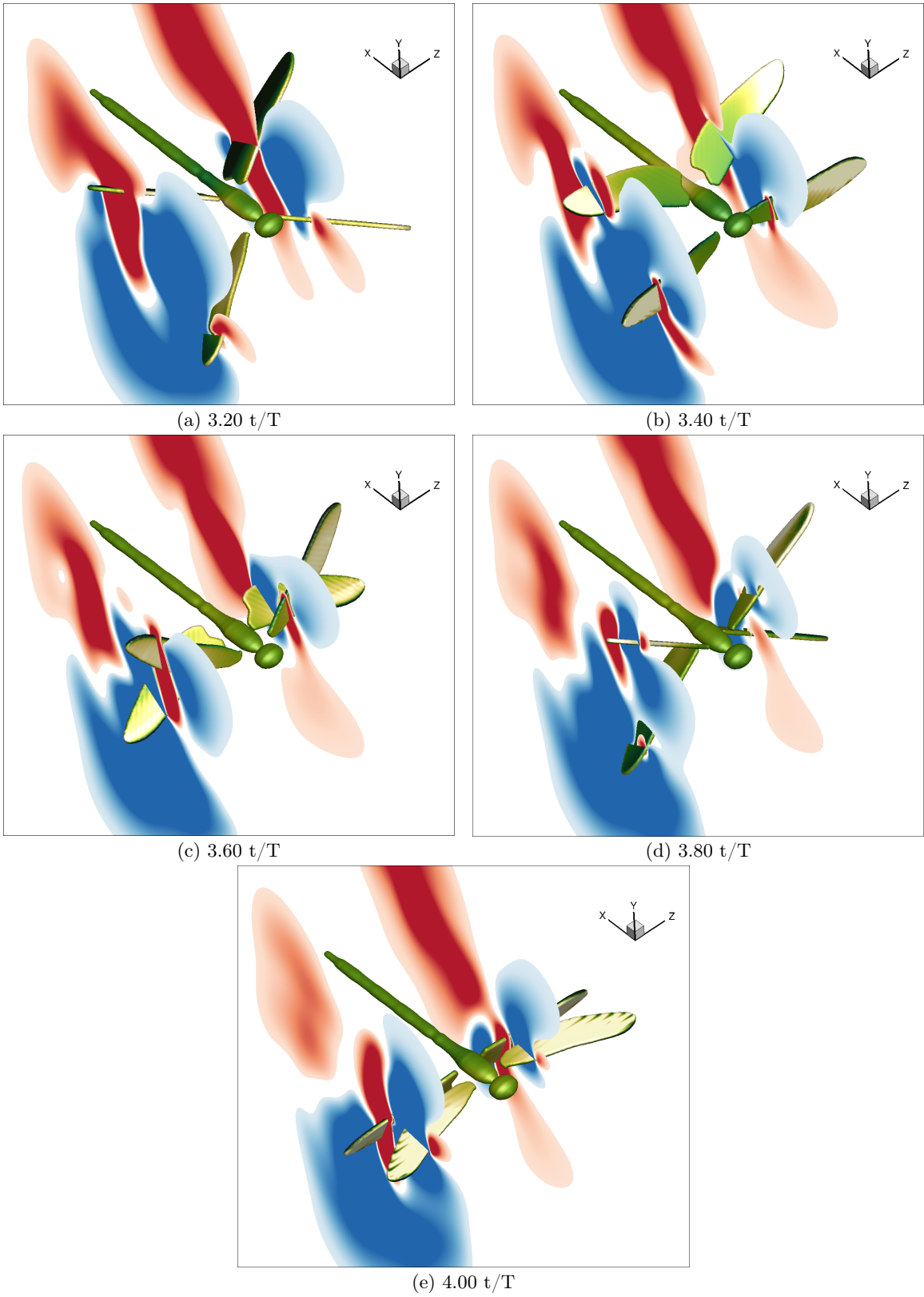
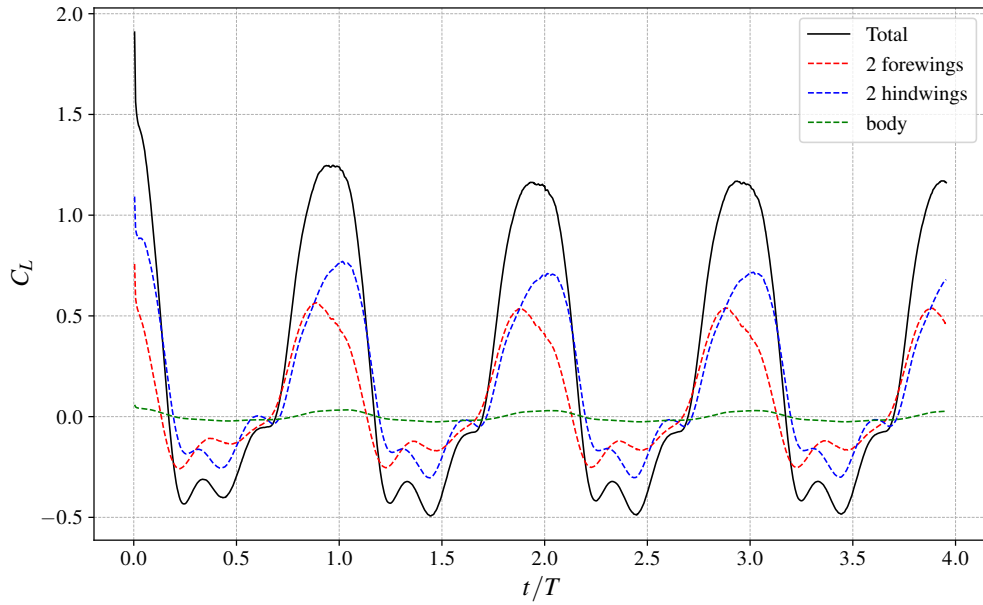


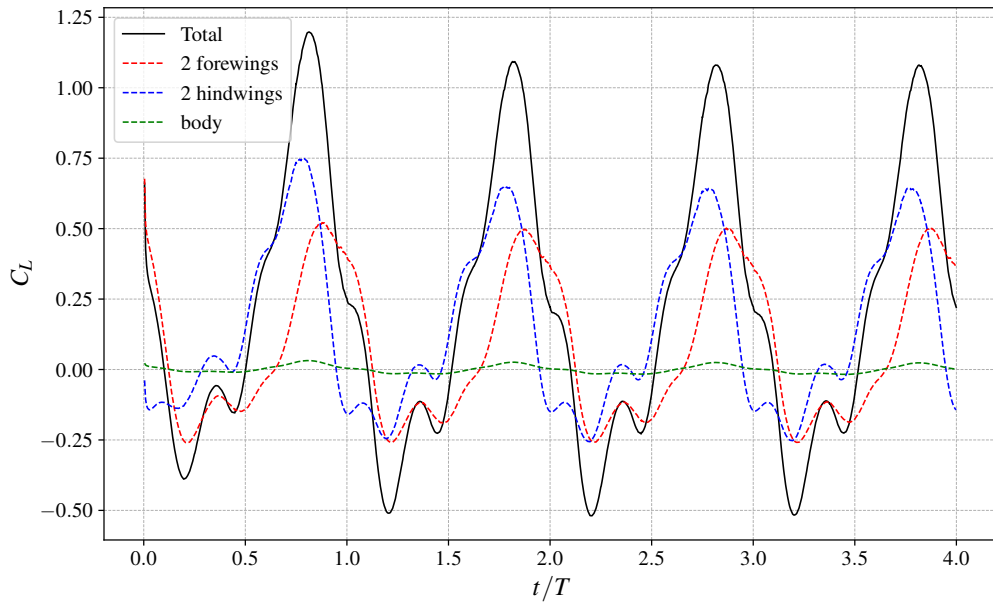
Figure B-12: Vertical y-velocity component slices.

Appendix C

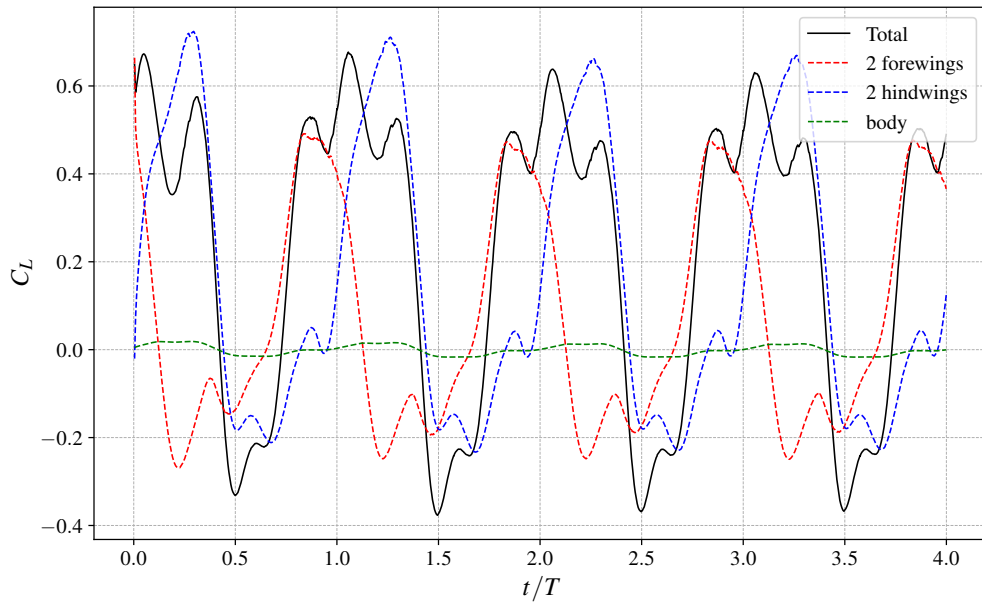
Dragonfly results for the 4 first strokes



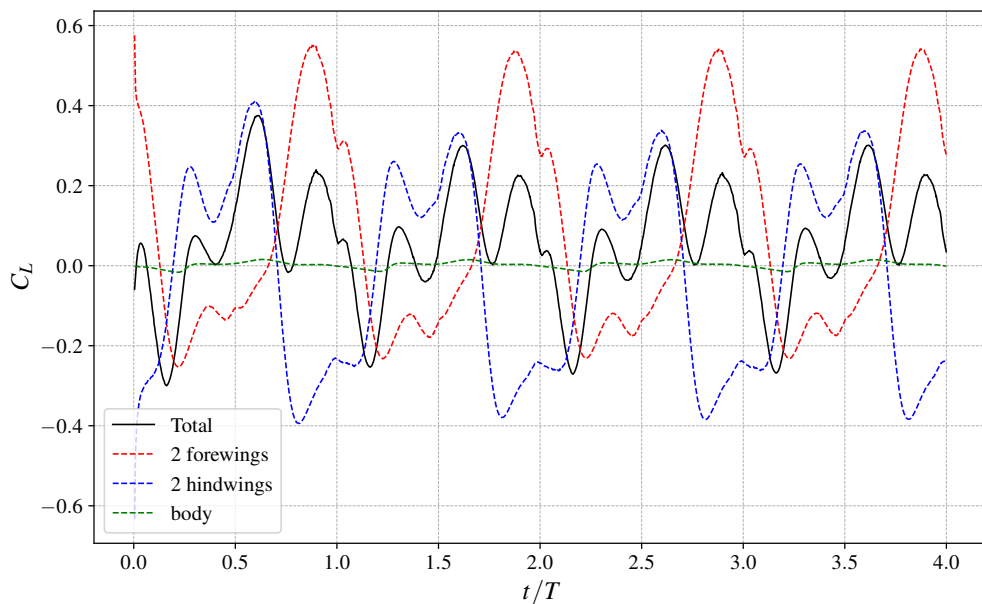
(a) Hovering, $\psi_0 = 0^\circ$, phased-stroking



(b) Hovering, $\psi_0 = 90^\circ$, leading-hindwing

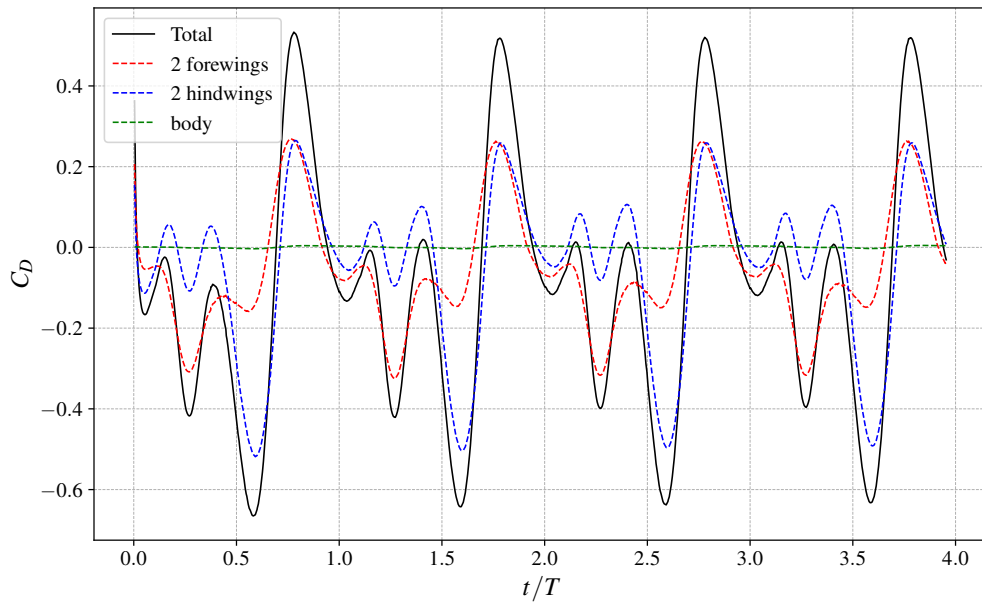


(c) Hovering, $\psi_0 = -90^\circ$, leading-forewing

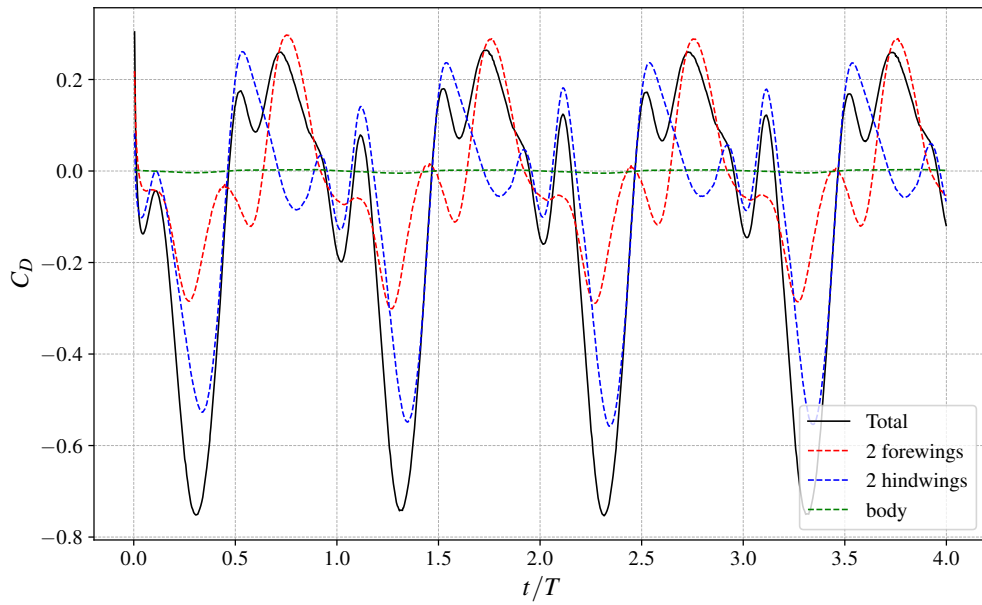


(d) Forward flight, $\psi_0 = 180^\circ$, counter-stroking

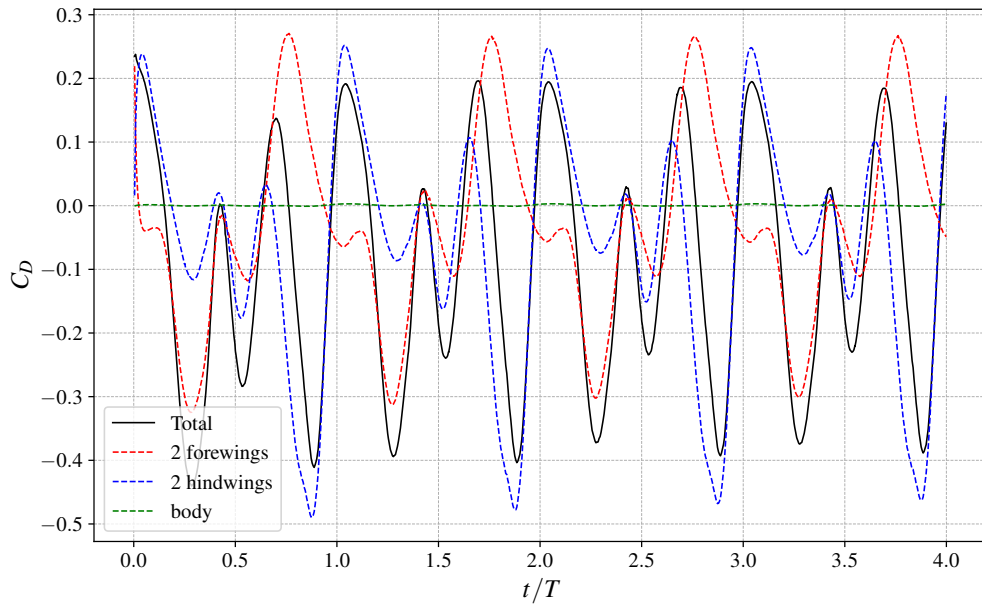
Figure C-1: Lift coefficients for different strokes. 4 first flapping cycles.



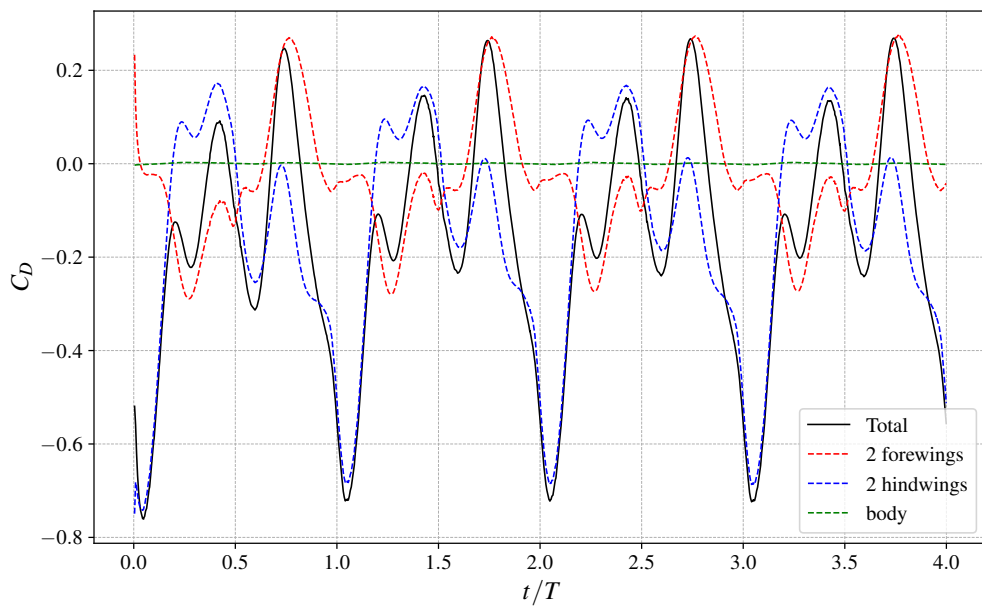
(a) Hovering, $\psi_0 = 0^\circ$, phased-stroking



(b) Hovering, $\psi_0 = 90^\circ$, leading-hindwing

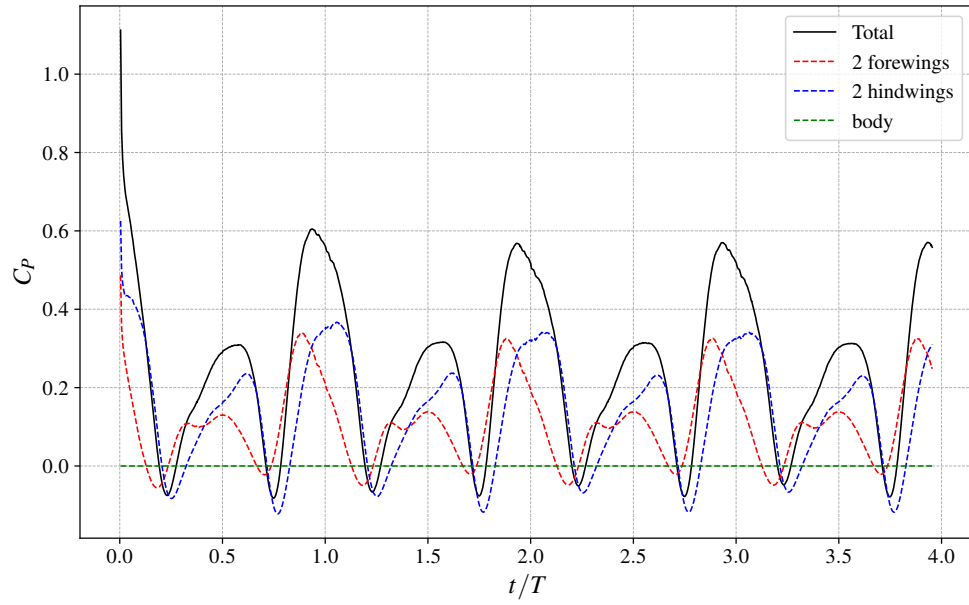


(c) Hovering, $\psi_0 = -90^\circ$, leading-forewing

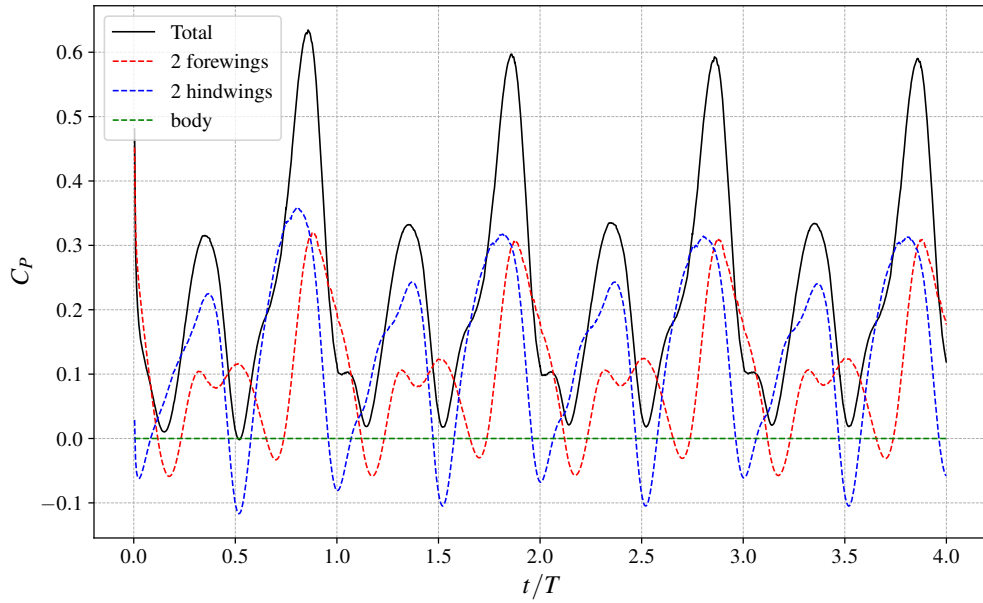


(d) Forward flight, $\psi_0 = 180^\circ$, counter-stroking

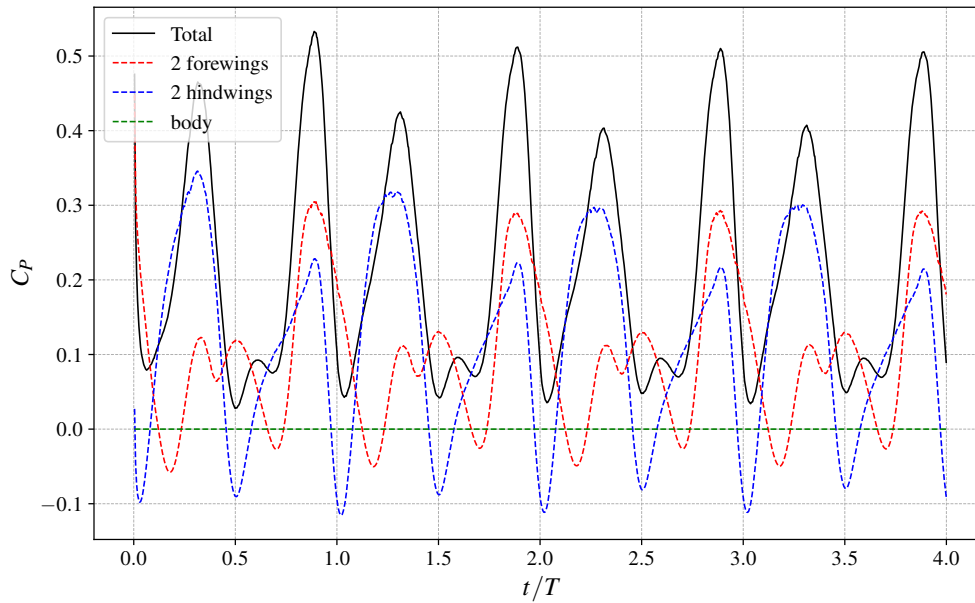
Figure C-2: Drag coefficients for different strokes. 4 first flapping cycles.



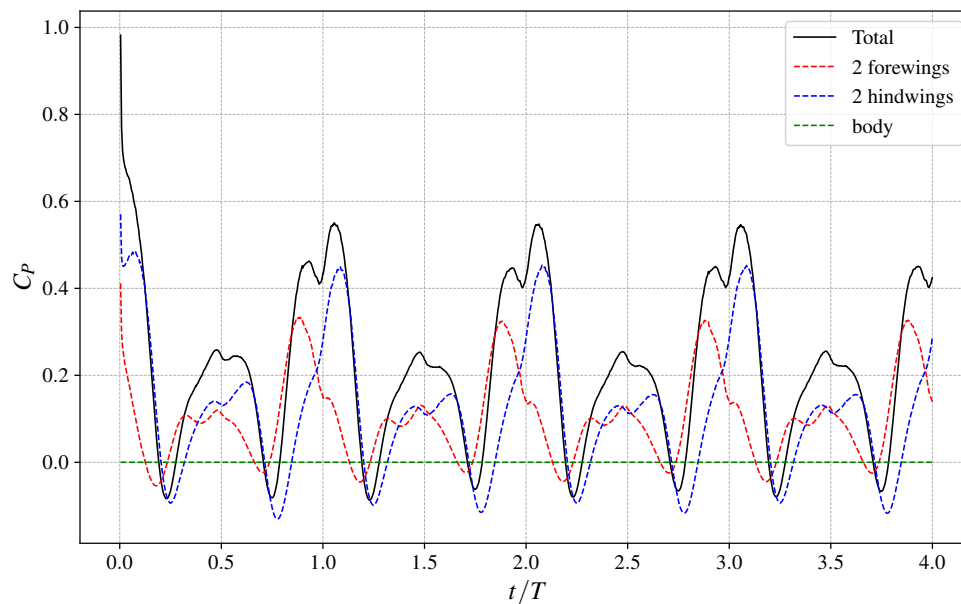
(a) Hovering, $\psi_0 = 0^\circ$, phased-stroking



(b) Hovering, $\psi_0 = 90^\circ$, leading-hindwing

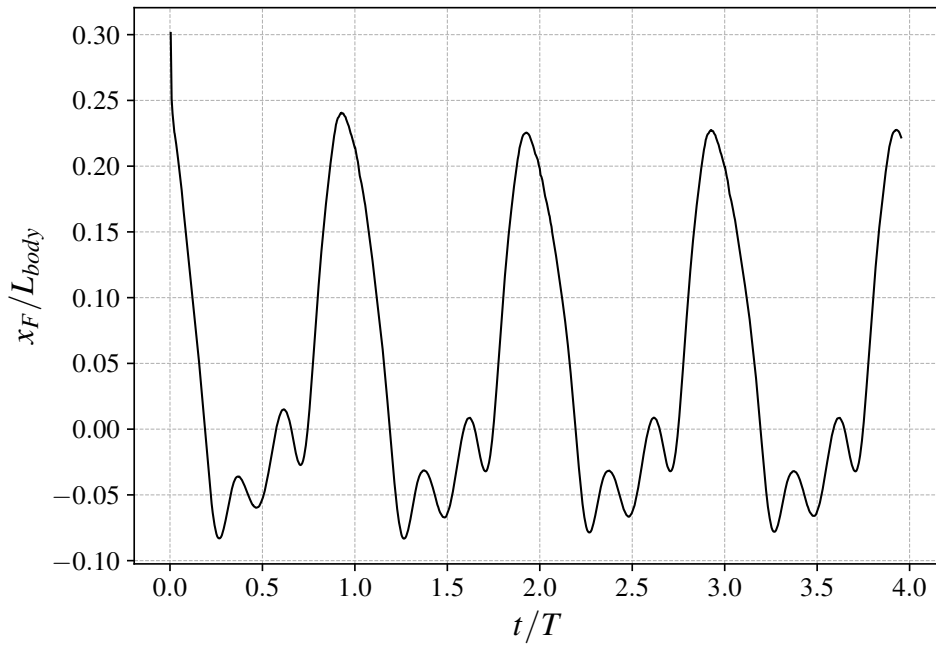


(c) Hovering, $\psi_0 = -90^\circ$, leading-forewing

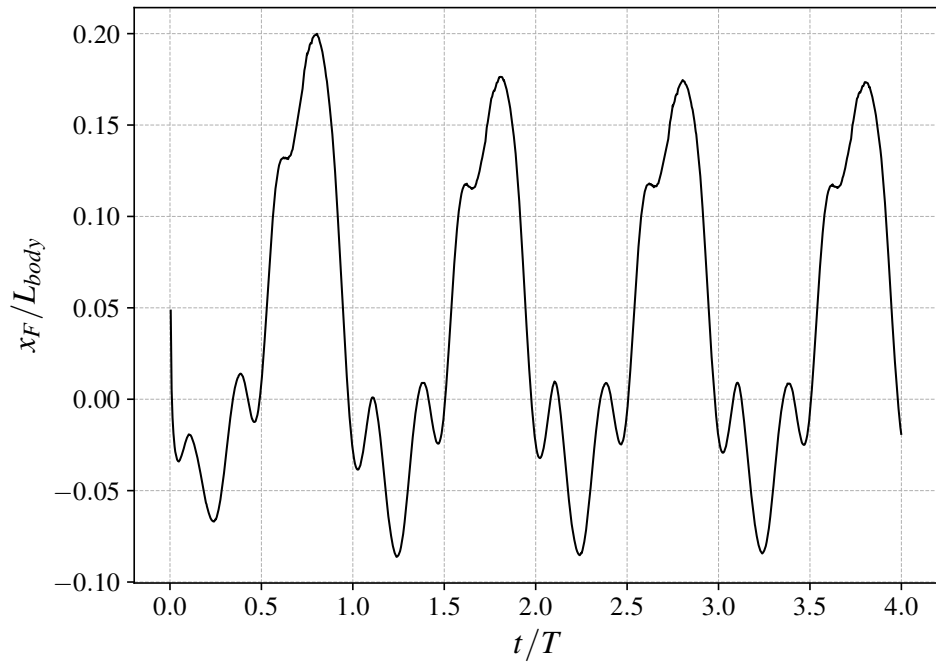


(d) Forward flight, $\psi_0 = 180^\circ$, counter-stroking

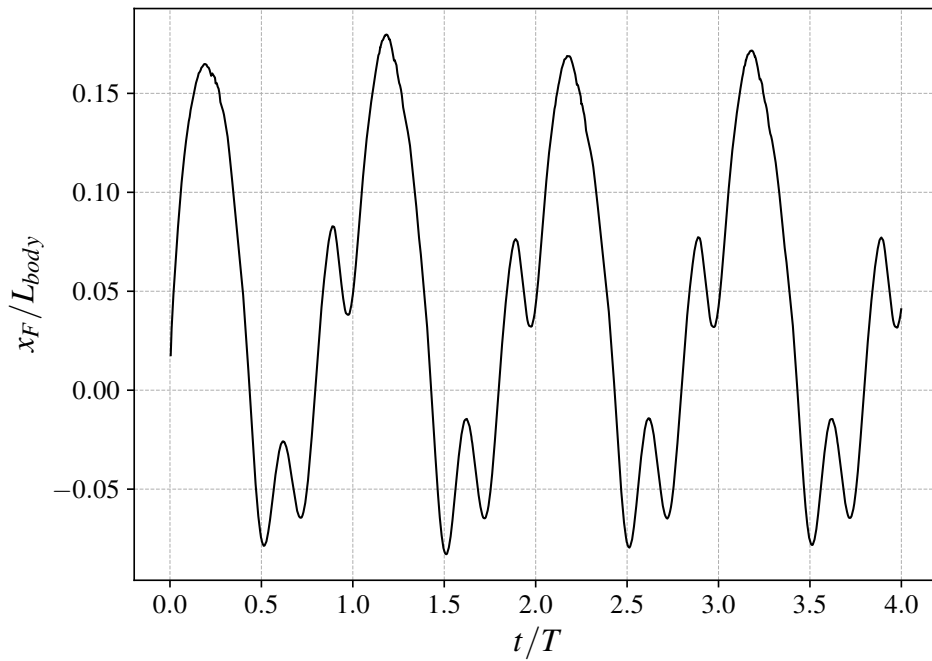
Figure C-3: Power coefficients for different strokes. 4 first flapping cycles.



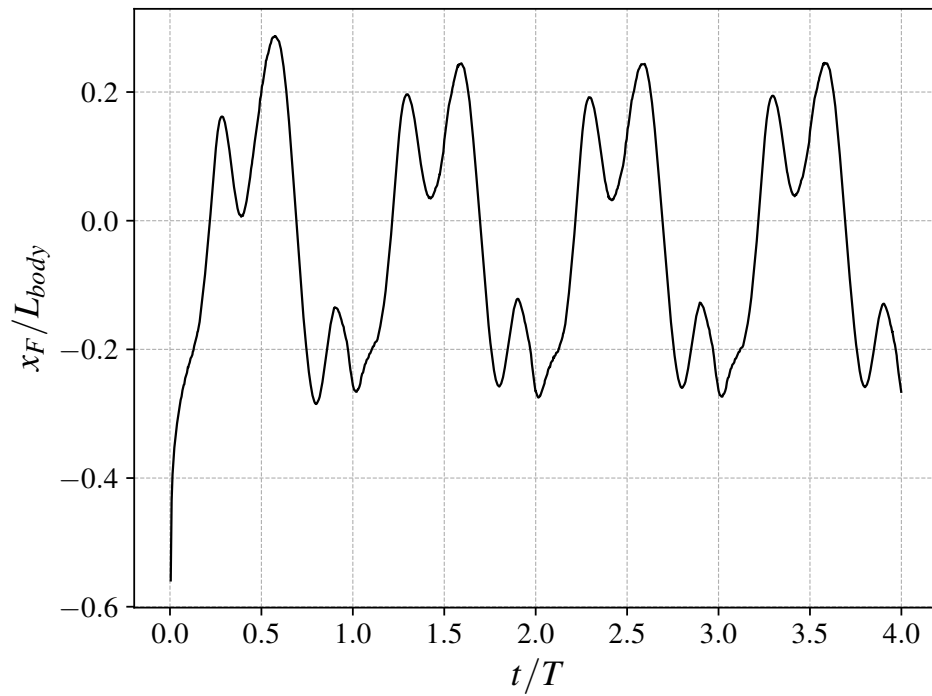
(a) Hovering, $\psi_0 = 0^\circ$, phased-stroking



(b) Hovering, $\psi_0 = 90^\circ$, leading-hindwing



(c) Hovering, $\psi_0 = -90^\circ$, leading-forewing



(d) Forward flight, $\psi_0 = 180^\circ$, counter-stroking

Figure C-4: Non-dimensional x-coordinate of point of force application. 4 first flapping cycles.

Bibliography

- [1] Dragonfly and damselfly spotting in the national park. british dragonfly society. <https://www.visitthebroads.co.uk/the-blog/dragonfly-and-damselfly-spotting-in-the-national-park> (accessed: 11.11.2024).
- [2] Mahmoud E Abd El-Latief, Khairy Elsayed, and Mohamed Madbouli Abdelrahman. Aerodynamic study of the corrugated airfoil at ultra-low reynolds number. *Advances in Mechanical Engineering*, 11(10):1687814019884164, 2019.
- [3] Erik Neumann. Double Pendulum. <https://www.myphysicslab.com/pendulum/double-pendulum-en.html> (accessed: 10.08.2023).
- [4] Stefan Hickel. INCA CFD. <https://inca.cfd/> (accessed: 26.10.2024).
- [5] David E Alexander. Wind tunnel studies of turns by flying dragonflies. *Journal of Experimental Biology*, 122(1):81–98, 1986.
- [6] Hikaru Aono, Fuyou Liang, and Hao Liu. Near-and far-field aerodynamics in insect hovering flight: an integrated computational study. *Journal of experimental biology*, 211(2):239–257, 2008.
- [7] Akira Azuma. *The Biokinetics of Flying and Swimming*. Springer Science & Business Media, 2012.
- [8] Akira Azuma, Soichi Azuma, Isao Watanabe, and Toyohiko Furuta. Flight mechanics of a dragonfly. *Journal of experimental biology*, 116(1):79–107, 1985.
- [9] Akira Azuma and Tadaaki Watanabe. Flight performance of a dragonfly. *Journal of experimental biology*, 137(1):221–252, 1988.
- [10] Caleb Barnes and Miguel Visbal. High-fidelity simulations of a corrugated airfoil. In *50th AIAA Aerospace Sciences Meeting including the New Horizons Forum and Aerospace Exposition*, page 753, 2012.
- [11] Yagiz Bayiz, Mohammad Ghanaatpishe, Hosam Fathy, and Bo Cheng. Hovering efficiency comparison of rotary and flapping flight for rigid rectangular wings via dimensionless multi-objective optimization. *Bioinspiration & Biomimetics*, 13(4):046002, 2018.
- [12] Hadar Ben-Gida and Roi Gurka. The leading-edge vortex over a swift-like high-aspect-ratio wing with nonlinear swept-back geometry. *Bioinspiration & Biomimetics*, 17(6):066016, 2022.
- [13] James M Birch and Michael H Dickinson. Spanwise flow and the attachment of the leading-edge vortex on insect wings. *Nature*, 412(6848):729–733, 2001.
- [14] James M Birch and Michael H Dickinson. The influence of wing–wake interactions on the production of aerodynamic forces in flapping flight. *Journal of experimental biology*, 206(13):2257–2272, 2003.

- [15] James M Birch, William B Dickson, and Michael H Dickinson. Force production and flow structure of the leading edge vortex on flapping wings at high and low reynolds numbers. *Journal of Experimental Biology*, 207(7):1063–1072, 2004.
- [16] Richard J Bomphrey, Toshiyuki Nakata, Per Henningsson, and Huai-Ti Lin. Flight of the dragonflies and damselflies. *Philosophical Transactions of the Royal Society B: Biological Sciences*, 371(1704):20150389, 2016.
- [17] M Braza, PHHM Chassaing, and H Ha Minh. Numerical study and physical analysis of the pressure and velocity fields in the near wake of a circular cylinder. *Journal of Fluid Mechanics*, 165:79–130, 1986.
- [18] Jason T Bried and Gary N Ervin. Intraspecific models and spatiotemporal context of size–mass relationships in adult dragonflies. *Journal of the North American Benthological Society*, 26(4):681–693, 2007.
- [19] Timothy M Broering and Yong-Sheng Lian. The effect of phase angle and wing spacing on tandem flapping wings. *Acta Mechanica Sinica*, 28:1557–1571, 2012.
- [20] Timothy M Broering, Yongsheng Lian, and William Henshaw. Numerical investigation of energy extraction in a tandem flapping wing configuration. *AIAA Journal*, 50(11):2295–2307, 2012.
- [21] Lorenzo Catalani. *Modelling of Vortex Generator*. PhD thesis, 07 2019.
- [22] Long Chen, Bo Cheng, and Jianghao Wu. Vorticity dynamics and stability of the leading-edge vortex on revolving wings. *Physics of Fluids*, 35(9), 2023.
- [23] Long Chen, Luyao Wang, Chao Zhou, Jianghao Wu, and Bo Cheng. Effects of reynolds number on leading-edge vortex formation dynamics and stability in revolving wings. *Journal of Fluid Mechanics*, 931:A13, 2022.
- [24] Long Chen, Jianghao Wu, and Bo Cheng. Volumetric measurement and vorticity dynamics of leading-edge vortex formation on a revolving wing. *Experiments in Fluids*, 60:1–15, 2019.
- [25] Long Chen, Jianghao Wu, and Bo Cheng. Leading-edge vortex formation and transient lift generation on a revolving wing at low reynolds number. *Aerospace Science and Technology*, 97:105589, 2020.
- [26] YH Chen, M Skote, Y Zhao, and WM Huang. Dragonfly (*sympetrum flaveolum*) flight: Kinematic measurement and modelling. *Journal of Fluids and Structures*, 40:115–126, 2013.
- [27] Bo Cheng, Sanjay P Sane, Giovanni Barbera, Daniel R Troolin, Tyson Strand, and Xinyan Deng. Three-dimensional flow visualization and vorticity dynamics in revolving wings. *Experiments in Fluids*, 54:1–12, 2013.
- [28] Nasim Chitsaz, Romeo Marian, and Javaan Chahl. Experimental method for 3d reconstruction of odonata wings (methodology and dataset). *PLoS One*, 15(4):e0232193, 2020.
- [29] Nasim Chitsaz, Kamran Siddiqui, Romeo Marian, and Javaan Chahl. An experimental study of the aerodynamics of micro corrugated wings at low reynolds number. *Experimental Thermal and Fluid Science*, 121:110286, 2021.
- [30] Nasim Chitsaz, Kamran Siddiqui, Romeo Marian, and Javaan Chahl. Numerical and experimental analysis of three-dimensional microcorrugated wing in gliding flight. *Journal of Fluids Engineering*, 144(1):011205, 2022.
- [31] Hugh W Coleman and W Glenn Steele. *Experimentation, Validation, and Uncertainty Analysis for Engineers*. John Wiley & Sons, 2018.

- [32] SA Combes, DE Rundle, JM Iwasaki, and James Dewitt Crall. Linking biomechanics and ecology through predator–prey interactions: flight performance of dragonflies and their prey. *Journal of Experimental Biology*, 215(6):903–913, 2012.
- [33] J CORNISH, III. Vortex flows. In *Applied Aerodynamics Conference*, page 1812, 1983.
- [34] GCHE De Croon, M Perçin, B Remes, R Ruijsink, and C De Wagter. The delfly. *Dordrecht: Springer Netherlands*. doi, 10:978–94, 2016.
- [35] Michael Dickinson. Insect flight. *Current Biology*, 16(9):R309–R314, 2006.
- [36] Michael H Dickinson, Fritz-Olaf Lehmann, and Sanjay P Sane. Wing rotation and the aerodynamic basis of insect flight. *Science*, 284(5422):1954–1960, 1999.
- [37] James Diebel et al. Representing attitude: Euler angles, unit quaternions, and rotation vectors. *Matrix*, 58(15-16):1–35, 2006.
- [38] Jeff D Eldredge and Anya R Jones. Leading-edge vortices: mechanics and modeling. *Annual Review of Fluid Mechanics*, 51:75–104, 2019.
- [39] Charles P Ellington, Coen Van Den Berg, Alexander P Willmott, and Adrian LR Thomas. Leading-edge vortices in insect flight. *Nature*, 384(6610):626–630, 1996.
- [40] Charles Porter Ellington. The aerodynamics of hovering insect flight. i. the quasi-steady analysis. *Philosophical Transactions of the Royal Society of London. B, Biological Sciences*, 305(1122):1–15, 1984.
- [41] Charles Porter Ellington. The aerodynamics of hovering insect flight. iv. aerodynamic mechanisms. *Philosophical Transactions of the Royal Society of London. B, Biological Sciences*, 305(1122):79–113, 1984.
- [42] Gary E Erickson and James F Campbell. Flow visualization of vortices locked by spanwise blowing over wings featuring a unique leading and trailing-edge flap system. Technical report, 1975.
- [43] Uwe Fey, Michael König, and Helmut Eckelmann. A new strouhal–reynolds-number relationship for the circular cylinder in the range $47 < \text{Re} < 2 \times 10^5$. *Physics of Fluids*, 10(7):1547–1549, 1998.
- [44] Peter Freymuth, Karl E Gustafson, and Robert Leben. Visualization and computation of hovering mode vortex dynamics. In *Vortex Methods and Vortex Motion*, pages 143–169. SIAM, 1991.
- [45] Yusuke Fujita and Makoto Iima. Aerodynamic performance of dragonfly wing model that starts impulsively: how vortex motion works. *Journal of Fluid Science and Technology*, 18(1):JFST0013–JFST0013, 2023.
- [46] Yusuke Fujita and Makoto Iima. Dynamic lift enhancement mechanism of dragonfly wing model by vortex-corrugation interaction. *arXiv preprint arXiv:2304.13942*, 2023.
- [47] Matteo Giacobello. *Wake structure of a transversely rotating sphere at moderate Reynolds numbers*. PhD thesis, University of Melbourne, Department of Mechanical and Manufacturing Engineering, 2005.
- [48] H Glauert. The force and moment on an oscillating aerofoil. R. & M. no. 1242. *British ARC*, 1929.
- [49] HR Hamdani, A Aizaz, and MA Naqvi. Force generation mechanisms by an insect wing in hovering motion with different flipping schedules. *Journal of Applied Fluid Mechanics*, 10(1):433–445, 2017.

- [50] Jeffrey W Hamstra. *The F-35 Lightning II: from Concept to Cockpit*. American Institute of Aeronautics and Astronautics, Inc., 2019.
- [51] Ronald D Henderson. Details of the drag curve near the onset of vortex shedding. *Physics of Fluids*, 7(9):2102–2104, 1995.
- [52] Cheng-Ta Hsieh, Chun-Fei Kung, Chien C Chang, and Chin-Chou Chu. Unsteady aerodynamics of dragonfly using a simple wing–wing model from the perspective of a force decomposition. *Journal of Fluid Mechanics*, 663:233–252, 2010.
- [53] Military.com. CH-53E Super Stallion. <https://www.military.com/equipment/ch-53e-super-stallion> (accessed: 23.08.2023).
- [54] Zheng Hu and Xin-Yan Deng. Aerodynamic interaction between forewing and hindwing of a hovering dragonfly. *Acta Mechanica Sinica*, 30(6):787–799, 2014.
- [55] Paulin Kantue. *Online parameter estimation of a miniature unmanned helicopter using neural network techniques*. PhD thesis, Doctoral dissertation, University of the Witwatersrand, South Africa, 2011.
- [56] Joseph Katz and Allen Plotkin. *Low-Speed Aerodynamics*, volume 13. Cambridge university press, 2001.
- [57] Matthew Keennon, Karl Klingebiel, and Henry Won. Development of the nano hummingbird: A tailless flapping wing micro air vehicle. In *50th AIAA aerospace sciences meeting including the new horizons forum and aerospace exposition*, page 588, 2012.
- [58] Manpreet Kohli, Harald Letsch, Carola Greve, Olivier Béthoux, Isabelle Deregnacourt, Shanlin Liu, Xin Zhou, Alexander Donath, Christoph Mayer, Lars Podsiadlowski, et al. Evolutionary history and divergence times of odonata (dragonflies and damselflies) revealed through transcriptomics. *Isience*, 24(11), 2021.
- [59] Weihong Kong and You Li. Experimental study on dynamic stall of airfoil in rotor reverse flow region. *Aerospace*, 10(2):170, 2023.
- [60] Ryoichi Kurose and Satoru Komori. Drag and lift forces on a rotating sphere in a linear shear flow. *Journal of Fluid Mechanics*, 384:183–206, 1999.
- [61] David Lentink and Michael H Dickinson. Rotational accelerations stabilize leading edge vortices on revolving fly wings. *Journal of Experimental Biology*, 212(16):2705–2719, 2009.
- [62] Chengyu Li and Haibo Dong. Wing kinematics measurement and aerodynamics of a dragonfly in turning flight. *Bioinspiration & biomimetics*, 12(2):026001, 2017.
- [63] Yongsheng Lian, Timothy Broering, Kyle Hord, and Russell Prater. The characterization of tandem and corrugated wings. *Progress in Aerospace Sciences*, 65:41–69, 2014.
- [64] C Liu, X Zheng, and CH Sung. Preconditioned multigrid methods for unsteady incompressible flows. *Journal of Computational Physics*, 139(1):35–57, 1998.
- [65] Tianshu Liu. Comparative scaling of flapping-and fixed-wing flyers. *AIAA Journal*, 44(1):24–33, 2006.
- [66] Krossblade Aerospace. Disc Loading and Hover Efficiency. <https://krossblade.com/disc-loading-and-hover-efficiency> (accessed: 01.09.2024).
- [67] Yuan Lu, Gong Xin Shen, and Wen Han Su. Flow visualization of dragonfly hovering via an electromechanical model. *AIAA Journal*, 45(3):615–623, 2007.
- [68] Guoyu Luo and Mao Sun. The effects of corrugation and wing planform on the aerodynamic force production of sweeping model insect wings. *Acta Mechanica Sinica*, 21(6):531–541, 2005.

- [69] Ruiz M. *Teoria de la Mecanica Clasica*. ETSIAE, 2021.
- [70] Will J Maybury and Fritz-Olaf Lehmann. The fluid dynamics of flight control by kinematic phase lag variation between two robotic insect wings. *Journal of Experimental Biology*, 207(26):4707–4726, 2004.
- [71] Michael Mongelli and Nicholas A Battista. A swing of beauty: pendulums, fluids, forces, and computers. *Fluids*, 5(2):48, 2020.
- [72] Van Duc Nguyen, Viet Dung Duong, Minh Hoang Trinh, Hoang Quan Nguyen, and Dang Thai Son Nguyen. Low order modeling of dynamic stall using vortex particle method and dynamic mode decomposition. *International Journal of Micro Air Vehicles*, 15:17568293221147923, 2023.
- [73] H Niazmand and M Renksizbulut. Surface effects on transient three-dimensional flows around rotating spheres at moderate reynolds numbers. *Computers & Fluids*, 32(10):1405–1433, 2003.
- [74] R Åke Norberg. Hovering flight of the dragonfly *aeschna juncea* l., kinematics and aerodynamics. *Swimming and Flying in Nature: Volume 2*, pages 763–781, 1975.
- [75] ULLA M Norberg. Aerodynamics, kinematics, and energetics of horizontal flapping flight in the long-eared bat *plecotus auritus*. *Journal of Experimental Biology*, 65(1):179–212, 1976.
- [76] Ulla M Norberg. Energetics of flight. In *Avian Energetics and Nutritional Ecology*, pages 199–249. Springer, 1996.
- [77] Jiří Náprstek and Cyril Fischer. Types and stability of quasi-periodic response of a spherical pendulum. *Computers & Structures*, 124:74–87, 08 2013.
- [78] A Obata and S Sinohara. Flow visualization study of the aerodynamics of modeled dragonfly wings. *AIAA Journal*, 47(12):3043–3046, 2009.
- [79] Titilayo Ogunwa, Blake McIvor, Nurkhairunisa Awang Jumat, Ermira Abdullah, and Javaan Chahl. Longitudinal actuated abdomen control for energy efficient flight of insects. *Energies*, 13(20):5480, 2020.
- [80] Masato Okamoto, Kunio Yasuda, and Akira Azuma. Aerodynamic characteristics of the wings and body of a dragonfly. *Journal of Experimental Biology*, 199(2):281–294, 1996.
- [81] Michael V Ol, Luis Bernal, Chang-Kwon Kang, and Wei Shyy. Shallow and deep dynamic stall for flapping low reynolds number airfoils. *Animal Locomotion*, pages 321–339, 2010.
- [82] Robert M Olberg, Andrea H Worthington, and Kurt R Venator. Prey pursuit and interception in dragonflies. *Journal of Comparative Physiology A*, 186:155–162, 2000.
- [83] Vito Pasquariello, Georg Hammerl, Felix Örley, Stefan Hickel, Caroline Danowski, Alexander Popp, Wolfgang A Wall, and Nikolaus A Adams. A cut-cell finite volume–finite element coupling approach for fluid–structure interaction in compressible flow. *Journal of Computational Physics*, 307:670–695, 2016.
- [84] Hoang Vu Phan, Taesam Kang, and Hoon Cheol Park. Design and stable flight of a 21 g insect-like tailless flapping wing micro air vehicle with angular rates feedback control. *Bioinspiration & Biomimetics*, 12(3):036006, 2017.
- [85] Jean Piquet and Xavier Vasseur. Comparisons between preconditioned bicgstab and a multigrid method for the resolution of the pressure equation in a navier-stokes solver. In *Multigrid Methods V: Proceedings of the Fifth European Multigrid Conference held in Stuttgart, Germany, October 1–4, 1996*, pages 225–242. Springer, 1998.

- [86] Max F Platzer, Kevin D Jones, John Young, and Joseph CS Lai. Flapping wing aerodynamics: progress and challenges. *AIAA Journal*, 46(9):2136–2149, 2008.
- [87] DI Pullin and Z Jane Wang. Unsteady forces on an accelerating plate and application to hovering insect flight. *Journal of Fluid Mechanics*, 509:1–21, 2004.
- [88] Youming Qin, Wei Xu, Adrian Lee, and Fu Zhang. Gemini: A compact yet efficient bi-copter uav for indoor applications. *IEEE Robotics and Automation Letters*, 5(2):3213–3220, 2020.
- [89] S. Rajasekaran. 2 - free vibration of single-degree-of-freedom systems (undamped) in relation to structural dynamics during earthquakes. In S. Rajasekaran, editor, *Structural Dynamics of Earthquake Engineering*, Woodhead Publishing Series in Civil and Structural Engineering, pages 9–42. Woodhead Publishing, 2009.
- [90] Hariharan Ramanathan and Ashok Gopalarathnam. Prediction of leading-edge-vortex initiation using criticality of the boundary layer. *Theoretical and Computational Fluid Dynamics*, pages 1–24, 2023.
- [91] Manikandan Ramasamy, Bradley Johnson, and J Gordon Leishman. Understanding the aerodynamic efficiency of a hovering micro-rotor. *Journal of the American Helicopter Society*, 53(4):412–428, 2008.
- [92] Christopher JC Rees. Aerodynamic properties of an insect wing section and a smooth aerofoil compared. *Nature*, 258(5531):141–142, 1975.
- [93] Leif Ristroph, Gunnar Ristroph, Svetlana Morozova, Attila J Bergou, Song Chang, John Guckenheimer, Z Jane Wang, and Itai Cohen. Active and passive stabilization of body pitch in insect flight. *Journal of The Royal Society Interface*, 10(85):20130237, 2013.
- [94] David Rival, Guillermo Hass, and Cameron Tropea. Recovery of energy from leading-and trailing-edge vortices in tandem-airfoil configurations. *Journal of Aircraft*, 48(1):203–211, 2011.
- [95] Vernon J Rossow. Lift enhancement by an externally trapped vortex. *Journal of Aircraft*, 15(9):618–625, 1978.
- [96] G Rüppell. Kinematic analysis of symmetrical flight manoeuvres of odonata. *Journal of Experimental Biology*, 144(1):13–42, 1989.
- [97] David Russell and Z Jane Wang. A cartesian grid method for modeling multiple moving objects in 2d incompressible viscous flow. *Journal of Computational Physics*, 191(1):177–205, 2003.
- [98] David Russell and Z Jane Wang. Numerical and experimental investigation into the aerodynamics of dragonfly flight. In *APS Division of Fluid Dynamics Meeting Abstracts*, volume 57 of *APS Meeting Abstracts*, page AD.008, November 2004.
- [99] David Baker Russell. *Numerical and Experimental Investigations into the Aerodynamics of Dragonfly Flight*. Cornell University, 2004.
- [100] Erfan Salami, Thomas A Ward, Elham Montazer, and Nik Nazri Nik Ghazali. A review of aerodynamic studies on dragonfly flight. *Proceedings of the Institution of Mechanical Engineers, Part C: Journal of Mechanical Engineering Science*, 233(18):6519–6537, 2019.
- [101] Sanjay P Sane and Michael H Dickinson. The control of flight force by a flapping wing: lift and drag production. *Journal of Experimental Biology*, 204(15):2607–2626, 2001.
- [102] Sanjay P Sane and Michael H Dickinson. The aerodynamic effects of wing rotation and a revised quasi-steady model of flapping flight. *Journal of Experimental Biology*, 205(8):1087–1096, 2002.

- [103] Stuart B Savage, Barry G Newman, and Denis T-M Wong. The role of vortices and unsteady effects during the hovering flight of dragonflies. *Journal of Experimental Biology*, 83(1):59–77, 1979.
- [104] Hanspeter Schaub and John L Junkins. *Analytical Mechanics of Space Systems*. AIAA, 2003.
- [105] Andrea Sciacchitano. Uncertainty quantification in particle image velocimetry. *Measurement Science and Technology*, 30(9):092001, 2019.
- [106] Andrea Sciacchitano. *Particle Image Velocimetry Lecture Notes*. Flow Measurement Techniques, TU Delft, 2022.
- [107] Jost Seifert. A review of the magnus effect in aeronautics. *Progress in Aerospace Sciences*, 55:17–45, 2012.
- [108] Ahmed A Shabana. *Dynamics of Multibody Systems*. Cambridge university press, 2020.
- [109] Lan Shilong and Sun Mao. Aerodynamic force and flow structures of two airfoils in flapping motions. *Acta Mechanica Sinica*, 17:310–331, 2001.
- [110] Troy Shinbrot, Celso Grebogi, Jack Wisdom, and James A Yorke. Chaos in a double pendulum. *American Journal of Physics*, 60(6):491–499, 1992.
- [111] Wei Shyy and Hao Liu. Flapping wings and aerodynamic lift: the role of leading-edge vortices. *AIAA Journal*, 45(12):2817–2819, 2007.
- [112] Chris Soms and Marvin Luttges. Dragonfly flight: novel uses of unsteady separated flows. *Science*, 228(4705):1326–1329, 1985.
- [113] K Subbaraj and MA Dokainish. A survey of direct time-integration methods in computational structural dynamics—ii. implicit methods. *Computers & Structures*, 32(6):1387–1401, 1989.
- [114] Mao Sun and Shi Long Lan. A computational study of the aerodynamic forces and power requirements of dragonfly (*aeschna juncea*) hovering. *Journal of Experimental Biology*, 207(11):1887–1901, 2004.
- [115] Xiaojing Sun, Xinyu Gong, and Diangui Huang. A review on studies of the aerodynamics of different types of maneuvers in dragonflies. *Archive of Applied Mechanics*, 87:521–554, 2017.
- [116] Graham K Taylor. Mechanics and aerodynamics of insect flight control. *Biological Reviews*, 76(4):449–471, 2001.
- [117] Adrian LR Thomas, Graham K Taylor, Robert B Srygley, Robert L Nudds, and Richard J Bomphrey. Dragonfly flight: free-flight and tethered flow visualizations reveal a diverse array of unsteady lift-generating mechanisms, controlled primarily via angle of attack. *Journal of Experimental Biology*, 207(24):4299–4323, 2004.
- [118] James R Usherwood and Fritz-Olaf Lehmann. Phasing of dragonfly wings can improve aerodynamic efficiency by removing swirl. *Journal of The Royal Society Interface*, 5(28):1303–1307, 2008.
- [119] Abel Vargas, Rajat Mittal, and Haibo Dong. A computational study of the aerodynamic performance of a dragonfly wing section in gliding flight. *Bioinspiration & Biomimetics*, 3(2):026004, 2008.
- [120] Miguel R Visbal. High-fidelity simulation of transitional flows past a plunging airfoil. *AIAA Journal*, 47(11):2685–2697, 2009.
- [121] C Vuik et al. *Scientific Computing (wi4201)*. TU Delft, 2023.

- [122] JM Wakeling and C Pt Ellington. Dragonfly flight: I. gliding flight and steady-state aerodynamic forces. *Journal of Experimental Biology*, 200(3):543–556, 1997.
- [123] JM Wakeling and CP Ellington. Dragonfly flight: Ii. velocities, accelerations and kinematics of flapping flight. *Journal of Experimental Biology*, 200(3):557–582, 1997.
- [124] JM Wakeling and CP Ellington. Dragonfly flight: Iii. lift and power requirements. *Journal of Experimental Biology*, 200(3):583–600, 1997.
- [125] Hao Wang, Lijiang Zeng, Hao Liu, and Chunyong Yin. Measuring wing kinematics, flight trajectory and body attitude during forward flight and turning maneuvers in dragonflies. *Journal of Experimental Biology*, 206(4):745–757, 2003.
- [126] Ji Kang Wang and Mao Sun. A computational study of the aerodynamics and forewing-hindwing interaction of a model dragonfly in forward flight. *Journal of Experimental Biology*, 208(19):3785–3804, 2005.
- [127] Z Wang. Dissecting insect flight. *Annual Review of Fluid Mechanics*, 37:183–210, 07 2004.
- [128] Z Wang. Dragonfly flight. *Physics Today*, 61, 10 2008.
- [129] Z Jane Wang. Two dimensional mechanism for insect hovering. *Physical Review Letters*, 85(10):2216, 2000.
- [130] Z Jane Wang. The role of drag in insect hovering. *Journal of Experimental Biology*, 207(23):4147–4155, 2004.
- [131] Z Jane Wang and David Russell. Effect of forewing and hindwing interactions on aerodynamic forces and power in hovering dragonfly flight. *Physical Review Letters*, 99(14):148101, 2007.
- [132] Torkel Weis-Fogh. Energetics of hovering flight in hummingbirds and in drosophila. *Journal of Experimental Biology*, 56(1):79–104, 1972.
- [133] Torkel Weis-Fogh. Quick estimates of flight fitness in hovering animals, including novel mechanisms for lift production. *Journal of Experimental Biology*, 59(1):169–230, 1973.
- [134] Robert Wood, Radhika Nagpal, and Gu-Yeon Wei. Flight of the robobees. *Scientific American*, 308(3):60–65, 2013.
- [135] Jianghao Wu, Long Chen, Chao Zhou, Shih-Jung Hsu, and Bo Cheng. Aerodynamics of a flapping-perturbed revolving wing. *AIAA Journal*, 57(9):3728–3743, 2019.
- [136] Jinliang Xu, Chuangxin Zhao, Yongli Zhang, and Yang Zhang. Effect of flapping trajectories on the dragonfly aerodynamics. *Chinese Science Bulletin*, 51:777–784, 2006.
- [137] Lincheng Xu, Fang-Bao Tian, John Young, and Joseph CS Lai. A novel geometry-adaptive cartesian grid based immersed boundary–lattice boltzmann method for fluid–structure interactions at moderate and high reynolds numbers. *Journal of Computational Physics*, 375:22–56, 2018.
- [138] R Yousaf, A Shahzad, MN Mumtaz Qadri, and A Javed. Recent advancements in flapping mechanism and wing design of micro aerial vehicles. *Proceedings of the Institution of Mechanical Engineers, Part C: Journal of Mechanical Engineering Science*, 235(19):4425–4446, 2021.